

A feasibility study of small modular reactor(SMR) power-performance optimisations based on the SMART system

By

YIMING ZHONG

A thesis submitted to
the University of Birmingham
for the degree of
DOCTOR OF PHILOSOPHY

Nuclear Physics Group
School of Physics and Astronomy
College of Engineering and Physical Sciences
University of Birmingham
January 2022

UNIVERSITY OF
BIRMINGHAM

University of Birmingham Research Archive

e-theses repository

This unpublished thesis/dissertation is copyright of the author and/or third parties. The intellectual property rights of the author or third parties in respect of this work are as defined by The Copyright Designs and Patents Act 1988 or as modified by any successor legislation.

Any use made of information contained in this thesis/dissertation must be in accordance with that legislation and must be properly acknowledged. Further distribution or reproduction in any format is prohibited without the permission of the copyright holder.

© Copyright by YIMING ZHONG, 2022

All Rights Reserved

ABSTRACT

Small modular reactors' development provides an alternative option for potentially using nuclear power more economically and effectively. SMART is the world's first licensed, integral, small pressurised water reactor. However, it should still be optimised for the UK's energy market. This thesis has used the stochastic method Monte Carlo codes MONK and OpenMC to investigate the neutronic related behaviours and assess the proposed optimisations. The numerical models based on both codes have been validated and verified, especially to the open-source code OpenMC. The neutron transport simulation and depletion calculation results show that a beryllium-based reflector material would significantly improve fuel assemblies' utilisation rate at the core edge area. This would give higher power output and reduce the frequency of reactor shutdown and refuelling. In addition to the Beryllium Oxide reflector, three types of variant fuel layout were designed. They respectively occupy 57, 44, 28 high enrichment fuel assemblies at different positions. This thesis then proposes two hypothetical construction paths to staggered build of a giga-watt scale, 10 SMART unit power station by combining and switching the core layout. Both paths could self-sustain the reloading fuels and, most importantly, decrease the demand for fresh fuel in every refuelling period.

ACKNOWLEDGMENTS

At first, I would like to sincerely express gratitude to my primary PhD supervisor Dr Paul Norman, who is also the head of my MSc program. He inspired me to do the nuclear reactor research works and gave me patient guidance in this PhD course. I want to thank other Nuclear physics group staffs, Professor Peter Jones, Dr David Forest, Dr Tzany Kokalova Wheldon, Dr Carl Wheldon and Dr Orlando Villalobos-Baillie. I did the teaching work with them in the nuclear laboratory and practical computing classes. They let me know how to be a good demonstrator and showed me some exciting knowledge in the nuclear physics area.

And many thanks should go to those people who helped me finish this research project. Dr Dennis Allen from Jacobs' ANSWERS Software Service and Dr Paul Romano, Dr Patrick Shriwise from the OpenMC development community have helped me solve some Monte Carlo simulation program problems. The computations described in this thesis were performed using the University of Birmingham's BlueBEAR HPC service, which provides a High-Performance Computing service to the University's research community. Our industrial collaborator, Dr Stephen Coulson from Green Frog nuclear company, has given me some opinion about developing a small modular reactor from the nuclear industry aspect, which is valuable.

Sincerely thanks go to the other postgraduate research students in Physics East 318 office. The other seven students started their PhD in the same year with me, Håkan Wennlöf, Pedro Santa Rita, Rebeckah Trinder, Stuart Pirrie, Oliver Jevons, Jakub Kvapil and Anthony Turner. And the students who start in other years, Jack Bishop, Harry Andrews, Nima Zardoshti, Emily Willsher, Simone Ragoni, Angus Hollands, Ross Allen, Sammy Colburn,

Mark Griffiths and Dawid Hampel. I enjoyed working with you guys, and we had great lunchtime and gaming nights together. I wish you all good luck in the future.

I also want to say thanks to those friends who I met in Birmingham during my time here, Buwei He, Yunpeng Li, Chunqiu Xia, Zhongming Zhang, and Hongyu Zhou. At last, I want to give the deepest thanks to my family member, my parent Hongliang Zhong and YanHua Hao. Without their support in all these years, I would not have the courage to study in the UK and finish this PhD. Give my sincere thanks to all the people who helped me in my studying abroad time.

Yiming Zhong, January 2022.

Contents

Page

1 Introductions **1**

1.1 Background 1

1.2 Small Modular Reactor 2

1.3 SMR in the United Kingdom 4

1.4 Thesis Objectives 7

2 Literature Review **9**

2.1 SMART Reactor 9

2.1.1 Development Process of SMART 9

2.1.2 Reactor Pressure Vessel 12

2.1.3 Reactor core and fuel management 19

2.2 Competitor for SMART 21

2.2.1 ACP100 21

2.2.2 Advanced SMRs 24

2.3 Optimisations 26

2.3.1 Fuel selections 27

2.3.2 Reflector saving 31

2.4 Summary of literature review 36

3 Methodology **38**

3.1 Criticality . . . 38
3.2 Burn-up . . . 40
3.3 Neutron transport . . . 42
3.3.1 Time-dependent . . . 47
3.3.2 K-eigenvalue problems . . . 51
3.4 Deterministic methods . . . 52
3.5 Stochastic methods . . . 56
3.5.1 Neutron History . . . 56
3.5.2 Monte Carlo methods . . . 57
3.5.3 Neutron tracking . . . 61
3.5.4 Results Estimates . . . 70
3.5.5 Results collection . . . 73
3.5.6 Accuracy estimation . . . 74
3.5.7 Non-analog Monte Carlo . . . 75
3.6 Summary of Methodology . . . 76

4 Model Build-up, Verification and Sensitivity Study 78

4.1 MONK . . . 79
4.1.1 Body geometry . . . 80
4.1.2 Hole geometry . . . 82
4.1.3 MONK SMART model . . . 83
4.1.4 Materials and source . . . 85
4.1.5 Criticality calculation . . . 86
4.2 MCBEND . . . 87
4.3 OpenMC . . . 88
4.3.1 Material Compositions . . . 90
4.3.2 Specifying Tallies . . . 91

4.3.3 Code verification . . . 92
4.3.4 Computing facility and parallelism . . . 93
4.3.5 Sensitivity study . . . 96
4.3.6 Temperature reactivity effect . . . 99
4.3.7 Burn-up zone study . . . 102
4.4 Chapter summary . . . 108

5 Results and discussion 110
5.1 Normal SMART . . . 110
5.1.1 Neutron flux spatial distribution . . . 112
5.1.2 Neutron energy spectrum . . . 118
5.1.3 Heating map . . . 122
5.2 Normal SMART depletion . . . 124
5.2.1 Eigenvalue variation . . . 124
5.2.2 Fission Rate and Uranium utilisation . . . 126
5.3 Reflector material selection . . . 130
5.3.1 Elastic scattering . . . 132
5.3.2 Inelastic scattering . . . 135
5.3.3 (n,2n) reaction . . . 136
5.4 Reflected SMART core . . . 138
5.4.1 Beryllium oxide reflector saving . . . 152
5.5 Variant core layouts . . . 161
5.6 Fuel shifting for the staggered build approach . . . 165
5.7 Chapter summary . . . 168

6 Conclusion 170

A Other reflector results 173

B OpenMC model code **183**

References **195**

List of Figures

1.1 Rolls-Royce SMR design of Reactor Coolant System[13]. 4

1.2 The Global SMR Market Assessment [14, 16]. 6

2.1 Various SMART Testing facilities in the basic development stage [17]. 10

2.2 The Development Program of SMART [20]. 11

2.3 The Schematic Diagram for the SMART reactor's Pressure Vessel[23]. 12

2.4 SMART Steam Generator.(a)The Schematic Diagram for helical coiled once-through SGs [20]. (b) The coolant flow path though SGs [24]. 14

2.5 Vertical Recirculating-type Steam Generator, using US-designed as a demonstration [25] 15

2.6 Canned motor reactor coolant pump of SMART [20]. 17

2.7 Schematic diagram of a typical PWR fuel assembly [32]. 19

2.8 SMART core loading pattern and control rod arrangement[18, 20]. 20

2.9 ACP100 reactor with other main equipment connected [36]. 22

2.10 Construction of the HTGR in Shandong Province,China [47]. 25

2.11 Transmutation-decay chains for ^{238}U and ^{232}Th[64]. 28

2.12 MOX fuel in PWR fuel assembly.(a): k_∞ versus burn-up for uranium and MOX fuel. (b): The schematic diagram for a 17×17 MOX fuel PWR assembly [72] 30

2.13 The view from top of the WWER-1000 nuclear core. The lower support structure, the neutron reflector and 11 assemblies [91, 92]. 32

3.1 Uranium burn-up chain [64]. 40
3.2 Neutron flow through planar surface element dS [116]. 43
3.3 The birth of a delayed neutron from Br-87 [120]. 48
3.4 Neutron energy group numbering scheme. 52
3.5 The homogenisation of the reactor core. (a) the structure of a fuel assembly. (b) Cell-by-cell homogenisation. (c) Complete homogenisation of the assembly. (d) Homogeneous reactor core. 55
3.6 Schematic diagram of a single neutron history [118]. 56
3.7 A random variable x sampling from an exponential probability distribution [130]. 60
3.8 The diagrams of CM- and L- frames. $\vec{V_{CM}}$ is the velocity of CM-frame origin refers to the L-frame origin [130]. 66
3.9 Neutron direction of incident $\vec{\Omega_c}$ and after collision $\vec{\Omega'_c}$, and polar θ_c and azimuth ϕ_c scattering angles [130]. 68

4.1 MONK geometry examples of nest, cluster and general parts. 81
4.2 Simplified SMART reactor core model. 83
4.3 MONK k-eff simulation results with 500 stages. 87
4.4 Radial and vertical directions slice plots of the OpenMC SMART core. . . . 89
4.5 The process of parallel computing. 94
4.6 Convergence process of k_{eff} values in the sensitivity study. 98
4.7 Schematic diagram of Burn-up material spatial repeating distribution. 103
4.8 The k_{eff} variations in several burn-up calculations with the different number of spatial zones. 105
4.9 The comparison between the results of single and 4×3 burn-up zones division and different moderator densities. 107

5.1 Updated OpenMC model of the SMART reactor core to have two enrichment levels (2.4% and 4.8%) for fuel shifting. 111
5.2 The thermal and fast neutron flux distributions in the two-batch refuelling scheme core. 114
5.3 Cold and hot state neutron flux distributions viewed along a diameter in the x-axis direction. 116
5.4 The slices of 3D thermal and fast neutron flux distribution. 117
5.5 The neutron energy spectrum of core, reflector and steel barrier in the cold and hot states. 119
5.6 The neutron energy spectrum of different position fuel assemblies. 121
5.7 The fission rate distributions on the XY and YZ planes 123
5.8 k_{eff} variation of the two-batch refuelling scheme core depletion by different integrator. 125
5.9 Burn-up results of 4×3 zones two batch refuelling scheme core. 127
5.10 The enrichment variations in the radial burn-up zones. 129
5.11 Elastic scattering ($MT = 2$) cross-sections ($0K$) of ^{1}H,^{2}H,^{9}Be,^{12}C, ^{16}O versus incident neutron energy. 133
5.12 The elastic scattering cross-section of heavy atomic mass isotopes ^{56}Fe, ^{183}W. 134
5.13 Inelastic scattering ($MT = 4$) cross-sections of ^{12}C, ^{16}O, ^{56}Fe, ^{183}W. 135
5.14 $(n, 2n)$ reaction, $MT = 16$ cross-section distributions of ^{2}H, ^{9}Be,^{56}Fe,^{183}W. 137
5.15 Bar charts of thermal and fast neutron flux mean values for core, reflector and barrier. 141
5.16 Thermal and fast neutron flux spatial distributions in the light water and BeO reflector. 142
5.17 Values of neutron flux versus the distance away from fuel assembly (FA) boundaries. 143
5.18 Neutron energy spectra in different neutron reflector materials. 144

5.19 Neutron reflectors' scattering rate distributions with neutron energy. 145
5.20 Heating maps of two-batch refuelling scheme core with light water reflector. . 148
5.21 Heating maps of two-batch refuelling scheme core with particular material reflectors. 149
5.22 The comparison between k_{eff} variations of normal SMART with different reflector materials. 150
5.23 The BeO neutron reflector effect to the enrichment variations. 153
5.24 Thermal and fast neutron flux distributions within BeO reflected and non-reflected core. 154
5.25 The fission rate versus neutron energy in different burn-up zone fuel assemblies. 155
5.26 The energy spectrum diagrams of the beryllium oxide reflected core. 156
5.27 Heating map throughout the fuelling cycle of the BeO-reflected reactor core. 158
5.28 The heating maps of the light water-reflected core and the BeO reflected core at different time points. 160
5.29 The geometry structures of variant core layouts and their normalised heating maps. 162
5.30 The burn-up calculation results of variant core layouts. 163

A.1 The ^{235}U enrichment variations in light water-reflected core layouts. 174
A.2 The ^{235}U enrichment variations in beryllium-reflected core layouts. 175
A.3 The ^{235}U enrichment variations in heavy water-reflected core layouts. 176
A.4 The ^{235}U enrichment variations in graphite-reflected core layouts. 177
A.5 The ^{235}U enrichment variations in steel-reflected core layouts. 178
A.6 The ^{235}U enrichment variations in tungsten carbide-reflected core layouts. . . 179
A.7 Heating maps of variant(a) core layout with different material reflectors . . . 180
A.8 Heating maps of variant(b) core layout with different material reflectors . . . 181
A.9 Heating maps of variant(c) core layout with different material reflectors . . . 182

List of Tables

1.1 Selected SMRs in the Feasibility Study [14]. 5

2.1 The technical parameters of the SMART RPV [20]. 13
2.2 The design parameters of SMART SG and RCP [20] 16
2.3 The technical parameters of SMART NPP [20, 31] 18
2.4 Major Technical Parameters of ACP100 [36]. 23
2.5 Effect of adding 0.1 w/o impurity on thermal neutron absorption cross-section of beryllium [100]. 34

3.1 Delayed neutron data for thermal fission in ^{235}U [121] 49

4.1 The OpenMC SMART reactor model's foundation materials compositions, which are specified by atom fractions. 90
4.2 The k_{eff} eigenvalue calculated results from OpenMC and MCNP benchmark. 93
4.3 OpenMC calculation speeds with parallelism models(Unit: Particles/second). 95
4.4 The k_{eff} results from the simulations with the different databases. 97
4.5 The temperature setting of fuel and water in the OpenMC simulations. . . . 101
4.6 The simulation results with different temperature conditions. 102
4.7 The k_{eff} results with different bun-up zone partition methods at selected steps. 106

5.1 The eigenvalues simulation results of the reactor cold and hot states. 115
5.2 k_{eff} values at the start and end of depletion and reactivity. 125
5.3 The burn-up results, number of ^{235}U change in one refuelling cycle. 128

5.4 Material properties of potentially available reflector materials. 131
5.5 Threshold of $(n, 2n)$ reactions and cross-sections. 137
5.6 Average thermal and fast neutron flux tally results(means and Standard deviations) in core, reflector and barrier. 139
5.7 The total scattering rate and absorption rate of reflector material. 146
5.8 Scattering rates and absorption rates of each nuclide in compound materials. 146
5.9 k_{eff} eigenvalue results of two-batch refuelling scheme core with different material reflector. 147
5.10 The k_{eff} values at the beginning and end of the cycle in each of the depletion calculations. 151
5.11 ^{235}U changes in SMART with BeO neutron reflector, and the differences with table 5.3. 152
5.12 k_{eff} results of original and updated large neutron history depletion. 158
5.13 The total number of ^{235}U atom in the BeO reflected and three variants SMART core. 164
5.14 Enrichment's variations in each radial BU zone of three variant core layouts. 165
5.15 The number of fresh and reloading FAs in the different core layouts. 166
5.16 Two hypothetical paths to staggered build of a 1100 MWe, 10 SMART units nuclear power plant. 167

A.1 The number of burned ^{235}U in light water-reflected core layouts. 174
A.2 The number of burned ^{235}U in beryllium-reflected core layouts. 175
A.3 The number of burned ^{235}U in heavy water-reflected core layouts. 176
A.4 The number of burned ^{235}U in graphite-reflected core layouts. 177
A.5 The number of burned ^{235}U in steel-reflected core layouts. 178
A.6 The number of burned ^{235}U in tungsten carbide-reflected core layouts. 179

Acronyms

ACP100 Advanced China Power 100. 21–24

AGR Advanced Gas-cooled Reactors. 24

API application program interface. 95

BOC beginning of the cycle. 126, 165

BU burn-up. 40–42, 77–79

CAD computer-aided design. 88

CDF cumulative distribution function. 58, 59

CIR continuum inelastic reactions. 70

CLASS Core Library for Advanced Scenario Simulation. 30

CLT central limit theorem. 74, 75

CM-frame centre-of-mass frame. 65–69

CNNC China National Nuclear Corporation. 21

CR control rod. 19–21, 93

CRDM control rod drive mechanism. 12

CSEWG cross section evaluation working group. 96

DRHRS direct passive residual heat removal system. 17

EFPD effective full power days. 20

ENDF evaluated nuclear data file. 96, 131, 132, 136, 138, 170, 171

EOC end of the cycle. 126, 129, 151, 163, 165, 171

FA fuel assembly. x, xiii, 19, 22, 23, 26, 28, 36, 83, 84, 88, 93, 104, 108, 110, 112, 113, 124, 126, 128, 129, 143, 153, 154, 156, 157, 161, 163–169, 171, 172

FP fission production. 92

FTC fuel temperature coefficient. 100, 101

GDA general design assessment. 7

HMR heavy material reflector. 35

HOCOTSG helical coil once-through steam generator. 13–16, 36

HPC high-performance computing. 93

HTGR High-temperature gas-cooled reactor. 5, 24, 35, 130

HTR-PM high-temperature gas-cooled reactor pebble-bed module. 24

IAEA International Atomic Energy Agency. 2, 6, 7, 33, 131

INL Idaho National Laboratory. 3

JEFF joint evaluated fission and fusion file. 96, 97, 100, 170

K.A.CARE King Abdullah City for Atomic and Renewable Energy. 11

KAERI Korea Atomic Energy Research Institute. 7, 9, 15, 170

KCE kinetic collision equations. 65, 66

L-frame laboratory frame. 65, 66, 68–70

LB-LOCA large break loss of coolant accident. 12, 16

LLN law of large numbers. 74, 75

LMFR Liquid Metal Cooled Reactor. 25, 27

MC Monte Carlo. 57, 65, 70, 73–80, 87, 88, 96, 99, 102, 108, 112, 122, 138, 172

MCNP Monte Carlo N-Particle Transport Code. 33, 35, 92, 93, 171

MDNBR minimum departure from nucleate boiling ratio. 15

MOXEUS MOX on enriched uranium support. 30

MP shared-memory parallelism. 88

MPI distributed-memory parallelism. 88, 94, 95

MSIP Ministry of Science and ICT and Future Planning. 11

MSR Molten Salt Reactor. 25

MTC moderator temperature coefficient. 100, 101, 107

NEA Nuclear Energy Agency. 97

NNL National Nuclear Laboratory. 5, 21, 31

NPP nuclear power plant. 1, 3, 11, 15, 17, 18, 22, 24

NRC nuclear regulatory commission. 3

NSSC Nuclear Safety and Security Commission. 10

OpenMP shared-memory parallelism. 94, 95

PDF probability density function. 58, 60, 77

PHWR pressurised heavy water reactor. 27

PSS passive safety system. 3, 5, 24

PWR pressurised water reactor. 4–6, 11–14, 19–21, 24, 25, 27–31, 35, 92, 100, 112, 130, 131, 170, 172

RCP reactor coolant pump. 12, 13, 16, 36

RCS reactor cooling system. 3, 15, 22

RIA reactivity-initiated accidents. 100

RPV reactor pressure vessel. 2, 3, 12, 13, 16, 18, 23, 25, 35, 36

SBLOCA small break loss of coolant accident. 16

SDA Standard Design Approval. 10

SFR sodium-cooled fast reactor. 92, 93

SG steam generator. 2, 12, 13, 16

SGTR steam generator tube rupture. 14, 17

SMART System-integrated Modular Advanced Reactor. 6–13, 15–24, 26, 29, 36, 38, 76, 78, 79, 83, 86, 88, 90, 101, 112, 130, 138, 152, 161, 164, 168–172

SMR Small Modular Reactor. 2–7, 14, 17, 21, 24, 26, 31, 32, 35, 36, 39, 170, 172

TH thermal hydraulic. 15–17, 40, 79

UAMPS Utah Associated Municipal Power Systems. 3

WNA World Nuclear Association. 1

Chapter One

Introductions

1.1 Background

Clean and affordable energy is a basic necessity for comprehensive social developments. In the predictions, the worldwide electricity demand is growing at an annual rate of 2.5% until 2030. In order to meet the demand, many countries consider mixing the non-fossil based energy source into their energy supply system [1]. Nuclear power is a reliable energy option that has zero greenhouse gas emissions during the power plant operation. According to World Nuclear Association (WNA)[2], about 30 countries are considering, planning, or starting their nuclear power programmes, and a further 20 countries have at some point expressed interest in nuclear power.

At the moment, the major growth of nuclear energy still comes from the countries where nuclear technology has already well established. In 2018, a total of 11.2 GW of new nuclear capacity had been brought online, which is the biggest addition since 1989, and 60 GW capacity still under construction. Moreover, the nuclear power plant (NPP) refurbishments are ongoing in several countries to extend the lifetime. In the United States, about 90 percent of NPPs have already renewed operating licences once, extending their lifetime

from 40 years to 60 years, and a few plants are seeking the second 20 years extension[3, 4]. However, the nuclear energy policy remains uncertain in many counties due to complex problems, such as the large early-stage capital investment, radioactive waste disposal, nuclear accident risk, and nuclear facilities decommissioning. The French government confirmed its objective to reduce the nuclear power share from 75% to 50% before 2035, and the Belgium government confirmed it would phase out nuclear generation (50%) by 2025, replaced by natural gas [3, 5].

Before the Fukushima Daiichi nuclear accident, a few researchers have already recognised the smaller sized reactors would have a significant role in the next nuclear era. [6]. The development of small reactors began at the early 1950s for the power source for the nuclear submarines. Over the years, many countries are continuously developing various types of small reactors, including the research and prototype reactors. The research target in this thesis is the potential small commercial power reactors. That would be called the Small Modular Reactor (SMR) in the following sections.

1.2 Small Modular Reactor

According to the definitions from the International Atomic Energy Agency (IAEA), the small reactors have the electrical output less than 300 MW(e), and a medium reactor as one having the power output between 300 and 700 MW (e). Contrast to the traditional large nuclear or fossil-fuel power generating facilities that usually have power output over 700 MW(e). SMRs are relatively small both of their power output and physical size.

Additionally, the other important design feature of SMRs is the modularity concept. This idea would be adopted in both manufacture and installation process. The major components of the power units, including the reactor pressure vessel (RPV), steam generator

(SG), and reactor cooling system (RCS) would be fabricated in the centralised manufacturing facilities. Meanwhile, the primary reactor parts can be integrated within the RPV, meaning a reduced need for external cooling pipework. The fabricated modules would be shipped for on-site installation. This approach has several advantages, such as the standardisation of components fabrication, shortening construction schedules [7]. These advantages can massively improve the economic performance of SMRs.

Therefore, the research target in this thesis actually is the small and medium-sized or modular reactors, generally named SMRs. Due to the nature of the small size and modular design, the SMRs usually adopts the passive safety system (PSS). The passive safety feature means the SMRs are able to shut down automatically while cooling without external power source or operator intervention. The classical PSS have residual heat removal system, accumulator, condensing heat exchangers, suppression pools and safety injection system [8]. These systems and facilities would cool the reactor through gravity, convection, and evaporation[9]. The absence of power-driven safety components would simplify the SMRs system and reduce construction costs. The PSS make the SMRs become more competitive in the global energy market.

The research and development (R&D) of SMRs get attentions in both nuclear established and newcomer countries. In the United States, the nuclear regulatory commission (NRC) completed the first certification step of the NuScale SMR design[10]. The NRC has targeted a completion date for the certification process by January 2021 [11]. The NPP construction plan also launched, as part of the Carbon-free power project, Utah Associated Municipal Power Systems (UAMPS) is proposing to build an SMR power generation facility which has 12 NuScale reactor modules at the Idaho National Laboratory (INL) site [12]. Other nuclear established countries such as Canada and Russia also have their own SMR development plans for power generation or export trade. The newcomer countries such as Saudi Arabia is cooperating with other countries to do the feasibility studies for various

nuclear power applications. UK government also has shown an interest in SMRs, and the R&D plan for SMRs in the UK will be introduced in the next section.

1.3 SMR in the United Kingdom

The UK SMR is developed by Rolls-Royce & Partners, the design is based on optimised and enhanced use of proven technologies. As shown in Figure 1.1, there are three coolant loops closely coupled with pressurised water reactor (PWR) core, providing power output at $400 - 450$ MWe from $1200 - 1350$ MWth, using industry-standard UO_2 fuel.

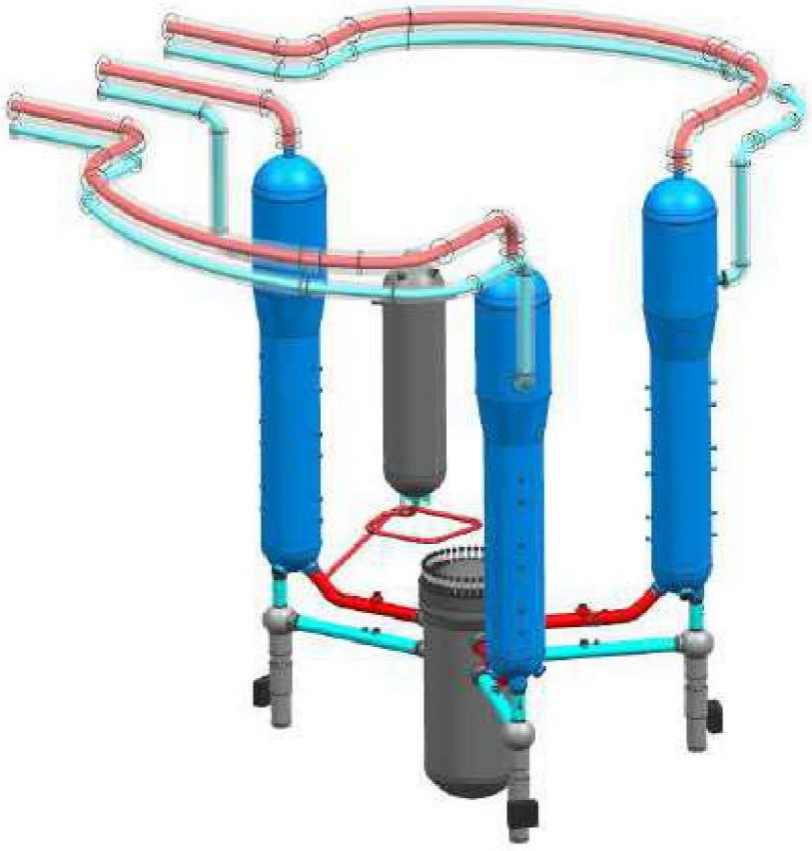


Figure 1.1: Rolls-Royce SMR design of Reactor Coolant System[13].

The design also includes multiple active and PSS, each with substantial internal redundancy. The Rolls-Royce SMR is designed to optimise the levelized cost of electricity against the capital cost. And that aims to deploy the first SMR in the UK by 2030 [13].

Meanwhile, the UK government also considering the SMR technologies from other countries. In 2014, the government published a report [14] produced by a consortium led by the National Nuclear Laboratory (NNL). The report summarises the feasibility studies to assess the technical, economic and commercial cases for the development of the SMRs in the UK and pointed out that some SMR designs were potentially viable within ten years time frame. Then they offer the possibility for the UK nuclear industry to engage in collaborations with the technology vendors. A shortlist of six SMR designs was identified than can meet the requirements from both the technical and financial sides.

Table 1.1: Selected SMRs in the Feasibility Study [14].

Design	Type	Output MW(th/e)	Designer	Country
ACP100+	Integral PWR	385/125	CNNC	China
ANTARES	Integral PWR	$625/ > 200$	AREVA	France
mPower	Integral PWR	575/195	Generation mPower	USA
Westinghouse	Integral PWR	$800/ > 225$	Westinghouse Electric	USA
NuScale	Integral PWR	160/50	NuScale Power	USA
U-Battery	HTGR	$2 \times 10/2 \times 3$	Urenco	UK

As shown in table 1.1, the most selected SMR technologies are integral PWR. AREVA used to develop an High-temperature gas-cooled reactor (HTGR) SMR, but they were no longer considering that. Instead of that, they started to design a PWR SMR and it has needed a longer time to finish the design process. The other HTGR in the table 1.1 is U-Battery, due to the relatively lower power output this design should be categorised as the

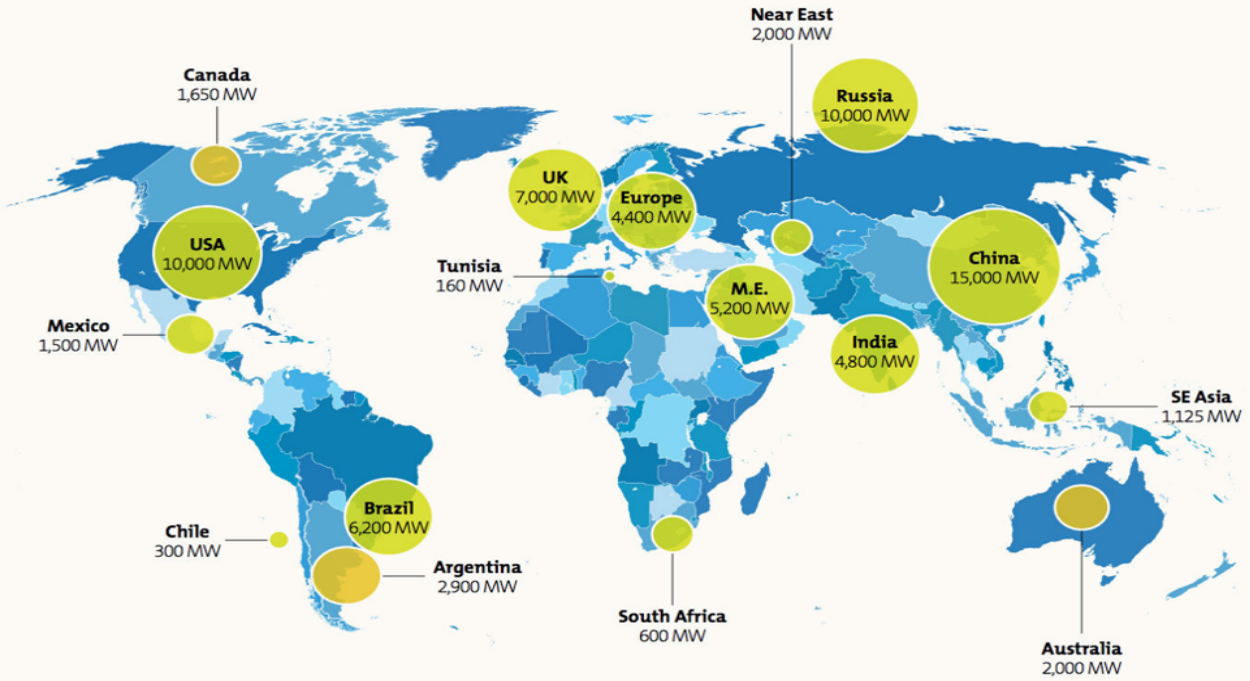


Figure 1.2: The Global SMR Market Assessment [14, 16].

micro-reactor. This concept is reasonably well developed in some areas, however as a total system it still has some immature parts, with potential technical, licensing and economic challenges. Therefore, this technology should be placed in a future technologies category, not in the ten years development plan. The Korean System-integrated Modular Advanced Reactor (SMART) reactor has also been considered. Comparing to the designs shown in table 1.1, SMART has a relative higher maturity. As the world's first licensed SMR [15] it was not included in the feasibility study stage in 2014. Since the SMART system and most of the designs in table 1.1 are integral small PWRs, this means their technology has the greatest maturity on both technical and economic aspects at the moment.

SMR technologies are developing in parallel worldwide. However, the power output of the UK owned Rolls-Royce SMR is obviously higher than the overseas SMRs at around $400-500$ MWe from $1200-1350$ MWth. This difference caused by the definition of SMR in the UK is different with the IAEA. In the UK, seeing any reactor from 1 MW to 600 MW is

an SMR, while as mentioned in the previous section, IAEA defines any reactor power output lower than 300 MW as an SMR. A higher power output SMR can meet the demands of the UK long-term energy market, and that plant can take up significantly less physical space than equivalent power output of wind and/or solar farms. Meanwhile, the higher power SMR technology could be exported to the overseas market. According to the market assessment in feasibility studies [14], the size of the potential global SMR market will be approximately $65 - 85$ GW by 2035, valued at $250 - 400$ billions pounds. The results of the global SMR market assessment have been shown in Figure 1.2.

1.4 Thesis Objectives

The Green Frog (GF) nuclear is a British independent Birmingham local power generation company. They are developing the world's only licensed SMR SMART with their Korean partners and try to bring SMART into the UK market. At the early stage of this PhD project, our research group had a meeting with the representatives of GF nuclear. They noted that any further improvements that could be used to enhance the UK SMART would increase the general potential for SMRs to be exploited in the UK. The UK nuclear regulator would then be happy to begin the general design assessment (GDA) process of these SMR technologies, and that would give investors more confidence to develop the SMRs in the UK.

For example, if the power output of SMART could be stretched to a higher value than 300 MWth or 100 MWe that the original designer Korea Atomic Energy Research Institute (KAERI) stated. This would then better satisfy the demand for UK energy, meaning that the development of SMART would have brighter prospect.

In order to answer the above questions the SMART reactor was chosen as the reference reactor design for this study. A neutron physics model of the SMART reactor core was built to analyse the reactor system performance. A series of innovative optimisations were applied to the SMART reactor model trying to get extra power output from the original design. These optimisations are focused on the SMART system design in this study, but the principle is not limited to this single design. Technically speaking, due to the similarity of reactor core design, other integral PWR designs such as ACP100 and NuScale also can benefit from the optimisations. The detailed technical parameters of the SMART reactor and the modifications for the integral PWRs studied by other researchers would be introduced in the below literature review.

Chapter Two

Literature Review

2.1 SMART Reactor

2.1.1 Development Process of SMART

As mentioned in chapter one, the SMART reactor is an integral type multi-purpose PWR designed by KAERI. Before studying the feasibility of the neutron physics optimisation on the original design, the development progress of SMART and its basic technological parameters will be reviewed in this section.

The reactor aims to generate $90MW$ of electricity and produce 40000 m^3/day of desalinated water. The first design stage focused on the reactor core, primary fluid system, and structural components. In this stage, the basic thermal-hydraulic tests were also performed [17]. The testing facilities are shown in Figure 2.1, such as the water chemistry and the critical heat experiment platforms. Moreover, the unique SMART design methodologies were built and validated, including computer codes and a reactor vessel assembly model [18].

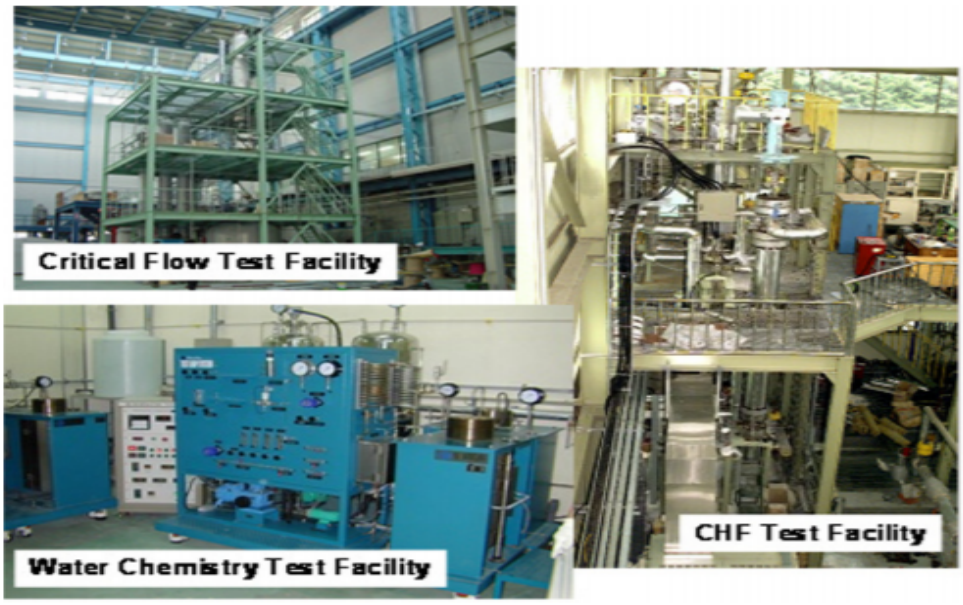


Figure 2.1: Various SMART Testing facilities in the basic development stage [17].

In 2002, a 20% SMART power level ($65MWth$) demonstration plant project was launched, called SMART-P. The objective of the SMART-P project is to polish the initial design technology further meanwhile assess overall performance and safety.[19]. During the SMART-P licensing process, the optimised design of SMART was still being carried out. Meanwhile, the major facilities' fabrication and maintenance demands were scrutinised. In this period, the design concept of SMART was modified via several aspects in order to make the licensing requirements better.

From 2009, the validation of SMART and the standard design approval processes were carried out. After that, the full set of licensing documents were submitted to the Nuclear Safety and Security Commission (NSSC) of Korea. The Standard Design Approval (SDA) for SMART was officially issued in July 2012, after one and a half years of licensing review and assessment time. This makes SMART the first licensed integral PWR in the world. The development of SMART took over 275 million USD and 1500 R&D man years [20]. The development process of SMART is summarised in Figure 2.2.

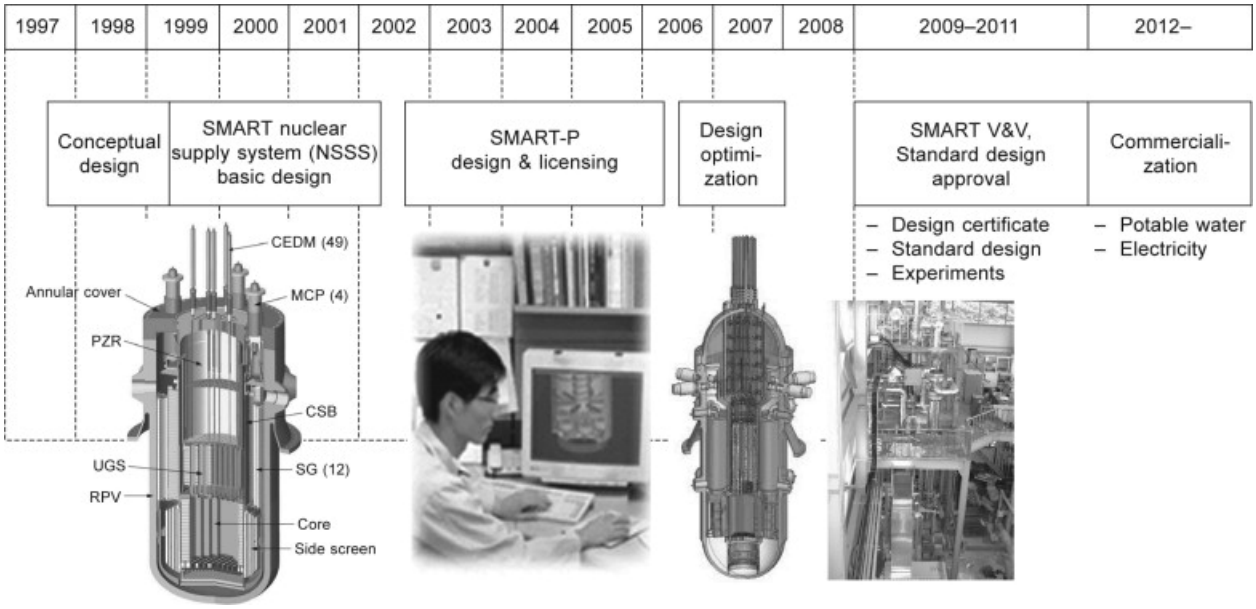


Figure 2.2: The Development Program of SMART [20].

On the third March 2015, a memorandum was signed between the Ministry of Science and ICT and Future Planning (MSIP) of South Korea and the King Abdullah City for Atomic and Renewable Energy (K.A.CARE) of the Kingdom of Saudi Arabia. Both countries will prepare for a preliminary safety analysis report on the first SMART NPP in Saudi Arabia. Both organisations agreed to cooperate on the commercialisation and export of SMART [21]. Afterwards, in early 2020, the organisations from South Korea and Saudi Arabia signed a renewed memorandum, which aims to shorten the review process in order to accelerate the construction of SMART and speed its licensing process [22].

In summary, SMART is a mature integral PWR technology. Significant time and effort has been spent on its development and commercialisation. It is ready to face the challenges from the market and from complex application environments. In the rest of this section, technological details of different components of the SMART system will be introduced.

2.1.2 Reactor Pressure Vessel

For an integral PWR like SMART, the importance of the RPV cannot be ignored. Figure 2.3 presents the schematic diagram of the SMART RPV. A single RPV unit contains the major primary systems such as nuclear fuel and core, 8 SGs, a pressuriser, 4 reactor coolant pump (RCP)s and 25 control rod drive mechanism (CRDM)s [20].

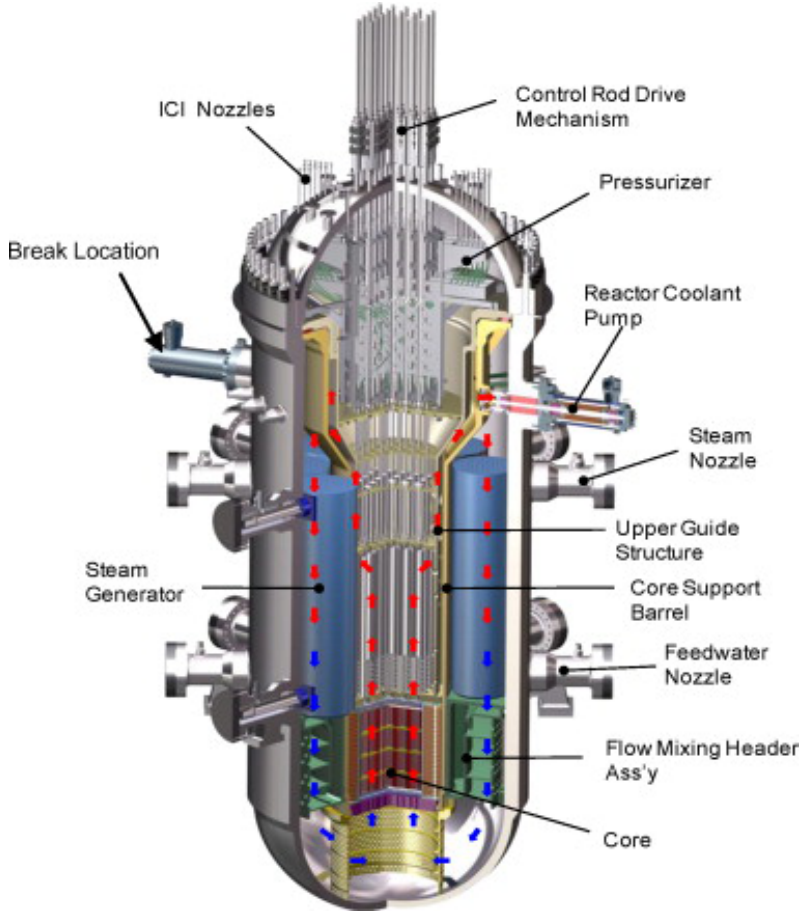


Figure 2.3: The Schematic Diagram for the SMART reactor's Pressure Vessel[23].

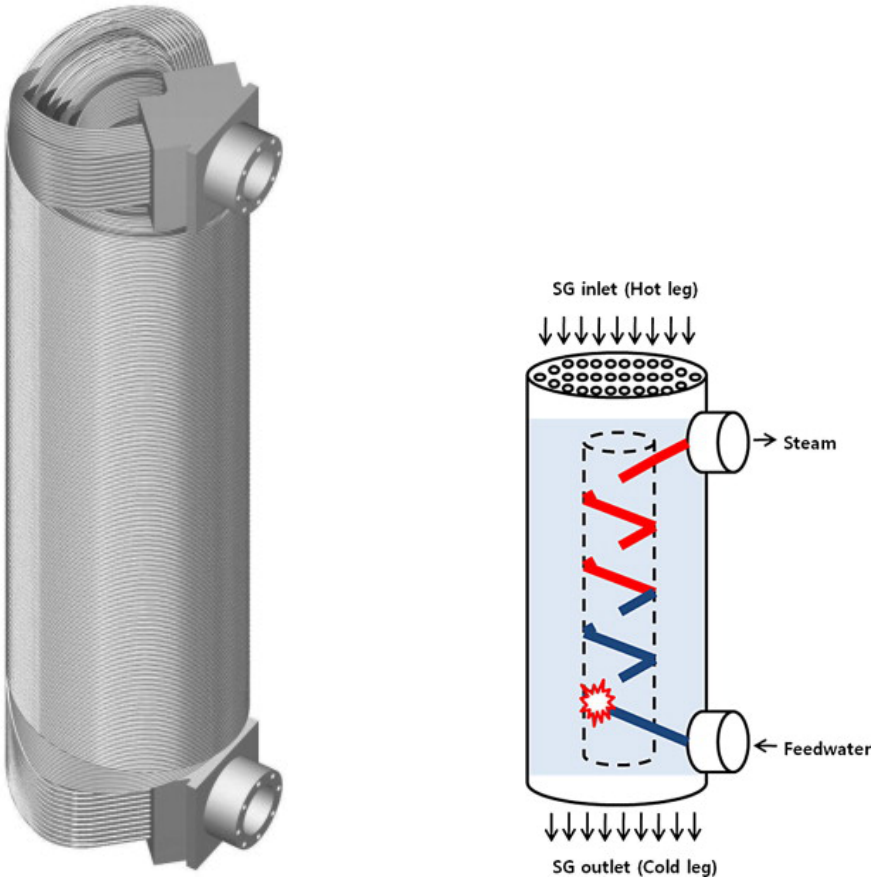
Compared with traditional large PWRs, due to the usage of the integrated arrangement RPV, it is no longer necessary to use large pipe connections between the major reactor components. Therefore, the risk of large break loss of coolant accident (LB-LOCA) would be eliminated fundamentally.

Table 2.1: The technical parameters of the SMART RPV [20].

Technical Parameters	Values
Inner diameter of cylindrical shell	5332mm
Design pressure	17 MPa
Design temperature	$360°C$
Base material	SA580,Class 3
Total height	15.5m

The parameters of the SMART RPV are shown in table 2.1. Inside the RPV, there are eight SGs installed at the higher position above the reactor core. The SGs adopt helically coiled heat transfer tubes to generate high grade steam when the reactor is operating. The primary coolant is pumped by RCPs from the bottom of the core, and then flows downward through the shell side of the steam generator. Meanwhile, the secondary side feed-water enters the helically coiled tube from the bottom of the SGs and flows upward to remove the heat from the shell side[24]. Figure 2.4(a) shows the schematic diagram of SMART SGs. And the figure 2.4(b) gives the path of reactor primary loop coolant and the fluid direction of the secondary feed-water. After exchanging heat in the SGs, the reactor coolant would exit the SGs at the bottom, then flow into the flow mixing header assembly, and then enter the core again. This type of helical coil once-through steam generator (HOCOTSG) is a characteristic design of integral PWRs.

The traditional large PWRs usually adopt re-circulation SGs which have U-tube bundles. The hot primary coolant flows through the inside of the U-tube. And the feed-water flows down outside of the tubes, where it would be mixed with water coming from the separator deck. The water enters the heating surface at the bottom of U-tube and rises through the SGs. Steam would be separated from the mixture at the separator and from there leave



(a) (b)

Figure 2.4: SMART Steam Generator.(a)The Schematic Diagram for helical coiled once-through SGs [20]. (b) The coolant flow path though SGs [24].

the SGs at the top, via a steam nozzle, and water would go back for re-circulation [26, 27]. Figure 2.5 presents the diagram of a classic vertical U-tube recirculating SG. Although the design of integral PWR systems has been influenced by the more established large PWR designs, there still exist some questions that need to be investigated.

The HOCOTSG is employed by SMRs because of its advantages on compact structure, enhanced heat transfer efficiency, and ease of manufacture [28]. The design parameters of the HOCOTSG are given in table 2.2. A series of safety parametric studies and the bounding case investigation for a steam generator tube rupture (SGTR) accident have also

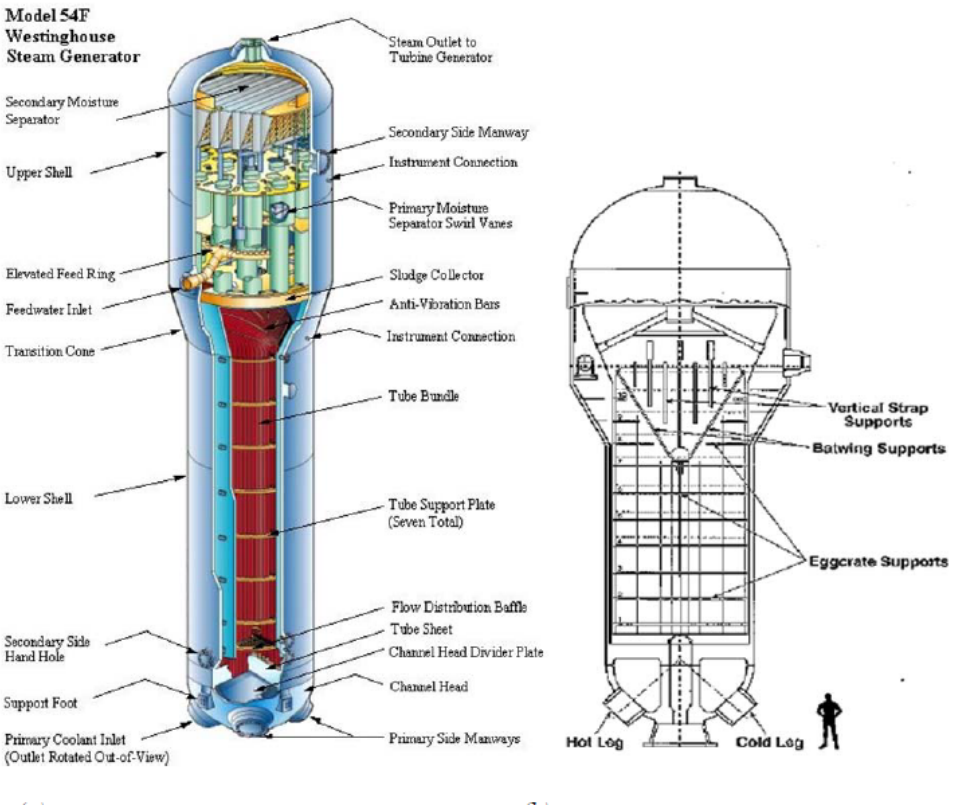


Figure 2.5: Vertical Recirculating-type Steam Generator, using US-designed as a demonstration [25]

been done by researchers from KAERI. Kim's study [24] has proven that the maximum RCS and secondary system pressures do not exceed the design pressure following an SGTR accident. The minimum departure from nucleate boiling ratio (MDNBR) remains above the safety limit value throughout such an accident. Also no violation of the fuel thermal limit occurs. The NPP keeps stable conditions during the entire transient time.

In order to study the thermal hydraulic (TH) problems and safety analysis of major components in the SMART reactor, a TH analysis, one step implicit numerical method code, TASS/SMR [29] has been developed and validated. The validation results showed the code predicted conservatively compared with the experimental results. TASS/SMR code also includes the models of HOCOTSG heat transfer and of condensate heat ex-changer.

Kim's study had adopted the TASS/SMR code to calculate the TH behaviours and perform a sensitivity evaluation during the accident analysis.

Table 2.2: The design parameters of SMART SG and RCP [20]

Technical Parameters	Values
Steam generator(SG)	
Number	8
Tube outside diameter	17mm
Tube material	Inconel 690
Reactor coolant pump(RCP)	
Circulation type	Forced
Number of pumps	4
Heat at rated conditions	27m
Flow at rated conditions	$0.89m^3/s$

The other unique design feature is the employment of the canned motor pumps, the parameters for which are shown in table 2.2. SMART has four RCPs installed horizontally on the upper part of the RPV. Being the canned motor pump variety does not require pump seals. Therefore, the small break loss of coolant accident (SBLOCA) associated with pump seal failure is eliminated [23]. The schematic diagram of SMART canned motor RCP is shown in figure 2.6. Each RCP is an integral unit containing a canned asynchronous three-phase motor. The pump rotor speed could reach 1800 rpm [20].

The above safety design characteristics adopted in the SMART reactor design enhance its accident resistance. The risks of LB-LOCA and SBLOCA have been eliminated by the integral core arrangement and the application of no seal RCPs. The HOCOTSGs are installed at the upper shell above the reactor core in the RPV. That could provide the driving force

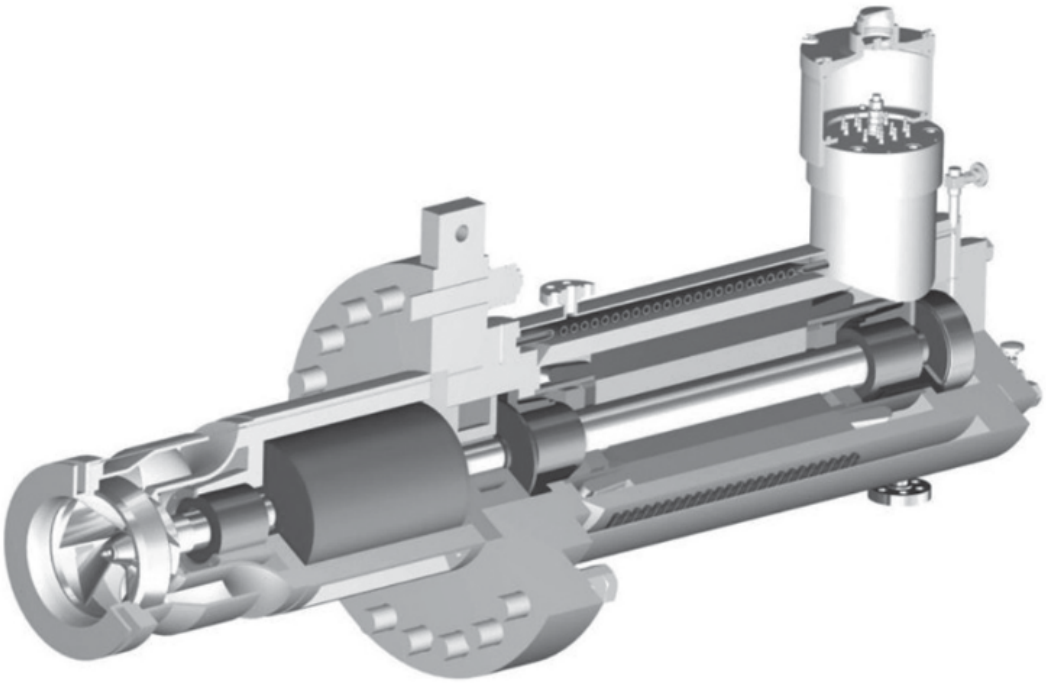


Figure 2.6: Canned motor reactor coolant pump of SMART [20].

for natural circulation flow. This design feature could guarantee the system has passive residual heat remove capability, and even the power-driven heat removal systems could not work as normal. The feasibility of the SMART direct passive residual heat removal system (DRHRS) under a station black out event has been studied by Kim [30]. The study results show that, during the event simulation, most TH behaviours showed reasonable trends in terms of pressure, temperature and water level. The reactor performance under the SGTR accident also has been assessed by the TASS/SMR code. The study results stated the SMR NPP remains stable under the accident transient operational conditions. The presented SMART design features and the major component's safety capability supply the intrinsic safety to the entire system. The parameters of the reactor vessel unit and the technical data about the NPP is given in the below table 2.3.

In this section, the arrangement of the SMART integral RPV unit and the major reactor components inside the vessel have been introduced. This design features and innovative facilities enhance the safety properties of the SMART reactor, and then allow for the SMART NPP (on the premise of safety) to have a better economic performance. The reactor core design and nuclear fuel management scheme will be presented in the next section.

Table 2.3: The technical parameters of SMART NPP [20, 31]

General Plant Data	Value
Reactor thermal output	330 MWth
Plant power output	net 90 MWe
Plant design life	60 years
Plant availability target	>95%
Primary coolant material	Light water
Moderator material	Light water
Non-electric application	Desalination, district heat
Safety goals	
Core damage frequency/reactor-year	< 1E−6
Large early release frequency/reactor-year	< 1E−7
Occupational radiation exposure(Person Sievert/reactor year)	<1,0
Operator action time	36 hours

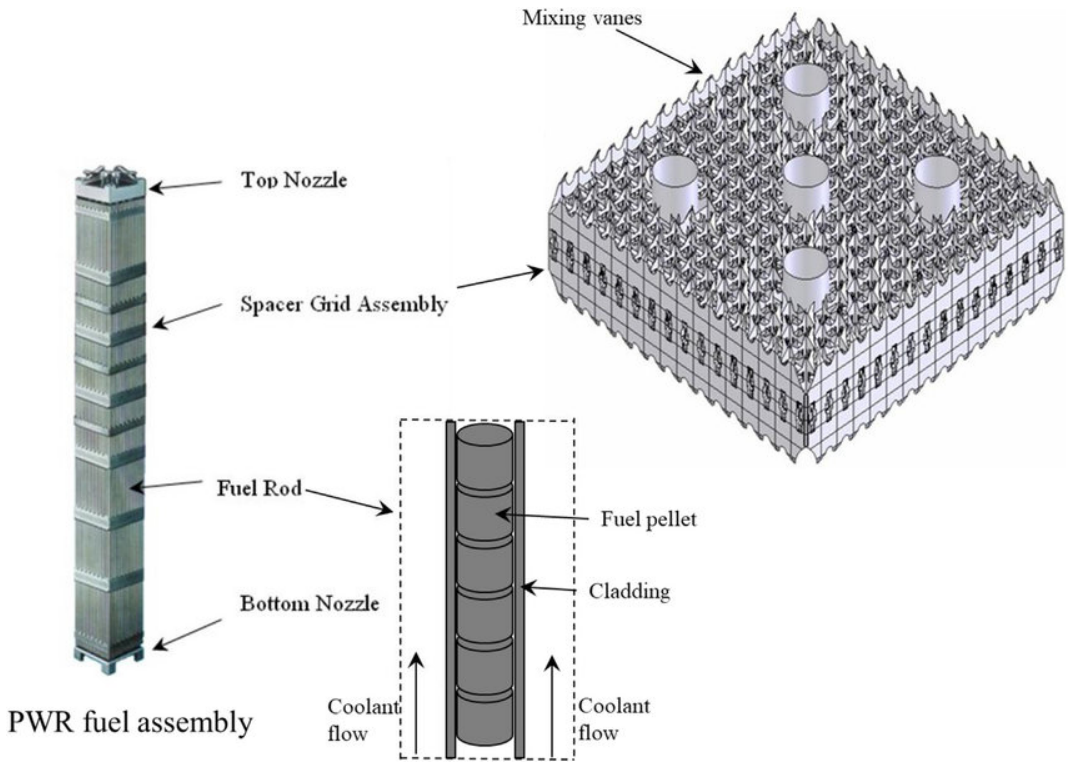


Figure 2.7: Schematic diagram of a typical PWR fuel assembly [32].

2.1.3 Reactor core and fuel management

From the neutron physics point of view, the reactor core is the most important part of the reactor system. The neutron multiplication and chain reactions take place in the core region and generates most of the heat. The SMART reactor core contains 57 FAs to produce 330MW thermal power. Each FA has 2 meters active height and united into a standard 17×17 square assembly of UO_2 ceramic fuel rods with the enrichment of less than 5%. The design was linked partially to standard PWR fuel. Figure 2.7 shows a schematic diagram of a typical PWR FA. Except for the fuel rods, it also has 24 control rod (CR)s guide tubes, and one instrumentation thimble would mechanically fit into the FA square array. Eight spacer grids hold the fuel rods at the specified vertical positions. A specially designed bottom end piece blocks debris from entering the core.

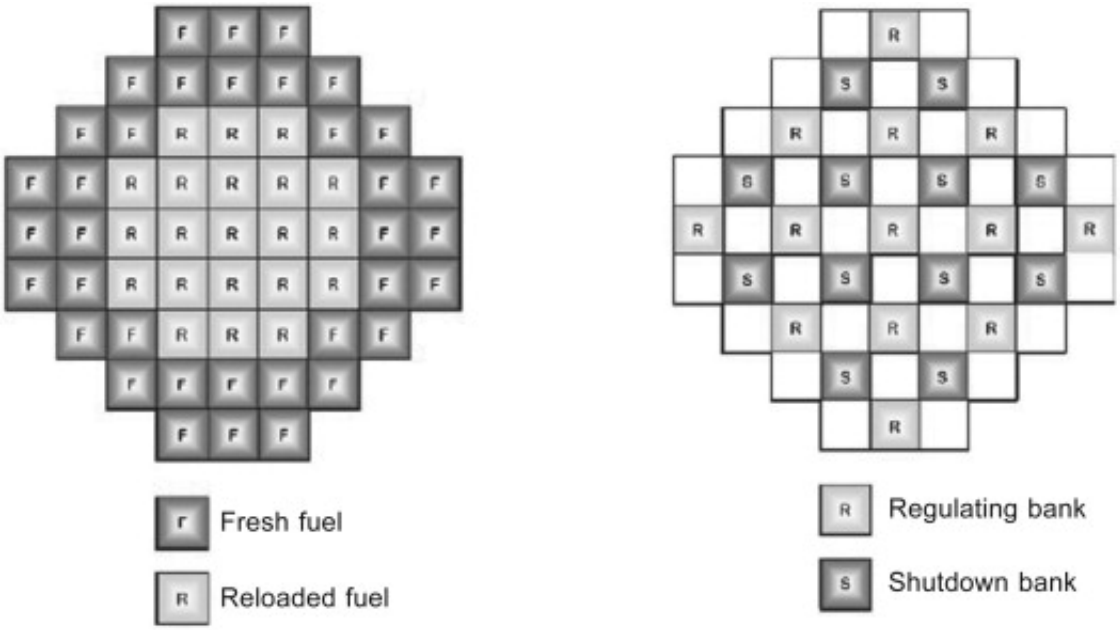


Figure 2.8: SMART core loading pattern and control rod arrangement[18, 20].

In order to reduce the critical boron concentration and to control the radial power peaking, a standard SMART FA contains several lumped burnable poison rods made of material comprised of gadolinium oxide (Gd_2O_3) mixed with uranium dioxide (UO_2), and its enrichment is 1.8%. Determined by the assembly locations in the core, the amount and array of burnable poison rods are different in the 17×17 lattice structure. Additionally, the maximum burn up of SMART fuel rod is estimated as 54000 MWD/MTU. Based on large PWRs' fuel management experience and some innovative study results [33–35], a two-batch refuelling scheme was designed for SMART which, without reprocessing, returns a cycle of 990 effective full power days (EFPD) for 36 months operation. Figure 2.8 presents the SMART core fuel assemblies arrangement and CR permutations. Based on the above nuclear design features, the SMART core has inherent safety characterised by:

- Low core power density.
- Longer cycle operation with a two-batch reload scheme.

- Adequate thermal margin more than 15%.
- Inherently free from xenon oscillation instability.
- Coupling with coolant temperature reactivity feedback, the requirement for CRs motion has been minimised.

The studies in this thesis focus on the SMART core nuclear performance. From the perspective of neutron physics the aim is to analyse the stability of the fission chain reaction. It theoretically assesses the feasibility of getting extra power from the SMART reactor without subverting its fundamental design philosophy. To elucidate this problem, this work has also summarised and referred to the technical characteristics of other SMR designs along with some of the innovative optimisations proposed by other researchers.

2.2 Competitor for SMART

As mentioned in the above sections, many countries are currently working on the design of innovative SMR systems. In order to improve the power output of the SMART reactor and make it more competitive in the worldwide nuclear power market it is necessary to consider its other SMR competitors. The advantages of the other mature reactor designs could possibly be used to improve the current SMART design.

2.2.1 ACP100

Advanced China Power 100 (ACP100) [36] is the other integral PWR design which is close to the nuclear market, and also has been assessed in the NNL's feasibility studies [14]. This technology was developed by China National Nuclear Corporation (CNNC), and aims to



Figure 2.9: ACP100 reactor with other main equipment connected [36].

produce $125MWe$ from $385MWth$. The neutronic feasibility and NPP safety characteristics of ACP100 have been well studied by the Chinese researchers[37–39]. These recently published works prove the capability of the RCS to remove decay heat during the long term cooling phase post-LOCA, and the safety parameters such as core damage frequency could be improved by the probabilistic safety assessment and risk-informed design technologies.

The applications of ACP100 are multiple. Besides electricity production, it also could provide local heating, seawater desalination, and industrial infrastructure functions. The schematic diagram of ACP100 has been shown in the above Figure 2.9 and the below Table 2.4 introduces part of the major technical parameters of ACP100.

Comparison of the parameters presented in Table 2.4 with the SMART parameters mentioned in the above sections, shows that strong resemblances between the two technologies is evident. These two designs both utilise the low enrichment uranium dioxide fuel of 17×17 square pitch FA arrangement, and the cores load 57 FAs. However, the power capac-

Table 2.4: Major Technical Parameters of ACP100 [36].

Parameter	Value
Reactor Type	Integral PWR
Thermal (MWth)/Electrical (MWe)	385/125
Core inlet/exit temperature($^{\circ}C$)	286.5/319.5
Fuel type/assembly array	$17 \times 17 UO_2$ square pitch arrangement
Number of fuel assemblies	57
Fuel enrichment	$< 4.95\%$
Fuel burnup (GWd/ton)	< 52000
Fuel cycle (months)	24
Design life (years)	60

ity of the ACP100 is relatively higher than the SMART, about 55 $MWth$ or $15MWe$. That is because of the FAs active length in the ACP100 is longer which is 2.15m, in the SMART core the FAs active length is 2.0m. That means there is a greater volume of fissile material loaded in the ACP100 reactor core. Meanwhile, double the configuration of SMART, 16 once-through steam generators are mounted in the RPV for transferring coolant fluid.

However, the ACP100 needs refuelling every 24 months, this cycling period for SMART is 36 months. Therefore, if the optimisations can improve the power output of SMART and also keep the more extended refuelling cycling time advantage, that may further improve the economic performance of SMART.

2.2.2 Advanced SMRs

The SMART and ACP100 reactors introduced above could be considered relatively developed based on the established PWR techniques from South Korea and China respectively. Apart from water-cooled reactors, the feasibility of other SMRs which do not make use of traditional forms of coolant or nuclear fuel are also being assessed. These reactor designs could be categorised into three groups and generally called advanced SMRs. The features of these designs including the PSSs and inherent safety properties which are inherited from the advanced water-cooled reactors. Furthermore, the targets of advanced SMR also are utilising the reprocessed nuclear fuel and to create a closed nuclear fuel cycle. These reactor are also called the fourth generation reactor [40–42]. A series of typical designs would be listed below:

- HTGR, The gas-cooled reactor has a long development history worldwide. In the UK, there are 7 well-established Advanced Gas-cooled Reactors (AGR) NPPs (strictly each station is a twin reactor site) that have been operating for more than 40 years. The AGR technology was developed from the Magnox reactor[43]. Via inheritance of the same sort of technological concept, gas-cooled reactor technology is still evolving. The HTGR is an innovative concept using helium gas as coolant, the nominal operating temperature could be up to $900°C$. The nuclear fuel is expected to be uranium nitride or carbide [44]. HTGR technologies are developing in many countries such as high-temperature gas-cooled reactor pebble-bed module (HTR-PM) reactor [38, 45] in China and GTHTR300 [46] from Japan. As shown in the figure 2.10, a demonstrating HTR-PM project is currently being built at the Shidao Bay in Shandong province. The first concrete was poured on December, 2012. The cold state test of facilities was done on October, 2020. Table 1.1 contains the U-Battery reactor, that means the HTGR technology is also involved in the UK's nuclear energy development plan, but needs a



(a) (b)

Figure 2.10: Construction of the HTGR in Shandong Province,China [47].

greater time to approach the market.

- Liquid Metal Cooled Reactor (LMFR), this type encompasses small reactors which would utilize the liquid metal as primary coolant. Currently, the development of sodium-cooled and lead-cooled (or lead-bismuth) reactors received extensive attention globally [48–51] . The LMFRs have the fast neutron spectrum due to the absence of moderator, and they are capable of breeding fissile materials such as ^{239}Pu and ^{233}U from the fertile materisls ^{238}U and ^{232}Th respectively [52]. Therefore, the range of nuclear fuel options could be expended, the mixed oxide fuel, and U-Pu-Zr fuel which are produced from reprocessing of spent fuel could be reused in the LMFRs. Also due to the breeding reaction, the LMFRs could be self-sufficient. That makes the core designed for a very long refuelling interval about $10 - 30$ years [53].

- Molten Salt Reactor (MSR), the primary feature of this type of fast fission reaction reactor is the application of the molten salt mixtures as the primary coolant, and even as the nuclear fuel itself [54]. In a MSR, the fissile materials are dissolved into the fluoride molten salt that circulates through the graphite core. Depending on the varied purposes, a range of fissile fluoride salts such as UF_4, PuF_3 or ThF_3 could be applied as the fuel [55, 56]. Generally, the MSRs operate at relativity high temperature $(700 - 750°C)$, higher than the PWRs and do not need the RPV. A unique design of MSR called the stable salt fast reactor is being developed by a UK company named

Moltex [57]. The salt fuel would be contained in fuel tubes and clusters of these used to form FAs.

The fourth-generation SMRs listed above have a series of innovative nuclear engineering features such as operation in the fast neutron spectrum and closed fuel cycle, which means the new fuel could be reprocessed from spent fuel and reduce the amount of waste generated. On the other hand, most of these reactors have stayed in the conceptual design stage, with only a few designs having built a demonstration project, so they still have a long way to go before commercial operation. The studies presented in this thesis will focus on optimisation, feasibility, and performance improvements of relatively mature SMR technologies. Therefore, the fourth-generation reactors will not be the major research objectives in this thesis. However, many research works related to fourth-generation reactors has relevance to the thesis, especially regarding study methods and materials selection. The next section will summarise a series of optimising ideas and research results obtained by other researchers.

2.3 Optimisations

This section straightens out and summarises a range of neutronic studies on SMR systems conducted by other researchers. These studies are not limited to the SMART reactor, but also include other types of SMR. Through reviewing the literature, one can try to determine the practical methods to improve the power output of the SMART reactor.

2.3.1 Fuel selections

Thorium fuel

It is intuitive to try to solve problems by changing to new types of nuclear fuel. Thorium is an easily exploitable resource which is 3 to 4 times more abundant than uranium, and widely distributed in many countries [58–60]. However, unlike the natural uranium which has the fissile isotope ^{235}U, natural thorium do not contains any fissile isotopes. The reason why researchers are still considering thorium is that the fertile isotope ^{232}Th can absorb a neutron and transmute to ^{233}U which is a fissile material. There are two subsequent methods to use the thorium [61–63].

- Chemically separate the ^{233}U from irradiated thorium-based fuel and re-fabrication via recycle into new fuel.
- Irradiating ^{232}Th in situ, and direct utilisation of the fission of ^{233}U.

Both methods could make thorium based fuel available for the PWR. The first method has not been introduced in many countries, due to the requirement of radio-chemical reprocessing systems. In India, in order to build a long term nuclear programme on limited uranium and vast thorium resource, a three-stage strategy was established. A range of nuclear power systems were involved in this plan, including pressurised heavy water reactor (PHWR), LMFR, and an advanced water-cooled thermal reactor which is capable of utilising the self-sustaining mixed $(^{232}Th - ^{233}U)O_2$ fuel. The mission of the PHWR and LMFR is to convert ^{232}Th to the ^{233}U, and then the spent ThO_2 pin is going to reprocessing for recovery of the ^{233}U which is then destined for the final thermal water cooled reactor[62, 65].

For the in-situ method, two main application methods have been studied: homogeneous and heterogeneous. For the reactor such as the Russian WWER-T (thorium) [66, 67],

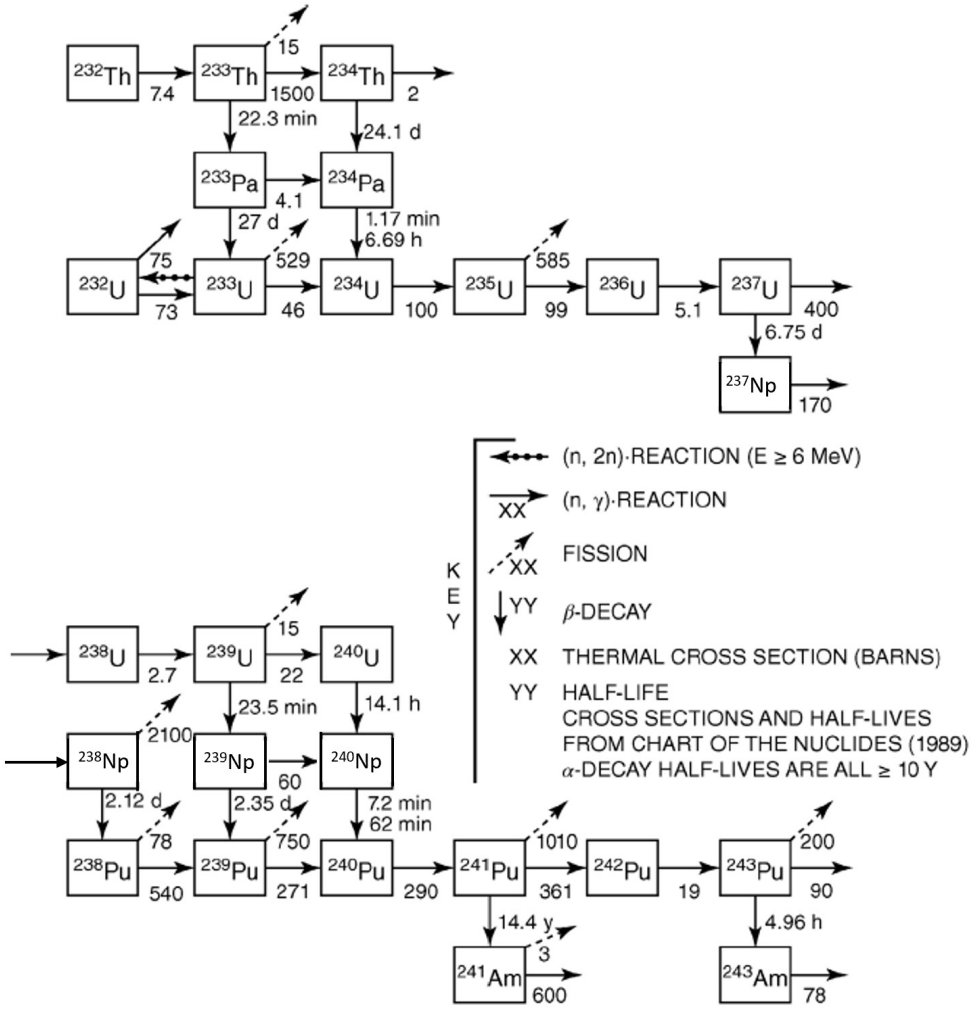


Figure 2.11: Transmutation-decay chains for ^{238}U and ^{232}Th[64].

each FA has a central seed region and a thorium blanket. The seed region contains fissile material such as medium-enriched uranium or plutonium. Different to a usual PWR, the thorium PWR need to separate the fissile seed and the blanket, with the seed component requiring frequent replacement during refuelling. Due to the spatially separated nature of fissile material and Th in the fuel assembly, this method is called heterogeneous.

In contrast, the homogeneous thorium based PWR employs a mixture of medium-enriched uranium oxide and thorium oxide as nuclear fuel in each fuel rod. The fraction and enrichment of uranium could be adjusted until one obtains a sufficient recycling length.

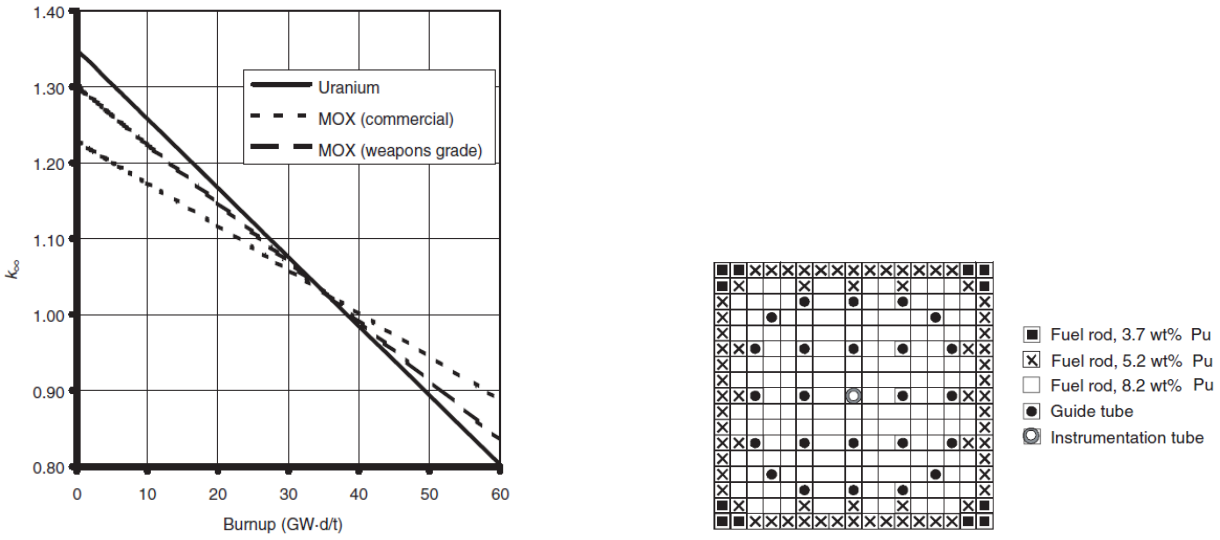
The other supplementary point of the homogeneous method is the possibility of burning the plutonium, at either a weapons or civil level. Moreover, the feasibility analysis for a thorium-fuelled reduced-moderation PWR to perform full transuranic recycle also has been done in 2014 [63]. The transuranic isotopes with a thorium mixture designed to be the fuel, and also the fuel-moderator ratio, need adjustment to achieve a negative reactivity feedback coefficient.

Similarly to the above work, researchers also studied the neutronic possibility of utilisation of the thorium-uranium fuel in the SMART reactor [68]. In this study, both of the homogeneous mixed U/Th fuel assemblies and the heterogeneous assembly arrangement concept have been investigated. The results state the employment of mixed thorium fuel with certain configurations, that could extend the refuelling cycle longer than the original design of reactor core. This is an interesting study, especially in that it directly links to the SMART reactor. The results are worthy to receive further validation.

MOX fuel

MOX fuel refers to the nuclear fuel which consists of UO_2 and PuO_2. The MOX UO_2 content could be natural, enriched or even depleted uranium, depends on the purpose of that fuel. The proportion of PuO_2 in MOX fuel is usually in the range of 3% to 5%. Even though the fraction of PuO_2 is small in the MOX fuel, the thermal behaviours of MOX fuel still will differ when compared to that of uranium oxide fuel [69, 70].

MOX fuel has been utilised in light water reactors in four European countries; Belgium, France, Germany, and Switzerland [71]. According to the IAEA's report [72, 73], compared to the uranium oxide fuel the MOX fuel has slower reactivity decrease with burn-up, the cross-comparison for which is shown in the figure 2.12(a). Moreover, the thermal neutron flux gradient is more significant in the MOX fuel assembly than in the uranium oxide



(a) (b)

Figure 2.12: MOX fuel in PWR fuel assembly.(a): k_∞ versus burn-up for uranium and MOX fuel. (b): The schematic diagram for a 17×17 MOX fuel PWR assembly [72]

fuel assembly. Therefore, a gradation of different Pu content MOX fuel rods are designed in the fuel assembly from the centre to edge, and three rod types of fuel rods are used for a PWR MOX fuel assembly. The figure 2.12(b) presents a PWR MOX fuel assembly which is designed of the 17×17 type with a fuel assembly averaged Pu concentration of $7.2wt\%$.

At the present time, the study regarding the feasibility of MOX fuel in PWR systems is still carrying on. In 2017, a published study utilised neural networks to build a fuel loading model, and focused on the elaboration of those models with PWR MOX on enriched uranium support (MOXEUS) fuel, which allows plutonium mono-recycling and multi-recycling in PWR systems [74]. In this study, the nuclear fuel cycle simulation code Core Library for Advanced Scenario Simulation (CLASS) [75] was used to calculate nuclide inventories and material flows in each part of the cycle. The neural networks were trained on a data-bank from MURE which is an MCNP based code for reactor evolution [76–78]. Similar to this study, recent work also uses CLASS to calculate the nuclide inventories but the data-bank is

trained by the lattice code DRAGON5 [79–81]. So novel computing methods are being used to analysis the MOX fuel in PWR problem. In terms of practical aspects, NuScale power from the US said their $50MWe$ integral PWR has the capability of utilising the plutonium - uranium MOX fuel, and a study from NNL has confirmed this point [82, 83].

On the other hand, as mentioned before, the MOX fuel also could refer to the mixed fuel of thorium and plutonium oxide, sometimes also called duplex fuel. Syed Bahauddin Alam's studies [84, 85] prove the duplex fuel can be utilised in a boron free SMR for civil marine propulsion, which has the possibility to achieve longer life and smaller reactivity swing. The neutronic analysis in these studies has been done on the fuel assembly and whole core levels. The MOX fuel fabrication and utilisation is a part of the UK's long term development plan [86]. The reason for this is a large amount of Pu storage, produced from reprocessing facilities, and the UK is looking for re-utilisation and building up a close fuel cycle [87].

In summary, researchers are looking for alternative fuel options for the SMR, compared to the normal uranium oxide fuel. From the neutronic point of view, these studies are brilliant, involving the MOX or thorium fuel into the fuel cycle of an SMR could save a significant amount of enriched uranium. Meanwhile, the stored resources could be utilised and brought into the industrial application.

2.3.2 Reflector saving

In nuclear reactor theory, whether nuclear energy may sustainably be emitted from the atom depends on the number of neutrons in the reactor core and their kinetic energy. A nuclear reactor cannot work properly if a large fraction of neutrons leak out from the reactor core. Therefore, a reflector has been added to the common design of the nuclear core, which



Figure 2.13: The view from top of the WWER-1000 nuclear core. The lower support structure, the neutron reflector and 11 assemblies [91, 92].

functions via reflecting some leaking neutrons back into the core. There are also other subsequent benefits to the presence of the reflector, such as flattening the neutron flux and distribution of power, reducing the loaded mass of fuel, and shrinking the size of the core and reactor as a whole [88–90]. Figure 2.13 shows an overhead view of a Russian WWER-1000 nuclear core, excepting the hexagonal fuel assemblies and support framework at the bottom, the reflector which is surrounding the fuel space also can be seen. Due to the small physical size of SMRs, the fission produced neutrons have a higher possibility of entering the reflector than in existing large reactors. A crucial factor in determining the physical viability and economic efficiency of an SMR design may be the reflector functions.

The presence of a reflector is thus of high importance and, moreover, it needs to work in the intensive radiation environment. Therefore, it is important to determine suitable materials for this purpose in a nuclear reactor. From the physical point of view, an effective reflector material should have the following properties: low absorption cross-section, high

scattering cross-section, radiation stability and resistance to oxidation. Neutrons should be scattered back to the core but not absorbed by the reflector materials once a neutron escapes from the core to the reflector. Meanwhile, from the safety principle, radiation stability and chemical stability are also important factors to a reflector material. The reflector is going to suffer a high level of different types of radiation, including gamma-rays and fast neutrons. If the reflector's surrounding chemical environment is also aggressive, the material should not get oxidised [93].

In addition, the choice of reflector material also depends on the type of reactor, especially the neutron spectrum of the reactor. For a water cooled, thermal neutron energy reactor, it is hoped that the leaking out of fast neutrons can lead to them reflected back to the core as thermal neutrons. Therefore, a suitable moderator material also can be a good reflector material. Water, heavy water, beryllium and graphite are commonly used as reflector. Changing reflector materials of the reactor core would thus somewhat affect the neutronic performance of the nuclear reactor. Several works have studied the various reflector materials' affect on a small research reactor. In 2015, S. Dawahra's work [94] used Monte Carlo N-Particle Transport Code (MCNP) to study the reflector affect on the IAEA referencing $10MW$ [95, 96], water moderated material test reactor. The reactor simulations were performed under 20%, 45%, 93% - so three enrichment levels of uranium fuels respectively. The reflector materials mentioned are four types. Similar research was published in 2016, when Farrokh Khoshahval [97] studied these four types of reflector and their neutronic effect on the $5MW$ Tehran research reactor by WIMS-D4 [98] and the CITATION [99] code. The fuel and moderator temperature affect have also been considered in this work. Both of these two works agree that beryllium is a particularly effective reflector material.

Beryllium metal and its compounds have features that indicate their use as a moderator and reflector or as a fuel cladding material in thermal reactors. That is primarily because of beryllium's nuclear properties, that it would produce neutrons from reactions

with electrons and react with fast neutrons to produce gaseous atoms, helium and tritium in (n, α) and $(n, 2n)$ reactions. The amount of helium formed is about $22cm^3$ per cm^3 beryllium per 10^{22} neutron/$cm^2(E > 1MeV)$. The thermal neutron capture cross-section of pure beryllium is 0.009 barn/atom. The impurities could increases this considerably though [100]. The impurities of beryllium and their effect on the thermal neutron absorption cross-section is given in table 2.5.

Table 2.5: Effect of adding 0.1 w/o impurity on thermal neutron absorption cross-section of beryllium [100].

Impurity	Impurity cross section (barns/atom)	Addition to cross section of pure Be (mb/atom)
Boron	766	638
Cadmium	2450	194
Lithium	71	92
Cobalt	37	5.7
Manganese	13.2	2.2
Nickel	4.8	0.7
Copper	4.0	0.56
Chromium	3.1	0.54
Iron	2.73	0.44
Calcium	0.44	0.10
Aluminum	0.24	0.08
Silicon	0.16	0.05
Magnesium	0.07	0.03

The effect from the beryllium reflector and its composition on small power reactors

have already been done in some USA studies [101, 102]. The results show that the burn-up of pre-existing impurities in the beryllium has a dominant effect on the reactivity of these reactors, despite the accumulation of the neutron poisons ^{3}He and ^{6}Li as a consequence of beryllium transmutation. Besides the water-cooled reactor, researchers also propose to use the beryllium material in the HTGR such as the aforementioned U-Battery reactor. S.Atkinson performed studies [103] that made a comparison of the nuclear properties, thermal-physical properties, and financial impact between beryllium oxide and nuclear graphite as a reflector for U-Battery.

On the other hand, some companies are validating the feasibility of heavy material reflectors, the aim of which is to build a reactor that could be capable of a lifetime of 60 years, and works with lower fuel enrichment. That constraint demands that the reflector provide better protection of the RPV and sends the neutrons back to the core at the same time. Related research has already been done by both deterministic codes and Monte Carlo method codes [104, 105]. At the moment, the most likely to be adopted heavy material reflector (HMR) material is stainless steel. Sargeni's work [104] focus on power tilt which means the differences between the ratios of the quarter core power values to the average core power. This asymmetry problem has been firstly studied by the diffusion code CRONOS2 [106, 107] and then benchmarked by MCNP. The results present that the core with stainless steel reflector has higher power tilt than the light water reflector core. The application of HMRs is still in the exploration stage, currently, and published research works about HMRs is focused largely on investigating their feasibility in large PWR systems. The potential of HMRs in the SMR type of systems still needs to be further studied.

From what has been discussed above, the neutron reflector is an important component of a reactor core, that could flat the power distribution and reduce the critical core size. Many researchers already studied the reflectors' effect on material test reactors. The materials of the reflector could be light materials such as light water, heavy water, graphite and beryllium,

or heavy material such as stainless steel. However, due to the requirements of higher power level and longer operation time, the feasibility of a neutron reflector and its effect on a commercial SMR is still worth deep consideration.

2.4 Summary of literature review

In this chapter, first of all, the detailed information about the reference reactor in this thesis, namely SMART, has been introduced. This part included the development process of SMART, and the technical parameters of the major parts. Due to the major reactor components, such as reactor core, power systems and reactivity control faculties, that would be contained in the RPV, the information of the RPV essentials has been presented. This section included introductions about the reactor primary loop faculties such as HOCOTSGs and RCPs. The details of nuclear parts of the reactor, such as core and FAs, have also been stated in this section.

Secondly, the information and existing research regarding some competitor reactors for SMART have been summarised. The ACP100 reactor from China has been specially introduced and made for comparison, because this design has many common points with SMART. The development status regarding advanced SMR systems have also been introduced in this part. These non water-cooled reactors would be prepared for the nuclear energy market in the next 20 years. Therefore, they are not the major research objectives in this thesis. However, the related studies still have reference value to this thesis.

Towards the end of this chapter, a series of neutronic optimisations proposed by other researchers have been concluded. These studies could be classified into two types, namely the fuel selection and the additional neutron reflector. Some innovative nuclear fuels have been tried to replace uranium oxide fuel, such as thorium fuel and MOX fuels, including $Pu - U$

fuel and $Th - U$ fuel, and neutron physics feasibility studies have been conducted in the referenced papers. The neutron reflector is an already proven useful method to save neutron economy for the core. The stated references tested how different reflector materials affect the small material test reactor, the materials including light substances such as light water, heavy water, graphite, beryllium, and heavy materials too.

Chapter Three

Methodology

Chapter two introduces much information about the SMART reactor and the neutronic studies related to this technology, which can be seen as the research background of this thesis. In this chapter the theories behind nuclear reactor performance, and the methods to solve these problems, will be stated and explained. The neutron physics and relevant reactor physics theories have already been well described in many published works [88, 108–110]. Therefore here will be provided just an overview and a few significant points to better present the proposed optimisations. The neutron physics phenomenon will be presented in the first place.

3.1 Criticality

In the nuclear reactor physics analysis area, a meaningful concept is the effective multiplication factor k_{eff} which represents the total number of produced fission neutrons. This quantity could be written as:

$$k_{eff} = \eta \epsilon p f P_{NL} = k_{\infty} P_{NL} \tag{3.1}$$

In the above equation 3.1, the first term reproduction factor, η means the average number of neutrons released per thermal fission reaction in the fuel. Single generation fission released neutrons' average energy will consistently stay in the fast energy range, majorly in the energy range higher than $1MeV$. Part of these fast neutrons will cause fission reactions with ^{238}U and other fissionable nuclides. The fast neutron multiplication is characterised by the term ϵ, which presents the ratio between the released neutron numbers from all fissions and those initiated just by incident neutrons only in the thermal energy range. Fast neutrons' energy loss process is also called moderation, and the non-capture probability in the fast neutron moderation process is referred to as the resonance escape probability, p. The term f is called the fuel thermal utilisation, which indicates the portion of neutrons that were absorbed in the fuel nuclides compared to in all materials in the reactor core. for the last factor, the P_{NL} means the probability that neutrons would not leak out of the system, including both for thermal and faster neutrons. On the right side of the equation 3.1, k_∞ is called the infinite multiplication factor. This parameter reflects the inherent multiplication ability of an infinite reactor assembly system, which contains the fuel and moderator materials and without neutron leakage concerns[88, 89, 111].

The finite form of k_∞, k_{eff} could evaluate the status of the neutron chain reaction in the reactor core of a real system with finite size. On average, one neutron must not be absorbed or leak out from the system to therefore be able to cause another fission. This condition is called critically, so at this moment, $k_{eff} = 1$. If $k_{eff} < 1$, the system is in the sub-critically state, such that the neutron population in the system will decrease. On the other hand, when the neutron population in the system will increase, that state of the system is referred to as super-critically [89, 109, 112]. The constant k_{eff} will be used in this thesis frequently and it aims to describe the SMR, whether critical or not, and express the evolving state of the total neutron number in the reactor core.

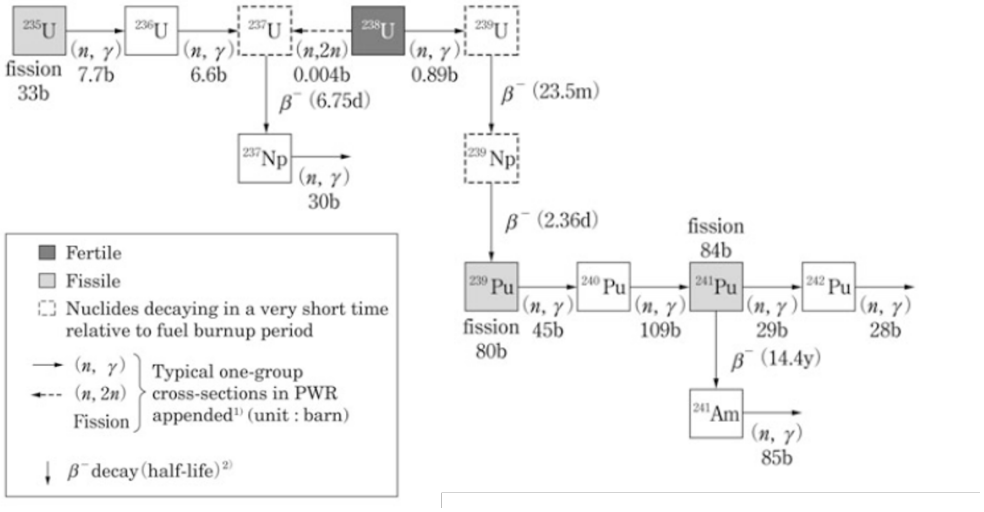


Figure 3.1: Uranium burn-up chain [64].

3.2 Burn-up

As mentioned in section 2.3.1, when a nuclear reactor is operating, various nuclear reactions are happening within the nuclear fuel induced by the neutron interactions, such as fission of fissile isotopes, the conversion of fertile nuclei into fissile ones, and the production of fission products [113]. The above reactions, and the reactivity control measures taken, will significantly vary the reactor's nuclear properties over its lifetime. The fuel utilisation rate and spatial power distribution could potentially heavily influence the reactor economics. The investigation to study the change of nuclide atomic densities and the time-dependent core power distribution is called burn-up (BU) analysis [114, 115]. These studies can provide meaningful information for the TH analysis and fuel management. Similar to the above figure 2.12, which presented the transmutation decay chains for ^{238}U and ^{232}Th, the BU chain of ^{235}U has been given in figure 3.1.

In the neutron physics area, a set of BU equations is applied to describe each nuclide's atomic number density in the BU chain. The atomic number density at position $\vec{r}$ and time t can be represented by $N(\vec{r}, t)$, the cross-sections of absorption, capture and (n,2n)

reactions can then be presented as $\sigma_a, \sigma_c, \sigma_{n,2n}$ respectively. The decay constants are called λ. Moreover, the neutron flux at position $\vec{r}$ and time t can be expressed by $\phi(\vec{r}, t)$ and is a scalar number defined as the number of neutrons travelling through a small sphere of radius R in a time interval, divided by πR^2 and the time interval, its unit are number of neutrons $cm^{-2}s^{-1}$. Additionally, the neutrons are assumed to be mono-energetic here to simplify the calculation.

Considering the balance between the production and destruction rates of a target nuclide, the uranium BU chain could be described by the following equations[64]. Here the nuclides are identified by two-digit superscript composed of firstly the last digit in the atomic number and secondly the last digit in the mass number.

$$
\begin{aligned}
^{235}U &: \frac{\partial N^{25}}{\partial t} = -\sigma_a^{25}\phi N^{25} \\
^{236}U &: \frac{\partial N^{26}}{\partial t} = \sigma_a^{25}\phi N^{25} - \sigma_a^{26}\phi N^{26} \\
^{237}U &: \frac{\partial N^{27}}{\partial t} = \sigma_c^{26}\phi N^{26} + \sigma_{n,2n}^{28}\phi N^{28} - \lambda^{27}N^{27} \\
^{237}Np &: \frac{\partial N^{37}}{\partial t} = \lambda^{27}N^{27} - \sigma_a^{37}\phi N^{37} \\
^{238}U &: \frac{\partial N^{28}}{\partial t} = -\sigma_a^{28}\phi N^{28} \\
^{239}U &: \frac{\partial N^{29}}{\partial t} = \sigma_c^{28}\phi N^{28} - \lambda^{29}N^{29} \\
^{239}Np &: \frac{\partial N^{39}}{\partial t} = \lambda^{29}N^{29} - \lambda^{39}N^{39} \\
^{239}Pu &: \frac{\partial N^{49}}{\partial t} = \lambda^{39}N^{39} - \sigma_a^{49}\phi N^{49} \\
^{240}Pu &: \frac{\partial N^{40}}{\partial t} = \sigma_c^{49}\phi N^{49} - \sigma_a^{40}\phi N^{40} \\
^{241}Pu &: \frac{\partial N^{41}}{\partial t} = \sigma_c^{40}\phi N^{40} - (\lambda^{41} + \sigma_a^{41}\phi)N^{41} \\
^{242}Pu &: \frac{\partial N^{42}}{\partial t} = \sigma_c^{41}\phi N^{41} - \sigma_a^{42}\phi N^{42} \\
^{241}Am &: \frac{\partial N^{51}}{\partial t} = \lambda^{41}N^{41} - \sigma_a^{51}\phi N^{51}
\end{aligned}
\tag{3.2}
$$

For the short-lived nuclides, they decay immediately after being produced and reach a balanced state between production and destruction. If the time differentials of ^{237}U, ^{239}Pu, and

^{239}Np are set to be zero, the BU equations of ^{237}Np and ^{239}Pu would change to,

$$\begin{aligned} {}^{237}Np : \frac{\partial N^{37}}{\partial t} &= \sigma_c^{26}\phi N^{26} + \sigma_{n,2n}^{28}\phi N^{28} - \sigma_a^{37}\phi N^{37} \\ {}^{239}Pu : \frac{\partial N^{49}}{\partial t} &= \sigma_c^{28} N^{28} - \sigma_a^{49}\phi N^{49} \end{aligned} \tag{3.3}$$

These approximations can provide benefits for the numerical solution of the BU equations. In the above equations, the nuclear reactions' cross-sections of the nuclides are variable with neutron energy. Therefore, the energy and spatial distributions of neutron flux ϕ are meaningful to calculate the composition variations of nuclear fuels during the reactor operating time. In the following section, the equation used to describe the neutron flux distribution and the computing techniques to solve that will also be introduced.

3.3 Neutron transport

Beside the BU analysis and the reactor core criticality problem, neutron movement is another significant challenge for nuclear reactor physics. As a consequence of the repeated collisions with nuclei in the core, neutrons originally in one part of the reactor and moving in a particular direction with a certain energy appear at a later time in another part of the system, and can be moving in another direction with another energy. Moreover, a series of reactions could happen during the neutron movement process, such as scattering, resonance capture and fission reactions, synchronously affecting neutrons' amount and speed. The general solution to the neutron transport problem in a known physical system aims at determining the neutron flux at all points.

In order to achieve this, a couple of physical quantities should be defined to state the neutron population. Assuming a group of neutrons are located at point $\vec{r}$ with energy E and moving in direction $\vec{\Omega}$ at time t, which have increments of volume, energy and solid angle, dV, dE and $d\Omega$. The angular neutron density $N(\vec{r}, \vec{\Omega}, E, t)$ could describe the number

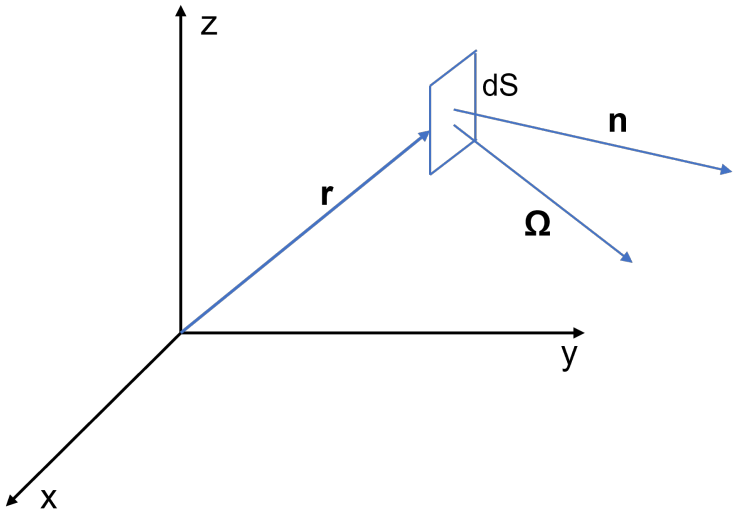


Figure 3.2: Neutron flow through planar surface element dS [116].

of these neutrons. This quantity includes a $3D$ variable $\vec{r} = (x, y, z)$, a $2D$ angular variable $\vec{\Omega}$, and an energy variable E. Therefore, angular neutron density N is a $6D$ phase space density with unit $cm^{-3}MeV^{-1}$. With this, at time t, the number of neutrons living in a physical system V sub-zone R, in the energy range E_1 to E_2 could be expressed below.

$$n(t) = \int_{E_1}^{E_2} \int_{4\pi} \int_{r} N(\vec{r}, \Omega, \vec{E}, t) dV d\Omega dE \tag{3.4}$$

Furthermore, as shown in figure 3.2, if there is a surface area element dS with a unit normal vector n, which stays at point $\vec{r}$, the angular neutron density could be used to calculate the neutron flow rate through dS at time t. Concerning a volume dV established by accumulating dS a distance $ds = vdt$ along the direction $\vec{\Omega}$, here v is the neutron speed, equal to $\sqrt{2E/m}$, dt is the time increment. The volume dV can be expressed by:

$$dV = dS(vdt)(\vec{\Omega} \cdot \vec{n}) \tag{3.5}$$

Therefore, within the increments dV, $d\Omega$, dE about $(\vec{r}, \vec{\Omega}, E)$, the neutron number is:

$$NdVd\Omega dE = [(\vec{\Omega} \cdot \vec{n})vN]dSd\Omega dEdt \tag{3.6}$$

Using the right side of equation 3.6 divided by dt can achieve the result:

$$(\vec{\Omega} \cdot \vec{n}) v N(\vec{r}, \vec{\Omega}, E, t) \tag{3.7}$$

Quantity 3.7 presents the neutron flow rate through dS, and moves in $d\Omega dE$ about $(\vec{\Omega}, E)$ in time t. There is a meaningful physics quantity called angular neutron flux [117] in equation 3.7, which is defined as:

$$\psi(\vec{r}, \vec{\Omega}, E, t) = v N(\vec{r}, \vec{\Omega}, E, t) \tag{3.8}$$

The unit of angular neutron flux is number of neutrons $cm^{-2} MeV^{-1} s^{-1}$. Again, eliminating time increment dt, one can achieve the ψ's volume-based explanation.

$$\psi(\vec{r}, \vec{\Omega}, E, t) dV d\Omega dE \tag{3.9}$$

Quantity 3.9 describes the rate of neutron path lengths in $dV d\Omega dE$ within $(\vec{r}, \vec{\Omega}, E)$ at time t. Considering the surface increment dS, an equivalent surface-based explanation of ψ can be obtained in the below quantity 3.10. This means the neutron's absolute rate through dS travelling in $d\Omega dE$ about $(\vec{\Omega}, E)$.

$$|\vec{\Omega} \cdot \vec{n}| \psi(\vec{r}, \vec{\Omega}, E, t) dS d\Omega dE \tag{3.10}$$

The angular neutron flux can present exhaustive information about the neutrons' movement. With this quantity, a neutron transport equation can mathematically describes the behaviour of neutrons, also called the Boltzmann equation [116, 118, 119]. The steady-state Boltzmann equation is given below.

$$\begin{aligned}
&\vec{\Omega} \cdot \nabla \psi(\vec{r}, \vec{\Omega}, E) + \Sigma_t(\vec{r}, E) \psi(\vec{r}, \vec{\Omega}, E) \\
&= \int_{\infty}^{0} \int_{4\pi} \Sigma_s(\vec{r}, \vec{\Omega}' \cdot \vec{\Omega}, E' \to E) \psi(\vec{r}, \vec{\Omega}', E') d\Omega' dE' \\
&+ \frac{\chi(\vec{r}, E)}{4\pi} \int_{0}^{\infty} \int_{4\pi} \nu \Sigma_f(\vec{r}, E') \psi(\vec{r}, \vec{\Omega}', E') d\Omega' dE' \\
&+ \frac{Q(\vec{r}, E)}{4\pi}, \qquad \vec{r} \in V, \quad \vec{\Omega} \in 4\pi \quad , 0 < E < \infty.
\end{aligned} \tag{3.11}$$

The complicated equation 3.11 actually is just a conservation equation to describe the neutron balance between its gain and loss mechanisms. The left side represents neutron loss, and the right describes neutron gain. The physical meanings of each term will be introduced below.

Net leakage rate term $\vec{\Omega} \cdot \nabla\psi(\vec{r}, \vec{\Omega}, E)$. Assuming R is a subarea of volume V, and its boundary ∂R has the unit outer normal unit vector $\vec{n}$. Combining this with the above angular neutron flux ψ. The angular neutron current $\vec{J_R}$ represents the neutron flow out of R at time t that can be presented as:

$$\vec{J_R} = \psi(\vec{r}, \vec{\Omega}, E, t)\vec{\Omega} \tag{3.12}$$

$\vec{J_R}$ can be calculated by the below equation:

$$|\vec{J_R}| = |\vec{J_R^+} - \vec{J_R^-}| = \int_0^\infty \int_{\partial R} \int_{4\pi} (\vec{\Omega} \cdot \vec{n})\psi(\vec{r}, \vec{\Omega}, E, t)d\Omega dS dE \tag{3.13}$$

Applying the equation 3.14 divergence theorem to $\vec{J_R}$:

$$\int_{\partial R} \psi(\vec{r}, \vec{\Omega}, E, t)(\vec{\Omega} \cdot \vec{n})dS = \int_R \vec{\Omega} \cdot \nabla\psi(\vec{r}, \vec{\Omega}, E, t)dV \tag{3.14}$$

The equation 3.13 can be equivalently reformed as:

$$|\vec{J_R}| = \int_0^\infty \int_R \int_{4\pi} \vec{\Omega} \cdot \nabla\psi(\vec{r}, \vec{\Omega}, E, t)d\Omega dV dE \tag{3.15}$$

Thus, if R is equal to an incremental volume dV it can yield the net neutron leakage flow at time t.

The second term on the left side of equation 3.11 represents the collision rate. $\Sigma_t(\vec{r}, E)$ is the total cross-section, which means the neutron-nucleus collision probability with neutron energy E at position $\vec{r}$. Collision here includes two reactions, neutron absorption and elastic or inelastic scattering. All of these interactions will cause neutron loss from the element of phase space $(\vec{r}, E, \vec{\Omega})$.

There are three neutron gain sources on the right side of equation 3.11, the first one is called the scattering source. The neutrons in position $\vec{r}$ which are originally travelling in the direction $\vec{\Omega}'$ with energy E' have a chance of turning into an after-scattering direction $\vec{\Omega}$ with energy E. $\Sigma_s(\vec{r}, \vec{\Omega}' \cdot \vec{\Omega}, E', \rightarrow E)$ is the cross-section of scattering. Integrating the product of angular neutron flux ψ and cross-section Σ_s over all possible original directions $\vec{\Omega}'$ and energy E' can obtain the in-scattering rate of neutron scatter into $d\Omega\ dE$ about $(\vec{\Omega}, E)$ at $\vec{r}$ in dV.

The second term is the fission source, which makes a significant contribution to neutron population multiplication. In this term, υ is the average number of released fission neutrons. $\chi(\vec{r}, E)dE$ represents the chance that a neutron has been emitted at $\vec{r}$ in energy dE about E, or also called the normalised fission spectrum. Σ_f means the fission reaction cross-section. Fission source is seen as isotropic and separable in both space and energy. The only undetermined element is space in this condition.

The third term shows internal neutron source. $Q(\vec{r}, E)dVdE$ presents the internal source released neutron rate in $dVdE$ about position $\vec{r}$ and energy E. Similar to the fission source, the internal neutron sources release neutrons that usually are isotropic. Radioactive decay makes a significant fraction of these internal sources.

The equation 3.11 is not completed yet. The boundary condition is also a necessary part to describe the neutron behaviours. The steady-state boundary condition is shown below:

$$\psi(\vec{r}, \vec{\Omega}, E) = \psi^b(\vec{r}, \vec{\Omega}, E), \quad \vec{r} \in \partial V, \quad \vec{\Omega} \cdot \vec{n} < 0, \quad 0 < E < \infty. \tag{3.16}$$

In equation 3.16, ∂V is applied to represent the outer boundary of the physical system V. Besides the above internal neutron source $Q(\vec{r}, E)$, here is an external neutron source out of volume V, the external angular neutron flux at the boundary is $\psi^b(\vec{r}, \vec{\Omega}, E)$, which has no exchange of the inner system's flux. The $\vec{n}$ is the unit normal vector at $\vec{r}$. The

product of $\vec{\Omega} \cdot \vec{n} < 0$ means all flight directions are pointed to the inner area of the system. The boundary condition 3.16 means, for all energy angular neutron flux, the inner system's inward boundary angular flux ψ at $\vec{r}$ is equal to the ψ^b induced by the external source. In this steady-state case, ψ^b is equal to 0, and named as the vacuum boundary. The above equation 3.11 is established on an assumption that the neutron interaction is only with the nucleus, not including the interactions with each other. The magnitude of neutrons in cm^3 of a typical reactor is about 10^{10}, and the amount of nuclei in the same volume roughly 10^{13} higher, at about 10^{23} [118]. Therefore, the neutron-neutron reactions are rare in the reactor, and the effect from that is sufficiently rare that it can be neglected.

The steady-state Boltzmann equation 3.11 could describe neutrons' spatial transport and energy change. However, that still cannot represent all neutron physics phenomena and neutron transport-related problems. A series of variants will therefore be introduced below for the specified problems.

3.3.1 Time-dependent

Timing effect has not been considered as an issue in the steady-state condition. A portion of neutrons will be released a few seconds after the initiating fission occurs. This portion of neutrons are called delayed neutrons, whilst on the other hand the fission emitted neutrons are called prompt neutrons.

The below figure 3.3 shows an example of delayed neutron emission from bromine-87. The fission product ^{87}Br is a β emitter, and it decays to ^{87}Kr with 55s half-life. If the daughter nucleus ^{87}Kr forms in the excited state, it could release the excitation energy by emitting the γ ray. However, if the excitation energy is as high as the binding energy of a neutron, the nucleus may de-excite by emitting a neutron. This is a delayed neutron

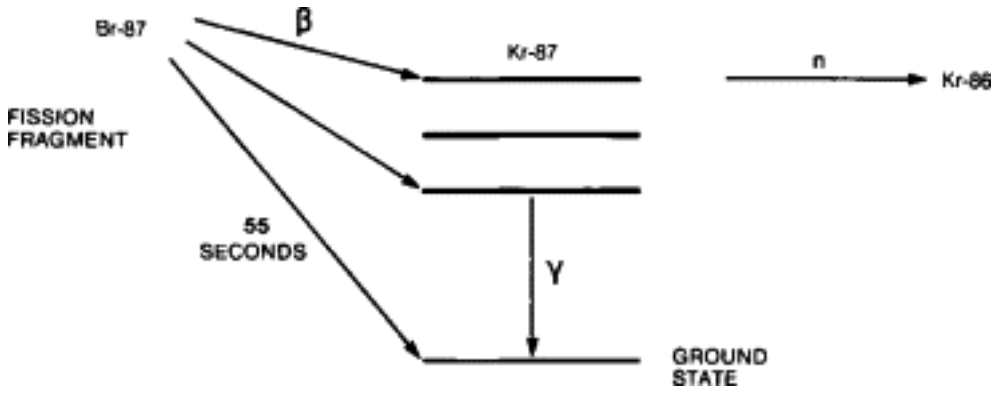


Figure 3.3: The birth of a delayed neutron from Br-87 [120].

as its presence is delayed by the decay time of the ^{87}Br precursor after fission. There are more than 50 fission products that could lead to delayed neutron emission. For convenience, usually, they are grouped initially into six groups. When the delayed neutrons are included into consideration, the generation time is equal to the sum of prompt and delayed neutron lifetimes weighted by their relative yields. Using β_i represents the fraction of fission neutrons which appear in the ith group. The total fraction of neutrons which are delayed is then:

$$\beta = \sum_{i=1}^{6} \beta_i \tag{3.17}$$

So that the fraction $1 - \beta$ of the fission neutrons is released as prompt neutrons. The below table shows delayed neutron data for thermal fission in ^{235}U.

Although the fraction of delayed neutrons comprise $< 1\%$ in the reactor core, they still play a key role to control nuclear reactors. At the startup of the reactor, the criticality remains within the limits $1.0 < k_{eff} < (1.0 + \beta)$, so the power increase will be dependent of the delayed neutron half-lives, which can be controlled by the reactivity control systems [122]. Therefore, the effect of the delayed neutrons is necessary within a neutron transport problem. Involving delayed neutron precursors, the Boltzmann equation could be written

Table 3.1: Delayed neutron data for thermal fission in ^{235}U [121]

Groups	Half-life(s)	Decay constant	Neutrons per fission	Fraction(β_i)
1	55.72	0.0124	0.00052	0.000215
2	22.72	0.0305	0.00346	0.001424
3	6.22	0.111	0.0031	0.001274
4	2.30	0.301	0.00624	0.002568
5	0.610	1.14	0.00182	0.000748
6	0.230	3.01	0.00066	0.000273
total			0.0158	0.0065(β_{total})

as:

$$\begin{aligned}\frac{1}{v}\frac{\partial\psi}{\partial t}(\vec{r},\vec{\Omega},E,t)+\vec{\Omega}\cdot\nabla\psi(\vec{r},\vec{\Omega},E,t)+\Sigma_t(E)\psi(\vec{r},\vec{\Omega},E,t)=\\ \int_0^\infty\int_{4\pi}\Sigma_s(\vec{\Omega}'\cdot\vec{\Omega},E'\to E)\psi(\vec{r},\vec{\Omega}',E',t)d\Omega' dE'\\ +\frac{\chi_p(E)}{4\pi}\int_0^\infty\int_{4\pi}[1-\beta(E')]\nu\Sigma_f(E')\psi(\vec{r},\vec{\Omega}',E',t)d\Omega' dE'\\ +\frac{1}{4\pi}\sum_{j=1}^{6}\chi_j(E)\lambda_j C_j(\vec{r},t)+\frac{1}{4\pi}Q(\vec{r},E,t)\end{aligned} \tag{3.18}$$

Meanwhile, the boundary condition 3.16 should be reformed to,

$$\psi(\vec{r},\vec{\Omega},E,t)=\psi^b(\vec{r},\vec{\Omega},E,t),\quad \vec{r}\in\partial V,\vec{\Omega}\cdot\vec{n}<0,\quad 0<E<\infty\quad ,0<t, \tag{3.19}$$

The above equation 3.18 is called the time dependent neutron transport equation. In comparison with steady-state neutron transport equation 3.11 there are a couple of extra terms in the updated equation 3.18, their physics implications will be explained below. Fundamentally, the timing difference dt is a primary variable for the neutron population increment dN within $dVd\Omega dE$ about $(\vec{r},\vec{\Omega},E)$ at time t, the time rate of dN change is:

$$\frac{\partial N}{\partial t}=\frac{1}{v}\frac{\partial\psi}{\partial t}(\vec{r},\vec{\Omega},E,t)dVd\Omega dE=(\text{Gain rate})-(\text{loss rate}) \tag{3.20}$$

Due to the existance of the time difference variable, the neutrons should be categorised into the prompt neutrons and delayed neutrons due to their production timing. The production rate of prompt neutrons about $(\vec{r}, \vec{\Omega}', E')$ with increments $dVd\Omega' dE'$ is expressed as:

$$[1 - \beta(E')]v(E')\Sigma_f(E')\psi(\vec{r}, \vec{\Omega}', E', t)dVd\Omega' dE' \tag{3.21}$$

Similar to above fission source term in equation 3.11, integrating equation 3.21 over all initial direction $\vec{\Omega}'$ and energies E', and multiplying by $[\chi_p(E)/4\pi]d\Omega dE$ obtains the prompt neutron production rate in $dVd\Omega dE$ about $(\vec{r}, \vec{\Omega}, E)$ at time t, represented as:

$$\left[\frac{\chi_p(E)}{4\pi}\int_0^\infty \int_{4\pi} [1 - \beta(E')]v\Sigma_f(E')\psi(\vec{r}, \vec{\Omega}', E', t)d\Omega' dE'\right] dVd\Omega dE \tag{3.22}$$

Besides this, the rate at which delayed neutrons are emitted into $dVd\Omega dE$ about $(\vec{r}, \vec{\Omega}, E)$ at time t, is expressed as:

$$\sum_{j=1}^{6} \frac{\chi_j(E)}{4\pi}\lambda_j C_j(\vec{r}, t)dVd\Omega dE \tag{3.23}$$

In the above equation 3.23, λ_i is the decay constant and C_i is the concentration of delay neutron precursor nuclides for the jth group. The number of delayed neutrons actually depends on the concentration of species-j precursor, its rate of change at position $\vec{r}$, time t, $\frac{\partial C_j}{\partial t}(\vec{r}, t)$ can be described by balance of nuclides. The decay rate of the precursors in $dV$is given by $\lambda_j C_j(\vec{r}, t)dV$. Meanwhile, the production rate of group-j precursor nuclei in $dVd\Omega' dE'$ about $(\vec{r}, \vec{\Omega}', E)$ at time t can be represented as:

$$\beta_j(E')\nu\Sigma_f(E')\psi(\vec{r}, \vec{\Omega}', E', t)dVd\Omega' dE'c \tag{3.24}$$

Again, integrating the expression over all $\vec{\Omega}'$ and E', the group-j precursor nuclei production rate in dV about $\vec{r}$ at time t is given by:

$$\left[\int_0^\infty \int_{4\pi} \beta_j(E')\nu\Sigma_f(E')\psi(\vec{r}, \vec{\Omega}', E', t)d\Omega' dE\right] dV \tag{3.25}$$

Therefore, the following equation could be used to represent the precursor densities:

$$\frac{\partial C_j}{\partial t}(\vec{r}, t) + \lambda_j C_j(\vec{r}, t) = \int_0^\infty \int_{4\pi} \beta_j(E')\nu\Sigma_f(E')\psi(\vec{r}, \vec{\Omega}', E', t)d\Omega' dE \tag{3.26}$$

The solution of equation 3.26 should then be joined with equation 3.18 as well. Therefore, its boundary condition should also be applied in the delayed neutron precursor densities equation 3.26. Meanwhile, the ψ and C_i also should follow the initial conditions:

$$\begin{aligned} \psi(\vec{r},\vec{\Omega},E,0) &= \psi^i(\vec{r},\vec{\Omega},E), \quad \vec{r}\in V, \quad \vec{\Omega}\in 4\pi, \quad 0<E<\infty, \\ C_j(\vec{r},0) &= C_j^i(\vec{r}), \quad \vec{r}\in V, \end{aligned} \tag{3.27}$$

The ψ^b, ψ^i, C_J^i are specified. The study of time-dependent reactor neutron transport problems is called reactor kinetics.

3.3.2 K-eigenvalue problems

As mentioned in the earlier section 3.1, the multiplication constant k can demonstrate the criticality of a reactor system. Extending the physical system V to be the entire reactor system, assuming the reactor has not started-up yet, the internal and boundary sources are zero. The other variant of the neutron transport equation which contains the multiplication constant k can be presented as:

$$\begin{aligned} &\vec{\Omega}\cdot\nabla\psi(\vec{r},\vec{\Omega},E)+\Sigma_t(\vec{r},E)\psi(\vec{r},\vec{\Omega},E) \\ &=\int_\infty^0\int_{4\pi}\Sigma_s(\vec{r},\vec{\Omega}'\cdot\vec{\Omega},E'\to E)\psi(\vec{r},\vec{\Omega}',E')d\Omega'dE' \\ &+\frac{1}{k}\frac{\chi(\vec{r},E)}{4\pi}\int_0^\infty\int_{4\pi}\nu\Sigma_f(\vec{r},E')\psi(\vec{r},\vec{\Omega}',E')d\Omega'dE' \end{aligned} \tag{3.28}$$

With conditions:

$$\begin{aligned} &\vec{r},\vec{\Omega}\in 4\pi, \quad 0<E<\infty, \\ &\psi(\vec{r},\vec{\Omega},E)=0, \quad \vec{r}<\partial V, \quad \vec{\Omega}\cdot\vec{n}<0, \quad 0<E<\infty \end{aligned} \tag{3.29}$$

When $\psi=0$, the equations 3.28, 3.29 always solved, and they are aiming to determine the largest k value such that a non zero solution ψ exists. The corresponding ψ is called the eigenfunction. The reason for defining k in an alternative method is given as follows.

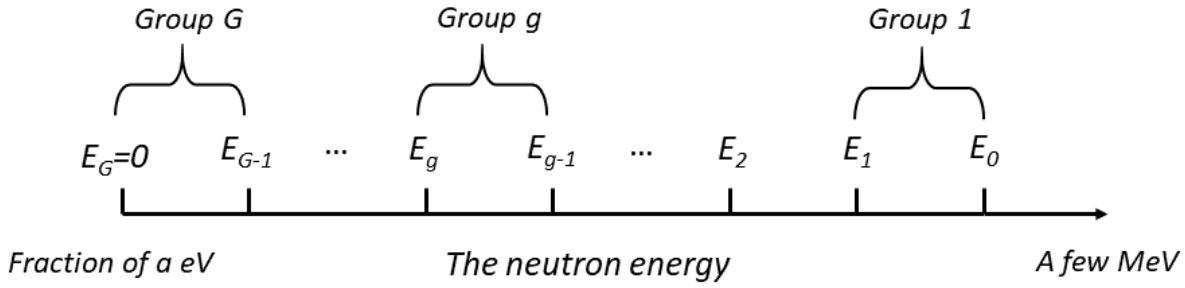


Figure 3.4: Neutron energy group numbering scheme.

In any fissile system, if fission neutron production precisely compensates for the neutrons loss caused by capture and leakage, then it is possible to provide a non-zero, steady-state neutron flux. This exact equilibrium can be achieved by adjusting the fission source's magnitude via the eigen-value k.

In practical problems, the solutions of the neutron transport equation are rarely analytical. Therefore, numerical analysis methods were set down to find numerical solutions. These numerical processes are called stochastic and deterministic techniques. Both of the two approaches could simulate the same physical problem. However, they have fundamental differences in their approach to problems and their solution techniques. The theories behind these two techniques will be introduced in the following sections.

3.4 Deterministic methods

The fundamental idea of deterministic methods is the numerical discretisation of all independent variables. Mathematically one then seeks to find its exact or approximate solution. The energy E will often be the first parameter to be discretised. As presented in Figure 3.4, let E_0 to be the maximum neutron energy. Then one divides the overall energy range [E_0,0] into discrete energy groups, decreasing progressively into sub-intervals numbered from 1 to

N. In each energy group, the single energy neutron transport equation could be applied to treat the neutron flux distribution. The equations are specific to each group, because there are not only real neutron sources emitting in the group but also rates of transfer into this group from the other groups. Meanwhile, cross-sections of all reaction types in the equation 3.11 are specified for each energy group, usually in the form of a histogram. Integrating the equation over each group, the updated equation is called the multi-group transport equation:

$$\begin{aligned}\vec{\Omega}\cdot\nabla\psi_g(\vec{r},\vec{\Omega})+\Sigma_{t,g}(\vec{r})\psi_g(\vec{r},\vec{\Omega}) = \\ \sum_{g'=1}^{G}\int_{4\pi}\Sigma_{s,g'\to g}(\vec{r},\vec{\Omega'}\cdot\vec{\Omega})\psi_{g'}(\vec{r},\vec{\Omega'})d\Omega' \\ +\frac{\chi_g(\vec{r},E)}{4\pi}\sum_{g'=1}^{G}\int_{4\pi}\nu\Sigma_{f,g'}(\vec{r})\psi_{g'}(\vec{r},\vec{\Omega'})d\Omega' \\ +\frac{Q_g(\vec{r})}{4\pi}, \qquad \vec{r}\in V, \quad \vec{\Omega}\in 4\pi, \quad 1<g<G,\end{aligned} \tag{3.30}$$

In equation 3.30, the $\psi_g(\vec{r},\vec{\Omega})$ represents the group fluxes, that could be mathematically represented as:

$$\psi_g(\vec{r},\vec{\Omega})=\int_{E_g}^{E_{g-1}}\psi(\vec{r},\vec{\Omega},E)dE \tag{3.31}$$

The coefficients in the equation $\Sigma_{t,g'}$, $\Sigma_{s,g'\to g}$ are called the group coefficients. The boundary condition with multi-group neutron transport is:

$$\psi_g(\vec{r},\vec{\Omega})=\psi_g^b(\vec{r},\vec{\Omega})=\int_{E_g}^{E_{g-1}}\psi^b(\vec{r},\vec{\Omega},E)dE, \quad \vec{r}\in V, \quad \vec{\Omega}\cdot\vec{n}<0 \tag{3.32}$$

With support from coefficients generation software, these could be calculated from cross-section libraries such as ENDF/B and then applied in the further analysis.

For the angular variable, two methods are generally applied to discretise that, called discrete ordinates S_N and spherical harmonics P_N method [123–125]. The discrete ordinates method is more widely used. This method no longer considers the neutrons are travelling in an arbitrary direction $\vec{\Omega}$ on the unit sphere. Instead of that, neutrons are seen as travelling in a limited number M_N of specified directions $\vec{\Omega}_n$, for $1\leq n\leq M_N$. In addition,

each discrete ordinate $\vec{\Omega}_n$ is associated with a cone on the w_n region unit sphere. The set $\left\{(\vec{\Omega}_n, w_n)|1 \leq n \leq M_N\right\}$ is called an angular quadrature set of order N. With the S_N approximation, the above equation 3.30 would become:

$$\begin{aligned}\vec{\Omega} \cdot \nabla\psi_{g,n}(\vec{r}) + \Sigma_{t,g}(\vec{r})\psi_{g,n}(\vec{r}) = \\ \sum_{g'=1}^{G}\sum_{n'=1}^{M_N} \Sigma_{s,g'\to g}(\vec{r}, \vec{\Omega'} \cdot \vec{\Omega}_n)\psi_{g',n'}(\vec{r})w_{n'} \\ + \frac{\chi_g(\vec{r}, E)}{4\pi}\sum_{g'=1}^{G}\sum_{n'=1}^{M_N} \nu\Sigma_{f,g'}(\vec{r})\psi_{g',n'}(\vec{r})w_{n'} \\ + \frac{Q_g(\vec{r})}{4\pi}, \qquad \vec{r} \in V, \quad 1 \leq n \leq M_N, \quad 1 < g < G\end{aligned} \tag{3.33}$$

With the boundary condition:

$$\psi_{g,n}(\vec{r}) = \psi^b_{g,n}(\vec{r}) = \int_{E_g}^{E_{g-1}} \psi^b_n(\vec{r}, E)dE, \quad \vec{r} \in V \tag{3.34}$$

The P_N method is used to expand the group angular fluxes into the spherical harmonic functions. The discretisation of the spatial variable is usually carried out by a few already developed techniques. Generally, these methods would take the physical system and impose it on a spatial grid, and then discretise each equation 3.33 on this grid.

The deterministic neutronics are the traditional and fundamental methods which are used for analysis or design of the reactor core. At the beginning of the calculation, a simple model which contains a single lattice cell (fuel pin cell, control rod cell, water hole cell) with infinite-media boundary conditions would usually be adopted. A range of multi-group precise transport calculations can be then performed on this model. These calculations could produce a pre-computed assembly homogenised cross-sections library and assembly discontinuity factors. These calculation results would then be applied in the final few-group core neutron transport calculations, and the whole calculation process is given in figure 3.5 [126].

The deterministic methods can provide significant, efficient and accurate solution

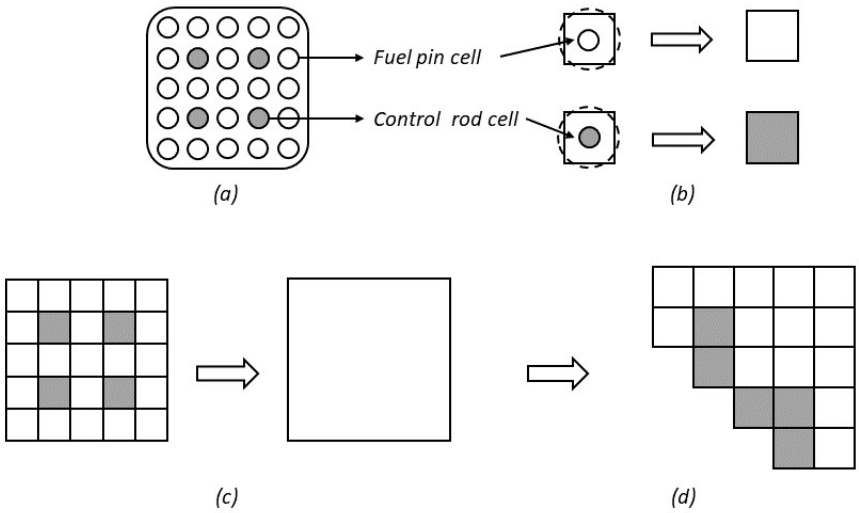


Figure 3.5: The homogenisation of the reactor core. (a) the structure of a fuel assembly. (b) Cell-by-cell homogenisation. (c) Complete homogenisation of the assembly. (d) Homogeneous reactor core.

when it is applied to the relatively low-heterogeneous light water reactors. However, with the development of nuclear engineering, the design of new generation reactors became a bit more complicated. Advanced nuclear fuels such as MOX fuel, thorium fuel, and others were adopted in the reactor core. Furthermore, some reactors required longer core life and higher burn-up loading. This progress brings challenges to the traditional methods, both the coarse mesh cell solution and few group core calculation could lead to significant errors. Thanks to the improvement of computing capability, now the fine mesh and higher group number calculations can be applied to improve the accuracy of calculation results.

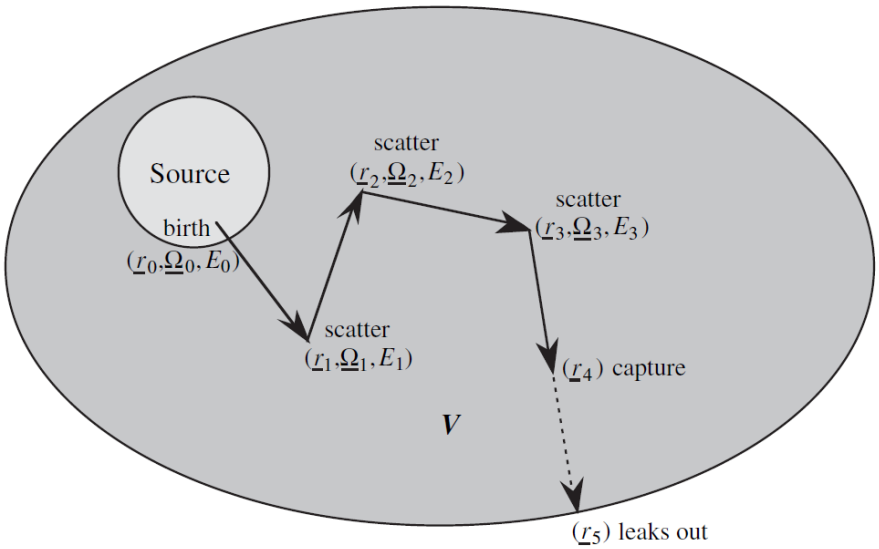


Figure 3.6: Schematic diagram of a single neutron history [118].

3.5 Stochastic methods

3.5.1 Neutron History

In the physical system V, effectively, a series of random occurrences make a single neutron history. While the solution of the above neutron transport equations do not contain randomness. As in the figure 3.6, a newly released neutron at random point $\vec{r}_0$ in the phase space with direction $\vec{\Omega}_0$, and energy E_0. Then it flies to the other random point $\vec{r}_1$ where a scatter reaction will occur, and its direction is changed to $\vec{\Omega}_1$ with new energy E_1. After this event, this neutron has a series of scattering reactions at points $\vec{r}_2$, and $\vec{r}_3$, consequently obtaining new directions and energies. Finally, this neutron could be captured at point $\vec{r}_4$, if not, it could leak out from the system at point $\vec{r}_5$. According to neutron physics theory, that single neutron history contains several random elements, such as the distance between collisions, the positions of events occurring, and the outgoing energies and directions after scattering of the neutron. For each transport neutron, these elements would be decided by

the numerical values of the cross-sections and the rules of probability [127]. However, the solution of the neutron transport equation does not contain the randomness. That then leads to the different principles of stochastic and deterministic methods.

The principle of the stochastic method is to leave the mathematical solution of the transport equation away and directly simulate extensive neutron histories. Through this can then be obtained a credible estimate of neutron flux. On the other hand, the principle of the deterministic method is to neglect the random aspects of individual neutron histories and find the mathematical solution by discrete numerical method, thereby converting the equations into a group of algebraic equations. Then solving these algebraic equation systems [128]. In the rest of this chapter, the details of the implementation of stochastic and deterministic methods will be discussed. The stochastic or so called Monte Carlo (MC) method will be mostly described, because the results in this thesis are given primarily by MC codes.

3.5.2 Monte Carlo methods

Numerical methods, which are called MC methods [128] could supply a statistical simulation solution to the neutron transport problem. The MC method can acquire statistical estimates of integral reaction rates without explicitly solving the neutron transport equation. Once a single neutron history simulation is complete, the result will be separated from the actual simulation. Such that the collection of results are based upon discrete events. The Markovian chains in the probabilistic analysis theory provide the mathematical proof of the general MC method.

Probability Distribution Function

A stochastic process associated with a random variable x is characterised by probability density function (PDF) $f(x)$. An event happening with probability between x and $x + dx$ can be written as:

$$dP = f(x)dx \tag{3.35}$$

With the variable x, the probability of the event occurring on interval $[a, b]$ can be represented by:

$$P(a < x < b) = \int_a^b dP = \int_a^b f(x)dx \tag{3.36}$$

Moreover, integrating equation 3.35 can obtain a cumulative distribution function (CDF), which is used to describe when an event takes place with a probability when the variable x is smaller than a particular value, given by:

$$F(x) = P(x' < x) = \int_{-\infty}^{x} f(x')dx' \tag{3.37}$$

The $f(x)$ integration should yield $P = 1$, or so called normalisation, over all values of the space and thus:

$$\lim_{x\to\infty} F(x) = 1 \tag{3.38}$$

To describe the simplest situation of the interval $[a, b]$ random variable x with a uniform distribution, the probability density function is then:

$$f(x) = \begin{cases} \dfrac{1}{b-a} & \text{when } a \leq x \leq b \\ 0 & \text{when } x < a \text{ or } x > b \end{cases} \tag{3.39}$$

Meanwhile, the cumulative distribution function could be given by:

$$F(x) = \begin{cases} 0 & \text{when } x < a \\ \dfrac{x-a}{b-a} & \text{when } a \leq x \leq b \\ 1 & \text{when } x > b \end{cases} \tag{3.40}$$

When $a = 0$ and $b = 1$, that is a special case of the uniform distribution. In the unit interval, the random variable is then uniformly distributed. The variables could be represented by ξ. The value for ξ could be generated by the pseudo-random number product code [129]. Selecting a random value from a probability is called sampling. The sampling process is processed with the appropriate distribution functions and numbers of evenly distributed random variables. By being coupled together, the probability distribution function and sampling method mean that the physical process can be simulated.

Inversion method

The inversion method is a kind of straightforward sampling procedure. This method is implemented using the CDF, $F(x)$ to sample variable x from distribution $f(x)$. Firstly, on the unit interval, selecting a uniformly distributed variable ξ. And then assuming the ξ value is equal to the event's cumulative probability, such that can use the inverse function of CDF to acquire the value of ξ.

$$F(x) = \xi \Longleftrightarrow x = F^{-1}(\xi) \tag{3.41}$$

This method selects x sampling values which are distributed depending on $f(x)$. Figure 3.7 has given an example of sampling a random variable from an exponential probability distribution. If the uniformly distributed variable ξ is equal to 0.8979 in the unit interval, so that it is able to calculate the related exponentially distributed variable x from CDF's inverse function, $x = F^{-1}(\xi) = 7.1552$. The red curve in figure 3.7 illustrated the distribution of random variable x values from 10000 times inversion method sampling.

Rejection techniques

Furthermore, in many practical cases, such as normal and Maxwell-Boltzmann distributions, the CDF is expensive or impossible to calculate. The other approach called rejection tech-

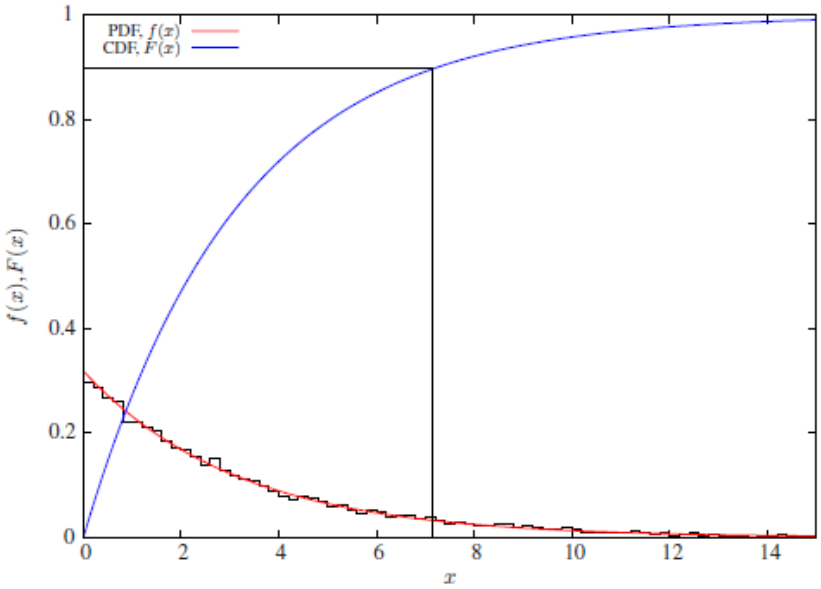


Figure 3.7: A random variable x sampling from an exponential probability distribution [130].

niques is able to do the sampling procedure of the random variable using only the PDF [131, 132]. In a straightforward way to present this, another density function,$g(x)$, and a constant $c \geq 1$ are artificially created for $f(x)$. Three terms satisfy the below inequality:

$$f(x) \leq cg(x) \tag{3.42}$$

For all x values, which will be sampled from distribution $g(x)$ at first. Meanwhile, for sampling another random variable ξ from unit interval, the value of x whether being recorded as a sample from $f(x)$ depends on the following inequality:

$$\xi < \frac{f(x)}{cg(x)} \tag{3.43}$$

The value is discarded if the inequality is not held, and the procedure is then repeated from the beginning. The distribution of the agreed values would fall following the form of $f(x)$.

For the function $g(x)$, there are certain properties that are required. It is evident that the function should be selected so that the sampling can be carried out using the inversion

process. Moreover, the similarity between functions $cg(x)$ and $f(x)$ ought to be as large as possible. A coefficient E called efficiency of the algorithm can be used to evaluate the precision. If the performance is poor, the re-sampling loop will attend to the process and repeat until it determines an appropriate value for the variable, although computational time is lost. The E could be calculated via the below function:

$$E = \frac{\int_{-\infty}^{\infty} f(x)dx}{\int_{-\infty}^{\infty} cg(x)dx} \tag{3.44}$$

3.5.3 Neutron tracking

The shortest path length of neutron interaction points is called the track. Simulating behaviours of a single neutron in a complex geometry system with different materials is called neutron tracking. [128, 133, 134]. As shown in figure 3.6, the entire track for a named neutron history could be made from the initial release point to the final absorption or leakage point. In order to simulate the neutron behaviour in the model, the basic method is sampling the free path length between collision points. In neutron physics, the macroscopic total cross section Σ_t can be used to describe the interaction probability that neutrons travel through an infinite homogeneous medium.

Therefore, while a neutron is moving through dx distance in the medium, the probability of interaction is then:

$$dP = \Sigma_t dx \tag{3.45}$$

And then making an assumption, that the neutron is located within the length x far away from the medium boundary, the probability that the neutron can arrive at the point x without any interaction would be set as $P_0(X)$. If the neutron keeps moving forward by the unit distance dx from x, the decrease of $P_0(X)$ could be considered as the probability that

a neutron interaction happened in the interval which is written down by the equation:

$$dP_0 = -P_0(x)dP = -P_0(x)\Sigma_t dx \tag{3.46}$$

Non-interaction probability can be presented as:

$$P_0(x) = e^{-x\Sigma_t} \tag{3.47}$$

Therefore, the probability a neutron freely moving journey x and then has the first interaction happening while in the next dx is:

$$P_0(x)dP = P_0(x)\Sigma_t dx = \Sigma_t e^{-x\Sigma_t} dx \tag{3.48}$$

The free path length probability density function could be written down by:

$$f(x) = \Sigma_t e^{-x\Sigma_t} \tag{3.49}$$

Meanwhile, the cumulative distribution function is:

$$F(x) = \int_0^x \Sigma_t e^{-x'\Sigma_t} dx' = 1 - e^{-x\Sigma_t} \tag{3.50}$$

Apparently, the probability distribution is exponential, due to the fact that the sample of free length could be selected by the inversion method mentioned above. Therefore, the free path distribution can be established:

$$x = -\frac{1}{\Sigma_t} ln(1-\xi) = -\frac{1}{\Sigma_t} ln\xi \tag{3.51}$$

Averaged non-interaction path length, or the mean free path ℓ can be calculated from the non-interaction probability.

$$\ell = \frac{\int_0^\infty x e^{-x\Sigma_t} dx}{\int_0^\infty e^{-x\Sigma_t} dx} = \frac{1/\Sigma_t^2}{1/\Sigma_t} = \frac{1}{\Sigma_t} \tag{3.52}$$

The approaches of this kind carry with them various limitations such that, in most cases, for the neutron it is impossible to travel in an infinite homogeneous medium. The geometry consists of several homogeneous material regions which can also be called cells.

Neutron tracking in geometry regions

Due to different material-interaction probabilities, the total macroscopic cross-sections are varied in the different geometry cells. Therefore, the sampled mean free path can be diverse for various materials. In order to obtain correct results, sampling of free path tracks should be terminated on one medium's boundary surface and re-sampled in the remaining distance to the following collision site. Let the macroscopic cross section in one material be Σ_{t1}, the distance to the closest boundary without interaction is d, the travelling distance beyond d would be dependent on macroscopic cross section Σ_{t2} from the second material. The neutron's free path as sampled in material 1 is x_1 such that at $x_1 > d$. In the second material, the remaining path length should be $x_1 - d$. Adjustments should not affect the sample statistical validity, which is guaranteed by preserving non-interactive probabilities:

$$\begin{aligned} e^{-x_2\Sigma_{t2}} = e^{-(x_1-d)\Sigma_{t1}} &\Longrightarrow -\Sigma_{t2}x_2 = -(x_1-d)\Sigma_{t1} \\ &\Longrightarrow x_2 = (x_1-d)\frac{\Sigma_{t1}}{\Sigma_{t2}} \end{aligned} \tag{3.53}$$

Therefore, the total length in two material regions from the initial emission point is then:

$$x = d + x_2 = d + (x_1 - d)\frac{\Sigma_{t1}}{\Sigma_{t2}} \tag{3.54}$$

With cross-section Σ_{t2} and new random number ξ, a statistically equivalent result can be acquired. In order to receive the shortest distance to the surface, the system's geometry usually is built up by using basic geometrical objects, such as planes and spheres.

In addition, if the program has successfully sampled a collision site, the simulation will sample the type of interaction. A material with macroscopic total cross-section Σ_t potentially contains multiple isotopes. For the isotope m being selected the probability is:

$$P_m = \frac{\Sigma_{t,m}}{\Sigma_t} \tag{3.55}$$

The probability of selecting reaction i from all potential reactions of isotope m is:

$$P_i = \frac{\sigma_{i,m}}{\sigma_{t,m}} = \frac{\Sigma_{i,m}}{\Sigma_{t,m}} \tag{3.56}$$

Therefore, the probability of isotope m occurs with reaction i is then:

$$P_{i,m} = P_i P_m = \frac{\Sigma_{i,m}}{\Sigma_{t,m}} \frac{\Sigma_{t,m}}{\Sigma_t} = \frac{\Sigma_{i,m}}{\Sigma_t} \tag{3.57}$$

Fission sampling

Based on the above neutron history method, the fission reaction can be sampled. The number of neutrons released per fission, $\overline{\nu}$, depends on the target nucleus and the incident neutron energy. In a practical Monte Carlo code, this sampling usually takes the truncated integer value V of $\overline{\nu}$ and potentially adds one neutron depending on the situation:

$$\nu = \begin{cases} N+1 & \text{if} \quad \xi \leq \overline{\nu} - N \\ N & \text{if} \quad \xi > \overline{\nu} - N \end{cases} \tag{3.58}$$

Coupled with a nuclear database that includes the delayed neutron parameters, the probability of emitting a delayed neutron is:

$$P_d = \frac{\overline{\nu_d}}{\overline{\nu_t}} = \frac{\overline{\nu_d}}{\overline{\nu_p} + \overline{\nu_d}} \tag{3.59}$$

So that for a prompt neutron, the probability is $P_p = 1 - P_d$. Just as mentioned in the above time-dependent neutron transport equation section, six precursor groups contain the prompt and delayed neutron numbers, the precursor abundances and decay constants. The emission time is dependent on the precursor isotope's decay, therefore, and that is distributed exponentially so that could be sampled by:

$$t = -\frac{1}{\lambda_j} \ln \xi \tag{3.60}$$

where λ_i is the related precursor's decay constant.

Neutron scattering

The technique to deal with scattering reactions in the MC method is more complicated than the fission reaction sampling. Because after the scattering reaction, the neutron history is not finished. After the scattering, the updated energy E and direction Ω need to be sampled. As previosuly mentioned, there are two categories of scattering between neutron and nucleus, elastic and inelastic.

The essence of elastic scattering collision is the two-body interaction with conservation of energy and momentum. Therefore, the treatment of elastic scattering requires solving the kinetic collision equations (KCE) while following the conservation laws of energy and momentum. The inelastic scattering sampling can be handled by a similar method. However, the Q-values of reaction represent that some constant discrete amount of the initial kinetic energy will be bound in the target nucleus in the process. Some inelastic scattering has the potential to be multiplicative, which means not only one neutron's energy and direction need to be considered after scattering. The KCE for a two-body problem can be written directly. In order to simplify the procedure, a transformation could be made firstly from the laboratory frame (L-frame) to the centre-of-mass frame (CM-frame).

In the L-frame, the target nuclei would be assumed as stationary or have some thermal motion velocity. In the CM-frame, the scattering neutron and nucleus are travelling toward each other before the collision, and turn back away from each other at a scattering angle. The reason it makes the collision treatment rather less complicated is that total momentum is always zero for an observer in the CM-frame. The target nucleus has velocity in the L-frame that is present only in the coordinate transformation and will not affect the CM-frame equations. For elastic reactions, the particles' kinetic energies remain conserved. Moreover, in both frames, the inelastic scattering Q-values are constant. Two coordinate systems are present in the below figure. If the initial neutron and target velocities in the L-frame are $\vec{v}$

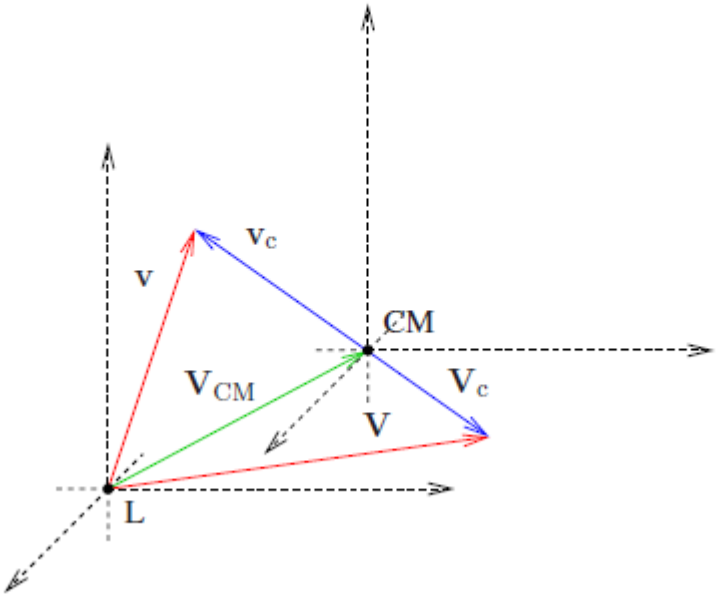


Figure 3.8: The diagrams of CM- and L- frames. $\vec{V_{CM}}$ is the velocity of CM-frame origin refers to the L-frame origin [130].

and $\vec{V}$, masses are m and M, the velocity of a two-body system in the L-frame is given by:

$$\vec{V_{CM}} = \frac{m\vec{v} + M\vec{V}}{m + M} = \frac{\vec{v} + A\vec{V}}{1 + A} \tag{3.61}$$

In equation 3.61, A represents the ratio of:

$$A = \frac{M}{m} \tag{3.62}$$

The neutron and target initial velocities are then given by:

$$\begin{aligned} \vec{v_c} &= \vec{v} - \vec{V_{CM}} = \frac{A(\vec{v} - \vec{V})}{1 + A} \\ \vec{V_c} &= \vec{V} - \vec{V_{CM}} = -\frac{\vec{v} - \vec{V}}{1 + A} \end{aligned} \tag{3.63}$$

KCE in the CM-frame are written as:

$$\begin{aligned} \frac{1}{2}mv_c'^2 + \frac{1}{2}MV_c'^2 &= \frac{1}{2}mv_c^2 + \frac{1}{2}MV_c^2 + Q \\ m\vec{v_c'} + M\vec{V_c'} &= m\vec{v_c} + M\vec{V_c} = 0 \end{aligned} \tag{3.64}$$

The term Q in equation 3.64 represents the inelastic scattering Q-value. The collided velocities are given by $\vec{v_c^{'}}$ and $\vec{V_c^{'}}$. Due to total momentum goes zero, the neutron and the target must be moving in opposite directions.

Simplifying the momentum part in equation 3.64 one can obtain:

$$\begin{aligned} \vec{v_c^{'}} = -A\vec{V_c^{'}} &\Longrightarrow v_c^{'2} = A^2 V_c^{'2} \\ \vec{v_c} = -A\vec{V_c} &\Longrightarrow v_c^2 = A^2 V_c^2 \end{aligned} \tag{3.65}$$

Replacing the square speeds in equation 3.64 for the neutron and the target gives:

$$\begin{aligned} v_c^{'2} + \frac{1}{A} v_c^{'2} &= v_c^2 + \frac{1}{A} v_c^2 + \frac{2Q}{m} \\ A^2 V_c^{'2} + A V_c^{'2} &= A^2 V_c^2 + A V_c^2 + \frac{2Q}{m} \end{aligned} \tag{3.66}$$

Finally, the speeds after collision can be solved as:

$$\begin{aligned} v_c^{'} &= \sqrt{v_c^2 + \frac{2AQ}{(A+1)m}} \\ V_c^{'} &= \sqrt{V_c^2 + \frac{2Q}{A(A+1)m}} \end{aligned} \tag{3.67}$$

From equation 3.67, the speed and energy of neutrons and target nuclei which are independent of directional change can be found. For the elastic scattering, where $Q = 0$, the speeds and energies of neutron and target will remain stable.

There are two independent scattering angles that are usually used to describe the final after-collision neutron directions ($\vec{\Omega_c} \rightarrow \vec{\Omega_c^{'}}$). The first of these is the polar angle θ_c, which is between the incident and final direction. The other one is the angle that determines the collided direction rotation over the incident motion direction, called azimuth angle ϕ_c. Figure 3.9 shows the positions of azimuth and polar angles. The azimuth angle ϕ_c can be isotropic in the CM-frame constantly if treating the target nucleus as a symmetric point particle. Whether the polar angle is isotropic or an-isotropic depends on the reaction. S-wave potential scattering, such as when a neutron collides with a light atomic mass nucleus

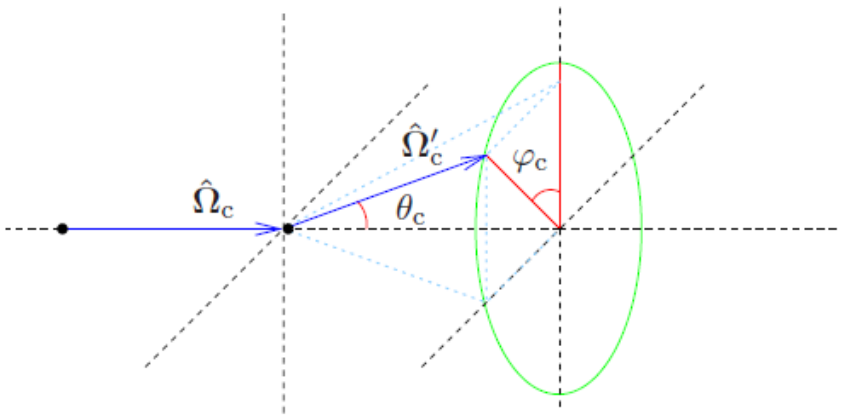


Figure 3.9: Neutron direction of incident $\vec{\Omega_c}$ and after collision $\vec{\Omega'_c}$, and polar θ_c and azimuth ϕ_c scattering angles [130].

with low energy, are always isotropic in the CM-frame. For higher energy neutron scattering with a heavy mass numbered nucleus, the polar scattering angle θ_c has a higher chance to be an-isotropic.

Generally, dealing with a collision sampling problem needs three steps. Firstly, sampling the initial velocities from L-frame and then transform that into the CM-frame, calculating the speed of the neutron and the target after collision from equation 3.64. Secondly, the scattering angles would be sampled in the CM-frame. The sampled polar scattering angle θ_c and uniformly distributed ϕ_c would make the transformation $\vec{\Omega_c} \rightarrow \vec{\Omega'_c}$, the new velocities are then given by:

$$\begin{aligned} \vec{v'_c} &= \vec{\Omega'_c}\vec{v'_c} \\ \vec{v'_c} &= -\vec{\Omega'_c}\vec{V'_c} \end{aligned} \tag{3.68}$$

Finally, converting the velocities to the L-frame by equation 3.63, that then completes the procedure.

In practice, the target velocity following the Maxwell-Boltzmann distribution could be sampled by the rejection method mentioned above, and then the speed could be calcu-

lated. And the motion direction is sampled from an isotropic distribution. The reaction's anisotropy could determine the scattering angle sampling. In the CM-frame, if the polar angle is isotropic, the vector $\vec{\Omega}_c^{'}$ could be sampled isotropically. On the other hand, the nuclear data library would give the distribution of the cosine of the polar angle, $\mu_c = \cos\theta_c$. The initial path vector is then tilted and rotated over the azimuth angle which is uniformly distributed. There are many procedures to perform in order to achieve this mission with the rejection method and the angles' conversion [134, 135]. One method is given below:

$$\begin{aligned}
\Omega_z^{'} &= \Omega_z \cos\theta + \alpha \cos\phi \\
\Omega_y^{'} &= \frac{1}{1-\Omega_z^2}(\Omega_y \beta + \Omega_x \alpha \phi) \\
\Omega_x^{'} &= \frac{1}{1-\Omega_z^2}(\Omega_x \beta - \Omega_y \alpha \sin\phi)
\end{aligned} \tag{3.69}$$

In equation 3.69 the direction vectors before and after rotation can be divided into the Cartesian components, which are $(\Omega_x, \Omega_y, \Omega_z)$ and $(\Omega_x^{'}, \Omega_y^{'}, \Omega_z^{'})$ respectively. The azimuth angle ϕ will be uniformly sampled from an interval between 0 and 2π.

$$\begin{aligned}
\alpha &= \sqrt{1-\Omega_z^2} \\
\beta &= \cos\theta - \Omega_z \Omega_z^{'}
\end{aligned} \tag{3.70}$$

There are certain physical restrictions for the inelastic scattering cases. In particular, the square roots in equation 3.67 must be positive. Therefore, the conditions could be written as:

$$\begin{aligned}
Q &> -(\frac{A+1}{A})\frac{1}{2} m v_c^2) \\
Q &> -(A+1)\frac{1}{2} M V_C^2
\end{aligned} \tag{3.71}$$

If converting the square speed to the L-frame by equation 3.63, both conditions would reduce to a single limitation:

$$Q > -(\frac{A}{A+1})\frac{1}{2} m (v-V)^2 \tag{3.72}$$

The inelastic scattering usually occurs above the thermal energy range which means the neutron velocity is much higher than the target velocity, $v \gg V$. The limitation in the

equation could be reformed using the neutron energy in the L-frame:

$$Q > -(\frac{A}{A+1})E \tag{3.73}$$

The above target nucleus's motion follows the Maxwellian distribution. Their collisions with neutrons can produce peaks in the thermal area of the neutron spectrum. However, the above description is incapable of sufficiently reproducing the scattering of such neutrons with hydrogen atoms bound within water. This is because the target nucleus can have a recoil energy that is close to that of the atom's molecular binding energy, such that the free particles model cannot properly deal with this nucleus in this scenario. Therefore, elastic scattering reactions with these non-free particles, such as for lower-energy neutrons upon bound, light atomic mass nuclei, are equivalently treated as particular versions of inelastic scattering, which are continuum inelastic reactions (CIR)s. The Q-value of CIR is presented by distribution, not by a discrete number. In practical problems, the energy and the scattering angle can be directly sampled from the distributions which are given by the interaction data in the L-frame. The energy and momentum do not need to be strictly conserved in individual reactions, but for a significant amount of collisions, their probability distributions should keep conservation laws on average. The neutron scattering reaction from bound nuclei is meaningful in nuclear reactor physics to describe the neutron reactions with commonly used moderator materials.

3.5.4 Results Estimates

The above sections introduce how the MC method simulates the neutron histories which consist of tracks between the sampled collision points. Meanwhile, the required physics quantities can be collected from the simulated events. The result collection process is somewhat similar to experimental measurement. The types of flux integral evaluations in the MC

method can be presented by the below equation:

$$R = \int_t \int_V \int_E f(\vec{r}, E)\phi(\vec{r}, E)dtd^3rdE \tag{3.74}$$

As shown, it involves integrating the multiplication over the target energy interval, time and some spatial volume. The response function $f(\vec{r}, E)$ could be unity or a reaction cross-section, that may represent any physical parameter within the integration domain. This value should be determined and uniform.

Due to the integration being carried out over time, the results of equation 3.74 are the number of responses, not the response rate. After the normalisation, the time-integrated results can be seen as equivalent to the time-averaged quantities. The simulated events such as fission, absorption, scattering collisions, which are recorded for results calculation, are called scores. The scores are going to combine in various methods and form the physical quantities of statistical estimates. A series of various estimated reaction rate methods will be stated in this section.

Analogue and implicit Estimator

Analogue estimator is a straightforward type of estimator for reaction rates. The basic concept is that the number of real reactions taking place is counted and used as an approximation of the reaction rate. For example, by using a corresponding macroscopic cross-section as the response function in equation 3.74, an analogue estimate could be produced by counting the number of pre-specified interactions in the sample. The analogue estimate can effectively derive the required parameters caused by complicated mechanisms in the simulation.

However, in many situations the analogue estimator could suffer higher variance due to rare events which may not occur often enough to get good statistics if they are being tallied. The implicit estimators are available and more efficient, taking the product of flux

estimator and response function value to calculate the integral reaction rates. This can be written mathematically as:

$$R = \sum_{i=1}^{I} s^i = \sum_{i=1}^{I} f^i \phi^i \tag{3.75}$$

The integration is implemented by summing over the scored values. Naturally, values will depend on neutron energy and spatial coordinates. However, these calculation results could not represent any physical results. The number of scores included in the sum will grow with more neutron histories running. The results should be sufficiently normalised and then coupled to the physical parameters.

Collision estimator

The collision estimator is an intuitive way to calculate flux integrals. Instead of counting a reaction only when it happens, the collision estimator would count the number of collisions and then evaluate the total interaction rate. Similarly, by summing the fractional reaction probabilities, the expected rate of an arbitrary reaction could be calculated. The equation for this has been mentioned above in equation 3.57. The scored value can be represented as:

$$\phi^i = \frac{1}{\Sigma_t^i} \Longrightarrow s^i = \frac{f^i}{\Sigma_t^i} \tag{3.76}$$

The collision site is located in the cell, which is filled by the material that has macroscopic total cross-section Σ_t^i. The summation is carried over the reciprocals of the total cross-section when the response function is treated as a unity. Its result represents the integrated flux and also is the total mean neutron path length of neutrons.

Track-length estimator

The track-length estimator is the other general homogeneous-material regions' integrated flux calculation method. The track length is recorded once a neutron track is completed

within the area. Either reaction sites or boundary surface contact may be the start and endpoints of the track. The recorded score can be presented as:

$$\phi^i = l^i \Longrightarrow s^i = f^i l^i \tag{3.77}$$

In the above equation 3.77, the l^i is the length of the track. The track-length estimator has better performance than the collision estimator in small geometry regions. The scores could be recorded when neutrons pass through the region without the collisions which actually occur. In materials with a small total cross-section, the distinction is emphasised. A no-neutron-reaction area, or so called void zone, is the most extreme case.

3.5.5 Results collection

The above sections introduce the estimate techniques of reaction rates in the MC method. In practical cases, it usually takes the total scores by batches of I_n values. The summation over all scores is given by:

$$I = \sum_{n=1}^{N} I_n \tag{3.78}$$

The size of batch I_n depends on random events. In criticality calculations usually a single batch will contain all scores within one generation.

Any given result from a calculation by the MC method, colloquially being referred to as a tally, represents an estimate of the mean of some random variable. Along with an accompanied standard deviation, which represents statistical accuracy, would also typically be given by the calculation at the same time. The mean value of estimate X is given by the arithmetic mean of the scores' summation over all batches:

$$\bar{X} = \frac{1}{N} \sum_{n=1}^{N} X_n \tag{3.79}$$

And the standard deviation is given by:

$$\sigma(X) = \sqrt{\frac{1}{N(N-1)} \sum_{n=1}^{N} (X_n - \bar{X})^2} \tag{3.80}$$

The standard deviation demonstrates how far a collected value is most likely away from the accurate result obtained if the simulation could be infinitely sustained. In principle, the MC simulation could produce an exact estimate of neutron flux in a perfectly known system which includes the system geometry and cross-sections at each point. However, computing facilities are incapable of processing an infinite number of neutron histories. Therefore, all MC simulations contain statistical errors inherently.

3.5.6 Accuracy estimation

Where the probability distribution is not defined, the standard deviation does not provide quantitative information on the statistical accuracy of the estimation X. The central limit theorem (CLT) stated that the distribution of the sample mean will converge to a normal distribution. Let $X_1, X_2, \ldots, X_n$ be an independent, identically-distributed random variables infinite sequence, that has expected values $E(X_i) = \mu$ and variances $Var(X_i) = \sigma^2 < \infty$. These random variables do not need to follow any particular distribution. According to the CLT, that as $n \to \infty$, the random variable $\sqrt{n}(\bar{X}_n - \mu)$ converges into the standard normal distribution or so called Gaussian distribution:

$$\sqrt{n} \left(\frac{1}{n} \sum_{i=1}^{n} X_i - \mu \right) \to N(0, \sigma^2) \tag{3.81}$$

The normal probability density distribution is present as:

$$f(x) = \frac{1}{\sigma\sqrt{2\pi}} e^{-\frac{(x-\bar{x})^2}{2\sigma^2}} \tag{3.82}$$

The other important statistical law is the law of large numbers (LLN), that states the average value of the result should approach the expected value for a large number of repeated

experiments. By using the infinite sequence of random variables $X_1, X_2, ..., X_n$ which are given above, the LLN presents that the sample mean $\bar{X}_n = X_1 + \cdots + X_n/n$ converges in probability to the true mean. Such as for all $\epsilon \geq 0$. The LLN could be mathematically presented as:

$$\lim_{n\to\infty} P(\left|\bar{X}_n - \mu\right| \geq \epsilon) = 0 \tag{3.83}$$

Being coupled with the CLT and LLN together, the MC simulation estimate results for X should follow the normal distribution. Moreover, the statistical accuracy of results always grows with the improving size of simulated histories.

3.5.7 Non-analog Monte Carlo

Similar to the aforementioned optimisation method for the neutron flux estimators, the non-analog concept could also be applied for actual MC simulations. Non-analog MC methods and variance reduction techniques play an essential role in various statistical areas. This optimisation is able to ensure the neutron histories which have more significant contribution to the result estimates are scored more frequently than others. In the non-analog MC simulation, each simulated neutron history would be assigned with a statistical weight which is equal to unity. If this weight is smaller than unity, it means this neutron history simulated by the analog method will make a more meaningful contribution. The scored values are multiplied by the weight when the neutron makes a score. The total weight would be normalised to a particular value before each cycle begins for maintaining the significance of the mean scores between the cycles.

The statistical weights are available here because the absorption reaction has the potential to be treated implicitly, but not to terminate the entire neutron history. The implicit treatment of absorption reaction means that the fractional absorption probability

decreases a fraction of the statistical weight:

$$W^{'} = W\left(1 - \frac{\Sigma_a}{\Sigma_t}\right) \tag{3.84}$$

In equation 3.84, the collision changes the neutron weights from W to W', and Σ_a, Σ_t are the absorption and the total cross-section. The decline in neutron weight is statistically equal to the end of the neutron history. By this method, more scores could be made in the region where neutrons are less frequently passing through. Once the statistical weight reduces to a certain low level, that contribution can be practically negligible. A procedure called Russian roulette could be applied to determine whether the weight of neutron has fallen lower than a limit in probability and to cut-off the neutron history. A straightforward method is to express the termination probability as:

$$P = 1 - \frac{W}{W_0} \tag{3.85}$$

Where W_0 is the initial neutron weight. In the simulation of neutron-multiplying scattering reactions, multiplying the neutron weight by the number of the emitted neutrons, only one neutron will be selected to carry on the simulation. The above method describes how the MC method could be simulating a neutron physics problem. In nuclear engineering the MC method is used to solve complex shielding problems and to benchmark deterministic calculations. Along with the development of computer science and parallel computing, MC is also being used to calculate general problems.

3.6 Summary of Methodology

In this chapter, in order to better understand out how the proposed optimisations affect the performance of the SMART system, a series of meaningful nuclear reactor physics phenomena have been introduced before description of the working process and results. In section 3.1, critically, and the effective multiplication factor k_{eff}, has been drawn into the studies. This

factor can directly describe the evolution of the number of neutrons in the reactor core and is used to evaluate whether the chain fission reaction is self-sustained. Meanwhile, when the fission reactions occur, and release fission neutrons, parallel or induced nuclear reactions are also continuing to happen. The composition of nuclear fuel constantly changes during the entire reactor lifetime, especially a few fission product isotopes have large neutron absorption cross-section and thus could significantly affect the reactor operation and its power distribution. Section 3.2 introduced BU equations that could be applied to study this problem.

The fundamental aspects of criticality and BU problems are important neutron behaviours inside the core. In section 3.3, the steady-state neutron transport equation or so called linear Boltzmann equation has been established. And the variant equations for delayed neutron and k-eigenvalue investigation have also been considered respectively.

However, it is difficult to solve the neutron transport equations analytically. In order to solve this problem, two numerical techniques which could be used to determine a solution, deterministic and stochastic (MC) methods, are introduced in the rest of this chapter. The content of the MC method occupies the main space in this section because that is the theory used by most of the major research codes in this thesis. The details of the MC method, such as PDF, sampling technologies, neutron reaction simulation, and results estimating are all covered and have been mathematically described.

Chapter Four

Model Build-up, Verification and Sensitivity Study

Chapter 3 has provided awareness of the physical theories of neutron transport, coupled with two numerical analysis approaches capable of solving the related mathematical equations, named deterministic and stochastic methods respectively. Based upon this, a series of induced nuclear reactor questions could be studied, such as the aforementioned criticality and BU problems. The works in this thesis mostly adopted the MC method codes as the research tool. The reactor core's geometry and material compositions have been faithfully reflected in the corresponding numerical models. Moreover, this should eliminate physics errors caused by the model set up and keep the statistical error at a sufficiently small value.

The build up of the MC model, and its verification will be shown in this chapter. Multiple MC codes have been applied to study the SMART neutronic problems. Some models were originally built by the MSc course students for their projects, and the author has advised their work on multiple occasions a project supervisor for such MSc level research. The modelling process and a part of those results will be cited briefly in this thesis, mostly just for the cross-comparison provided and code verification. This chapter includes MC codes

independently developed by industry corporations or the scientific community.

In the early stage of this PhD program, the ANSWERS code package containing MONK, MCBEND and WIMS were applied to build a prototype model of the SMART reactor core. However, due to the interrupted code's license, the usage of these codes could not continue until March 2020. The MCBEND' license was resubscribed but mostly for educational purposes. In the absence of time on the ANSWERS code package, an open-source MC neutron and photon transport simulation code OpenMC was used to build the reactor core model and analyse the reactor physics problems. The features of each code and the model build-up process will be presented below.

ANSWERS codes are developed and further maintained by JACOB's ANSWERS software service team. The codes suite is widely used in over thirty countries worldwide for the research of reactor physics, radiation shielding, nuclear criticality, dosimetry, and nuclear data. Other than the MC codes MONK and MCBEND, the suite also includes a range of practical codes such as: reactor physics code WIMS that is based on the deterministic energy multi-group method, thermal reactor core neutron diffusion and the coupled neutronics and TH code PANTHER.

4.1 MONK

MONK is the first MC code that was used in this PhD program. The code is designed to assist in criticality safety and reactor physics problems. The origins of MONK were called GEM, which was produced in the UK's post-war nuclear weapons programme. In order to satisfy the demand of the UK nuclear fuel reprocessing industry for criticality safety, the code had since been further developed. Meanwhile, the code was also enhanced for reactor physics analyses which contains the features of microscopic BU treatment, and

adjoint solution capability and point estimation of flux. The version MONK10B was used in this project. The primary aim of MONK is to calculate the neutron multiplication factor k_{eff} by the computer simulation of the birth, movement, absorption and leakage of the finite neutron sample. The related theories of that were already introduced in the above chapter. The utilisation of MONK would begin at the reactor geometry modelling stage.

4.1.1 Body geometry

A key property of MC codes is to model the geometry as accurate as possible. The MONK geometry package enables the creation of a considerably complex model, with both efficiency and reasonable ease. The geometry function includes two distinct but closely-related sections, sample body and hole geometries. When tracking a neutron within a sample body geometry, the code would calculate the distances between its current neutron position and the boundaries of the neighbouring bodies. The sample body that has the shortest path would be selected to be entered next. The shortest distance would be compared with the distance to the next neutron interaction in the tracking medium, which is obtained by sampling from the transmission probability distribution.

The sphere, box, rod, trapezoidal prism, torus, hemisphere and hexagonal prism are basic body shapes. Each sample shape is assembled into the basic geometry unit called *part*, which can be contained in other parts and so on until the whole system geometry is built in a global part with suitable external boundary conditions. Each part is a self-contained sub-system with local coordinates of its own. The part's outer surface is referred to as the part container body. This modelling system is tailored to the repeated structures commonly existing in criticality and reactor physics applications. This modelling structure is similar to the process in the engineering area, where the detailing of components would be drawn at first and then combined together into a larger assembly.

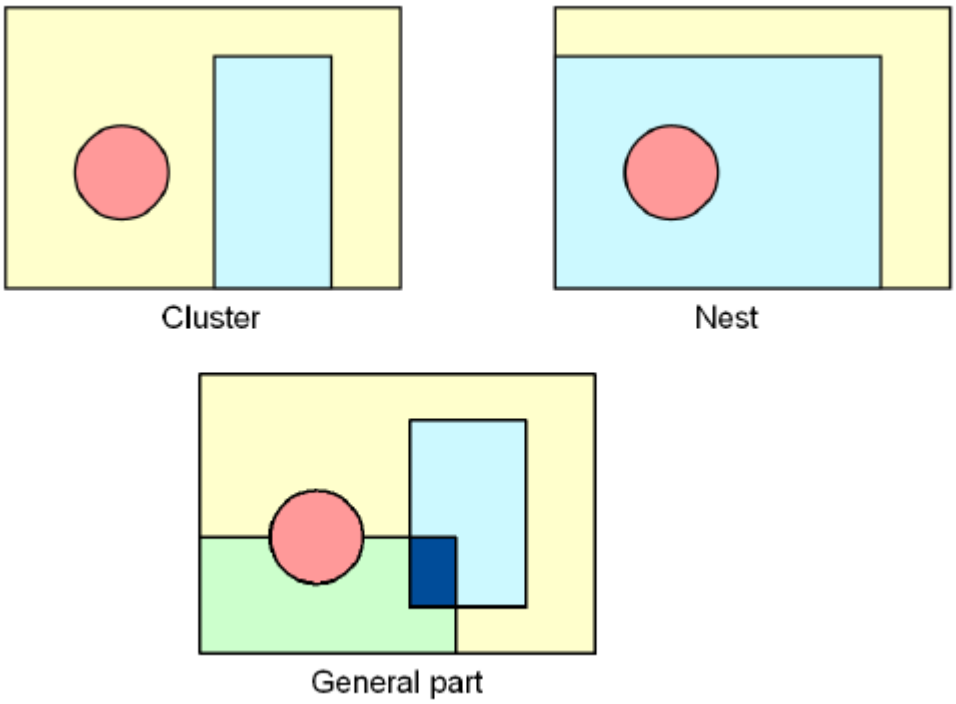


Figure 4.1: MONK geometry examples of nest, cluster and general parts.

There are three common methods to assemble any number of simple bodies to a part, and these are called the nest, the cluster, and the general part. As shown in 4.1, in a nest structure, the bodies must lie one inside another. For a cluster, each body is completely inside the container and distinct from all other bodies. And the general part structure allows complete freedom of overlap. Each simple body within a part has an inside portion delineated to hold its contents. The contents of a simple body could be a defined material which is a homogeneous mixture of nuclides or a heterogeneous nuclide mixture that has geometric detail named a hole geometry. The other kind of part, called array, is a box body that could be cut by parallel planes in each of three directions. Each cuboids compartment created contains a subsidiary part that must fit exactly into the geometry body space. Additionally, a hexagonal prism body could be formed by a variant array called hexagonal.

4.1.2 Hole geometry

As mentioned in Chapter 3, explicit tracking would bring a few limitations to the simulation. Using the sample bodies to model a complex situation can result in many boundary distances that need to be calculated and compared. Preparing the data for these types of cases would be difficult for the computer and cause slow execution speed. Therefore, MONK offers an alternative method called Woodcock tracking. The hole geometry is the place where the Woodcock tracking is being carried out.

The basic idea of Woodcock tracking is artificially giving a constant mean free path λ which equals the shortest λ of those materials filled in the hole. The tracking process could use this given value instead of calculations of boundary distances. Moreover, if the given λ is shorter than the real mean free path of the travelling medium, it should introduce extra collisions called pseudo collisions, which would be treated as a non-event. The neutrons would travel in the same direction and speed as before the pseudo collision. On some rare occasions, the appearance of a pseudo collision could lead to a performance downgrade. For example, one of the real materials has a much bigger total cross-section than all other material. However, it just occupies a small fraction of the total hole geometry. This condition will cause a very large number of pseudo collisions. Therefore, one should avoid strong neutron absorber materials only in relatively small proportions of hole.

There are many different types of hole geometries which are available in MONK. Their size depends on the container sample body shape. Combining the sample body and hole geometries, a MONK code SMART reactor model has been built-up. The schematic diagrams of this model is given in Figure 4.2. The next section will explain the modelling process.

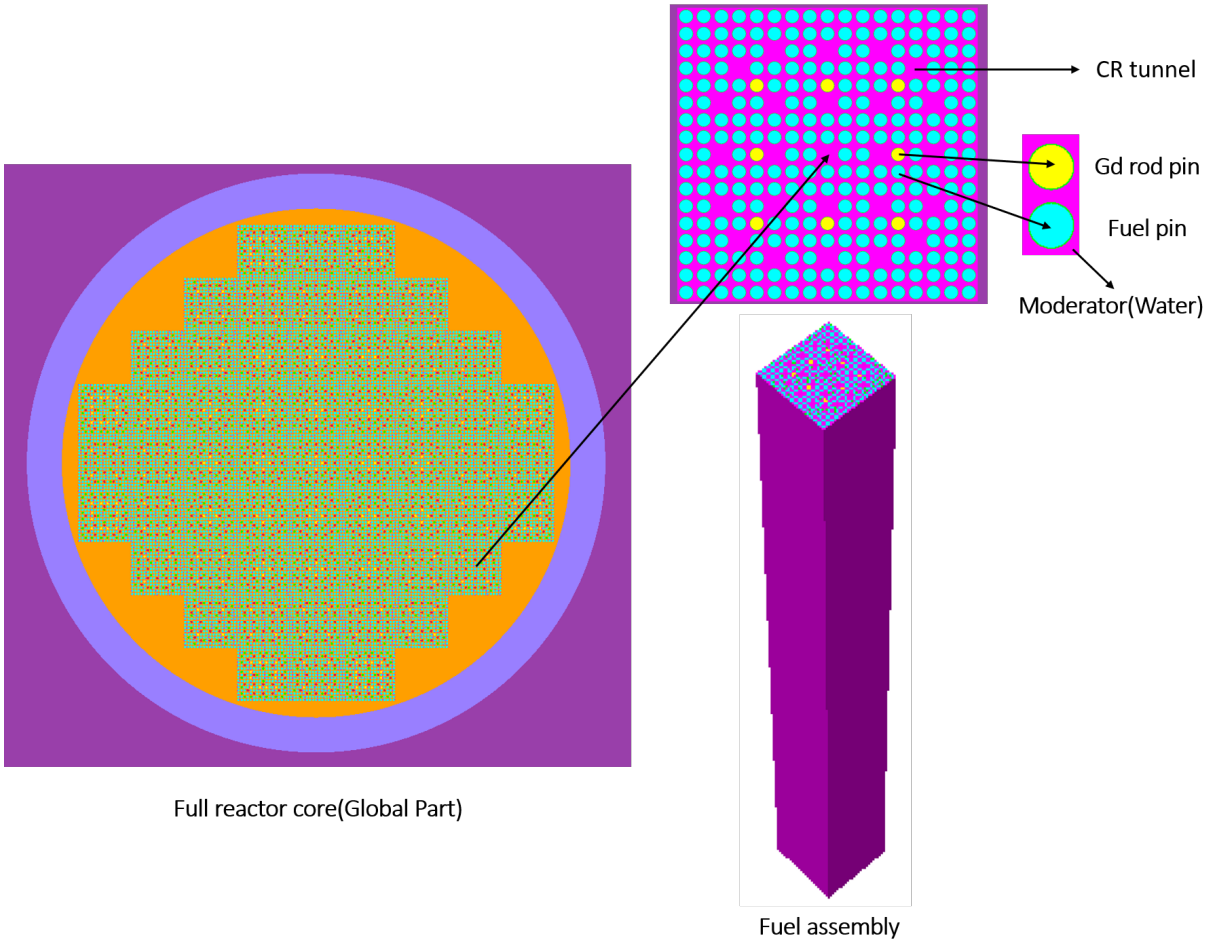


Figure 4.2: Simplified SMART reactor core model.

4.1.3 MONK SMART model

The geometry of the MONK SMART core model refers to Alzaben's work in 2016 [136]. That assumes there are three types of FA in the core, which individually has different number of neutron absorbers in the 17×17 array. The neutron absorber has the gadolinium-uranium oxide mixture, $Al_2O_3 - B_4C$ providing shim of two kinds. The MONK SMART model in this thesis followed these characters and assumptions.

First of all, the *globe* hole geometries is used to define a series of pin structures. A globe hole consists of a set of concentric annuli around the z-axis, The *globe* holes of the

UO_2 fuel rod has two concentric annuli, the inner one represents the fuel rod itself, and the outer part is zircaloy cladding. The radius of the fuel rod is $0.4465cm$, and the thickness of cladding is $0.0285cm$. On the other hand, the reactivity control rods do not have cladding, which has a radius of $0.475cm$.

Secondly, using the already defined *globe* holes as the subsidiary contents and then periodically replicating them in the various orders to form the rectangular arrays. In this step, the subsidiary $(n \times m)$ rectangular array is created by the *lattice* hole option that has 17×17 pins, and every pin is a square with the side length of $1.2cm$. Varying the position and number of defined globe *hole* subsidiaries in the *lattice* hole array could model the aforementioned three type of FAs.

And then, the defined *lattice* holes would be separately assigned in three *box* simple bodies. Their dimensions are $20.4cm, 20.4cm, 200.00cm$. Meanwhile, another three *box* bodies containing material water are created to coincide with the *lattice* holes and constitute the *nest* parts. The aforementioned *array* body geometry is used to cut the larger box bodies into a set of smaller and uniform size boxes as big as the FAs body. The longest layer has 9 boxes. The number of boxes would uniformly reduce 2 in each layer along the X-axis and Y-axis until the core edge, which only has 3 fuel assemblies in the outermost layer. All the *array* body layers will stack together into a *cluster* body because their surfaces contact one another.

Finally, a set of $ZROD$ bodies, which is the simple rod shape in the Z-axis, is created to contain the defined cluster body. From the reactor core to the outside wall surface, two bigger sized $ZROD$ bodies contain all real defined materials.

4.1.4 Materials and source

Among the geometry modelling process, a series of defined materials have assigned in the simple body or hole geometries. In a MONK simulation input file, the material specification unit defines the chemical and isotopic compositions of the materials in a particular problem. This unit defines the constituent elements of the material compositions by various proportion terms, including volume, weight and atom type, leading the code to cite the specified cross-section library.

A keyword TYPE followed by one selection of BINGO, DICE, MULTI or WIMS is required in the real material definition. The DICE and BINGO represent the point energy and continuous energy neutron data library, and the MULTI option links to the multi-group coefficients data library. Option WIMS is related to the interface with the WIMS code in the software suite. Moreover, in many practical cases, the temperature of materials in the model needs to be specified, and then the simulation could acquire suitable data from the library. The keywords KELVIN and CELSIUS could be applied to specify the preferred temperature unit.

The starting source is the other meaningful definition in the MONK input file. The code performs the staged calculation, and the initial source needs to be provided for the first guess of neutron distribution. In most cases, the starting neutron source is normally occupied by fissile materials located in all regions. Its spatial distribution can be done by selecting the material or its volume. The default starting source's energy distribution is that the neutrons have the energy sampled from a ^{235}U fission spectrum. The default angular distribution is isotropically sampled neutrons.

4.1.5 Criticality calculation

MONK will perform a few initial stages with a given initial source distribution but does not count their results into the scoring statistics. This settling process is needed for the neutron distribution to approach the true situation from a guessed one. Several control parameters are required for acquiring accurate k_{eff} values and its standard error. Each stage's neutron population size should be sufficiently large. The samples in a calculation must be sufficient to provide a normal distribution.

Meanwhile, running the calculation n times with different random number seeds to get additional independent results, n is the number of stages, which is a better approach to achieve more precise results. The results from different stages then are combined by the following equations:

$$k = \frac{\left(\frac{k_1}{\sigma_1^2} + \frac{k_2}{\sigma_2^2} + \frac{k_3}{\sigma_3^2} + \cdots + \frac{k_n}{\sigma_n^2}\right)}{\left(\frac{1}{\sigma_1^2} + \frac{1}{\sigma_2^2} + \frac{1}{\sigma_3^2} + \cdots + \frac{1}{\sigma_n^2}\right)}$$
$$s = \frac{1}{\sqrt{\frac{1}{\sigma_1^2} + \frac{1}{\sigma_2^2} + \frac{1}{\sigma_3^2} + \cdots + \frac{1}{\sigma_n^2}}} \tag{4.1}$$

Figure 4.3 presents the k_{eff} simulation results from the MONK SMART core model that was built and described in the above section 4.1.3. The values from the earlier stages were not eliminated to demonstrate the convergence process. The error bar on each data point indicates the size of the standard deviation at that stage. The estimated k_{eff} value drops down rapidly in a few preliminary stages with big standard deviations, and then it fluctuates in the next about 300 stages and eventually approaches convergence at 1.1207 ± 0.0001.

Due to the MONK licences' ending, many results could not be further polished. Therefore that will not be presented in this thesis. But the modelling process by MONK is valuable

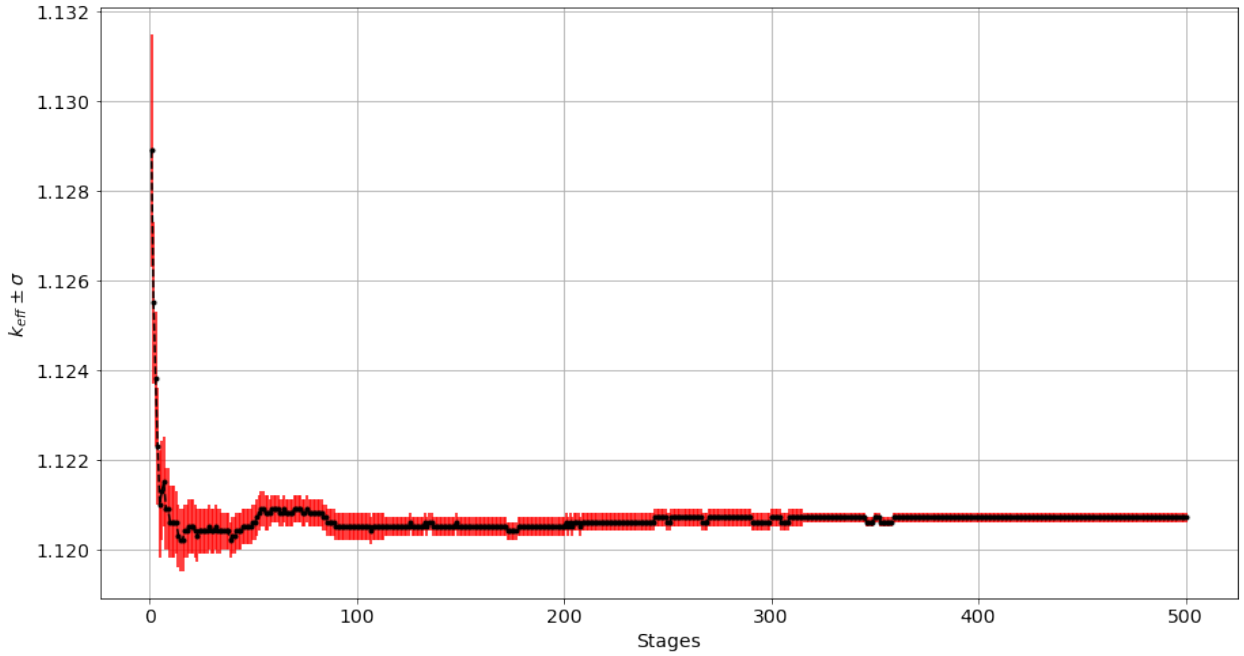


Figure 4.3: MONK k-eff simulation results with 500 stages.

and influential to the usage of other MC codes in this project, in particularly helping to valid their results with even greater confidence.

4.2 MCBEND

The other MC code in the ANSWERS suite, called MCBEND, is designed for general radiation transport analysis in a sub-critical system. MCBEND is capable of performing multi-particle transport simulation from their birth to their ultimate fate, for available particles including neutrons, gammas, electrons and positrons.

MONK and MCBEND, as a pair of twin codes, have many common features, such as geometry package and materials specification. As a multi-particle simulation code, MCBEND has a specifically developed source definition module. The unified source module allows for describing a particle source using a collection of bodies that can be flexibly oriented. The

source bodies could be defined by a similar method to the material geometry bodies. Meanwhile, several source spectra are already built into the code. The users also could customise the source spectrum by a series of functions such as *histograms*.

A range of response functions in MCBEND could calculate the specific reaction rate in a detailed group scheme. In 2020, the MSc students studied the SMART radiation shielding material and ICRP-74 dose rate problems by MCBEND for neutrons and gamma-rays, which have utilised the above-described model originally developed for MONK.

4.3 OpenMC

OpenMC is a community-developed MC neutron and photon transport simulation code. The code is capable of modelling and studying geometry by either a constructive solid geometry or computer-aided design (CAD) representation methods and then performing fixed source, k-eigenvalue, and sub-critical multiplication calculations. OpenMC could execute the neutron transport calculation in both continuous-energy and multi-group modes. A hybrid shared-memory parallelism (MP) and distributed-memory parallelism (MPI) programming model is applied to support code parallelism. The OpenMC depletion function with multiple time integration methods is launched in the update at the late of 2019 [137, 138].

A $3D$ SMART reactor core model has been built from a single fuel rod pin by the OpenMC supplied Python API called the *openmc.model.rectangular_prism* The model's geometry and building process are similar to the above MONK model. The assumption of three types of FAs do not been adopted in the OpenMC model to exclude the neutron absorbers effect to the investigation of the maximum power output and full power depletion. Each assembly has 25 grids that are not occupied by fuel rods and left for the control rods and instrument tubes. The slice plots of the model would be given in the below figure.

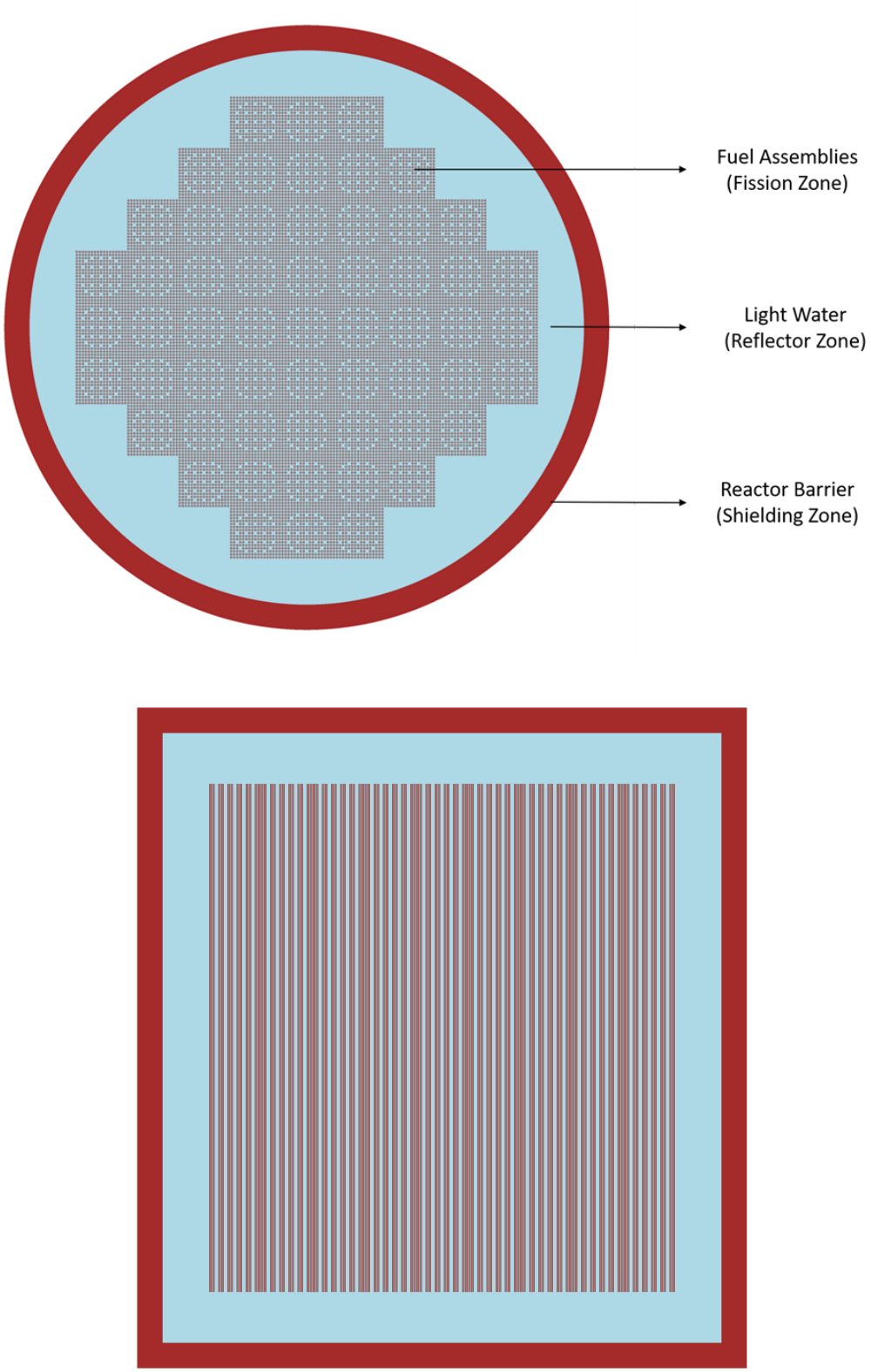


Figure 4.4: Radial and vertical directions slice plots of the OpenMC SMART core.

4.3.1 Material Compositions

Similar to MONK, the material definition in OpenMC could use *openmc.material* class to set the specified nuclides' densities. Furthermore, the material also could be defined by the element itself. OpenMC internally stores data on the atomic mass and natural abundances of all known isotopes and use these data to determine the isotopes types and compositions of material. The compositions of the foundation materials of the SMART model would be given in the below table.

Table 4.1: The OpenMC SMART reactor model's foundation materials compositions, which are specified by atom fractions.

Category	Material	Density(g/cm3)	Major Nuclides	Compositions(ao)
Nuclear fuel	UO_2	10.97	^{234}U,^{235} U,^{238} U	$4.34 \times 10^{-4}, 0.04858, 0.951$
			^{236}U,^{16} O,^{17} O	$2.23 \times 10^{-4}, 1.99, 7.58 \times 10^{-4}$
Coolant	H_2O	$0.7 - 1.0$	^{1}H,^{16} O	$2.0, 1.0$
Cladding	Zr Alloy	6.56	^{90}Zr,^{91} Zr,^{92} Zr	$0.5032, 0.1097, 0.1678$
			^{94}Zr,^{96} Zr,^{117} Sn	$0.1700, 0.0274, 0.0009$
			^{118}Sn,^{120} Sn,^{93} Nb	$0.0029, 0.0039, 0.01$
Barrier	Steel	7.92	^{54}Fe,^{56} Fe,^{57} Fe	$0.0564, 0.8859, 0.0205$
			^{58}Fe,^{58} Ni,^{62} Ni	$0.0027, 0.0048, 0.00025$
			^{28}Si,^{29} Si,^{30} Si	$0.00369, 0.00019, 0.00012$
			^{98}Mo,^{55} Mo,^{0} C	$0.006, 0.015, 0.0025$

In order to approximate the material compositions to the reality, the materials in table 4.1 are defined by the *openmc.element* method. All known isotope abundances of the materials are loaded to the OpenMC executable file. For mixtures like steel, table 4.1 does not list its isotopes with relatively low concentrations. Argument *ao* represents the densities

which are specified by the atom fraction, the other argument *wo* means weight fraction. The densities for each element are relative and would be re-normalised using the material's overall density. The *enrichment* argument could add the isotopes at a specified enrichment in the material. In this case, the enrichment of ^{235}U is set as 4.8% to simulate the enriched uranium oxide fuel.

4.3.2 Specifying Tallies

As mentioned in the methodology, the estimation of physical quantities in OpenMC is called a tally. A tally in OpenMC could be presented by the below equation, which is a combination of $filter$ and $scores$.

$$X = \underbrace{\int d\vec{r} \int d\vec{\Omega} \int dE}_{\text{filters}} \underbrace{f(\vec{r}, \vec{\Omega}, E)}_{\text{scores}} \psi(\vec{r}, \vec{\Omega}, E) \tag{4.2}$$

There are three parts in equation 4.2, except the neutron flux term $\psi(\vec{r}, \vec{\Omega}, E)$. The $filters$ can identify the region in the phase space by the material or cell to tally the events that have occurred in. The $scores$ is functional to specify the desired reaction in that specific filter region. The other commonly applied filter is $energyfilter$ that can set multiple series of energy bins over the scored reactions to record the incident and outgoing energies. Independent of the real defined material geometry, $openmc.MeshFilter$ could create a regular, rectangular mesh net-grid to cover the part or whole model in $2D$ or $3D$. The events would be tallied in each pin of the mesh, which is an important function in this study.

The *score* results have different units. The unit of general flux scores is particle-cm per source particle. For the particular responses function, such as fission, elastic scattering, and absorption, the units are reactions per source particle. The absorption here represents the reactions that do not produce the secondary neutrons.

4.3.3 Code verification

In the OpenMC development process, its physics and geometry modelling functions have been well validated and verified [139]. The initial developers chose the widely used and validated code MCNP to build the benchmark models, and these simulation results have been compared with OpenMC outputs. The benchmark problems included thermal scattering, full-core problems and so on. Meanwhile, the ACE format cross-section database that MCNP adopted is also available for OpenMC. The inherent interference from different databases could be excluded from benchmark calculations. Any results differences between two code simulations could therefore be sure that they are caused by the underlying algorithms. The OpenMC first stage verification shows a good agreement with MCNP for the neutron transport problems.

In addition, the OpenMC depletion solver has carried out the same calculations with the other open-source developing code Serpent [140] to validate the recently released depletion feature. The selected problems include the depletion in both thermal and fast spectrum, model geometries that respectively are for a PWR pincell as shown in figure 4.2 and a single sodium-cooled fast reactor (SFR) fuel assembly. The study results show that when OpenMC operates with the full depletion chain, the estimation k_{eff} of both models only has $20-30pcm$ difference with the Serpent calculated values in each depletion step. For the fission product concentration calculation, which is the other meaningful mission of depleting solver, the results from both codes have an agreement within 1% for most fission production (FP)s. The significant differences only appear for a few cases because of the varying treatment in energy dependence of fission product yields.

Besides the studies done by developers, the validation and verification works are also carried on by worldwide users and community developers. Before extensively applying OpenMC to study the neutron behaviours in SMART, our study group members also verified

this code by the university licensed version MCNP in a few small-scale practical reactor physics problems. In 2018, two MSc students respectively used the OpenMC and MCNP to build the SFR full-core models. This core model is composed of 6 layers of hexagonal lattice assembly. The fuel is a MOX fuel that has fuel ratio, $Pu/(U + Pu) = 13.7\%$, the ^{235}U enrichments are rising from inner to outer layer, from natural uranium to 6%. The calculation results are given in the below table.

Table 4.2: The k_{eff} eigenvalue calculated results from OpenMC and MCNP benchmark.

	Effective neutron multiplication factor(k_{eff})		Relative error
	OpenMC	MCNP	
Fuel pin	0.02019	0.02041	1.078%
FA with CR	0.22938	0.19546	2.507%
FA without CR	0.22938	0.23396	1.958%
Full core with CR	0.85294	0.86595	1.502%
Core without CR	1.06685	1.04399	2.190%

The above table 4.2 shows good agreement between the OpenMC and MCNP calculations, and the relative errors do not get higher than 3%. However, limited by the project timing and computing capabilities, the advanced OpenMC functions haven't been fully validated by ourselves. The following section will present the effort that has been done to maximise the performance of OpenMC.

4.3.4 Computing facility and parallelism

OpenMC is developed for simulation on existing and future high-performance computing (HPC) platforms with parallel architectures. BlueBEAR is the University of Birmingham's

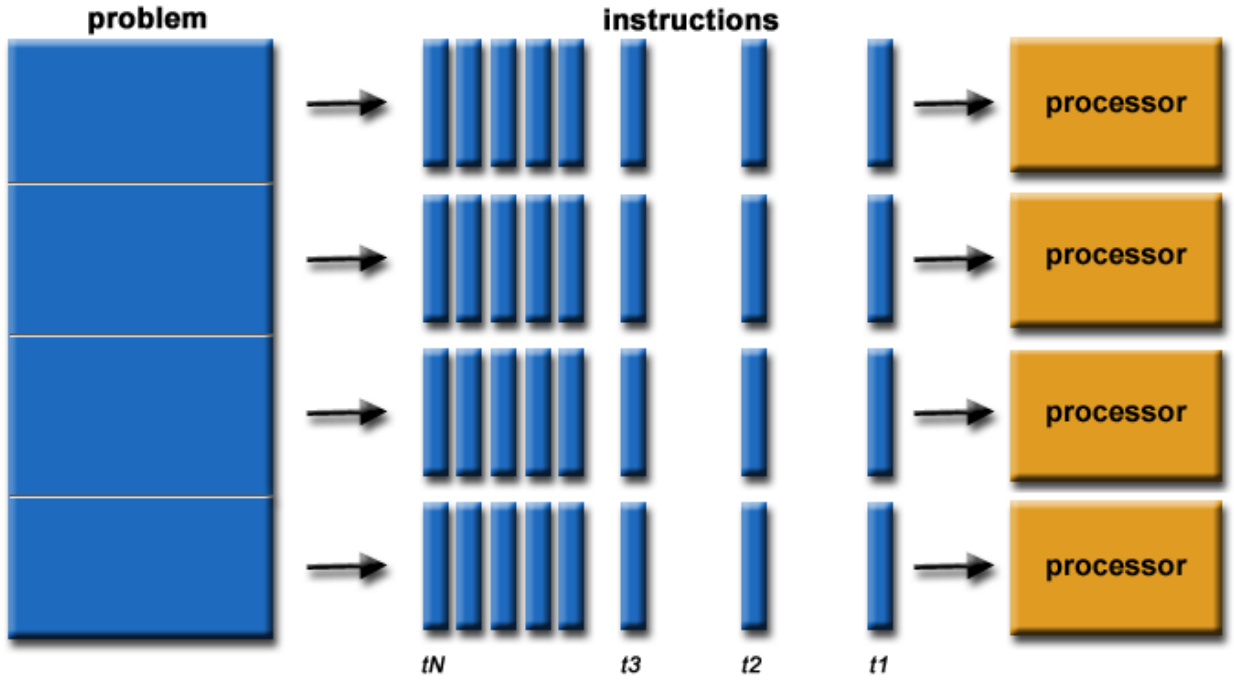


Figure 4.5: The process of parallel computing.

supercomputer that employs some of the latest technology to deliver the fast and efficient processing capacity for research work. Two parallelism methods called shared-memory parallelism (OpenMP) and MPI both are available on BlueBEAR. Therefore that is suitable enough for accelerating OpenMC performance.

The simultaneous employment of many computing resources to solve a computational problem is known as parallel computing, its schematic diagram has been given in the above figure 4.5. The key rule of parallel computing is dividing the whole mission into separate parts, further divided into a series of instructions. The different processors execute the instructions simultaneously. An overall control system would be employed to monitor the whole process. The features of parallelism models will be briefly introduced here.

OpenMP

OpenMP [141] is an application program interface (API) used to perform the multi-threaded, shared memory parallelism. All processors involved in the task are accessing all memory as global address space. When utilising OpenMP to execute an OpenMC computation, the multi-threads would be launched, and each one will simulate a particle history independently of the rest. Per thread only requires a little extra memory in a calculating node.

MPI

Unlike the shared-memory model, the processors need their own local memory and operate independently in the distributed-memory parallelism model. Meanwhile, it requires a communication library to contact between the inter-processor memory, and the memory address in one processor does not map to another one. Currently, there are two major MPI applications, OpenMPI and MPICH. On BlueBEAR, OpenMC has been compiled at the same time with prerequisite packages, including OpenMPI.

Table 4.3: OpenMC calculation speeds with parallelism models(Unit: Particles/second).

	No parallelism	shared-memory (30 cores)	Distributed-memory (20 process)
Calculation rate(Inactive)	1708.69	15516.9	15620.1
Calculation rate(active)	1243.97	9805.36	8632.23

This study has employed both parallelism models, and their performances in the practices is summarised in the below table 4.3. Both parallelism models could significantly improve the OpenMC simulation speed on BlueBEAR. The efficiency in inactivating generations is a bit higher. Bonuses that arise from the accelerations mean that it's possible to

investigate the many optimisations of SMART by the large particle number MC simulations, without worrying about the expensive running time.

4.3.5 Sensitivity study

The nuclear cross-section library has been mentioned many times in the above sections. Its intrinsic errors would fundamentally affect the accuracy of MC simulation results, including the estimation of effective multiplication factor k_{eff} and the neutron flux. The uncertainty analysis of the nuclear database to the continuous-energy MC code is called a sensitivity study.

OpenMC supports the usage of multi-libraries, such as evaluated nuclear data file (ENDF) and joint evaluated fission and fusion file (JEFF). Both are widely used in nuclear physics studies. Their characters will be briefly introduced later. In the simulation preparing stage, the cited cross-section files are converted from their original format to the HDF5, which is readable by the OpenMC particle transport solver.

ENDF

ENDF/B-VII.1 and ENDF/B-VIII.0 two versions are available for OpenMC. ENDF libraries are developed by the cross section evaluation working group (CSEWG), which is a cooperating team of the research institutes in northern American. An OpenMC simulation usually requires the data files related to the incident neutron, thermal scattering, and windowed multi-pole data. The latest released version is ENDF/B-VIII.0 [142] that in particular includes progress for the actinides, which have a significant influence on the criticality analysis.

JEFF

JEFF is the other evaluated library produced by the Nuclear Energy Agency (NEA) data bank participating countries. The most recent version is JEFF 3.3 [143]. Apart from the data of neutron and protons reactions, it also consists of particle data for fusion studies. Such as the nucleus of deuterium, tritium, and helium. JEFF's development is prompted by the demand for projects of advanced reactor and innovative irradiation facilities.

The above three databases have been individually employed in the SMART core model's simulation in this sensitivity study, and the model has been shown in figure 4.4. To achieve that, the environment variable *openmc_cross_sections* needs to be indicated to the particular *cross_section.xml* file before starting simulations. The *export* command in the Linux environment or the Python package *OS* are available for this operation. The k_{eff} eigenvalue calculation results are given in the below table, each simulation would run 250 generations with 100 inactive ones, a million neutron histories would be consisted in one generation.

Table 4.4: The k_{eff} results from the simulations with the different databases.

	ENDF/B-VII.1	ENDF/B-VIII.0	JEFF 3.3
k-eff(Collision)	$1.29319 \pm 12 \times 10^{-5}$	$1.28866 \pm 10 \times 10^{-5}$	$1.26958 \pm 10 \times 10^{-5}$
k-eff(Track-length)	$1.29312 \pm 16 \times 10^{-5}$	$1.28878 \pm 13 \times 10^{-5}$	$1.26958 \pm 13 \times 10^{-5}$
k-eff(Absorption)	$1.29301 \pm 8 \times 10^{-5}$	$1.28876 \pm 8 \times 10^{-5}$	$1.26958 \pm 8 \times 10^{-5}$
Combined k-eff	$1.29306 \pm 7 \times 10^{-5}$	$1.28870 \pm 8 \times 10^{-5}$	$1.26958 \pm 7 \times 10^{-5}$
Leakage Fraction	0.00217 ± 0.00	0.00208 ± 0.00	0.00214 ± 0.00

From the results in table 4.4, when using different databases to run the same simulation, the k_{eff} values have obvious differences. Three combined k_{eff} have the same standard

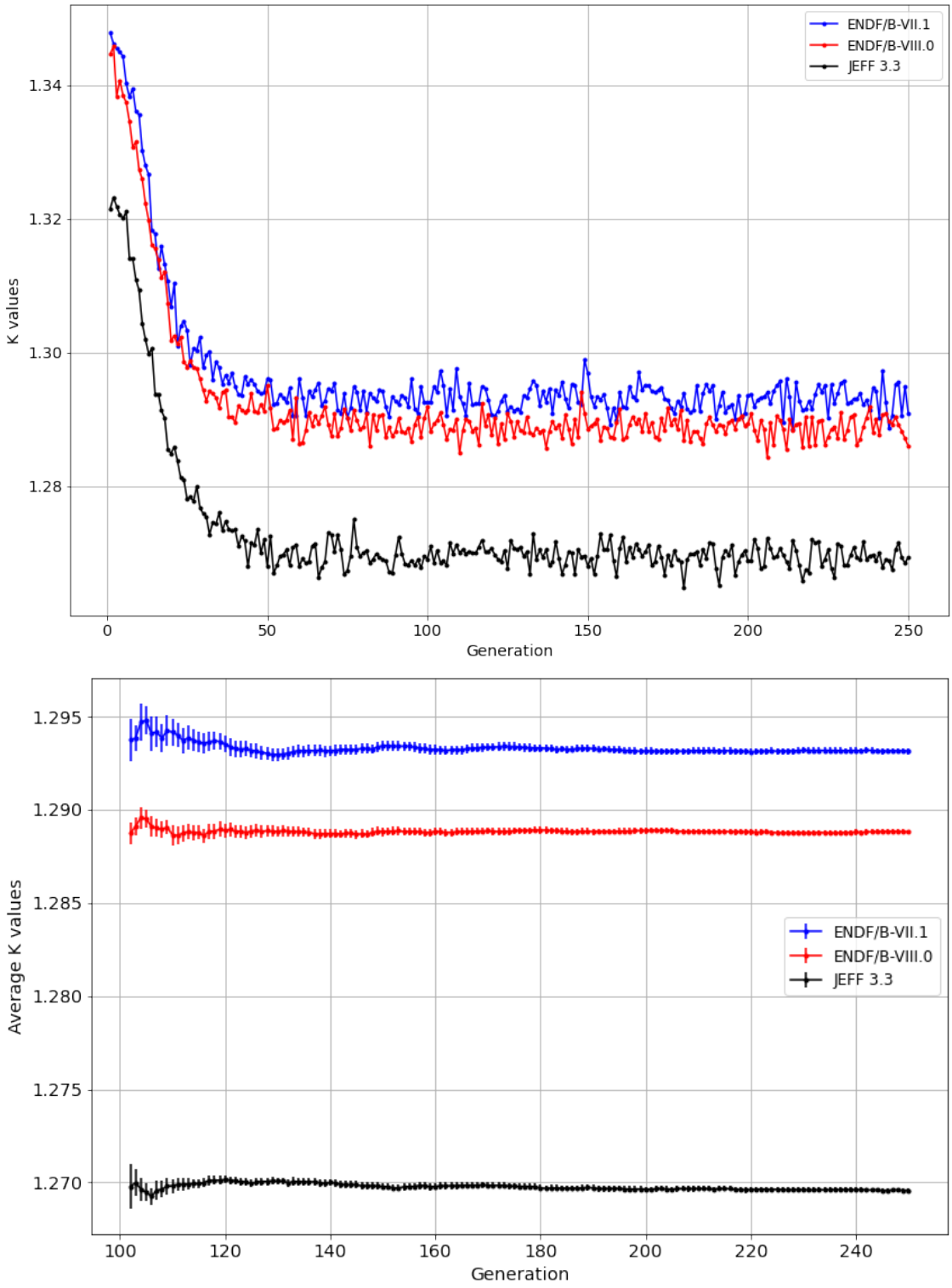


Figure 4.6: Convergence process of k_{eff} values in the sensitivity study.

deviation σ level. Moreover, the results from ENDF/B-VII.1 is the highest one in all three. The reactivity has $262pcm$ and $1431pcm$ higher than its newer version ENDF/B-VIII.0 and JEFF 3.3.

Figure 4.6 have given the values of the k_{eff} convergence process in all three simulations. The first subplot contains the earlier 100 inactive generations, which would not perform the sampling process. The second subplot begins at the 100th generation, and each data point has the error bar to present its own σ size. The three diagrams have a similar trend to the above figure 4.3, and it's clear that the estimated k_{eff} values are going to converge, and they do not have data points that are too discrete. The differences that have been found in table 4.4 are apparently consistent in the whole calculation. This means that the differences in combined k_{eff} are not caused by statistical reasons or the code fundamental algorithms.

The above investigations found that using a particular version of the nuclear database would significantly affect the MC simulation results. Therefore, further studies should employ one database to ensure the intrinsic uncertainty in the data library would not be propagated to the SMART power analysis. The ENDF/B-VII.1 was selected to perform the rest of the studies because it was already widely used in multiple codes and calculations. Moreover, OpenMC officially provides a depletion chain which is based on the ENDF/B-VII.1 libraries, including the fission product yield and decay data. Databases used in neutron transport calculations should keep uniform with the depletion analysis.

4.3.6 Temperature reactivity effect

In the above MONK section, the temperature setting in the material definition has been briefly introduced. Material temperature is also an important parameter for the OpenMC

simulation. In the selected ENDF/B-VII.1 library, incident neutron data is available at six temperatures: $250K$, $293.6K$, $600K$, $900K$, $1200K$ and $2500K$. The JEFF data library has the same temperature options. The temperature of nuclear fuel and moderator could significantly affect the simulation results due to the cross-section variations.

Changing the fuel temperature majorly affects the resonance escape probability p in equation 3.1. The microscopic cross-sections would change due to the thermal agitation of atoms, basically by broadening the resonance form, which is called Doppler broadening. The resonant absorption rates of the heavy nuclei in the fuel would increase, especially due to the large amount of ^{238}U. The rise of fuel temperature always gives a negative reactivity feedback to a civil reactor system. Fuel temperature coefficient (FTC) is defined as the change in reactivity per degree fuel temperature increase [109], which is the first and the most critical feedback compensating for the inserted positive reactivity, particularly in all reactivity-initiated accidents (RIA). The FTC is also called the prompt temperature coefficient because it causes an immediate response in the nuclear reactor operation.

The moderator temperature coefficient (MTC) is defined as the change in the reactivity per degree in varying of moderator temperature. MTC is a major design parameter for PWRs. Based on this safety principle, PWRs should be designed to maintain negative MTC over a large range of core cycle operating conditions. First of all, when the moderator temperature increases, the ratio of moderating atoms decreases as water thermal expansion results. The decrease of moderator density makes the neutrons stay at a higher energy range for a more extended period, making these neutrons highly likely to be non-fission captured. This process is called the hardening of the neutron spectrum. Besides that, neutron leakage also makes a contribution to MTC. The fast neutrons need a longer moderation length to slow down in the expanded, lower density water, which means more neutrons would leak out of the determined size core.

A series of OpenMC simulations with various temperature settings have been done to observe the FTC and MTC in the SMART model. Appropriate information about temperature settings is given in the below table.

Table 4.5: The temperature setting of fuel and water in the OpenMC simulations.

	Temperature Setting 1	Setting 2	Setting 3
Fuel Pins (UO2)	$293.6K$	$1200K$	$1200K$
Moderator(Water)	$250K$	$250K$	$600K$
Water density	$1.0g/cm^3$	$1.0g/cm^3$	$0.7g/cm^3$

The default room temperature for the fuel rod is $293.6K$, and for the moderator it is $250K$. In each simulation, 1.5 million neutron histories are tracked through their lifetime, iterating over 250 generations to obtain accurate results. In each generation, once the fission occurs, OpenMC will record the fission site's spatial coordinates. The fission neutron's sampled outgoing energy and direction would be stored in a fission bank for use in subsequent generations. To avoid recording inaccurate data from the source distribution not yet being converged, the first 100 neutron generations would not be activated. The simulation results are given in the below table 4.6.

In table 4.6, the combined k_{eff} decreases with the temperature of fuel and moderator temperatures going up. When the temperature of fuel rods jump from $250K$ to $1200K$, the value of k_{eff} decreases from 1.41601 ± 0.00007 to 1.38364 ± 0.00006, the reactivity drops down $1652pcm$. Furthermore, when the temperature of the moderator improves to $600K$, the value of k_{eff} is 1.29312 ± 0.00006, $5059pcm$ lower than the temperature setting 2 and $6711pcm$ lower than the temperature setting 1. It is therefore obvious that the MTC is more significant than the FTC for the SMART reactor core.

Table 4.6: The simulation results with different temperature conditions.

Temperature Settings	k_{eff} (Collision)	k_{eff} (Track-length)	k_{eff} (Absorption)	Combined k_{eff}
Fuel=293.6K	1.41604±	1.41605±	1.41600±	1.41601±
Moderator=250K	10×10^{-5}	13×10^{-5}	7×10^{-5}	7×10^{-5}
Fuel=1200K	1.38373±	1.38369±	1.38362±	1.38364±
Moderator=250K	10×10^{-5}	12×10^{-5}	6×10^{-5}	6×10^{-5}
Fuel=1200K	1.29311±	1.29321±	1.29311±	1.29312±
Moderator=600K	8×10^{-5}	10×10^{-5}	6×10^{-5}	6×10^{-5}

4.3.7 Burn-up zone study

A general method to build a full reactor core model in an MC neutron physics program is to define a single nuclear fuel material and repeat it into every fuel pin location. That is acceptable from a pure neutron transport perspective consideration. However, one should be cautious about using this kind of model for burn-up problems. According to equation 3.2, the reaction rate of nuclei highly depends on the neutron flux ϕ. Using a single set of neutron flux and reaction rates to produce a new material composition for the next burn-up step would obviously pose issues and inaccuracy in the depletion.

To run a spatially based depletion estimation, it is necessary to manually divide the initial reactor core model into many burn-up zones. Then a series of copied fuel materials would be created specifically to fill their corresponding burn-up zones. Hence, the depletion solver would calculate the characteristic flux and reaction rate for each burn-up zone, which estimates the latest material compositions for the following period. However, the growing number of burnable materials in the model would significantly bring progressively more intensive tasks to the computing facility.

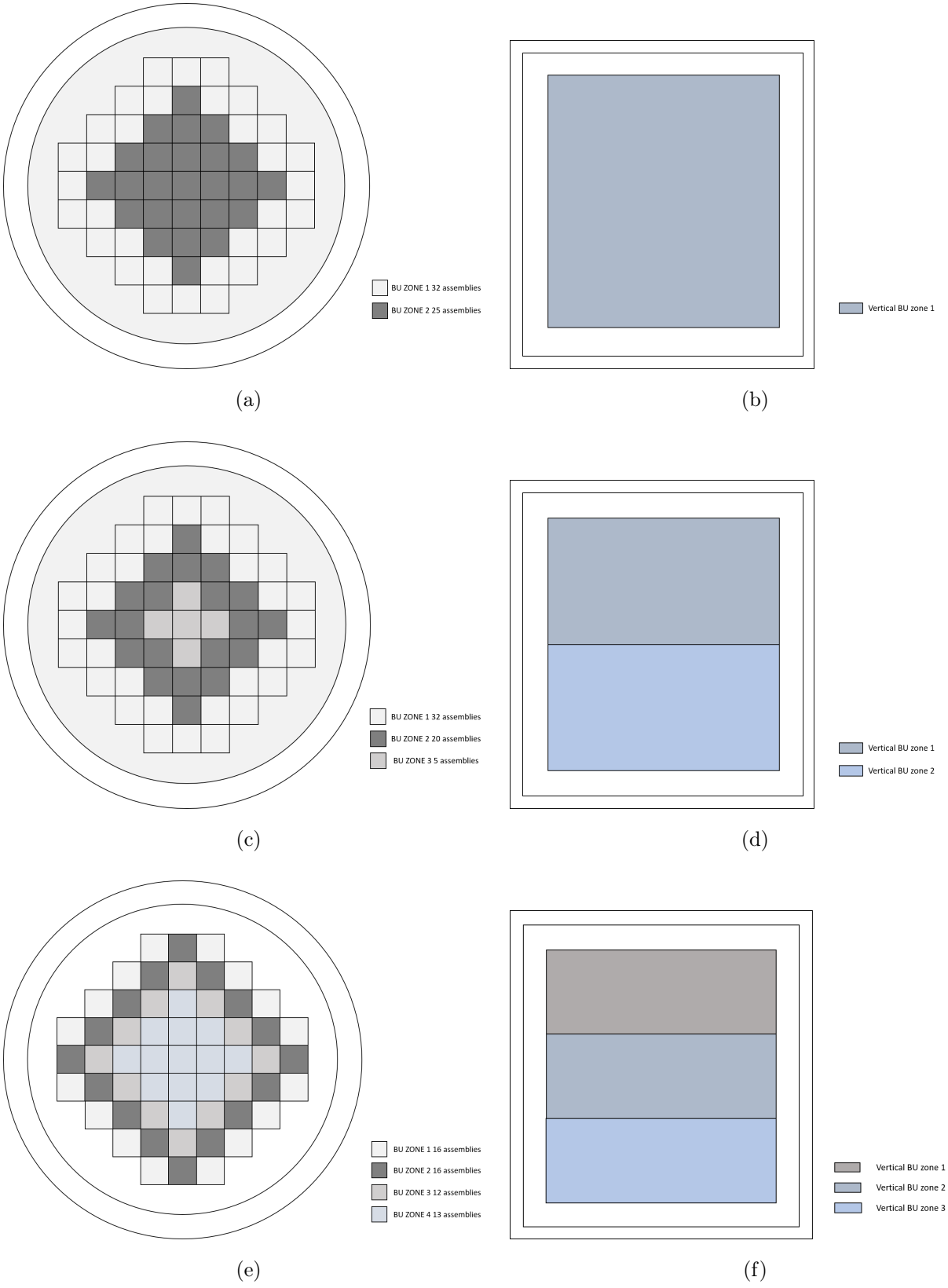


Figure 4.7: Schematic diagram of Burn-up material spatial repeating distribution.

A series of burn-up calculations have been done to find the reasonable burn-up zone dividing method on both the radial and axial direction of the core model, keeping a balance of results in terms of accuracy and computing cost. The number of radial burn-up zones rises from 1 to 5. For the vertical direction, this number is from 1 to 3. The above figure 4.7 presents the burn-up zone spatial positions. Using the 4×3 model, subplot 4.7e as an example, spatial zones were labelled as burn-up zone 1-4 from the edge to centre in the radial direction. Burn-up zone 1 and 2 respectively occupy 16 FAs, zone 3 has 12 FAs, and 13 FAs are loaded in the centre area zone 4. In the vertical direction, $200cm$ height FAs are evenly separated into 3 zones, labelled as burn-up zone $1-3$ from top to bottom. Each burn-up zone was filled in an especially defined fuel material. Therefore, there are 12 repeated fuel materials in this 4×3 model in total. The different colours were used to represent the depletable materials in figure 4.7.

Assuming full-power operating time for each calculation is 1129 days, slightly longer than 36 months, which is the length of the refuelling cycle of the original SMART design. The entire depletion period was divided into 58 steps with nonuniform step lengths. In the beginning, the step sizes are very short, like an hour, for building the equilibrium of fission product nuclides that have large absorption cross-sections, such as xenon-135 and samarium-149. The length of the burn-up step gradually increases with the depletion level as it goes deeper, from an hour to half a year. The calculation results and cross-comparison between several simulations is given in the below figure 4.8.

Even though the model has a different number of burn-up zones, the initial k_{eff} values are very close, about 1.38267. That means the existence of the burn-up zones does not affect the pure neutron transport simulation results. The difference becomes significant as the depletion going deeper. When the model is spatially separated, even though it only has two zones in the radial direction, the last k_{eff} data point in the curves decreases to the lower position. The difference is $1195pcm$ at the end of the calculation.

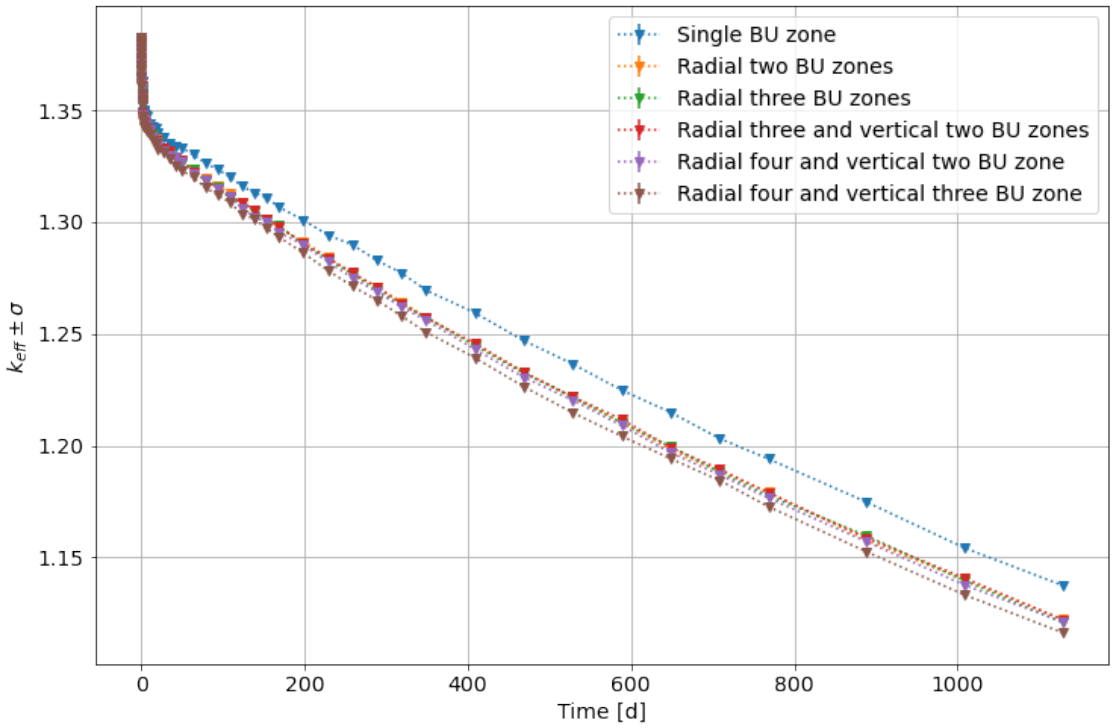


Figure 4.8: The k_{eff} variations in several burn-up calculations with the different number of spatial zones.

The slopes of the depletion curves are relatively stable even though the model is divided into more burn-up zones, particularly in the radial direction. Until there are 3 zones in the vertical direction, the k_{eff} value is decreased to around 1.116 at the ending step. The 4×3 burn-up zones partition model will be used to study SMART economic performance further. More complicated spatial separation and material definition could improve the results' accuracy but cannot change the results substantively. Meanwhile, this would pose challenges to the data analysis and extend the computing time. The combined k_{eff} values at some time steps are picked up from figure 4.8 and summarised in the below table 4.7.

Table 4.7: The k_{eff} results with different bun-up zone partition methods at selected steps.

Burn-up time	1 zone	2 zones	3zones
Start-up	$1.38267 \pm 56 \times 10^{-5}$	$1.38267 \pm 56 \times 10^{-5}$	$1.38267 \pm 56 \times 10^{-5}$
3 days	$1.38207 \pm 64 \times 10^{-5}$	$1.34591 \pm 63 \times 10^{-5}$	$1.34484 \pm 57 \times 10^{-5}$
49 days	$1.33318 \pm 53 \times 10^{-5}$	$1.32675 \pm 53 \times 10^{-5}$	$1.32647 \pm 59 \times 10^{-5}$
409 days	$1.25929 \pm 55 \times 10^{-5}$	$1.24501 \pm 58 \times 10^{-5}$	$1.24462 \pm 53 \times 10^{-5}$
1129 days	$1.13750 \pm 63 \times 10^{-5}$	$1.12225 \pm 63 \times 10^{-5}$	$1.12091 \pm 63 \times 10^{-5}$
	6 zones (3×2)	8 zones (4×2)	12 zones (4×3)
	$1.38163 \pm 53 \times 10^{-5}$	$1.38163 \pm 53 \times 10^{-5}$	$1.38207 \pm 64 \times 10^{-5}$
	$1.34529 \pm 66 \times 10^{-5}$	$1.34583 \pm 62 \times 10^{-5}$	$1.34239 \pm 59 \times 10^{-5}$
	$1.32740 \pm 68 \times 10^{-5}$	$1.32680 \pm 61 \times 10^{-5}$	$1.32305 \pm 58 \times 10^{-5}$
	$1.24564 \pm 55 \times 10^{-5}$	$1.24302 \pm 55 \times 10^{-5}$	$1.23921 \pm 57 \times 10^{-5}$
	$1.12223 \pm 61 \times 10^{-5}$	$1.12126 \pm 61 \times 10^{-5}$	$1.11640 \pm 62 \times 10^{-5}$

Moreover, to investigate the moderator temperature and how its density affects the results of OpenMC depletion, another group of calculations were done and cross-compared. The water density is set as $1.0 g/cm^3$ at room temperature and $0.7 g/cm^3$ at $600K$. The

models within the single burn-up zone and 4×3 partition were used to study depletion respectively with moderator temperature at room temperature and $600k$. The below figure gives the calculation results.

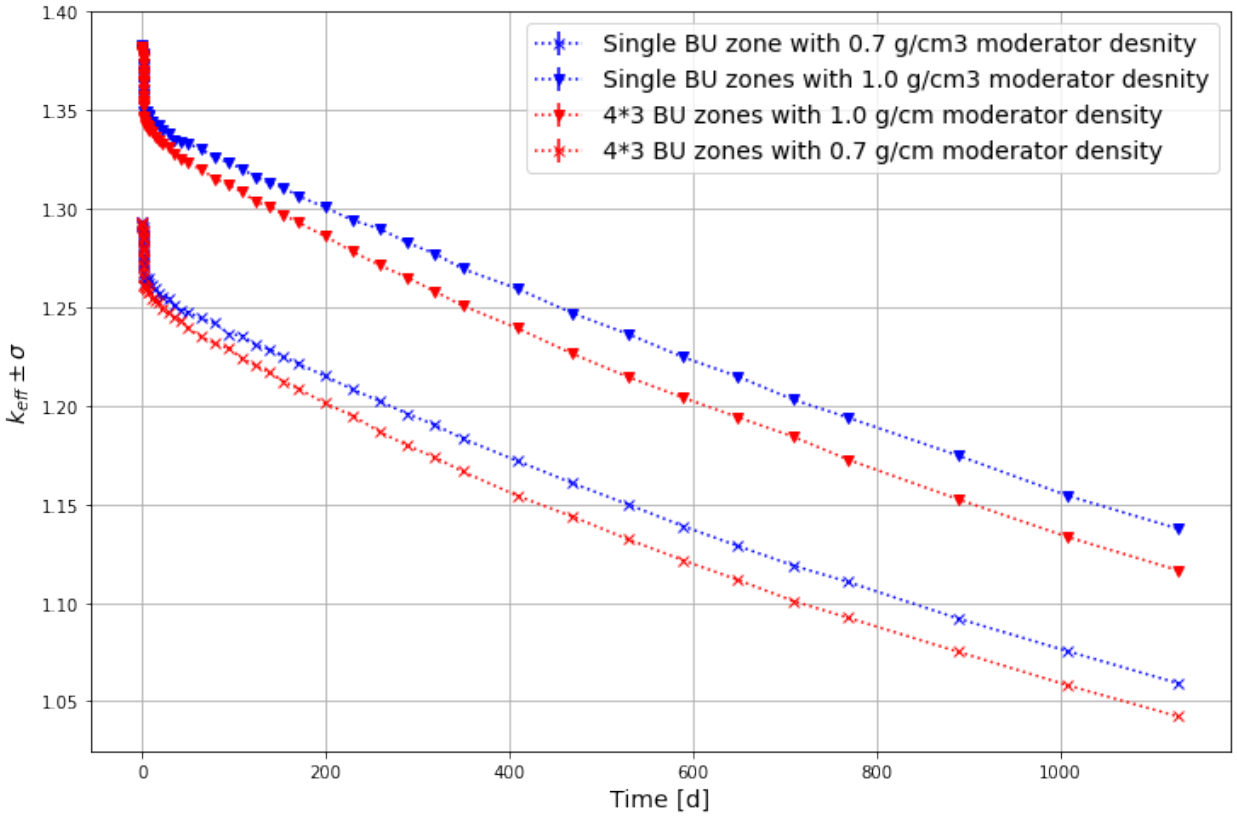


Figure 4.9: The comparison between the results of single and 4×3 burn-up zones division and different moderator densities.

Observing the results in figure 4.9, it is obvious that the negative effect of water density expansion is more significant than the burn-up zone spatial separations. The MTC is constant in the burn-up process. When water density decreases $0.3g/cm^3$, the k_{eff} drops down about 0.078 in all steps. Meanwhile, the effect of burn-up zones is increasingly noticeable. If the water density is determined, whatever is 1.0 or $0.7g/cm^3$, the k_{eff} values are close at the beginning but have roughly 0.017 difference after longer than 36-months of full-power operation.

In the further simulations of SMART, the model would adopted the water density as $0.7 g/cm^3$ and has 4×3 burn-up zone partitions. Because these simulation parameters could approach the reactor core at the full-power operation, where the condition is at the maximum level.

4.4 Chapter summary

This chapter has introduced the MC codes that have been used in this PhD program. Including the industry application codes MONK and MCBEND, and the scientific community developed open-source code OpenMC. The author has used MONK and OpenMC to build the SMART reactor core models and has been involved in teaching and research projects using MCBEND. This chapter also introduces the modelling, testing and optimisation process for each model.

As a widely used, mature, industry level code, MONK has a user-friendly geometry system. The combined *body* and *hole* geometries could efficiently build a complicated model that has a detailed inner structure. In the work of this thesis, a range of hole geometries were used to model a single 17×17 lattice FA at the first instance. After this, the holes would be nested into the shaped bodies, which would be further repeated at different positions to form a full-core model finally. A *globe* body is defined to contain the whole geometry. The results obtained from MONK in this thesis are limited. However, the experience from the modelling is valuable.

The OpenMC SMART model has been built by a similar path, and has been carefully tested. In this chapter, the result from the OpenMC simulation have been compared with the selected benchmark code MCNP. Moreover, three different nuclear data libraries have been individually adopted into simulations to do the sensitivity study. After determined

the suitable database, a series of reactivity studies have been done to find the best simulation parameters approaching the full-power operating core. These investigations contain the material temperature reactivity coefficients and the burn-up zone spatial division. The comparison of these study results could ensure the OpenMC model could give reasonable simulation results. The parallelism features of OpenMC will be further utilised in the following studies.

Chapter Five

Results and discussion

Chapter 4 has presented the validations and tests to the OpenMC SMART full-core model. This model now should be used to demonstrate credible simulation results and reflect the neutron physics variations due to reactor operations or material usage. The optimisations that have been done in this thesis are relatively conservative. The major technical parameters and material selections are kept uniform with the original design. The proposed modifications are limited to the usage of different reflector material, and the number of high enrichment FAs, as well as their position. The combination of mature nuclear reactor technologies and innovative designs could improve the performance of SMART and extend its application prospects. The results are given below.

5.1 Normal SMART

Before modifying the SMART reactor core, the original design should be studied and from this determined which property aspects have the greatest potential to be optimised. The model in figure 4.4 needs to be slightly changed for this purpose.

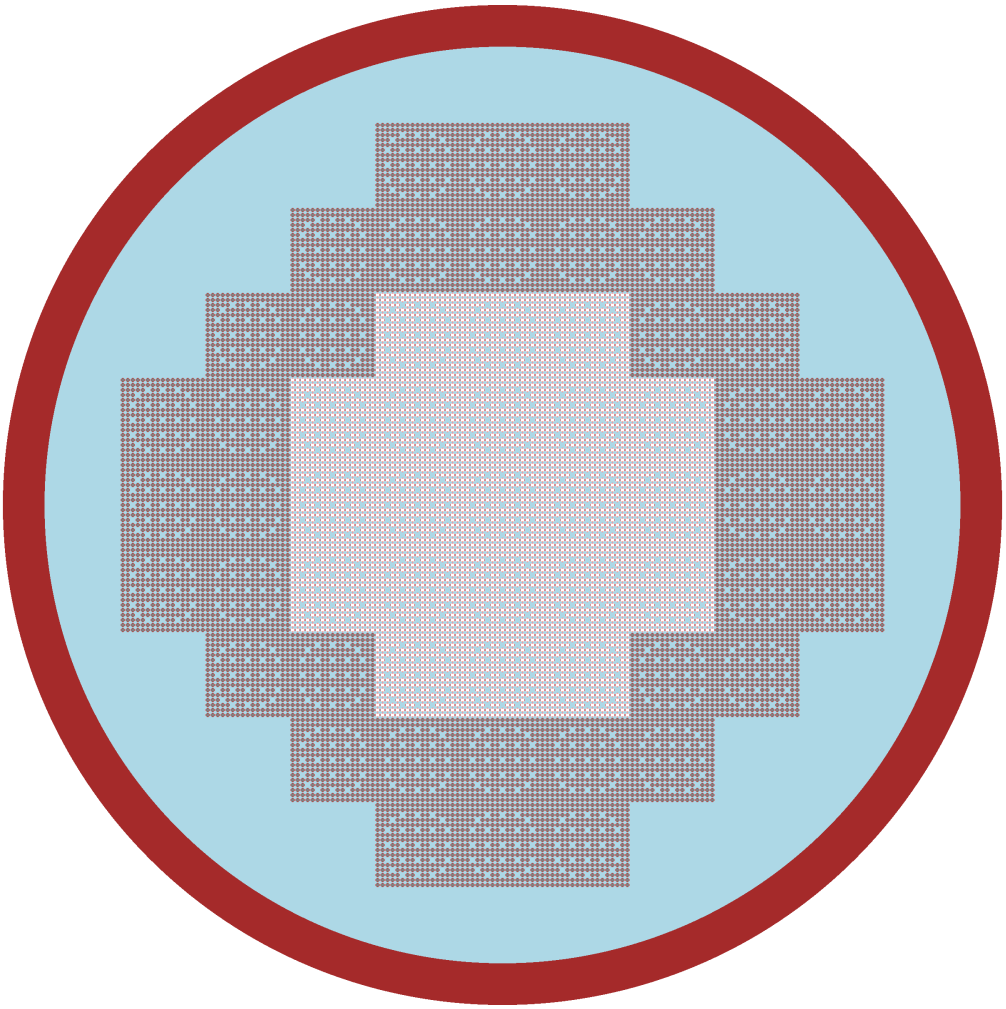


Figure 5.1: Updated OpenMC model of the SMART reactor core to have two enrichment levels (2.4% and 4.8%) for fuel shifting.

The enrichment of 21 FAs in the centre core area has been redefined as 2.4% to reflect the two-batch refuelling scheme FAs layout in figure 2.8, and the updated model are given in the following figure 5.1. To clearly point out the modifications, use of different colours is made to classify the enrichment level. The 2.4% enrichment level rods are represented by white cell pins, and the rest, grey rod pins, are 4.8% enriched UO_2, which are contained in 36 FAs.

The neutron transport MC simulation results, such as neutron flux and fission rate distributions, will be presented first to evaluate the power peaking and fuel utilisation rate. Then, the results from burn-up calculations in one refuelling cycle are used to analyse the reactor uranium economics, including ^{235}U amount alterations in the various positions of fuel and a more straightforward enrichment reduction plot. The setting of several burn-up calculations are the same as the above burn-up zone studies. To figure out the maximum inherent capacity of SMART, the general PWR reactivity control systems are off-line in this investigations. The control rods are withdrawn from the core, no integrated burnable poison rods have been assembled besides fuel rods, and coolant water does not have soluble boron.

5.1.1 Neutron flux spatial distribution

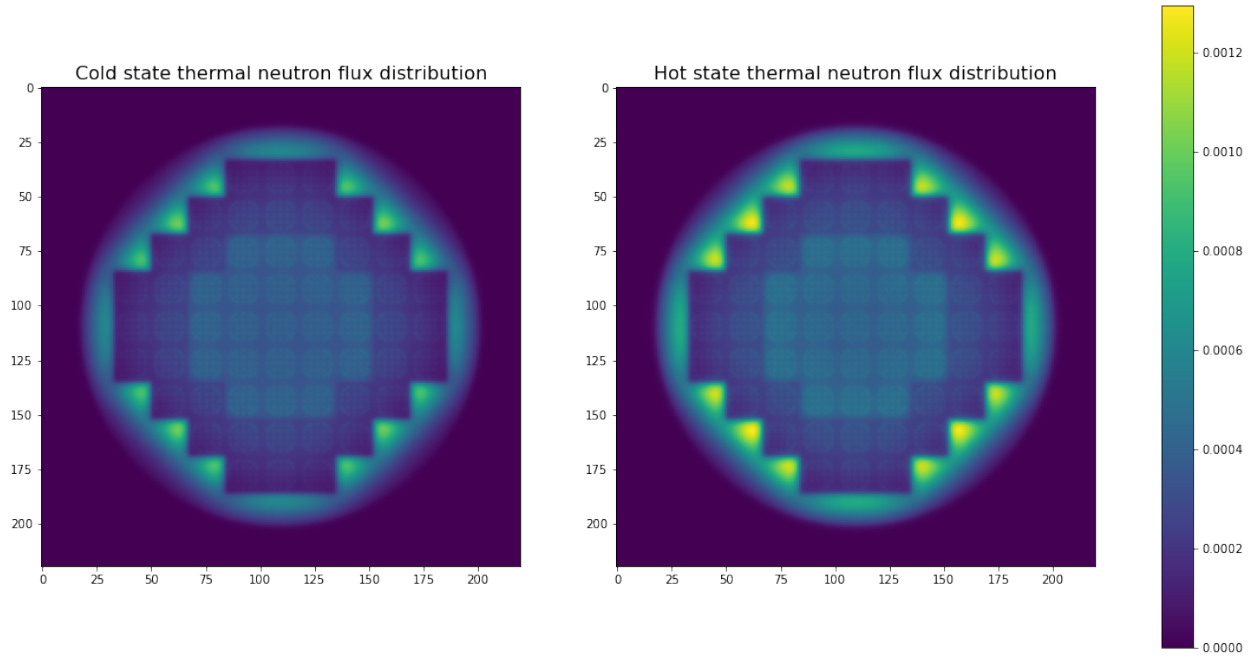
Several nuclear reactor physics phenomena have been introduced in the above sections. Whatever the temperature reactivity coefficients or fuel composition changes, they eventually affect the reactor performance through neutron flux ϕ. Therefore, once the core model has been tested and verified, the first goal in this study is to determine the neutron flux distribution in the whole core range.

In order to achieve this target, a number of OpenMC filters were applied to specify the regions of phase space and the neutron energy division. Two above mentioned $MeshFilters$ were created to define the regular Cartesian mesh grids to cover the model geometry and score the events. The first one is in $2D$, the size of each grid is $1.2 \times 1.2cm$ and has the layout of 220×220 in both direction. The other mesh is in the $3D$, which is a $260.0cm$ z-axial direction extension version of the $2D$ mesh, and each pixel's height is $1.3cm$. Therefore there is a total of $220 \times 220 \times 200$ pixels in the $3D$ mesh.

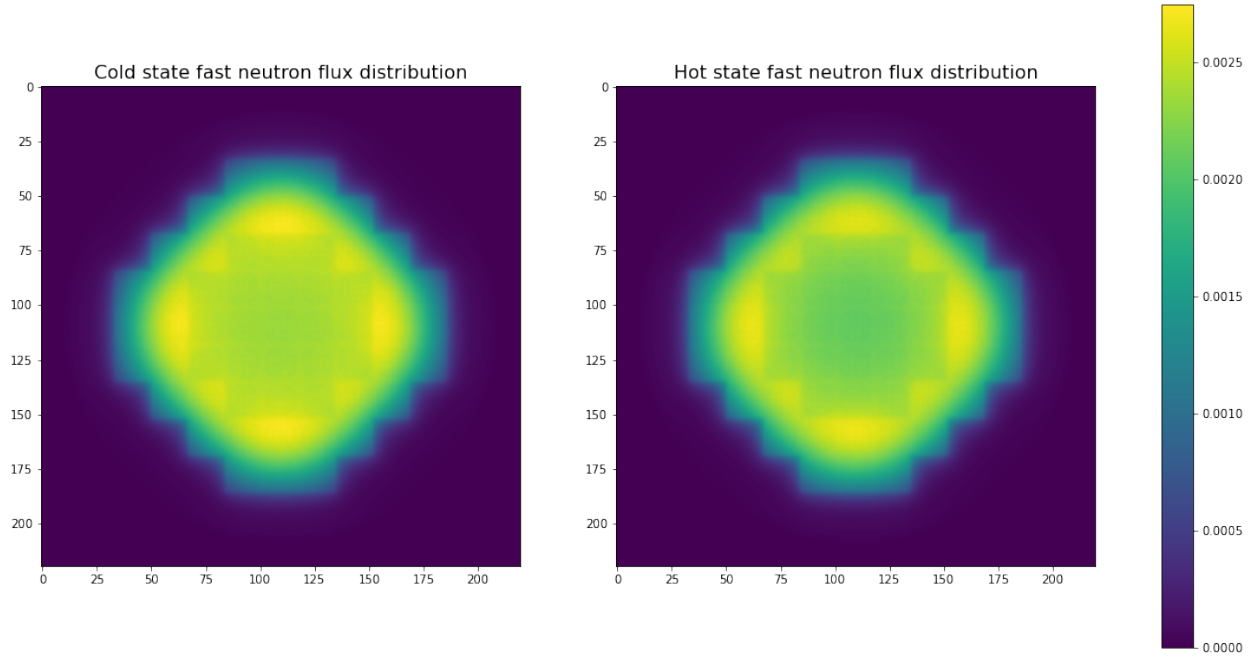
Meanwhile, an $EnergyFilter$ is defined to score events based on incident particle energy, which is classified into $0 - 0.625eV$ and $0.625 - 20.0 \times 10^6 eV$,two energy subgroups. They are individually representing the thermal and fast energy neutrons. The events at the specific locations and incident energy are being recorded by combining the filters with various scoring functions. The calculation results are given below.

The $green - yellow$ colour map in figure 5.2 represents the results which are recorded from the $2D$ mesh filter. This same standard will be applied to the rest of the contents as well. Figure 5.2 presents the normalised thermal and fast neutron flux distributions in both the cold and hot conditions. The cold state means the moderator and fuel pins are at their room temperatures, $250K$ and $293.6K$. The hot state represents the reactor operating condition, which employs temperature setting 3 in the above table 4.3. The results are given in the below table and figure.

In Table 5.1 and Figure 5.2 show that the material temperature significantly affects the k_{eff} value, but the spatial distribution of the neutron flux does not change drastically. The peaks of thermal neutron flux are located in the reflector zones. High energy neutrons would be sufficiently moderated by a large number of hydrogen atoms in this area. Conversely, the fast neutron flux peak is located in the fission zone, where the fresh FAs have higher fast neutron flux density inside. When the fission chain reaction is successfully established, the



(a)



(b)

Figure 5.2: The thermal and fast neutron flux distributions in the two-batch refuelling scheme core.

Table 5.1: The eigenvalues simulation results of the reactor cold and hot states.

	k_{eff}(Collision)	k_{eff}(Track-length)	k_{eff}(Absorption)	Combined k_{eff}
Cold state	1.26517	1.26524	1.26506	1.26510
	$\pm 1.2 \times 10^{-5}$	$\pm 13 \times 10^{-5}$	$\pm 9 \times 10^{-5}$	$\pm 8 \times 10^{-5}$
Hot state	1.22906	1.22903	1.22907	1.22906
	$\pm 9 \times 10^{-5}$	$\pm 11 \times 10^{-5}$	$\pm 8 \times 10^{-5}$	$\pm 7 \times 10^{-5}$

entire core heats up. The thermal peaks at the reflector zone become more significant, and the fast neutron flux density in the reloading fuel zone has a slight drop-down. In order to observe the variation between the two states, the data have been picked out from figure 5.2 along the diameter on the X-axis direction and plotted in the below figure.

The above results present the neutron flux spatial distributions in the reactor cold and hot states. When the reactor is operating, the primary cycle coolant pumped through is from the core bottom to the top, taking the fission heat and providing transfer of that to the steam generator. Therefore, it is necessary to investigate the neutron spatial distribution inside the core, especially in the vertical direction. The results of this are given in the below figure 5.4.

The entire $3D$ array tallying results are sliced by the planes XY and YZ and then plotted out as data, and the colour bars and the scales of each plot are also given. The reason for this is the plotting process is independent in each subplot. The maximum values in all 4 subplots are different, and the scale of colour bars have not been normalised. Another type of colour map is used to plot the $3D$ mesh filter results, which is used to distinguish two-dimensional results.

Observing figure 5.4, whether it be the fast or thermal neutrons, their flux distribu-

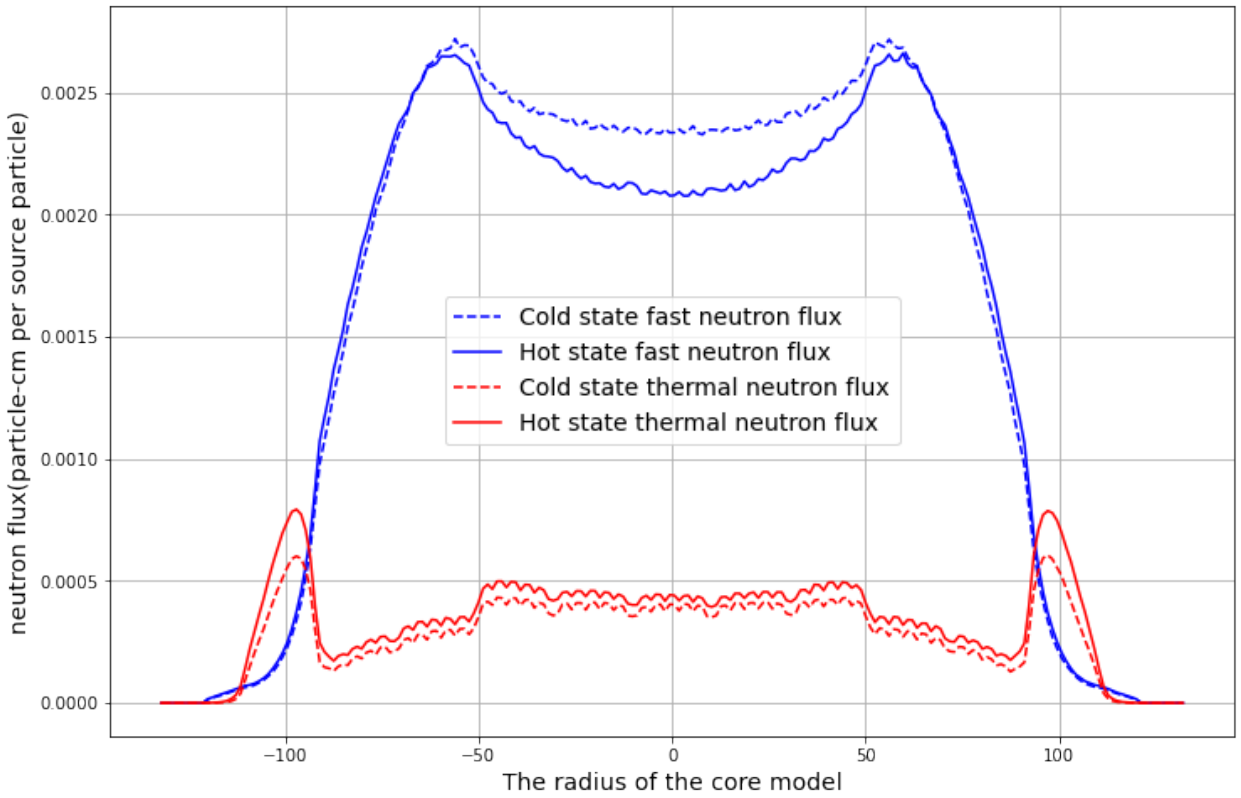
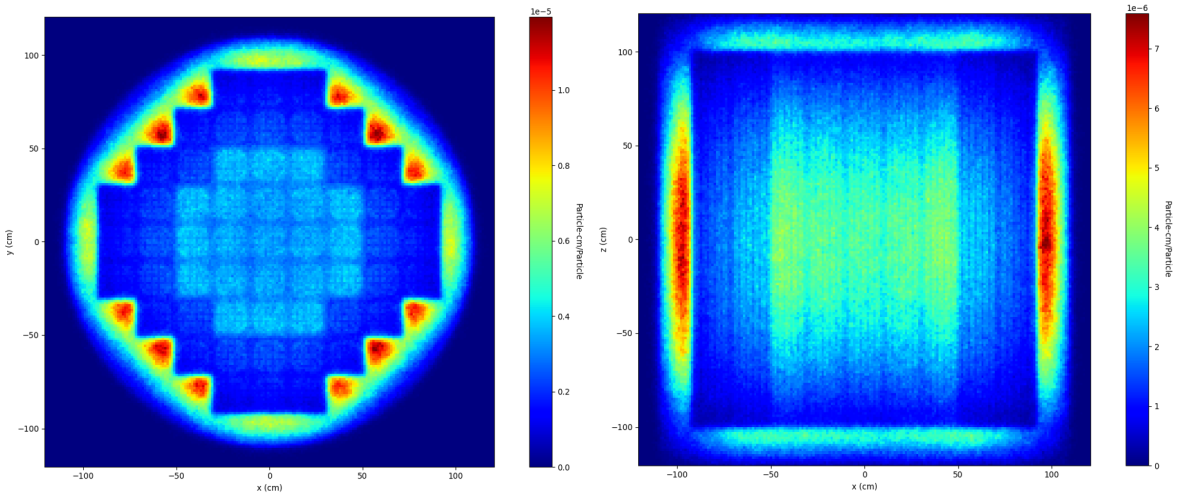
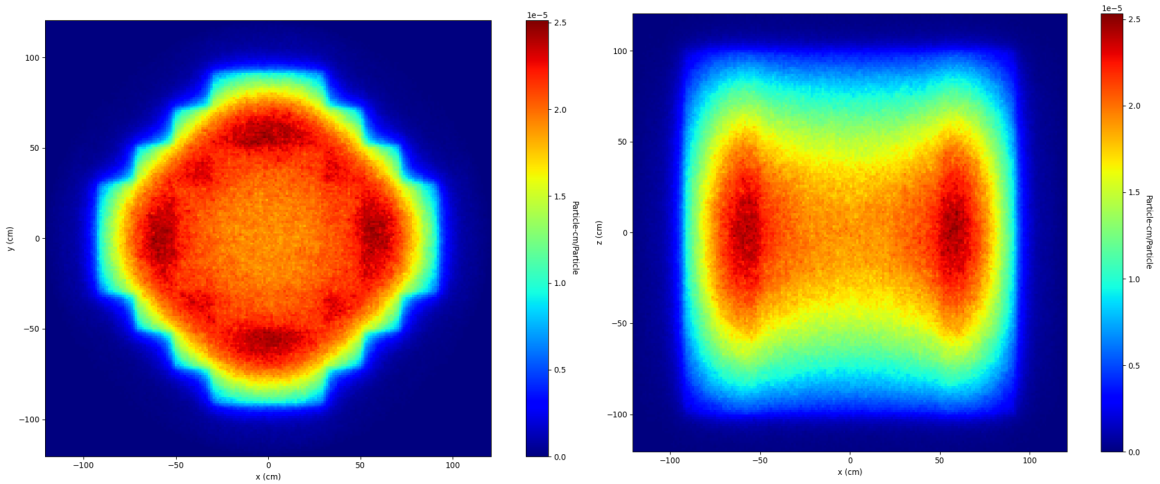


Figure 5.3: Cold and hot state neutron flux distributions viewed along a diameter in the x-axis direction.



(a) Thermal neutron flux on XY and YZ planes



(b) Fast neutron flux on XY and YZ planes

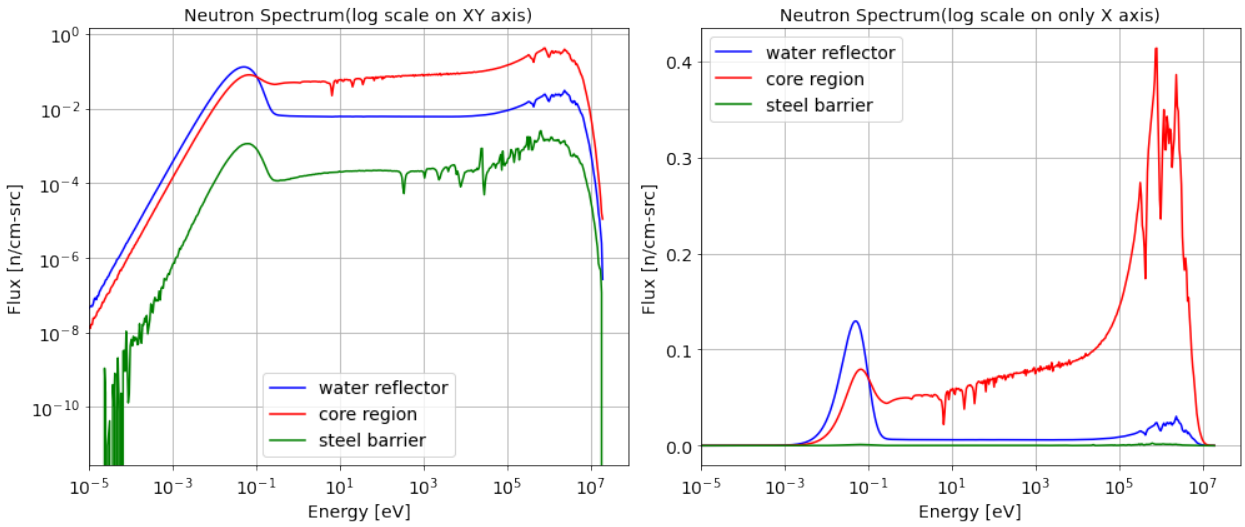
Figure 5.4: The slices of 3D thermal and fast neutron flux distribution.

tions on the XY plane are similar to the above figure 5.2. On the YZ plane, the vertical neutron flux distributions have significant unevenness. For the thermal neutrons, the high flux density area is located at the half-height of the reflector zone, and the thermal flux density decreases along the axial direction. Meanwhile, the fast neutron flux density is higher at the same vertical position. A greater amount of fast neutrons are produced in the fresh fuel assemblies than in the 2.4% enrichment ones. However, the neutron flux densities at the top and bottom of fuel assemblies are relatively low. As a result, the uranium utilisation rates in these places are not optimised. According to the above results, if the thermal neutrons could be scattered back to the fission zone when the reactor is operating, that could improve the thermal neutron flux density at the core edge and thus increase the reactor core's power density.

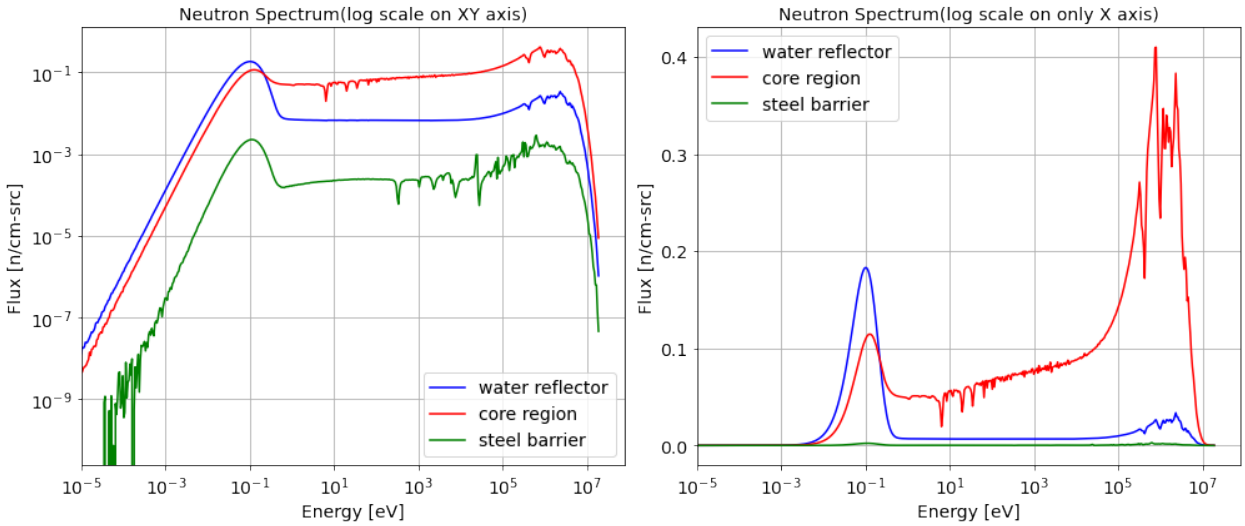
5.1.2 Neutron energy spectrum

Section 5.1.1 gives the neutron flux spatial distribution in the core. Moreover, in addition to this the neutron energy distribution is the other important issue that should be determined from the simulations. The incident neutron's energy would directly affect the cross-sections of a series of nuclear reactions, not only for fission itself. The related simulation results for the neutron energy spectrum are given in the below figures.

The neutron energy has no more been categorised into thermal and fast two groups to achieve data from the simulation process. Instead of that, the neutron energy range from $10^{-5} - 20 \times 10^{6} eV$ is logarithmically divided into 500 spaces and then instantiating this energy range into another energy filter. Coupling the logarithmic energy filter with the cell or material filters, which is able to score the neutron flux in the particular part of the core model by detailed dividing of energy sets.



(a) Cold state neutron energy spectrum

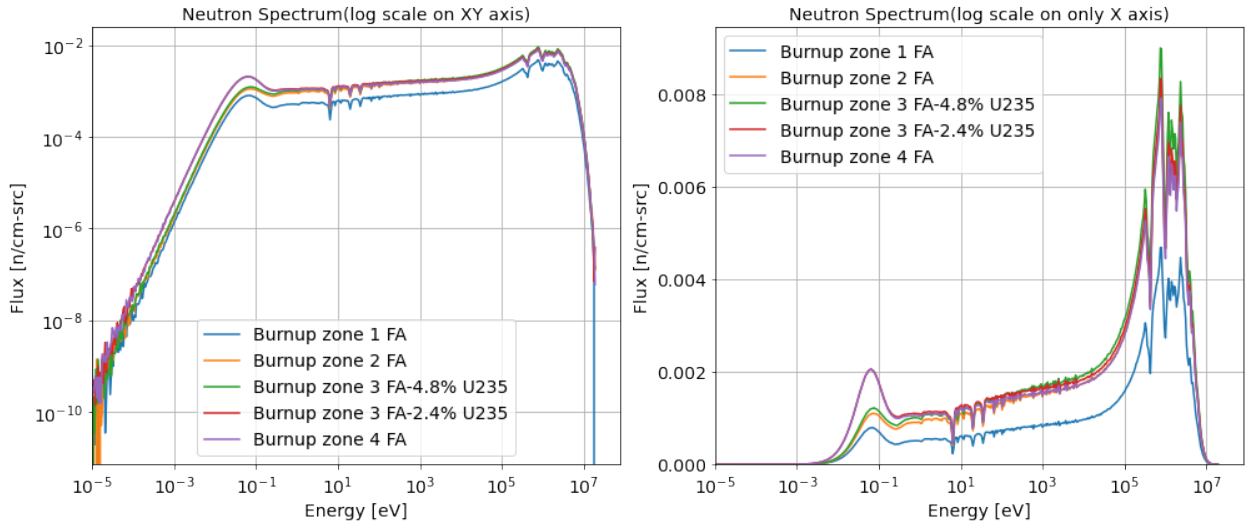


(b) Hot state neutron energy spectrum

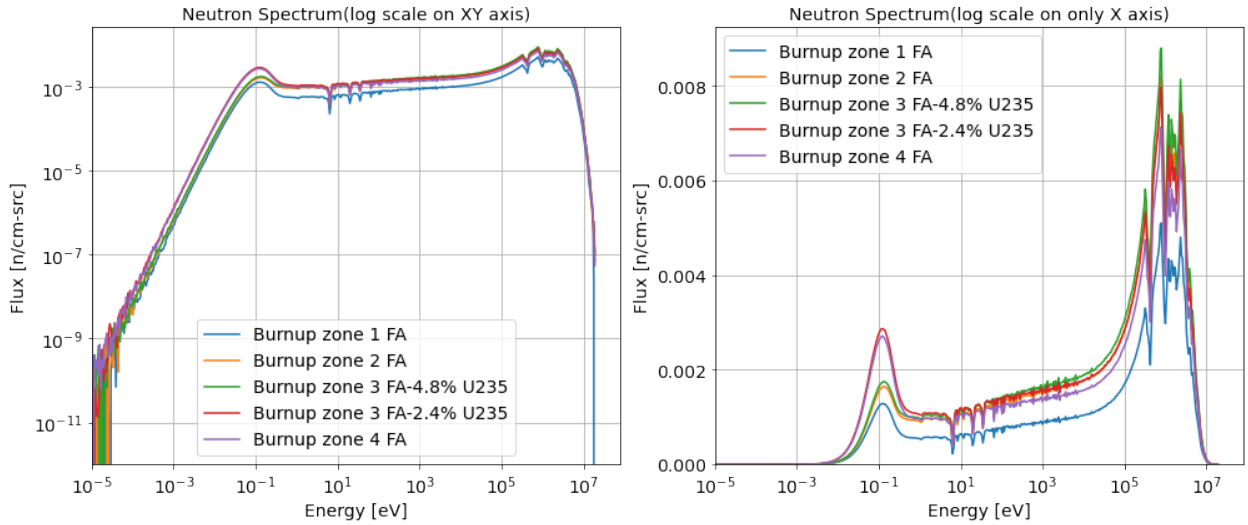
Figure 5.5: The neutron energy spectrum of core, reflector and steel barrier in the cold and hot states.

For example, in the subplots of figure 5.5, the left side spectrum has log scales on both X and Y-axis to observe the results with relatively small values, especially in the low energy range. The right side spectrum is different on the X-axis, which is a linear scale, to conveniently observe the difference at the peak height and oscillations in all of the energy range.

The diagrams in figure 5.5 represent the neutron energy spectrum in the different parts of the model, including core, reflector area and steel barrier. Subplot (a) and (b) are respectively collected from the cold and hot state simulations. The spectrum shapes of a particular part are similar at different working conditions. Usually, the tallied spectrum has a peak at the thermal energy range, which is around $10^{-1}eV$, and it also has a series of spikes at the fast energy range, from $10^5 - 10^7eV$. A rising continuous fluctuation links the peaks of the thermal and fast energy range.



(a) Cold state neutron energy spectrum



(b) Hot state neutron energy spectrum

Figure 5.6: The neutron energy spectrum of different position fuel assemblies.

Once the reactor starts-up, the entire core spectrum would rise to a higher level. Moreover, its thermal peak is trending to higher energy due to loss of moderation. The migration of the thermal peak is more obvious in the reflector spectrum. The leaked neutrons in the steel barrier also have higher energy in the reactor hot state.

The situation inside the core has been further studied and given in figure 5.6. The diagrams are collected from the same set of simulations as figure 5.5. As mentioned in the above burn-up zone studies, all 57 fuel assemblies have been assigned into the different burn-up zones labelled as burn-zone $1-4$ from the edge to centre. Figure 5.6 gives a series of spectra in the assemblies that are located at different burn-up zones. The observable difference between these energy spectra is centred on the thermal energy peaks. Their variations are synchronised with the spectrum of the entire core cell. The thermal peaks are trending towards higher neutron flux density and energy direction. Meanwhile, the thermal peaks of burn-zone 4 and zone 4' 2.4% enrichment FA overlap in the cold state but significantly differ in the hot state results. That means the higher material temperature would amplify the radial neutron flux density heterogeneity.

The above studies prove the unevenness of core neutron flux on both spatial and energy distribution levels. This unevenness would cause a non-uniform fission rate in the phase space. And subsequent uneven heat distribution in both radial and vertical direction.

5.1.3 Heating map

According to the above results, under the combined effect of the uneven digital density and energy distribution of the neutron flux, the fuel does not uniformly produce heat when the reactor is operating. The above neutron flux distribution results could not be seen as the same as the heat production map. The ideal method to see the power production is directly tallied from the MC simulation. For this reason, the $fission$ score is coupled with a $3D$ mesh filter and filled in a tally of the hot state simulation. The unit of fission score is reactions per source particle.

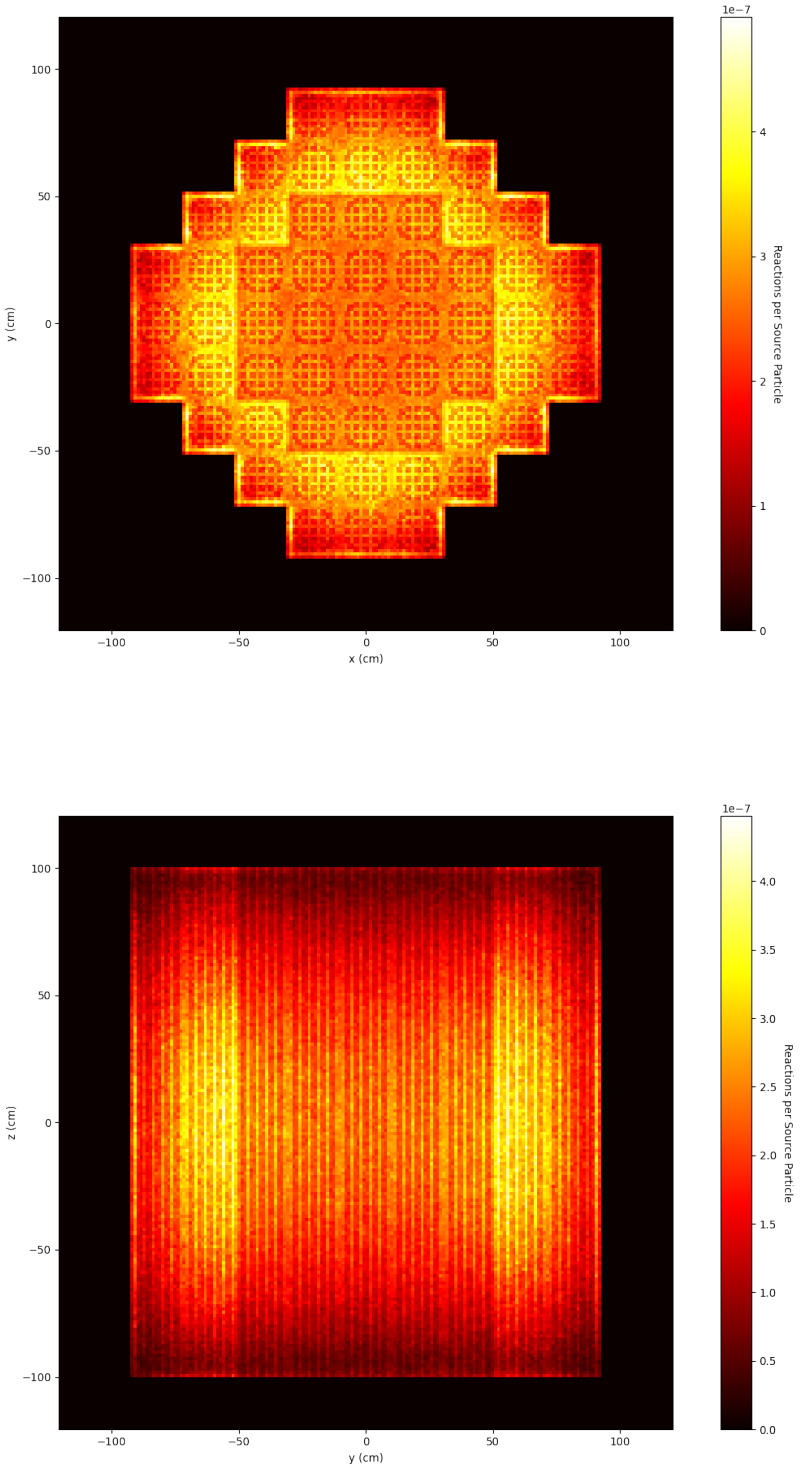


Figure 5.7: The fission rate distributions on the XY and YZ planes

Figure 5.7 presents the fission rate distribution in the core, or so called heating map. The highlighted area of the fission reaction rate is highly coincident with the high fast neutron flux density area, which is around the reloading FA zone. An extra hot belt surrounds the core at the edge. The reason is part of the large number of thermal neutrons produced in the water outside the core is scatter back and induces intensive fission reactions in this area.

5.2 Normal SMART depletion

In the last section, the neutron flux spatial distributions, energy spectrum, and the heating map of the SMART reactor in the cold and hot states have been observed and analysed. This section will present the burn-up analysis results and give some dynamic information about the reactor operation and uranium economy.

5.2.1 Eigenvalue variation

In the first instance, the k_{eff} variation of a two batch refuelling scheme core in the depletion period, which is slightly longer than 3 years, is presented in the below figure 5.8. An OpenMC burn-up calculation is a coupling process of a neutron transport operator and a time integration scheme. Except for the basic first-order predictor integrator, OpenMC also provides several implementations of different higher-order time-integration algorithms. The predictor integrator algorithm could be mathematically described below.

$$\begin{aligned} y^{'} &= A(y,t)y(t) \\ A_p &= A(y_n,t_n) \\ y_{n+1} &= e^{A_p h} y_n \end{aligned} \tag{5.1}$$

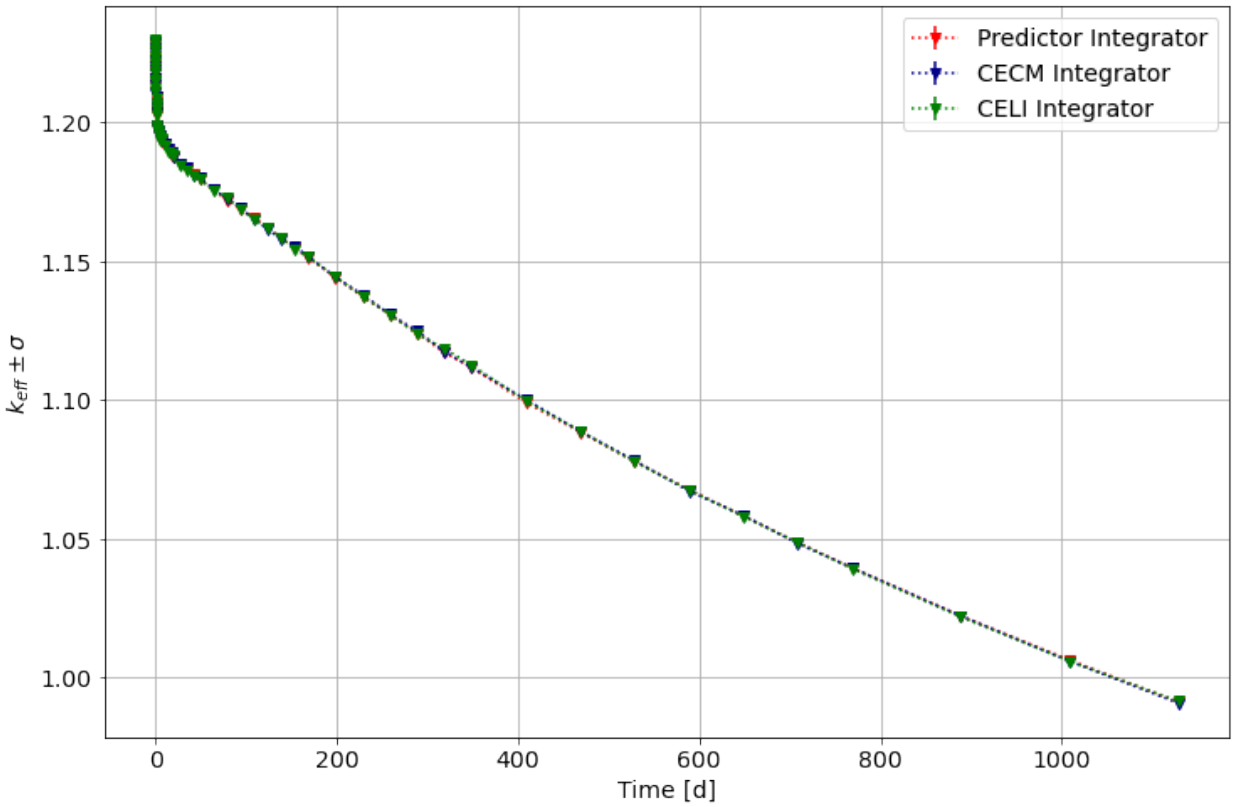


Figure 5.8: k_{eff} variation of the two-batch refuelling scheme core depletion by different integrator.

Table 5.2: k_{eff} values at the start and end of depletion and reactivity.

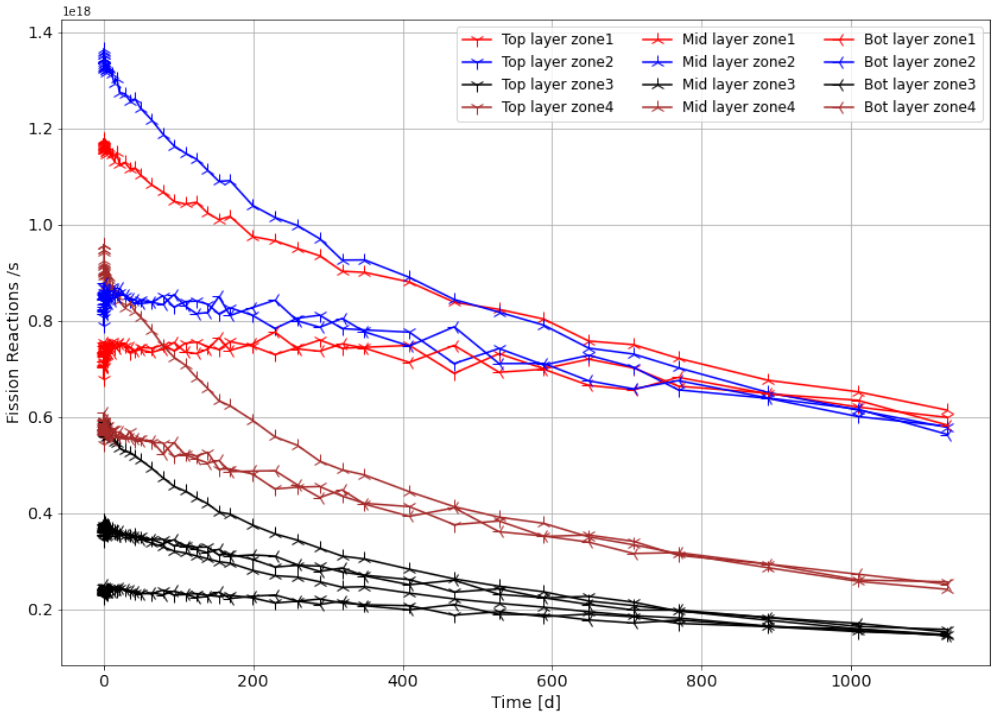
Time-integration	Beginning of cycle $k_{eff} \pm \sigma$	Reactivity (pcm)	End of cycle $k_{eff} \pm \sigma$	Reactivity (pcm)
Predictor Integrator	$1.22913\pm 34 \times 10^{-5}$	18641.6	$0.99126\pm 34.6 \times 10^{-5}$	-881.4
CECM Integrator	$1.22957\pm 32 \times 10^{-5}$	18671.0	$0.99089\pm 30.6 \times 10^{-5}$	-918.9
CELI Integrator	$1.22957\pm 32 \times 10^{-5}$	18671.0	$0.99155\pm 33.5 \times 10^{-5}$	-852.3

In order to further validate the accuracy of depletion calculations in this practical study, another two higher order algorithms, CE/CM and CE/LI were used to run the same depletion calculation. Constant extrapolation on the predictor and constant midpoint on the corrector is called CE/CM. CE/LI algorithm also has constant extrapolation but the corrector is linear interpolation [144]. The calculation results have been given in the above figure 5.8 and table 5.2. Figure 5.8 shows good agreement between the diagrams at each data point. The higher-order algorithms give close k_{eff} values at the beginning and end of the cycle. The effect on reactivity is not significant. This finding explains the predictor integrator is capable of giving reasonable results.

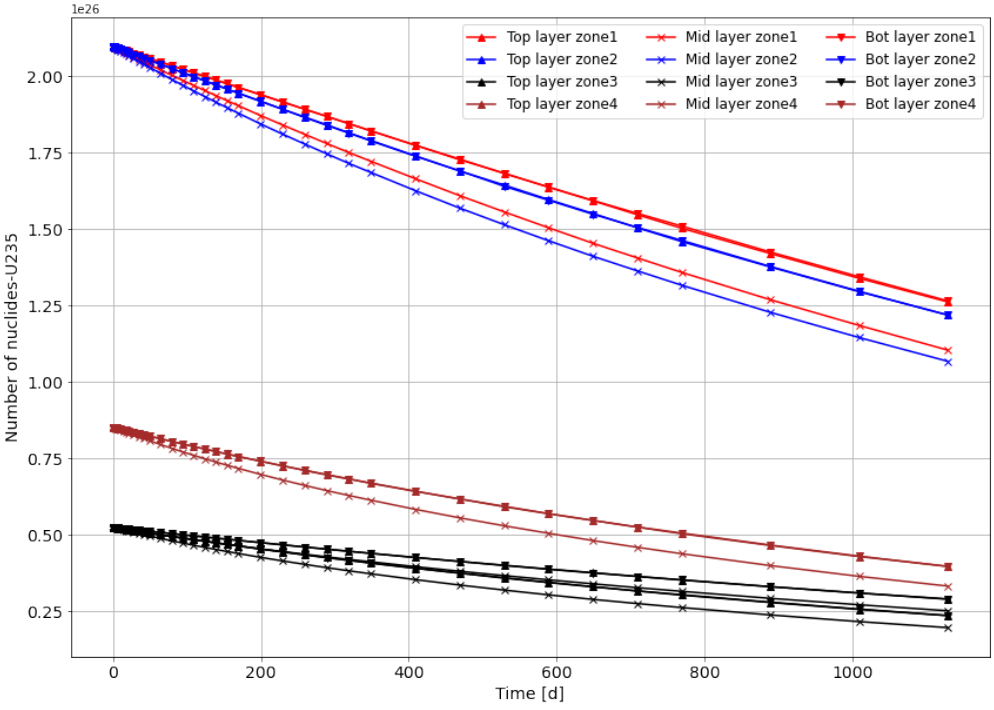
The value of k_{eff} is about $1.223 \pm 3.44 \times 10^{-4}$ at the beginning of the cycle (BOC), the excess reactivity ρ_{ex} is $18167pcm$. After 1129 days of hot full-power operation, k_{eff} value decreases to $0.991 \pm 3.46 \times 10^{-4}$ at the end of the cycle (EOC). The fission product equilibrium will be built up relatively soon, in about 12 hours once the depletion process began. According to the calculation results, this model's core can provide more than one thousand full power ($330MWth$) operating days, just as the original designer stated. However, this fuel layout cannot support the refuelling cycle length extended more than 1000 days, about 20% longer than it used to be. To further analyse the change of fuel composition and uranium utilisation conditions, the variations of fission rate and the number of ^{235}U have been plotted and given below.

5.2.2 Fission Rate and Uranium utilisation

Before describing the results in figure 5.9, a feature needs to be pointed out first. To simulate the core with two batch refuelling schemes, the 4×3 burn-up zones model has been modified a bit. Two enrichment levels FAs are filled into radial zone 3. Four fresh FAs have enrichment 4.8%, and the rest 8 FAs are defined as 2.4% enrichment to approach the reloading fuels.



(a) variations of fission rate



(b) number of ^{235}U variations

Figure 5.9: Burn-up results of 4×3 zones two batch refuelling scheme core.

Therefore, there are 15 repeating defined fuel materials in the burn-up calculation model. The depletion results of two types of FAs have be plotted out, but they are still labelled as radial zone 3 for further comparison.

In Figure 5.9, the neutronic parameter fluctuations in each burn-up zone have been summarised. In both plots, the same radial zone's diagrams have united colour to clearly present the data and use a specified marker to represent zones' results at the same height. Observing results with these conditions, the fission rate and induced ^{235}U depleting speeds significantly differ in the vertical direction. The middle height zone has a larger fission rate in any radial position than the zones above and below that. Due to the neutron sampling always being isotropic, the fission rate values are close in the top and bottom zones at all steps. Even though existing oscillations at a few steps, their mean values still can be fitted in the smoothly decreasing curve. Considering the difference between the radial regions, if the three vertical burn-up zones' results at the specified radial position are added up and then compared, the results can be organised in the below table.

Table 5.3: The burn-up results, number of ^{235}U change in one refuelling cycle.

Radial zone	Beginning of cycle	End of cycle	Burned ^{235}U	Depletion rate
Zone 1	6.2922×10^{26}	3.6316×10^{26}	2.6661×10^{26}	42.28%
Zone 2	6.2922×10^{26}	3.5057×10^{26}	2.7865×10^{26}	44.28%
Zone 3	3.1461×10^{26}	1.4994×10^{26}	1.6467×10^{26}	52.34%
Zone 4	2.5563×10^{26}	1.1258×10^{26}	1.4305×10^{26}	55.95%

In table 5.3, there is a total of about 8.524×10^{26} ^{235}U atoms that have been depleted and released energy. The depletion rate is the fraction of burned ^{235}U amount in each radial zone. The centre zone 4 has the highest depletion rate 56.0%, even though the FAs here only have 2.4% enrichment. The utilisation of edge area fresh FAs is limited, the depletion

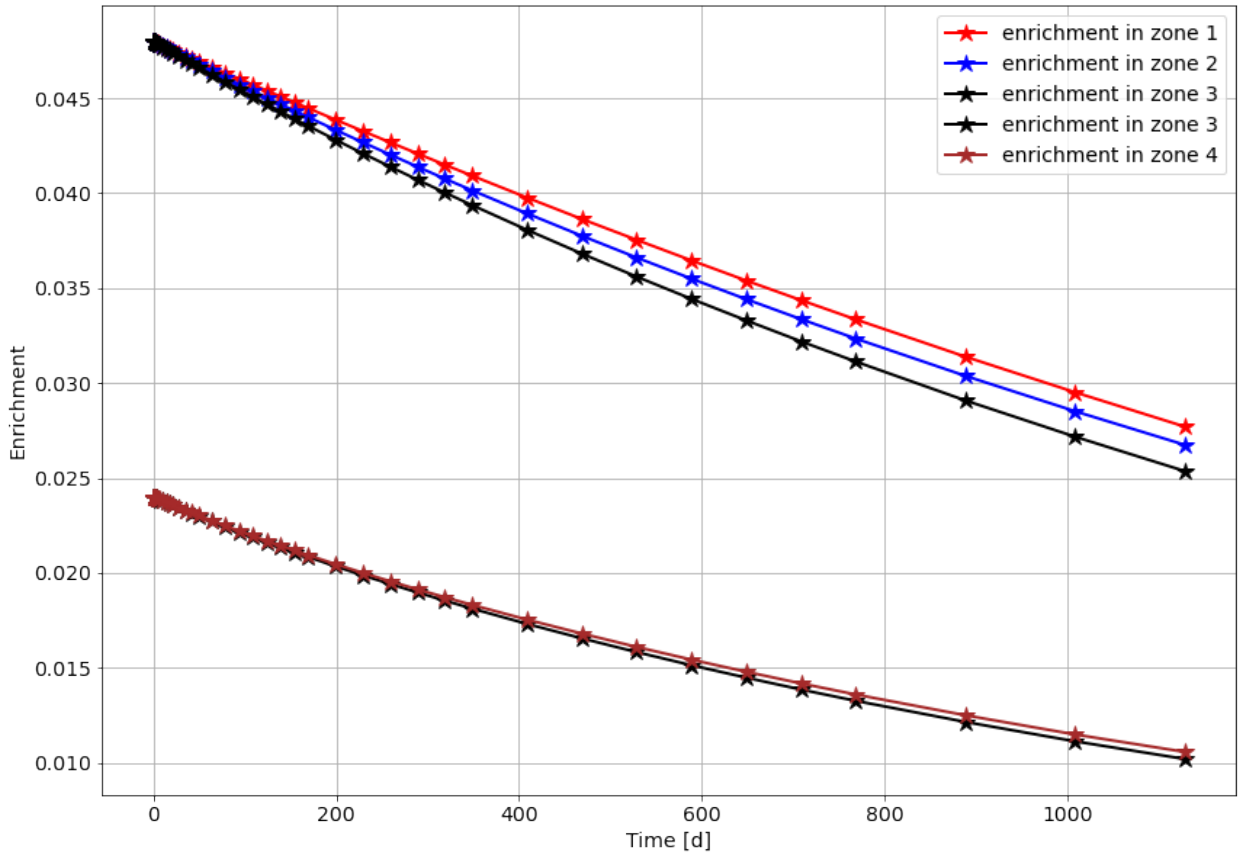


Figure 5.10: The enrichment variations in the radial burn-up zones.

rates of zone 1 and 2 are 42.3% and 44.3%, not more than half. Since the number of FAs in each burn-up zone is not uniform, only studying the number of ^{235}U could lead to the misunderstanding of results.

The averaged enrichment of fuels in each radial burn-up zone have been calculated and plotted out at every depletion step. In figure 5.10, the enrichment of reloading FAs drops to a poor level, slight higher than 0.01%. Two black diagrams represent the enrichment variations of zone 3's FAs. For the high initial enrichment FAs in the radial zone3, its enrichment has a significant drop, about 2.53% at the EOC. On the other hand, the high initial enrichment FAs in other radial burn-up zones have not been sufficiently depleted like in zone 3. The ending enrichment levels are 2.77% and 2.67%, respectively, for radial zones 1 and 2. That is

still higher than the initial enrichment for the reloading fuels, 2.4%. Therefore, based on the above results, if in one refuelling cycle, the ^{235}U in the edge burn-up zones could be further utilised, this could improve the average power output in the cycle. The neutron reflector is a common facility to save neutrons in the reactor. The reflector's effect on SMART has been done in this thesis.

5.3 Reflector material selection

As mentioned in the above section, the neutron reflector can scatter the leaked neutrons back into the core whilst meanwhile thermalising them into the high fission cross-section energy range. A suitable moderator material is thus also typically an acceptable reflector material because of their low absorption σ_a and high scatter reaction cross-sections σ_s. In this study, the normal SMART OpenMC model is used to determine the best reflector material for increasing power output. The potential materials are light materials such as heavy water, graphite, beryllium, beryllium oxide, and a couple of heavy metal materials, stainless steel and tungsten carbide. Their material properties are summarised in the below table.

As shown in table 5.4, the light water itself also could be treated as reflector material. The corresponding calculation results have already been given in the normal SMART section. As mentioned in the above literature review, heavy water D_2O and graphite have been widely used materials in nuclear reactor designs. Several PWRs utilise heavy water as primary circle coolant and moderator, such as the CANDU reactor from Canada and IPHWR-700 from India, which could use natural uranium as fuel. Many high coolant temperature reactor designs use graphite as a moderator, such as the second generation nuclear reactor technology, advanced gas-cooled reactors in the UK. The recently developed pebble-bed HTGR also use graphite to make sphere size media that contain thousands of micro-fuel particles called

Table 5.4: Material properties of potentially available reflector materials.

Material	Effective element	Atomic mass(u)	Melting point (°C)	Density (g/cm^3)
Light water	^{1}H,^{16}O	1.00784, 15.9949	0	0.997
Heavy water	^{2}H,^{16}O	2.014102, 15.9949	3.81	1.11
Graphite	^{12}C	12	≈ 3600	2.26
Beryllium	^{9}Be	9.012182	$1,287$	1.85
Beryllium oxide	^{9}Be,^{16}O	9.012182, 15.9949	$2,530$	3.02
Stainless steel	^{56}Fe	55.93494	1510	7.92
Tungsten Carbide	^{183}W	183.84	$2,870$	15.63

TRISO fuel. The beryllium-based materials were studied for space reactors due to their low density and outstanding thermal performance. The melting points are $1287°C$ and $2530°C$ for beryllium metal and beryllium oxide.

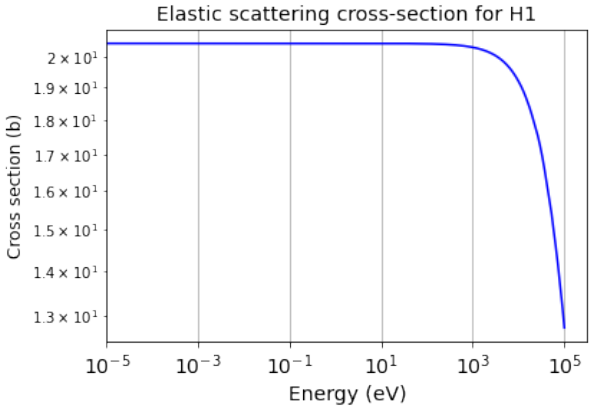
On the other hand, heavy metal materials are usually difficult to slow down neutrons with. But that could protect the reactor pressure vessel better and scatter the fast neutrons back to the core. The application of stainless steel as a neutron reflector has been well studied. Even its melting point is about $1510°C$ but still it has enough margin for a PWR, where the operating coolant temperature is usually at $275°C$. Compared with stainless steel, tungsten carbide has a very high melting point at $2870°C$, which was used as a neutron reflector for a nuclear weapon in the early stage of nuclear power development. The analysis of reflector materials should begin at their cross-sections. The cross-sections of potential reflector materials for particular nuclear reactions have been collected from IAEA evaluated nuclear reaction libraries ENDF. The results and analysis shall be given in the following sections.

5.3.1 Elastic scattering

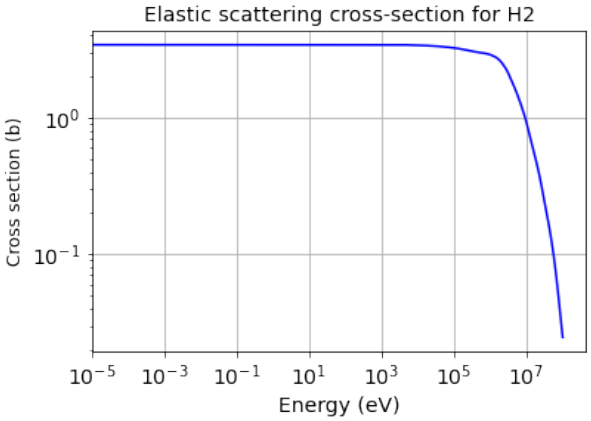
Neutron scattering is the fundamental mechanism to moderate fast neutrons. Elastic scattering is a collision between a neutron and a nucleus. Part of the neutron's kinetic energy is transferred to the recoil nucleus in the process. The total kinetic energy in the system will be equal to the original colliding neutron energy. In the ENDF nuclear data library, the elastic scattering reaction is labelled as $MT = 2$, and MT is the sign of ENDF reaction nomenclature. OpenMC code reserves an OpenMC.data package in the Python API. The basic function of this package are the analysis and conversion of nuclear data from the ACE files. It is also capable of generating nuclear data libraries in the HDF5 format that OpenMC would read in the transport solver.

The ENDF data is also available for this feature. An evaluation represented the analysis of experimentally measured parameters, including cross-sections and combined the result with nuclear model calculations to extract the true value of desired parameters. The results data would then be parameterised and reduced to a tabular form that is readable by nuclear data programs. Each isotope's parameters are specified and ordered by atomic mass number in its particular material category.

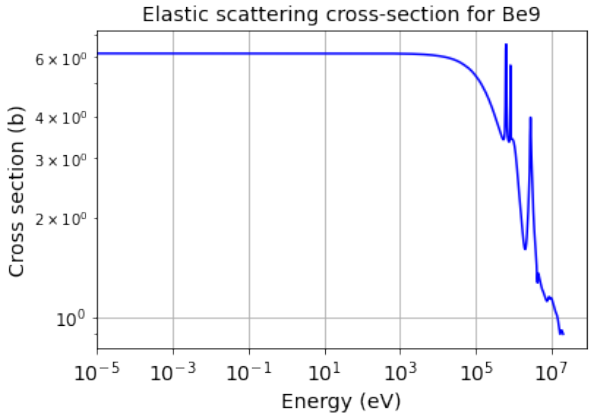
The resonance parameters would also be divided into incident neutron ranges ordered by increasing energy. Except for the parameterised resonance ranges, the resolved and unresolved resonance regions are two special areas in the full energy range containing the cross-sections in point-wise form in the evaluated data files. When loading data from an ENDF package by OpenMC, a special attribute is accessible containing the resolved and unresolved resonance region data. The elastic scattering cross-sections for each light atomic mass isotopes are given in figure 5.11.



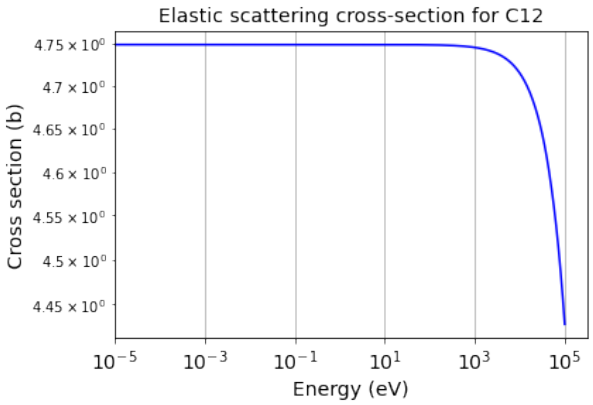
(a) ENDF/B-VII.1 ^{1}H



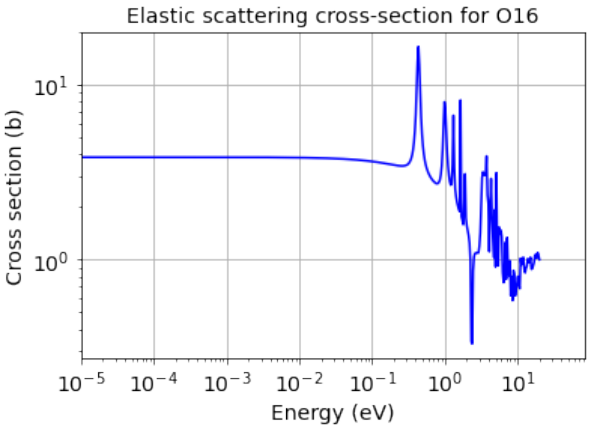
(b) ENDF/B-VII.1 ^{2}H



(c) ENDF/B-VII.1 ^{9}Be



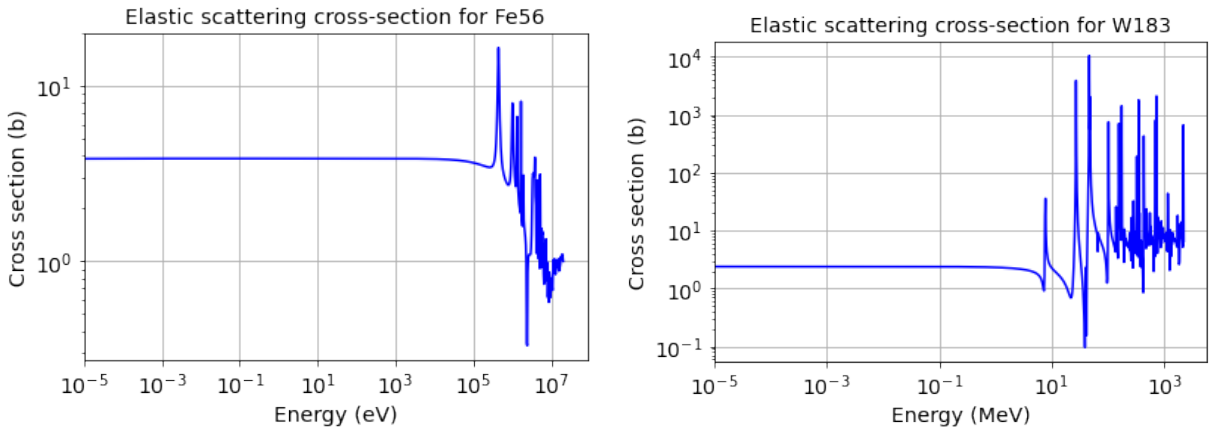
(d) ENDF/B-VIII.0 ^{12}C



(e) ENDF/B-VII.1 ^{16}O

Figure 5.11: Elastic scattering ($MT = 2$) cross-sections ($0K$) of ^{1}H,^{2}H,^{9}Be,^{12}C, ^{16}O versus incident neutron energy.

Five light atomic mass isotopes introduced in table 5.4 all have considerable cross-section for elastic scatter with incident neutrons. For neutrons with energy lower than $1eV$, the ^{1}H atom has a cross-section of $20b$, which is the biggest one in the above 5 plots. For ^{2}H, ^{9}Be and ^{12}C, this parameter is $3.5b$, $6b$ and $4.75b$. The cross-section values in subplots (a)-(d) would decrease when the incident neutrons speed up. However, they still have the probability of slowing down the fast neutrons. Subplot (e) gives a cross-section distribution of ^{16}O. In table 5.4, it compounds with the aforementioned isotopes in H_2O, D_2O, and BeO. ^{16}O also has a significant elastic scattering cross-section to thermal energy neutrons but it is not sensitive to neutrons whose energies are higher than $10eV$.

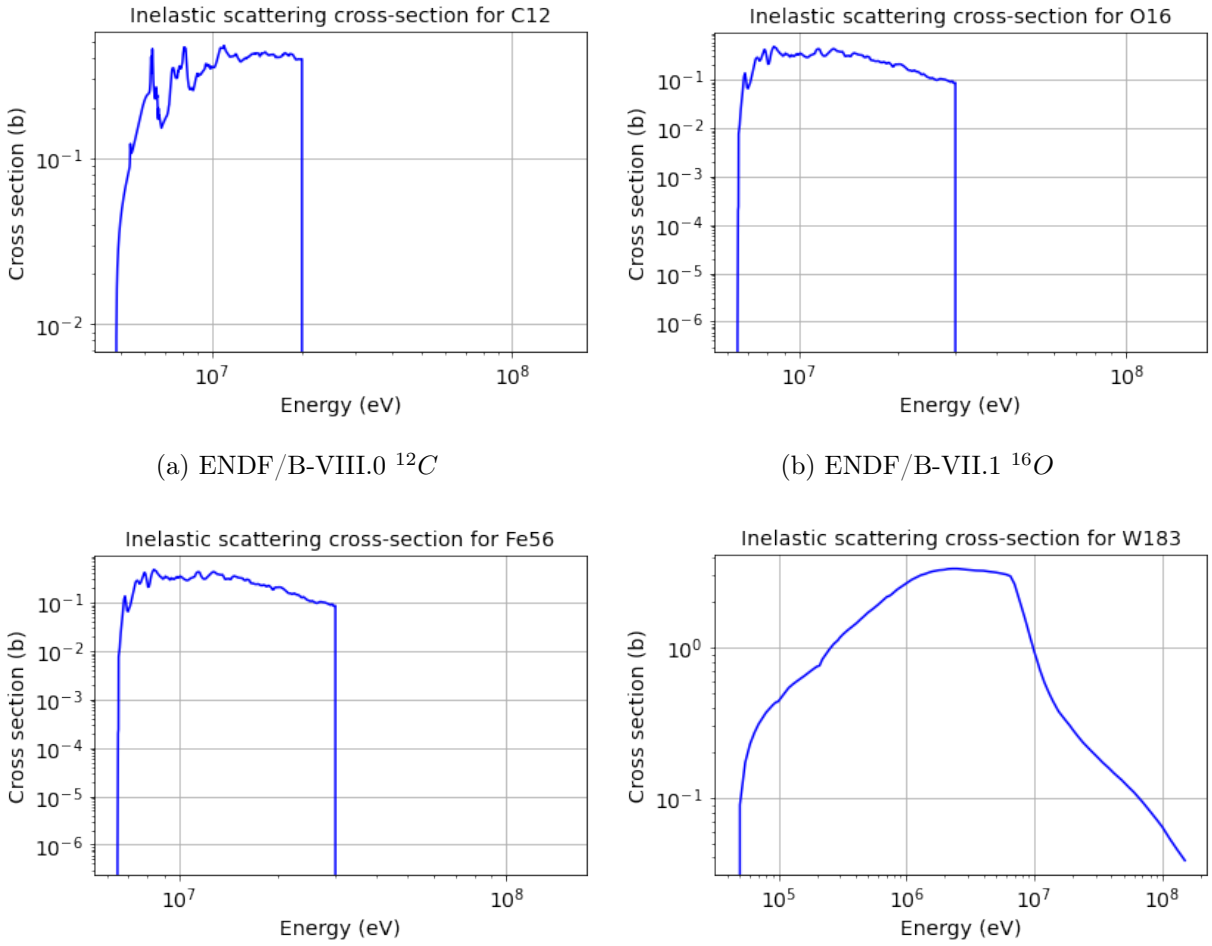


(a) ENDF/B-VII.1 ^{56}Fe

(b) ENDF/B-VII.1 ^{183}W

Figure 5.12: The elastic scattering cross-section of heavy atomic mass isotopes ^{56}Fe, ^{183}W.

Figure 5.12 gives the resolved resonance energy range elastic scattering cross-section distributions of heavy atomic mass isotopes ^{56}Fe and ^{183}W. In this region, the experimental resolution is enough to observe the resonances and determine their parameters by area or shapes analysis. The sensitivity area of ^{56}Fe is between 10^5 to 10^7eV. ^{183}W isotope can scatter the neutrons for which their energy is lower than 10^3eV. Its maximum value of cross-section is about 10^4b. The elastic scatter characteristic of ^{56}Fe and ^{183}W isotopes are similar to the ^{16}O.



(a) ENDF/B-VIII.0 ^{12}C

(b) ENDF/B-VII.1 ^{16}O

(c) ENDF/B-VII.1 ^{56}Fe

(d) ENDF/B-VII.1 ^{183}W

Figure 5.13: Inelastic scattering ($MT = 4$) cross-sections of ^{12}C, ^{16}O, ^{56}Fe, ^{183}W.

5.3.2 Inelastic scattering

The isotopes in table 5.4 also have a probability to inelastic scatter incident neutrons. In an inelastic scattering process, the incident neutron would be absorbed by the target nucleus and form a compound nucleus in the excited state, and then the nucleus would emit a lower kinetic energy neutron and one or two gamma rays back to its ground state. The kinetic energy of the colliding system is not conserved in inelastic scattering.

The parameters of inelastic scattering are labelled as $MT = 4$ in the ENDF data library. By individually checking the data-sets, the ^{12}C, ^{16}O, ^{56}Fe, and ^{183}W all have the chance to give inelastic scattering. The cross-section distributions with energy have been plotted in the above Figure 5.13.

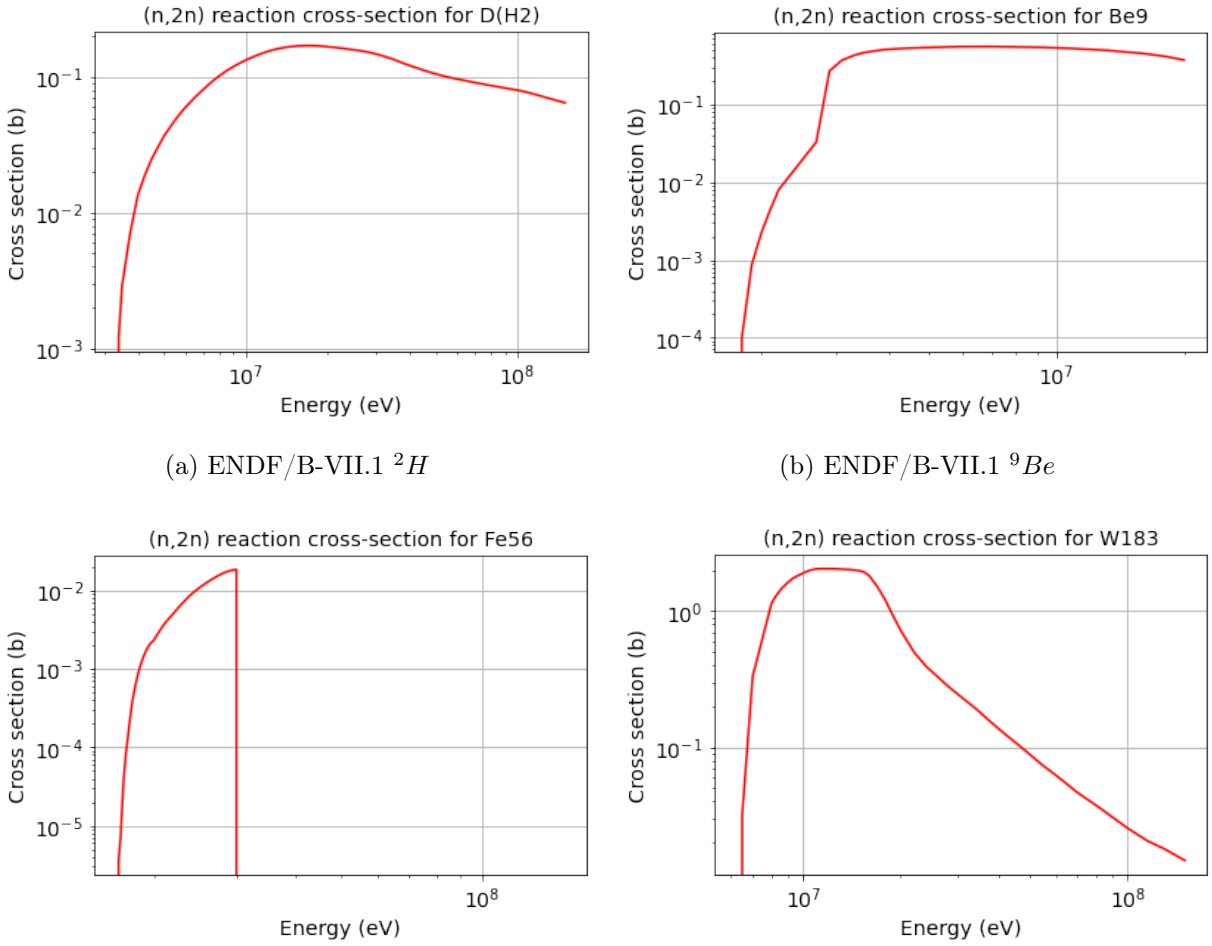
Observing the results in figure 5.4, the ^{12}C, ^{16}O, and ^{56}Fe all have relatively high thresholds to induce inelastic scattering. The energy of thresholds are around $10^7 eV$. Therefore their effect on neutron reflection is limited. The ^{183}W isotope would have an inelastic scattering reaction of neutrons with energy from 10^5 to $10^8 eV$. The cross-sections are higher than $1b$ for the neutrons with energy from 10^6 to $10^7 eV$.

5.3.3 (n,2n) reaction

The other type of nuclear reaction that has been investigated is the $(n, 2n)$ reaction, $MT = 16$ in ENDF nuclear data library. As mentioned in the literature review chapter, beryllium has a $^9Be(n, 2n)^8Be$ reaction. Therefore, it also can be a neutron multiplier to compensate one extra neutron back to the core per reaction. Checking the ENDF files of the above potential reflector material isotopes, the ^2H, ^{56}Fe and ^{183}W also have probabilities for there to occur an $(n, 2n)$ reaction. Their cross-section distributions have been extracted and plotted in the below figure 5.14.

The incident neutron must be higher than a particular energy threshold to induce $(n, 2n)$ reactions with isotopes in figure 5.14. The following table gives the threshold energy and cross-sections at the initial points.

Observing parameters in figure 5.14 and table 5.5, the ^9Be has an $(n, 2n)$ reaction threshold of $1.8 MeV$, which is the lowest one in these four isotopes. That cross-section would be higher than $0.27b$ and stay stable when neutron energy is over $2.9 MeV$. The other



(a) ENDF/B-VII.1 ^{2}H

(b) ENDF/B-VII.1 ^{9}Be

(c) ENDF/B-VII.1 ^{56}Fe

(d) ENDF/B-VII.1 ^{183}W

Figure 5.14: $(n, 2n)$ reaction, $MT = 16$ cross-section distributions of ^{2}H, ^{9}Be,^{56}Fe,^{183}W.

Table 5.5: Threshold of $(n, 2n)$ reactions and cross-sections.

Nucleus	Threshold(eV)	Cross-section at threshold(b)
^{2}H	3.4×10^{6}	0.0012
^{9}Be	1.8×10^{6}	1.0×10^{-04}
^{56}Fe	16.82×10^{6}	3.579509×10^{-6}
^{183}W	6.5×10^{6}	0.0322599

light atomic mass isotope ^2H could give an $(n, 2n)$ reaction with neutrons in the energy range from $3.4MeV$ up to $150MeV$. The maximum $\sigma_{n,2n}$ value for ^2H is $0.1712b$ when the neutron energy is $16MeV$. Heavy isotope ^{183}W has the same response energy range as ^2H. Its cross-section is significant for fast energy neutrons, $\sigma_{n,2n}$ is bigger than $2b$ for the neutron energy range from $11-14MeV$. The $\sigma_{n,2n}$ will decrease lower than $1b$ if the incident neutron energy exceed $19MeV$.

The cross-sections for elastic, inelastic scattering and $(n, 2n)$ reaction of potential reflector's isotopes have been individually extracted from their available ENDF nuclear data libraries and cross-compared. The nuclear data studies in this work are helpful to qualitatively select the proper reflector material for SMART power output optimisation. However, only by comparing the cross-section data one could not fairly determine the reflector capability. Due to the difference in material densities, the number of isotope atoms in particular geometry spaces would significantly differ. The following sections will introduce the MC simulations results of different materials in a reflected SMART core.

5.4 Reflected SMART core

This section will present the reflector effect to the SMART core performance from pure neutron transport and depletion aspects. Figure 5.4 types of mesh plots are often helpful to observe the neutron flux spatial distributions and fluctuation intuitively. However, it is difficult to estimate the amount of flux in the particular cell space, especially for the low neutron flux cells. To evaluate the effect of reflectors on the reactor core and the steel barrier, the average flux values of core, reflector, and barrier three cells have been respectively tallied. The results are then given in the below table 5.6, which are in the form of mean with standard deviation, for which the unit is $(n/cm - src)$.

Table 5.6: Average thermal and fast neutron flux tally results(means and Standard deviations) in core, reflector and barrier.

	Core		Reflector		Barrier	
	Thermal	Fast	Thermal	Fast	Thermal	Fast
	std.dev.	std.dev.	std.dev.	std.dev.	std.dev.	std.dev.
Light water	4.3911	33.7306	5.0485	2.3860	0.0677	0.1372
	0.0005	0.0014	0.0019	0.0007	0.0001	0.0002
Heavy water	4.2683	33.4716	7.4812	7.2111	0.2718	0.5127
	0.0005	0.0016	0.0029	0.0019	0.0002	0.0003
Graphite	4.324	34.899	3.650	9.838	0.134	0.001
	0.007	0.016	0.020	0.035	1.032	0.008
Beryllium	4.254	33.949	9.454	8.551	0.198	0.390
	0.005	0.017	0.042	0.022	0.001	0.004
Beryllium Oxide	4.2421	34.1979	8.3436	8.8959	0.1852	0.4135
	0.0005	0.0013	0.0034	0.0022	0.0001	0.0003
Steel	4.42940	35.78504	0.08558	5.84530	0.00361	0.76579
	0.00054	0.00134	0.00008	0.00204	0.00002	0.00044
Tungsten carbide	4.53081	35.83028	0.01674	2.30397	0.00062	0.09571
	0.00052	0.00137	0.00002	0.00087	0.00001	0.00017

The standard deviations in the table 5.6 are small, no bigger than 0.1% if they are divided by their corresponding mean values, which means the results are statistically acceptable. In the reactor core cell itself, whatever it is surrounded by is which kind of material reflector. The average fast and thermal neutron flux values are generally close. The gap between maximum and minimum fast neutron flux is $2.1n/cm - src$, and for thermal neutron it is $0.2n/cm - src$. On the contrary, reflector cells' flux values have obvious differences in the thermal or fast energy group. Figure 5.15 uses bar heights to present the flux values.

The reason causing the flux variance in reflectors is the cross-sections of reactions and the difference of leaked neutron energy. The Be metal reflector owns the highest average thermal neutron flux which is $9.45375n/cm - src$, and the second one is in BeO, $8.34364n/cm - src$. Heavy materials have two orders of magnitude less thermal neutron flux than light materials. For the fast neutrons, its maximum flux is in the graphite reflector. The green bars represent the neutron flux in the steel barrier that should not be neglected. Steel and WC block the most thermal neutrons from getting into the barrier. However, the steel cannot effectively function to shield the fast neutrons. $0.7657n/cm - src$ is the biggest remaining fast neutron flux value after the reflection and shield in all simulations.

Besides the numerical results that have been given in table 5.6, the neutron flux spatial distribution in particular material reflectors also have been investigated. This kind of study is helpful to observe how the neutrons have been moderated in the reflector. Moreover, the geometry parameters of the reflector in this study are constant. The spatial distribution results can provide a meaningful reference to determine the size of the reflector made by a particular material.

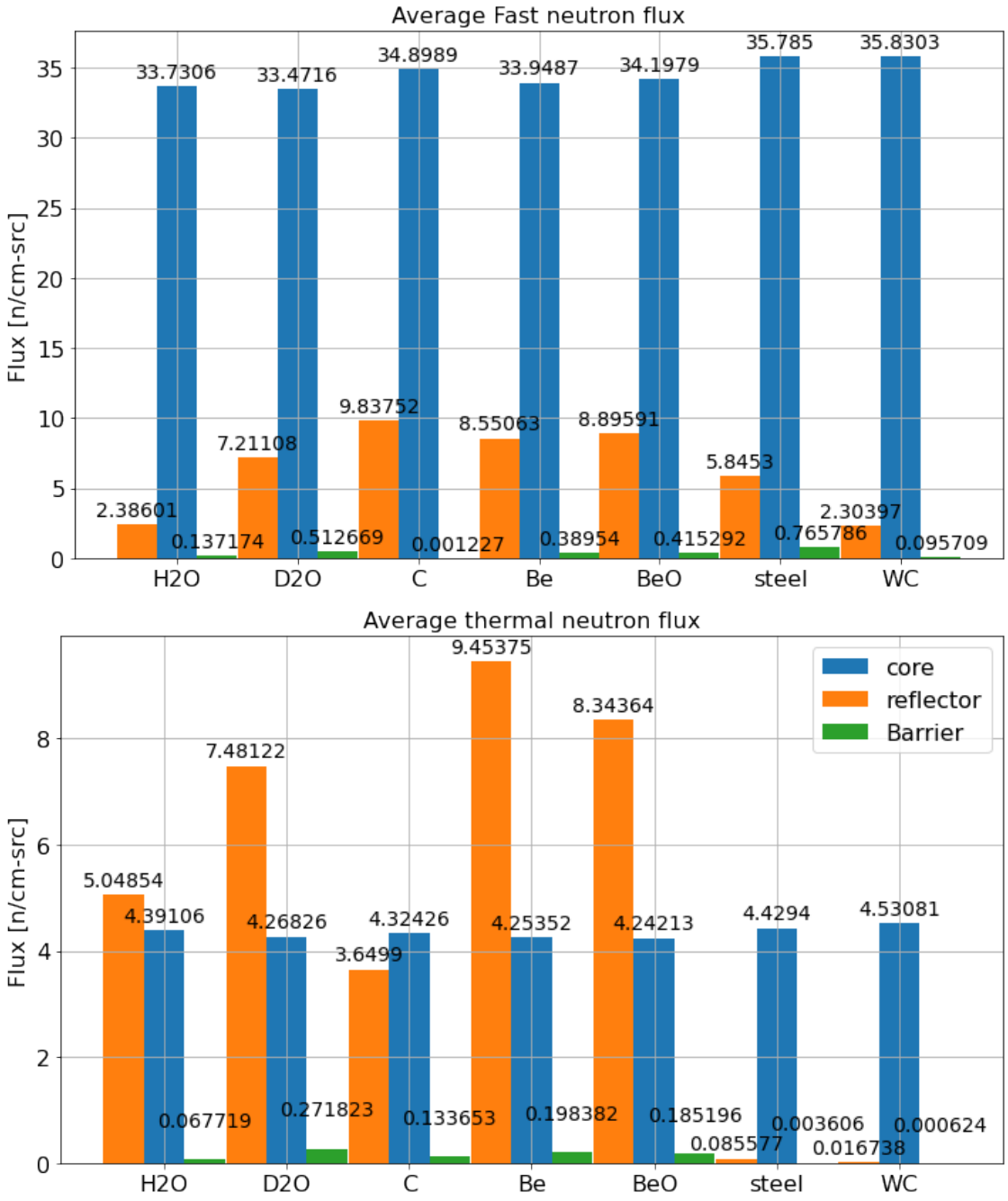


Figure 5.15: Bar charts of thermal and fast neutron flux mean values for core, reflector and barrier.

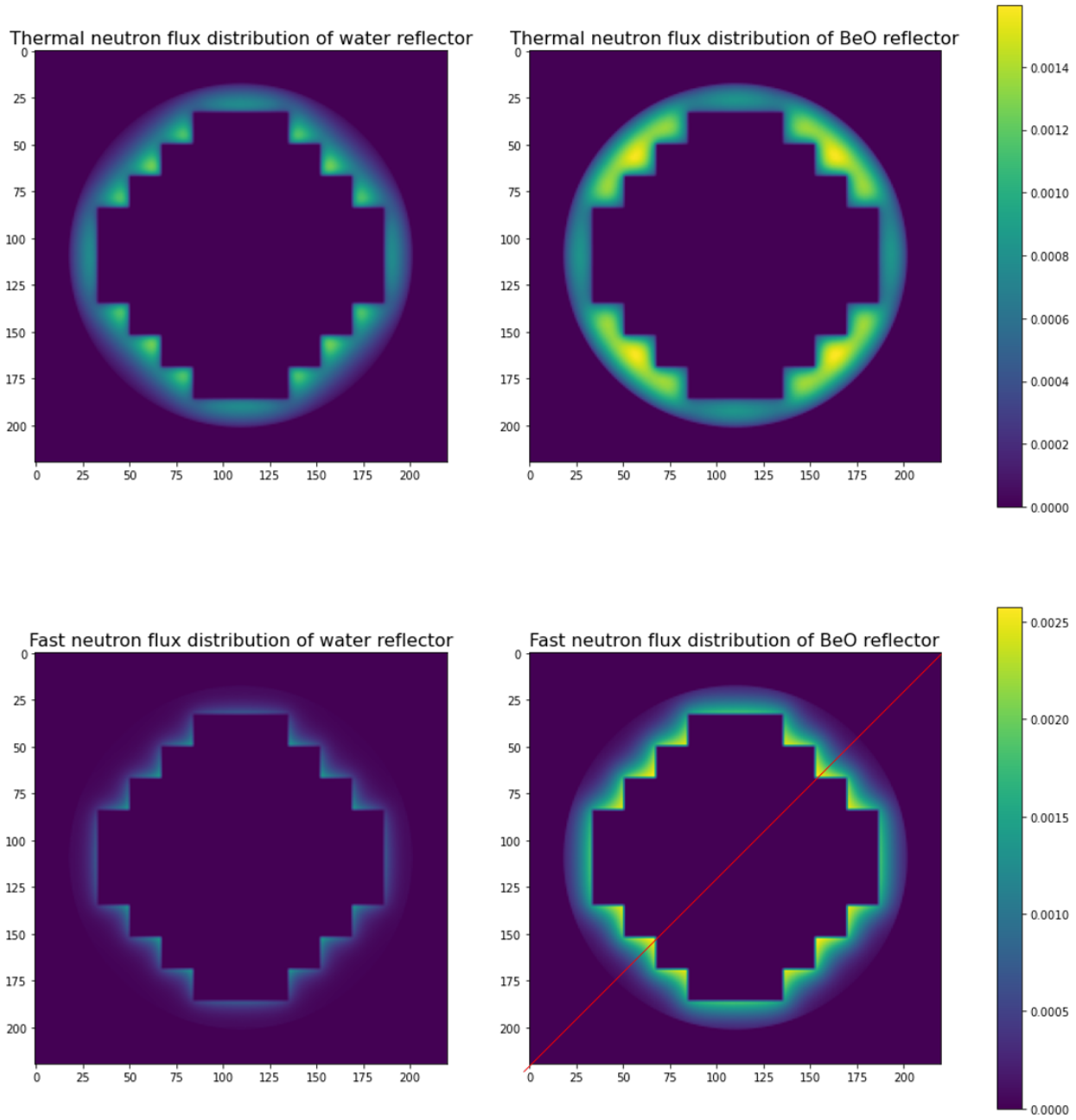


Figure 5.16: Thermal and fast neutron flux spatial distributions in the light water and BeO reflector.

Figure 5.16 gives a series of similar mesh plots as the above figure 5.2, but only focus on the reflector cell. The normalised fast and thermal neutron flux distributions in the light water and BeO reflectors have been plotted in figure 5.16 as examples. It is obvious to see both thermal and fast neutron flux are more significant in the BeO reflector. The amount of fast neutrons near the boundary of FAs have been improved to a higher level. Meanwhile, the thermal flux peak appears around the middle width position in the BeO reflector. Generally, the neutron flux is symmetrical in the radial direction and it is unevenly distributed in the reflectors. Similar plots are also made for other reflectors. Meanwhile, the flux values have been selected from the mesh in the diagonal direction for cross-comparison.

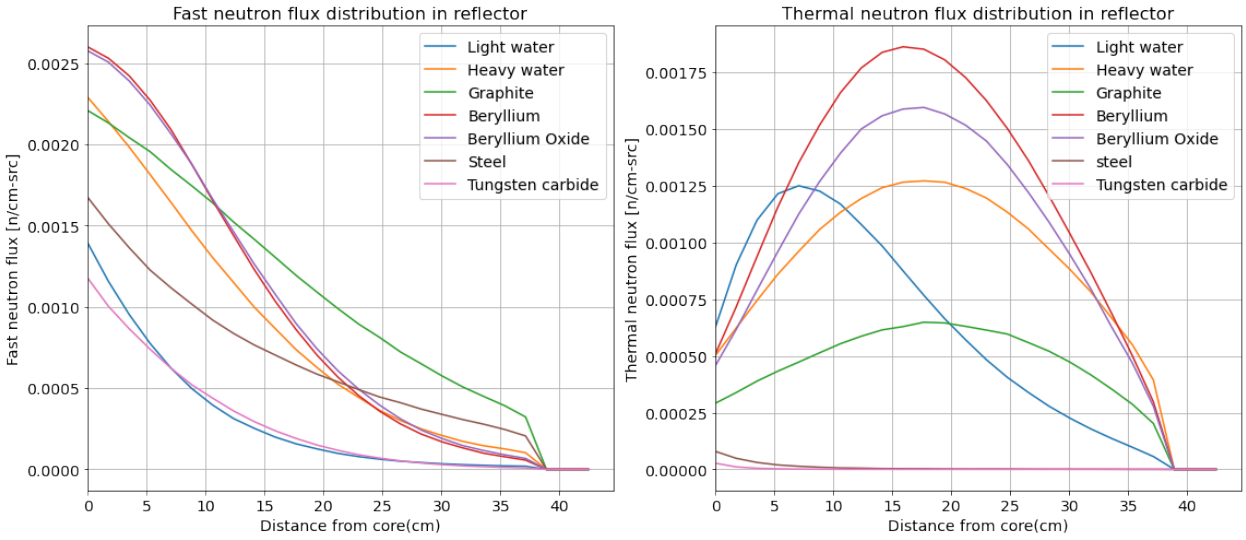


Figure 5.17: Values of neutron flux versus the distance away from FA boundaries.

Curves in Figure 5.17 represent the fluctuations of neutron flux in the reflector along the model's diagonal line, just like the red line has been shown in the BeO reflected core fast neutron flux distribution plot. The fast neutron flux values near the FAs boundary are improved from that in the original model, with 4 light mass materials and steel reflectors. That means when these types of reflector appear in the model, there are more fission reactions occuring in the core and release more induced neutrons. The beryllium-based materials have

the most significant improvements to fast neutron flux in the range of potential materials. The fast neutrons require a certain travelling length to slow down, which produce a series of thermal neutron flux peaks. And the thermal neutron flux peak in the light water is closer to the boundary than in other light mass reflectors.

As mentioned in the nuclear data study results, the isotopes' cross-section for a particular reaction is dependent of the incident neutron energy. Therefore, the neutron energy distributions in the various materials of reflector are necessary to be investigated. The results are given in the below figure 5.18.

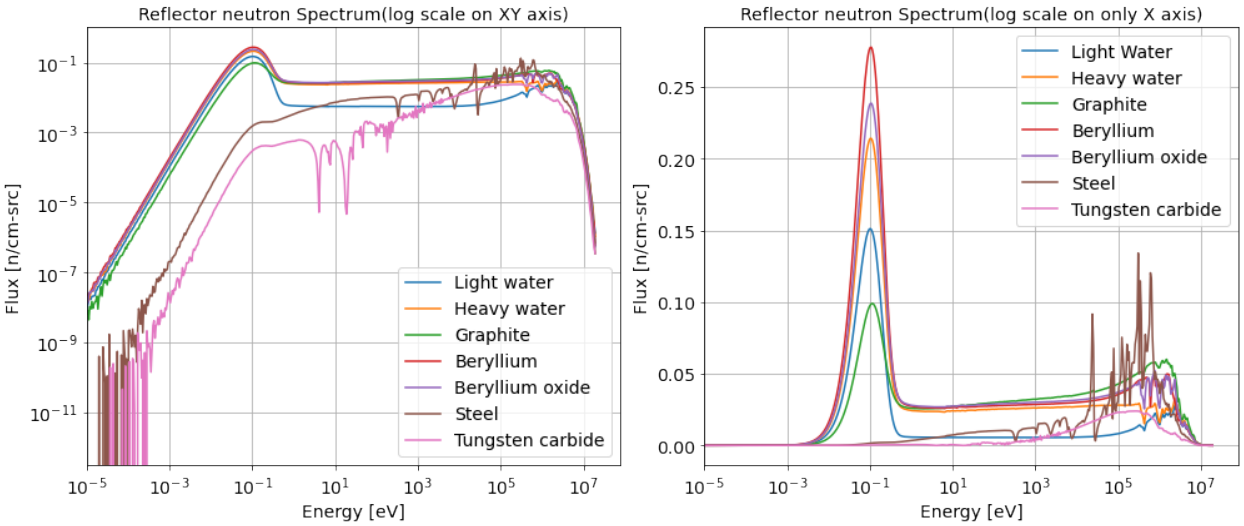


Figure 5.18: Neutron energy spectra in different neutron reflector materials.

The plots in figure 5.18 could be seen as a supplement to explain the results in figure 5.15. The height of bars that has presented for the flux values now have been broadened into the energy spaces. Meanwhile, the scatter reaction rate in each energy space also has been recorded. The results are then given in figure 5.19.

Observing the spikes located at $10^{-1}eV$ in Figures 5.18 and 5.19, the neutron flux in light water is lower than that in heavy water. However, the neutron scattering rate is actually higher. The beryllium metal reflector has the most significant scattering reaction

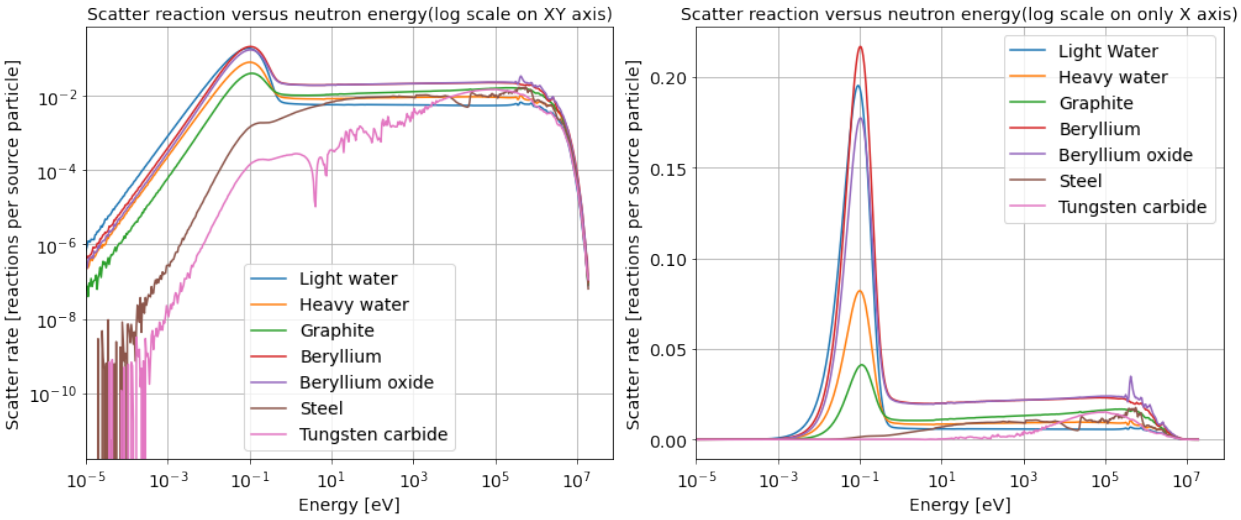


Figure 5.19: Neutron reflectors' scattering rate distributions with neutron energy.

rate for all energy ranges. When neutron energy is around $10^{-1}eV$ the scattering ability of BeO is weaker than light water and beryllium metal. The neutron energy increase will enhance the BeO's reflection ability. The scattering reaction diagrams of Be based materials basically overlap, only having a few variances when neutron energy is between 10^5 to 10^6.

Similar to the above table 5.6, the numerical average scattering reaction rate in each reflector material has been tallied. The absorption rates have also been recorded in the simulations. The below tables present the numerical tally results. For the compound materials, the parameters for each nucleus have been respectively recorded.

The results in table 5.7 and 5.8 could explain why hydrogen atoms in light water have the highest elastic scattering cross-section in the potential reflector materials but do not have the best reflection ability. The neutron absorption rate of light water is the highest in all potential materials, including heavy metal materials. The ^1H atom makes the most contribution to the neutron absorption in light water. Moreover, the scattering rates of ^{16}O are variable in different compounds. The differences in reflectors' energy spectrum are the major reason for that.

Table 5.7: The total scattering rate and absorption rate of reflector material.

Reflector materials	Scatter (mean)	std.dev.	Absorption (mean)	std.dev.	Scatter/ absorption	std.dev.
Light water	8.829	0.003	0.04862	2×10^{-5}	181.6	0.09
Heavy water	5.456	0.002	4.81×10^{-4}	3.1×10^{-7}	11345	8
Graphite	5.116	0.002	8.46×10^{-4}	5.1×10^{-7}	6041	4
Beryllium	13.34	0.004	0.01194	4×10^{-6}	1117	0.5
Beryllium Oxide	12.14	0.0036	0.0075	2×10^{-6}	1622.37	0.7143
Steel	2.484	0.001	0.0212	1.1×10^{-5}	117.3	0.076
Tungsten carbide	1.505	0.0006	0.04542	2×10^{-5}	33.14	0.02

Table 5.8: Scattering rates and absorption rates of each nuclide in compound materials.

Nucleus	Scatter mean	std.dev.	Absorption mean	std.dev.	Scatter/ absorption	std.dev.
^{1}H	8.169	0.003	0.04842	2×10^{-5}	168.7	0.09
^{16}O	0.6596	0.0002	0.0002	2.4×10^{-7}	3305	4
^{2}H	3.59	0.0011	1.55×10^{-4}	0.6×10^{-7}	23197	11
^{16}O	1.865	0.0006	3.26×10^{-4}	2.9×10^{-7}	5720	5
^{9}Be	7.358	0.002	0.00680	22×10^{-7}	1083	0.5
^{16}O	4.78	0.0014	6.5×10^{-4}	4.9×10^{-7}	7347	6

Besides the investigations around the neutron flux, the k_{eff} eigenvalues of different materials of reflector for normal core models have been calculated. The below table 5.9 gives the results.

Table 5.9: k_{eff} eigenvalue results of two-batch refuelling scheme core with different material reflector.

Material	k_{eff}(Collision)	k_{eff}(Track-length)	k_{eff}(Absorption)	Combined k_{eff}
Light water	1.22906±	1.22903±	1.22907±	1.22906±
	9×10^{-5}	11×10^{-5}	8×10^{-5}	7×10^{-5}
Heavy water	1.25920±	1.25908±	1.25921±	1.25921±
	9×10^{-5}	11×10^{-5}	7×10^{-5}	7×10^{-5}
Graphite	1.25155±	1.25172±	1.25152±	1.25157±
	9×10^{-5}	10×10^{-5}	7×10^{-5}	7×10^{-5}
Beryllium	1.27617±	1.27614±	1.27612±	1.27613±
	9×10^{-5}	11×10^{-5}	7×10^{-5}	7×10^{-5}
Beryllium	1.27456±	1.27449±	1.27445±	1.27446±
Oxide	9×10^{-5}	11×10^{-5}	6×10^{-5}	6×10^{-5}
Steel	1.22762±	1.22759±	1.22752±	1.22754±
	9×10^{-5}	10×10^{-5}	6×10^{-5}	6×10^{-5}
Tungsten	1.21342±	1.21337±	1.21344±	1.21344±
carbide	9×10^{-5}	11×10^{-5}	7×10^{-5}	7×10^{-5}

The variation of combined k_{eff} values could represent the quantity upgrade to reactivity from the different reflectors. The beryllium based materials' neutron reflector could give an extra 0.05 improvement to the original design's eigenvalue. The heavy water and graphite could promote the original design's eigenvalue from 1.22907 to a level that is higher

than 1.25, and the enhancement from heavy water is slightly stronger than graphite. The initial k_{eff} values of heavy metal reflected models are even lower than the original design. In order to estimate the reflectors' effect on the power output and distribution, the heating map of different materials of reflected core has been tallied.

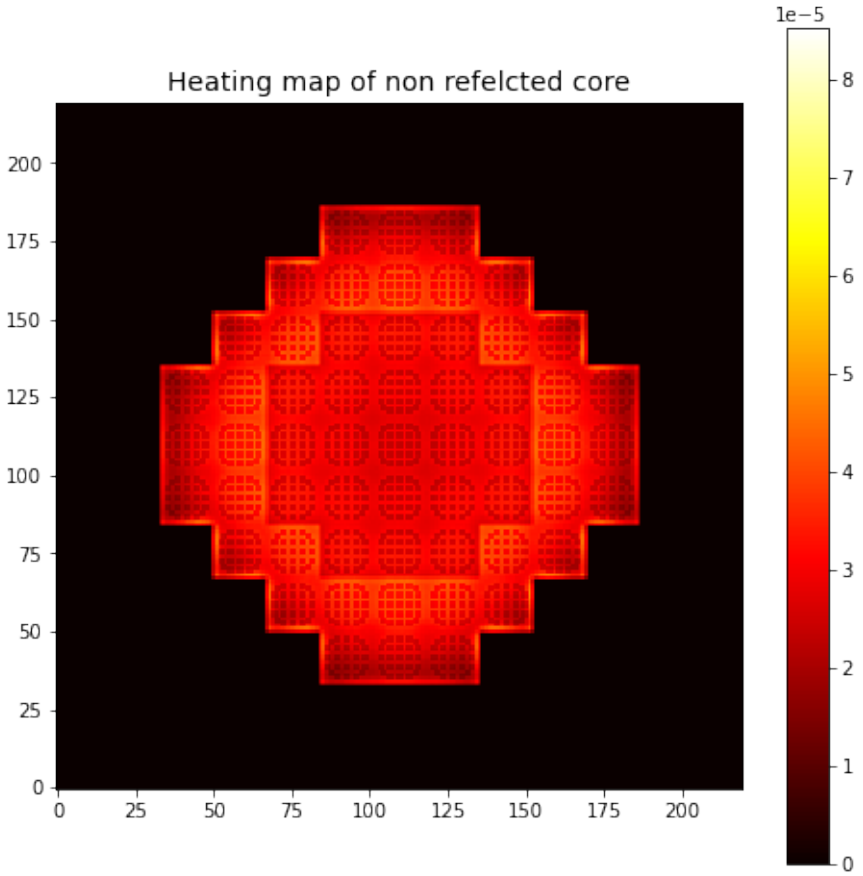


Figure 5.20: Heating maps of two-batch refuelling scheme core with light water reflector.

Figure 5.20 is the heating map of normal layout core model with light water reflector. This plot is shown separately as the benchmark. Other heating maps would be given in figure 5.21. The colour map scales of figure 5.20 and 5.21 have been normalised to show the differences.

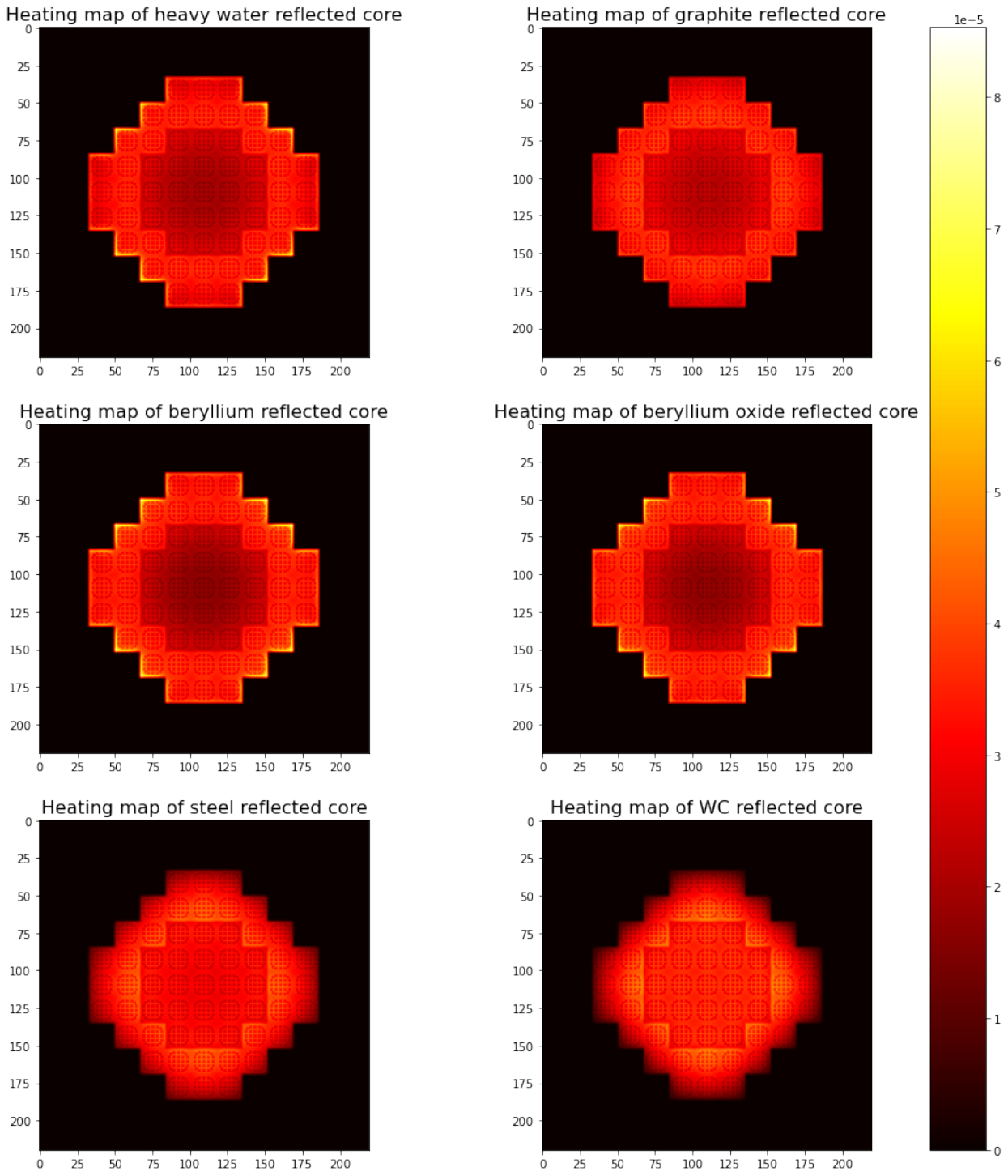


Figure 5.21: Heating maps of two-batch refuelling scheme core with particular material reflectors.

The effect from the neutron reflector is more intuitive through observing the heating maps. The plots of beryllium-based materials are obviously brighter than the rest, especially at the core edge. The existence of bright belts means the uranium utilisation rates have been improved even higher than in the middle of the core. Heavy water reflector could give a high fission rate belt to the core edge as well. However, its total improvement is not as significant as beryllium based materials.

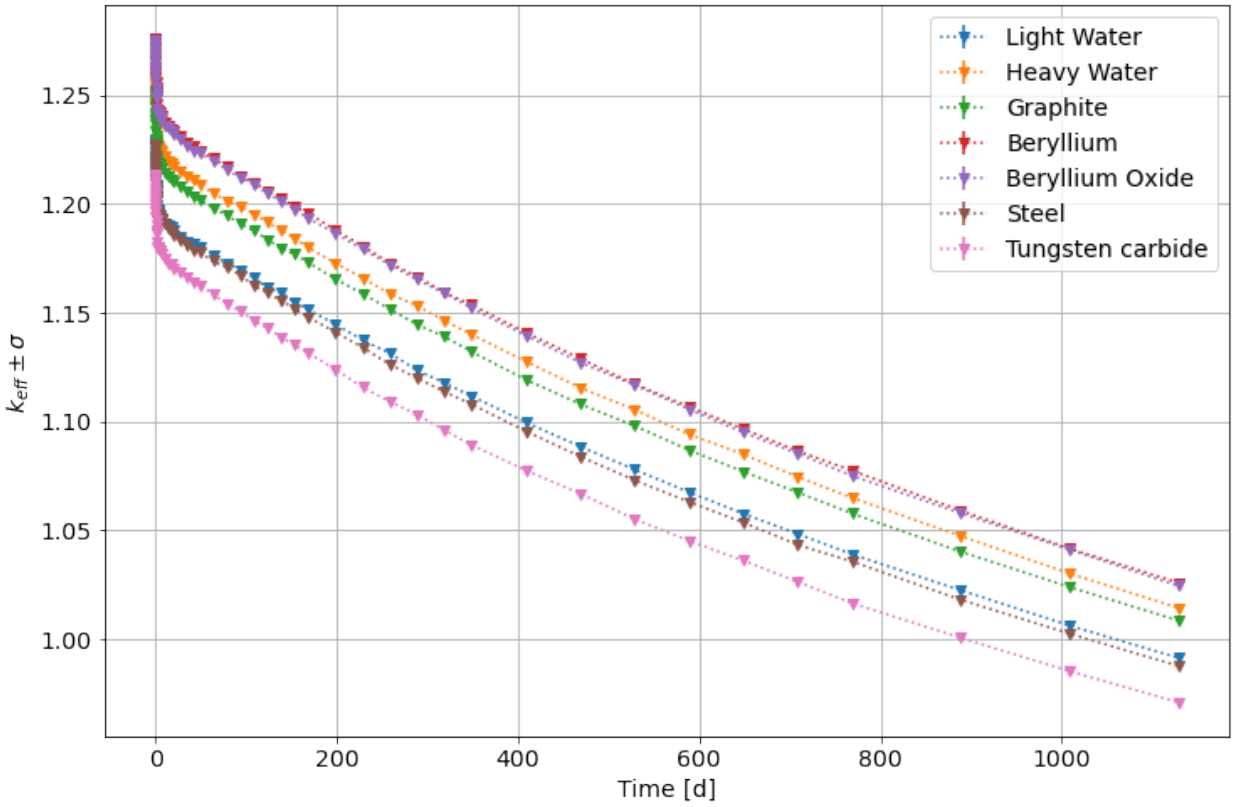


Figure 5.22: The comparison between k_{eff} variations of normal SMART with different reflector materials.

The burn-up calculations of potential available materials of reflected core also has been done. The k_{eff} value variations of each calculation have been plotted in the above figure 5.22. Compared with the originally designed water reflected core, the aforementioned four types of light materials of reflector all improved their depletion diagrams to a higher level,

which have EOC k_{eff} higher than 1. The depletion diagrams of beryllium-based materials of reflected core always stay at the top of the figure in the whole burn-up process. The more detailed results of burn-up calculations are given in the below table.

Table 5.10: The k_{eff} values at the beginning and end of the cycle in each of the depletion calculations.

Reflector materials	Combined k_{eff} (BOC) std.dev.	Combined k_{eff} (EOC) std.dev.	depleted reactivity (pcm) $\rho_{BOC} - \rho_{EOC}$
Light water	1.22957	0.99136	19542.97
	32×10^{-5}	34×10^{-5}	
Heavy water	1.25926	1.01431	19176.8
	34×10^{-5}	34×10^{-5}	
Graphite	1.25190	1.00848	19279.99
	33×10^{-5}	30×10^{-5}	
Beryllium	1.27581	1.02580	19092.6
	33×10^{-5}	34×10^{-5}	
Beryllium	1.27526	1.02438	19204.17
Oxide	34×10^{-5}	32×10^{-5}	
Steel	1.22751	0.98760	19790.04
	37×10^{-5}	29×10^{-5}	
Tungsten	1.21310	0.97092	20558.35
carbide	36×10^{-5}	29×10^{-5}	

According to the above analysis, even though the depleted reactivity in one refuelling cycle time of beryllium-based material for reflected core is not the biggest. However, the appearance of these material reflectors truly can bring maximum improvement to the depletion

diagram. Therefore, the beryllium based materials could be determined as an ideal type of material for SMART neutron reflector to optimise the power output and distribution.

The BeO and Be metal could bring a similar improvement to the SMART core from the neutron physics point of view. However, the oxide of beryllium has better material properties than it's pure metal, such as the higher melting point. Therefore, the BeO reflected core model will be applied in the following studies.

5.4.1 Beryllium oxide reflector saving

This section would give some detailed study results of BeO material reflected SMART core. Making the comparison with the original light water reflector core or so called non-reflector core. The following table 5.11 gives comprehensive burn-up results of each radial burn-up zone.

Table 5.11: ^{235}U changes in SMART with BeO neutron reflector, and the differences with table 5.3.

Radial burn-up zone	End of cycle ($\times 10^{26}$)	Burned ^{235}U ($\times 10^{26}$)	Difference ($\times 10^{24}$)	Depletion rate	Differ rate
Zone 1	3.2311	3.0611	40.0542	48.64%	6.36%
Zone 2	3.4770	2.8152	2.8707	44.74%	0.45%
Zone 3	1.6224	1.5237	−12.2978	48.43%	−3.90%
Zone 4	1.3075	1.2488	−18.1676	48.85%	−7.10%

With the additions from the BeO reflector, there are about 8.6489×10^{26} ^{235}U atoms have been burned in total 12 Burn-up zones, 1.2459×10^{25} more than the non-reflected SMART. This improvement mainly comes from radial zone 1, which is at the core edge.

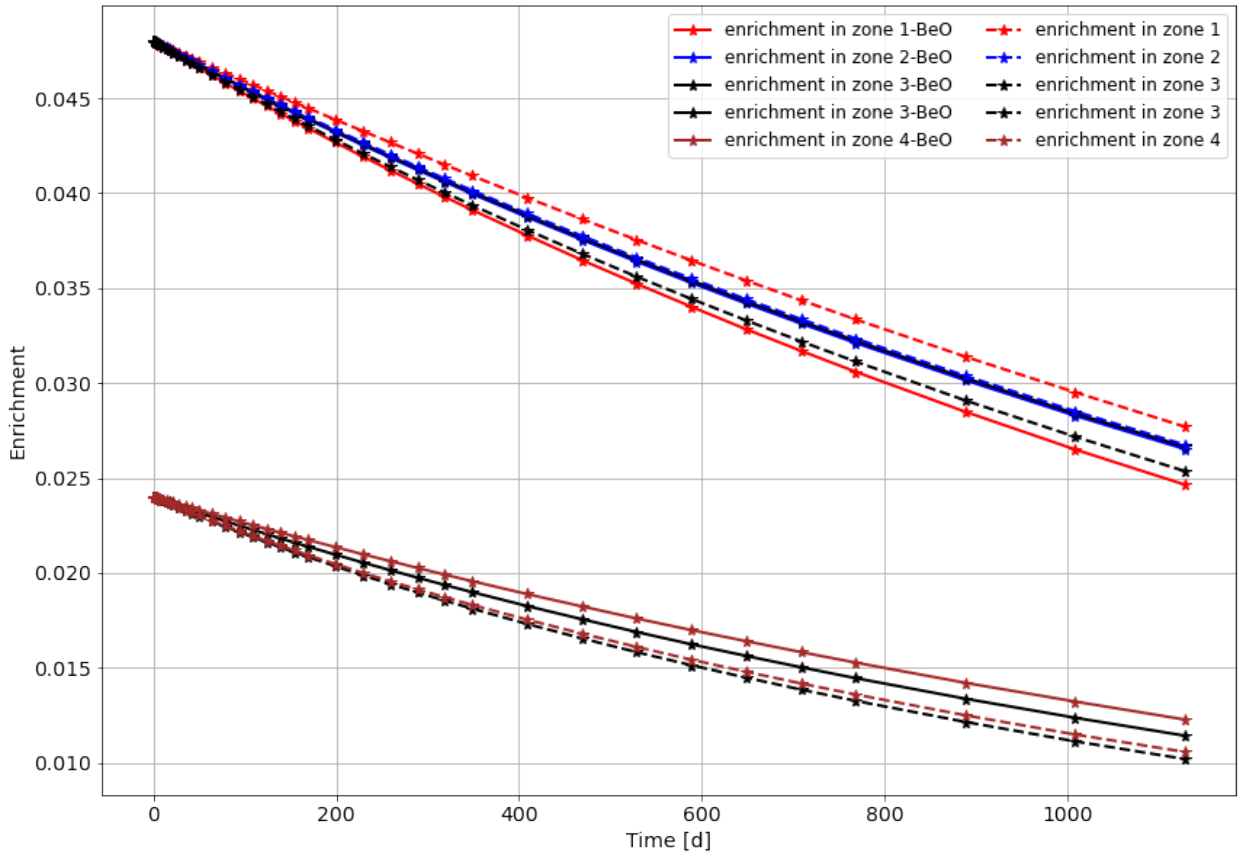


Figure 5.23: The *BeO* neutron reflector effect to the enrichment variations.

Meanwhile, a negative effect has been given to the centre reloading FAs, and their depletion rates have decreased. That may introduce the depletion depths that are starting to normalise in the whole range. The enrichment variations of the *BeO* reflected core also has been plotted.

The dotted lines in figure 5.23 reappear the data in figure 5.10, and the solid lines are results from the burn-up simulation of the *BeO* reflected SMART core. When a *BeO* neutron reflector exists and surrounds the FAs lattice, only the burn-up depth at the edge of the core, radial zone 1, will increase significantly. The enrichment in radial burn-up zone 2 only has a limited response to the *BeO* reflector. As for the reloaded FAs in the centre area, the depletion peaking scenario has been relieved. The final enrichments for radial zone

3 and 4 are 1.14% and 1.23%, respectively. These FAs are heading to the fuel storage pool and would be reprocessed once their decay heat is eliminated.

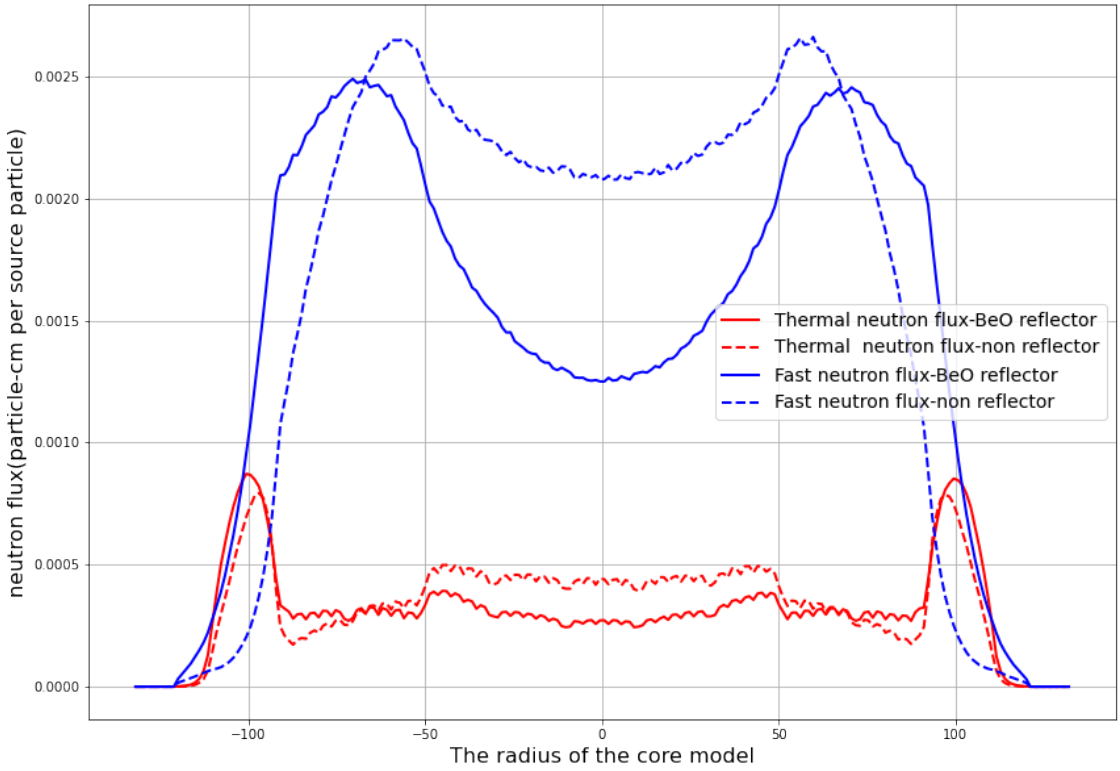
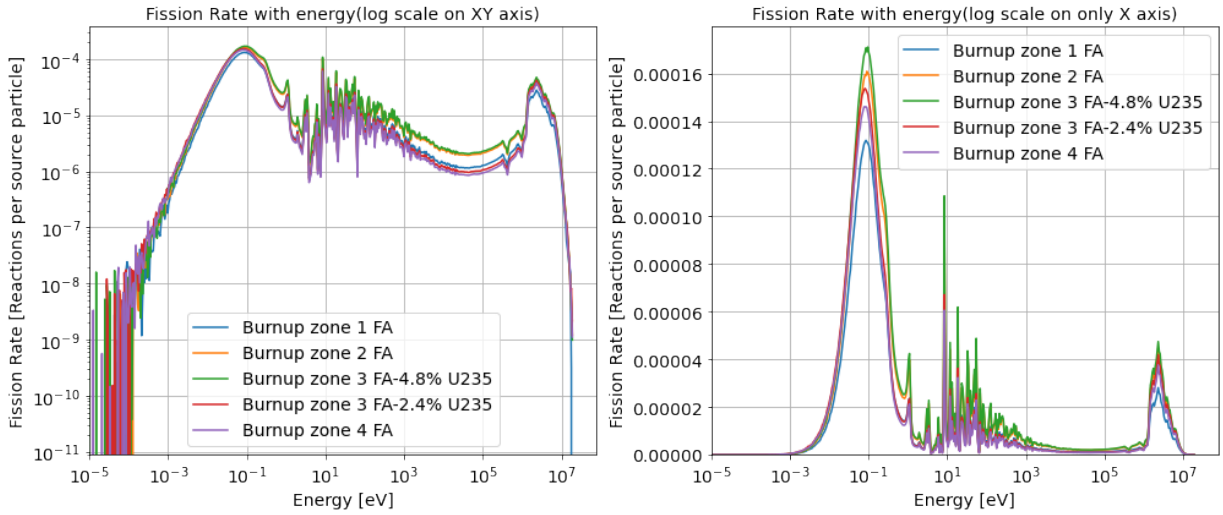
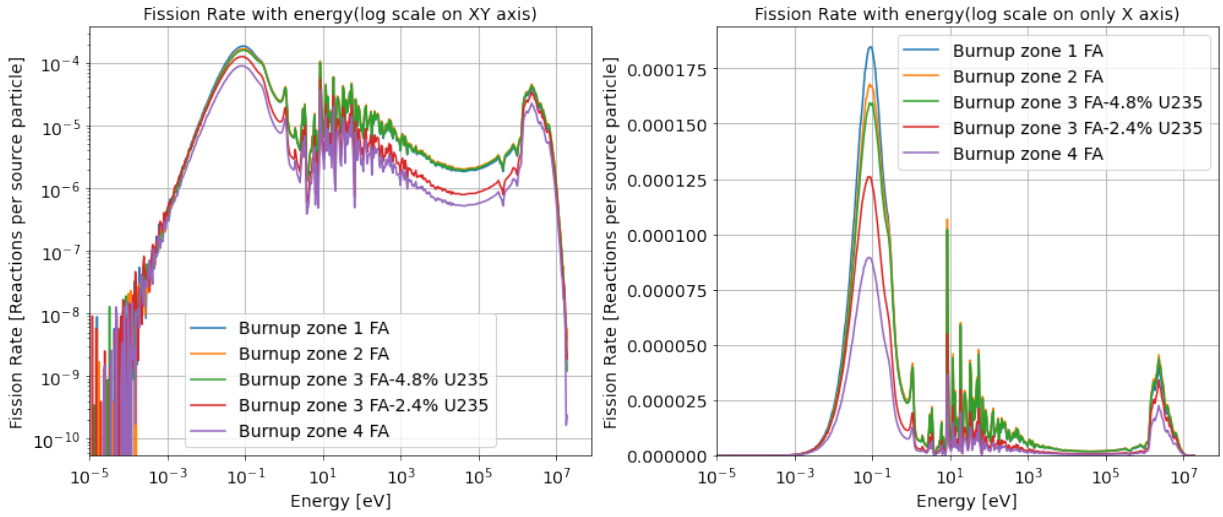


Figure 5.24: Thermal and fast neutron flux distributions within BeO reflected and non-reflected core.

Similar to the above figure 5.3, the thermal and fast energy neutron flux distribution of reflected core in the radial direction has been plotted in figure 5.24. This could explain the reason for enrichment level change at the end of depletion. The thermal neutron flux level in the centre reload FAs decreases, oppositely, to that increase at the edge area. The thermal neutron distribution is flattened due to the combined functions of reloading FAs and *BeO* reflector. The distribution peaks of fast neutrons are reduced and broadened in the fresh fuel area, exporting more energy to the coolant.



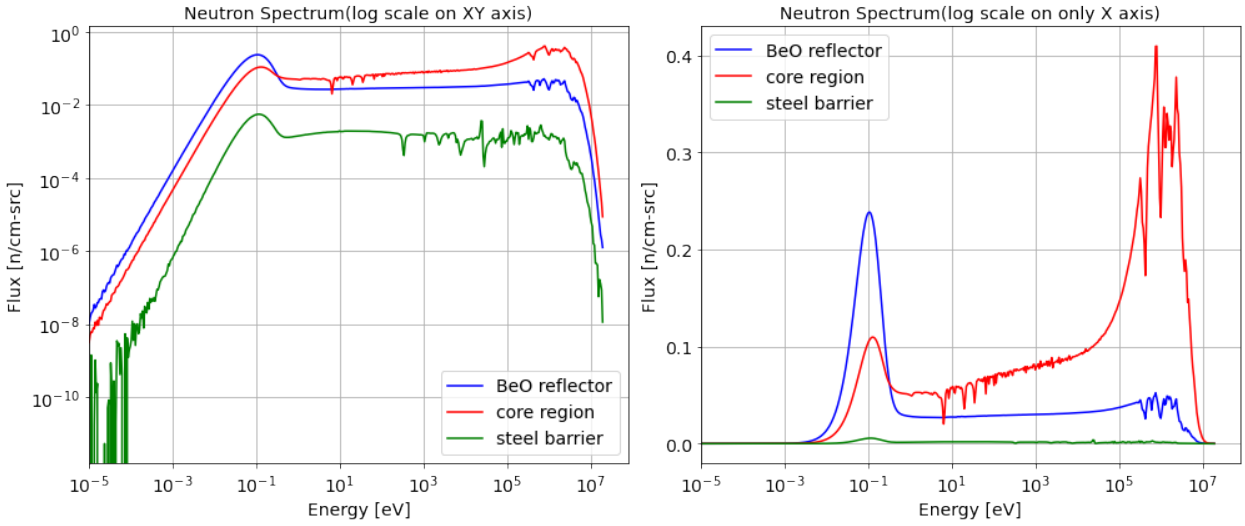
(a) Light water reflector core



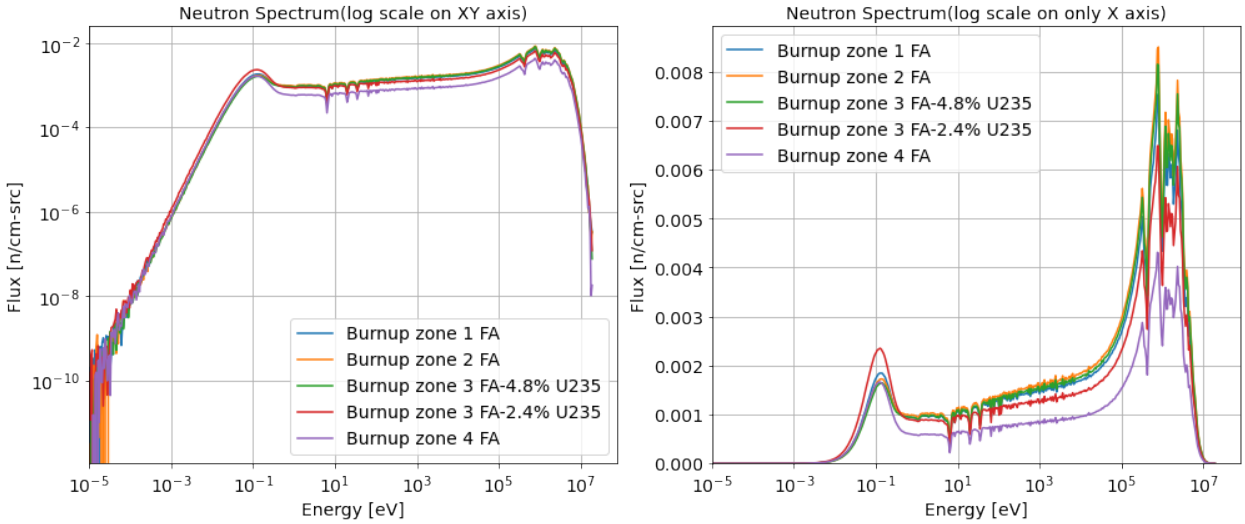
(b) Beryllium oxide reflector core

Figure 5.25: The fission rate versus neutron energy in different burn-up zone fuel assemblies.

The fission rate distributions versus neutron energy in different burn-up zone FAs are plotted in figure 5.25. The highest fission rate reaches above 1.75×10^{-4} reactions per source particle in burn-up zone 1, which used to be the lowest fission rate zone in the light water reflected reactor core. For the low enrichment fuel assemblies, the relatively low fission rate at the initial state could extend up to the usage time of reloading assemblies. Thus the reactor core achieves a longer refuelling period.



(a) The energy spectrum of different cells



(b) The energy spectrum of different burn-up zone fuel assemblies

Figure 5.26: The energy spectrum diagrams of the beryllium oxide reflected core.

Figure 5.26 contains similar plots as the above figure 5.5 and 5.6. The neutron flux energy spectrum diagrams have been recorded from simulations. In the subplot(a), when the general numerical flux results are expanded into the energy space, it is clear to see that the effect from BeO neutron reflector to the flux distribution is mostly concentrated within the reflector itself. The whole spectrum is improved to a higher level. The peak value of thermal neutron flux is above $0.2n/cm - src$ in the BeO reflector. Due to the reflection effect, the neutron flux in the steel barrier also has slightly increased. However, the energy spectrum diagrams of the reactor core do not have significant change.

In the subplot(b), when the BeO neutron reflector appeared in the model, the neutron energy spectrum of burn-up zone 1 has been improved from the lowest one to the second-highest level. Meanwhile, the whole energy range neutron flux decreases in the reloading FAs region, which are burn-up zone 4 and part of burn-up zone 3. The fluctuation in the radial distribution of neutron flux is why the core energy spectrum only has a limited effect from the BeO reflector.

Moreover, the above results are collected from either the pure neutron transport or burn-up calculation. In addition to that, coupling these two aspects of calculations should be capable of giving the evolution of reactor core performance over time with the burn-up function. In these calculations, the number of neutron histories per generation at each burn-up step has been increased to a million to keep the results' accuracy uniform with the above neutron transport calculations. Meanwhile, in order to eliminate the expensive computing time caused by the larger number of neutron histories the original 58 steps are merged into the new 5 steps, and the total length still is 1129 days. The following table 5.12 presents the k_{eff} values from the two burn-up calculations, and the results are tallied from the same time points. The standard deviations of eigenvalues are shrunk when the number of neutron histories goes up. The differences of k_{eff} values are small, which means the longer step length does not significantly affect the estimation of k_{eff} in the OpenMC depletion.

Table 5.12: k_{eff} results of original and updated large neutron history depletion.

Time	Original k_{eff}	std.dev	updated k_{eff}	std.dev	k_{eff} Differences(pcm)
Beginning	1.27448	8×10^{-5}	1.27410	24×10^{-5}	-38
12 hours	1.25893	7×10^{-5}	1.25934	24×10^{-5}	44
48.5 days	1.22320	7×10^{-5}	1.22335	24×10^{-5}	15
Ending	1.02503	8×10^{-5}	1.02487	24×10^{-5}	-16

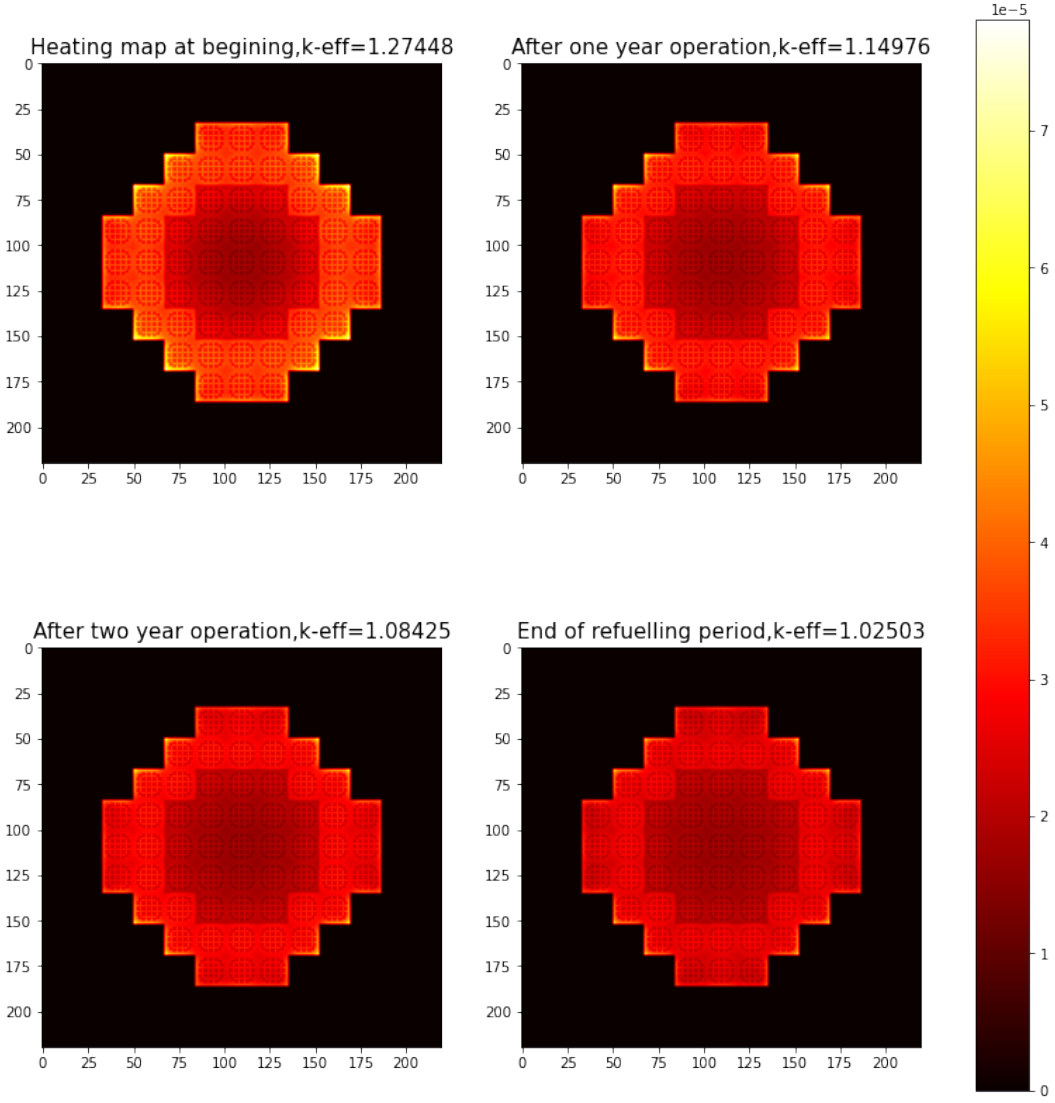


Figure 5.27: Heating map throughout the fuelling cycle of the *BeO*-reflected reactor core.

The above figure 5.27 gives the heating maps of the BeO-reflected core at different time points. The corresponding k_{eff} values also have been given in the title of each subplot. As the core depletion goes deeper, the fission rates decrease over the full core range. Once the fission product equilibrium is built up, the k_{eff} value would drop down about 0.06 in one year full-power operation time. The high fission rate belt at the core edge is produced by the improvement from the BeO reflector, which is always functional in the whole refuelling cycle period. Even though the core has been depleted for more than three years, one still can see the relatively hotter points at its edge.

The following figure 5.28 compares the different time points' fission rate maps of the original light water-reflected and the optimised BeO-reflected core. Their k_{eff} values and heating maps of operation starting points already been compared in the above sections. This figure focuses on the heating map variations during the depletion process, and the scale of figure 5.28 has been normalised with figure 5.27 to conveniently observe the fission rate variation. One can see the dark area along the boundary of the light water surrounded core in all three-time points heating maps, where all have become bright due to the appearance of BeO material reflector. The improvement of the BeO neutron reflector on the power flattening affects the reactor start-up point and constantly works throughout the whole refuelling cycle.

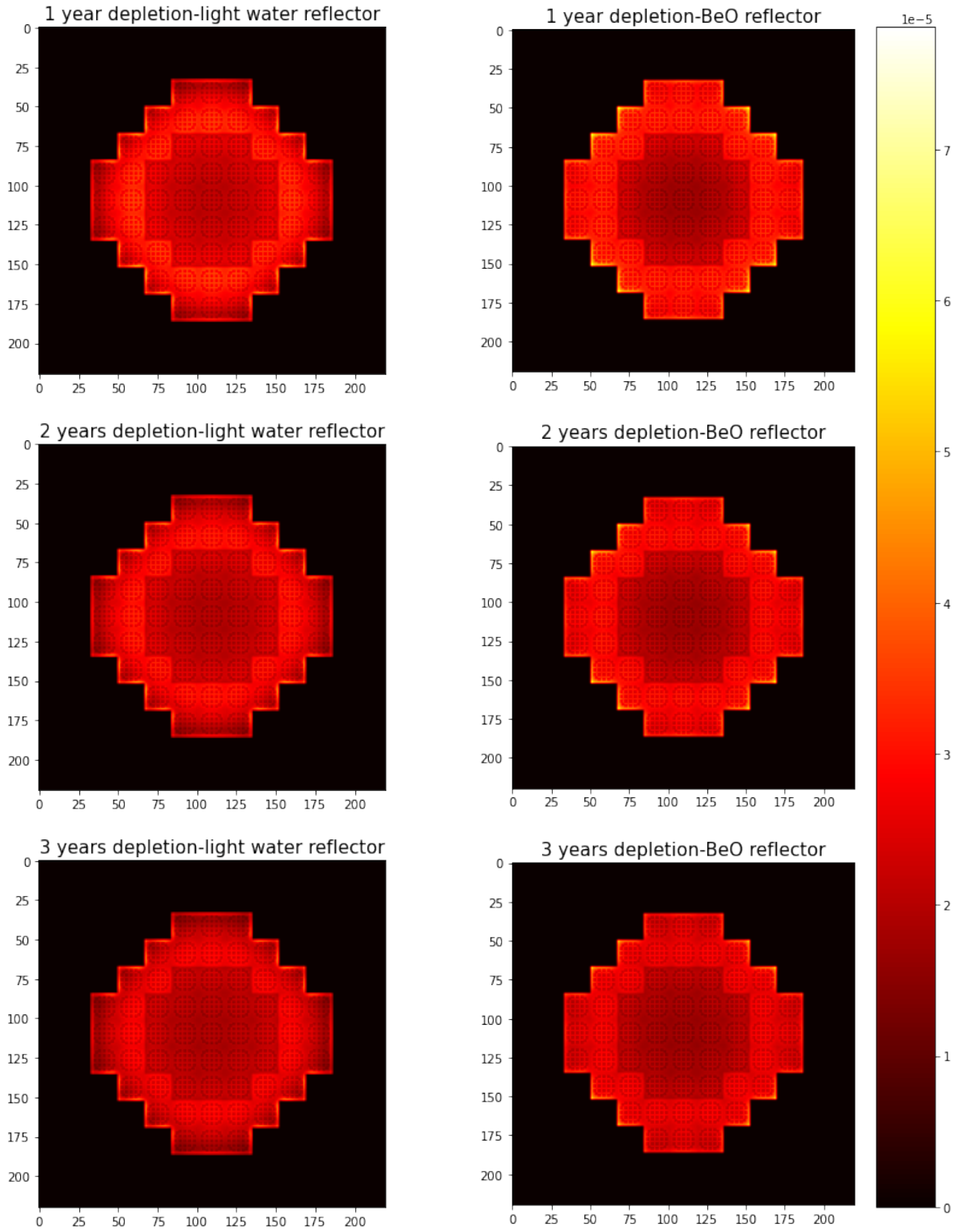


Figure 5.28: The heating maps of the light water-reflected core and the *BeO* reflected core at different time points.

5.5 Variant core layouts

The above results prove the BeO material is helpful to uranium economics, and SMART may provide higher value power output because of that. Moreover, one is also concerned about the two-batch refuelling scheme itself. After one refuelling cycle, an original SMART core will produce 21 dry FAs and 36 half depleted FAs. 21 of them can be reused with 36 fresh FAs for the next burn-up cycle. However, if the other SMART unit in this plant finishes the installation process and gets ready for operation in these three years then the first core could not provide enough half-depleted FAs to itself and the second SMART unit simultaneously, with 6 FAs in shortage in this circumstance. Therefore, with the proven addition from the BeO neutron reflector, a few types of variant SMART core layouts were proposed and tested. Based on the study results, it could be possible to stagger building a GW scale multi-SMART reactors nuclear power plant.

Three types of variant core layout were proposed in this study and are given in the below figure 5.29. Although these are called variant cores, the basic characteristics such as material selections and core geometry parameters remain the same as the above normal two batch refuelling scheme layout. The proposed evaluations concern the amount and positions of high enrichment FAs in the core. The BeO material neutron reflector's size is also constant, and that was placed at the same position in the OpenMC models.

The normalised heating maps of all three variant core layouts are also given in figure 5.29. Variant (a) could be called homogeneous core because it assumes all 56 FAs have the same 4.8% enrichment level. Variant (b) is a slightly updated version of two batch refuelling scheme core, the number of reloading FA reduce to 13, which means there are 8 extra 4.8% enriched FAs in the core in its initial state. There are three enrichment levels inside variant (c), except 13 reloading FAs in the centre, which also has 16 2.4% enrichment FAs at the core corner. Between two low enrichment zones, a fresh fuel belt has 28 FAs placed in, with

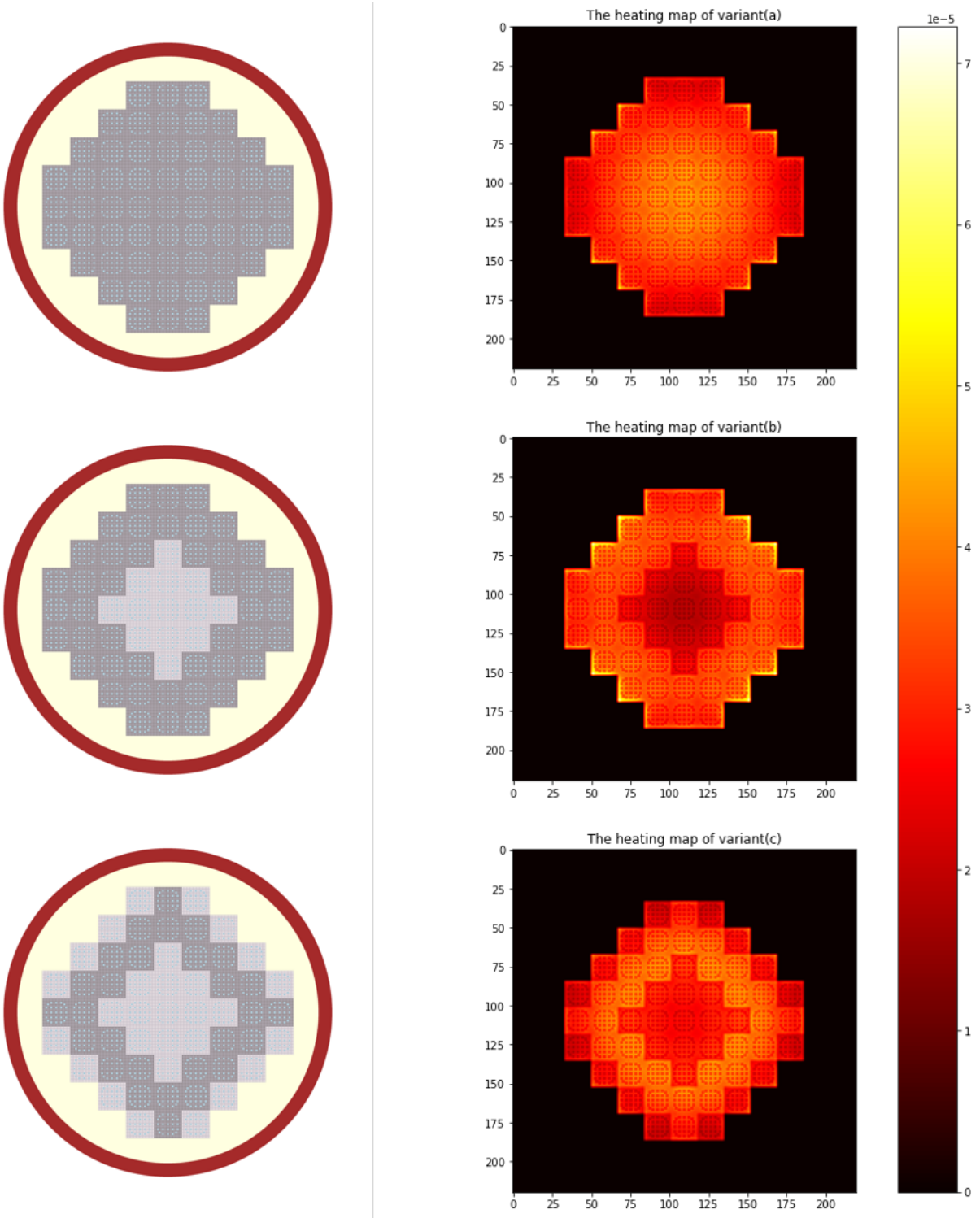


Figure 5.29: The geometry structures of variant core layouts and their normalised heating maps.

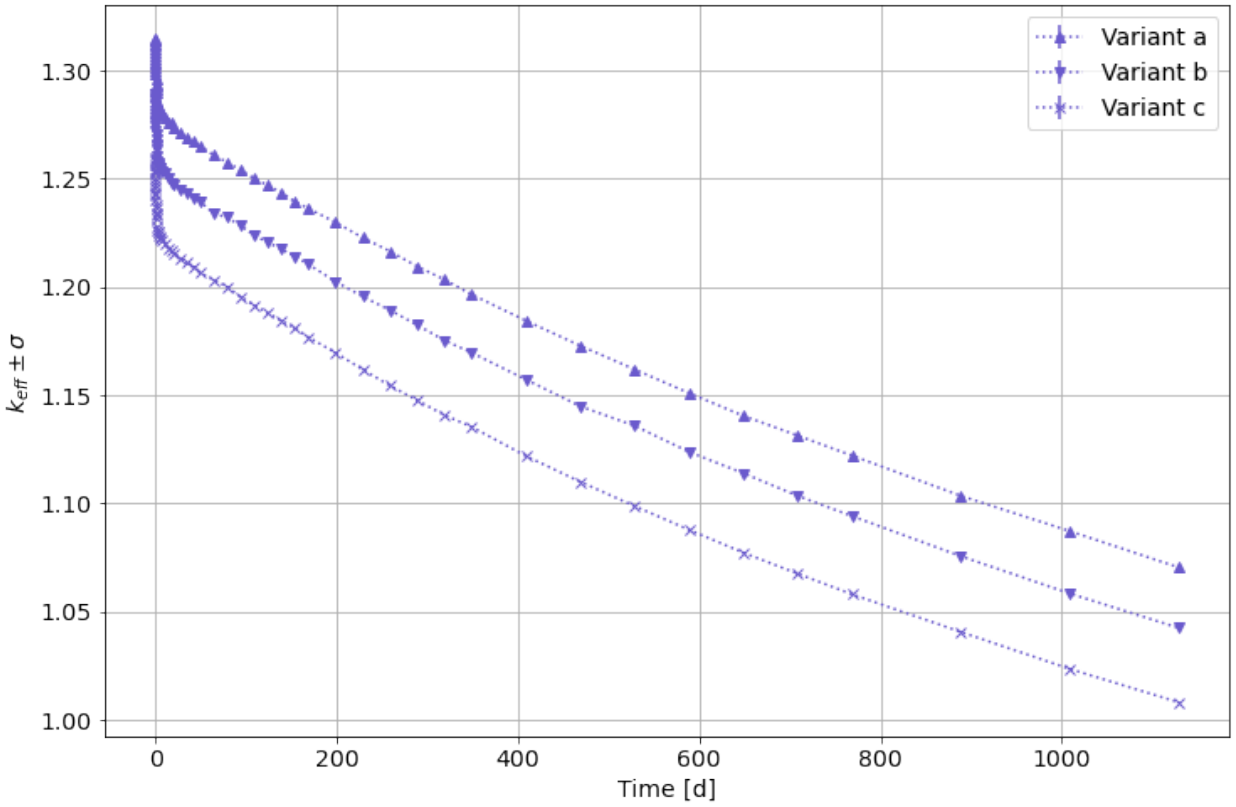


Figure 5.30: The burn-up calculation results of variant core layouts.

4.8% enrichment. The k_{eff} variations in the burn-up calculations of the three variants are summarised in the below figure.

In figure 5.30, with the BeO material neutron reflector, the EOC's k_{eff} values are all greater than one. For variant (a) to (c), the ending k_{eff} values are $1.0703 \pm 3.69 \times 10^{-4}$, $1.0424 \pm 3.47 \times 10^{-4}$, and $1.008 \pm 3.27 \times 10^{-4}$. Especially for variant (c), where there are 8 fewer high enrichment FAs than the original design, it still can support the reactor operation longer than 3 years. The excess reactivity values are $239230pcm$, $224207pcm$ and $205841pcm$. In order to estimate the amount of energy released during the refuelling cycle, the depletion amount of ^{235}U in each variant is also calculated. The results are shown in the following table 5.13. The total ^{235}U number is the summation of the total of 12 burn-up zones within each model.

Table 5.13: The total number of ^{235}U atom in the BeO reflected and three variants SMART core.

Core layouts	BOC $\times 10^{27}$	EOC $\times 10^{27}$	Burned ^{235}U $\times 10^{27}$	Depletion rate
BeO SMART	1.8287	0.9638	0.8649	47.29%
Variant(a)	2.2416	1.3107	0.9309	41.52%
Variant(b)	1.986	1.0941	0.89185	44.90%
Variant(c)	1.6714	0.847	0.8244	49.32%

In table 5.13, the variant (a) and (b) burned more ^{235}U nuclei in the core, about 0.066×10^{27} and 0.027×10^{27} times more than the BeO reflected SMART. That is reasonable because these two variants have a greater amount of high-level enrichment FAs loaded in. However, their depletion rates are not satisfied. For one refuelling cycle, variant (a)'s depletion rate has a 5.77% decrease, for variant (b) the depletion rate decrease is 2.39%. Conversely, variant (c) more effectively utilises the relatively small amount of ^{235}U in the whole core. The depletion rate could arrive at 49.32%, even higher than the BeO reflected core. To better arrange the fuel shifting schemes, each radial burn-up zones' enrichment value's variations are given in the next table.

Similar to the above results for the variant cores, the BeO neutron reflector still mostly functions on the edge area, which is the radial zone 1 in a 4×3 burn-up zones model. For variant (a), the edge enrichment could be depleted to 2.82%. The final enrichment of the rest zone $2-4$ gradually reduces from the outside zone to the centre area. For variant (b), the enrichment values of zone 2 and 3 after depletion are relatively high and uniform, which are around 2.73%. The 2.4% enrichment FAs in variant (c) are burned to a very low level, only remaining at 1.07% enrichment. The 4.8% enrichment FAs have the biggest

Table 5.14: Enrichment's variations in each radial BU zone of three variant core layouts.

Core layouts	Variant(a)		Variant(b)		Variant(c)	
	BOC	EOC	BOC	EOC	BOC	EOC
Zone 1	4.8%	2.82%	4.8%	2.581%	2.4%	1.071%
Zone 2	4.8%	2.903%	4.8%	2.728%	4.8%	2.641%
Zone 3	4.8%	2.787%	4.8%	2.731%	4.8%	2.527%
Zone 4	4.8%	2.689%	2.4%	1.216%	2.4%	1.055%

consumption in all three variant layouts, down to 2.641% and 2.527%.

Generally, the fresh FAs in all three variants remain more than 2.4% enrichment, which means that it is acceptable to be used in the next refuelling cycle as well. The reloading FAs are exhausted after more than 1100 days of full-power depletion, whether they are placed in the central area or in the area where contact with the reflector exists. The fission rate distributions have been presented in figure 5.29. The change of FA layouts may affect the power flattening. Some other effective reactivity control methods can be considered to flatten the power distribution peak, such as control rods insertion or assembling the integral burnable poison rods with the fuel rods.

5.6 Fuel shifting for the staggered build approach

The different core layouts could be combined and staggered to build a gigawatt scale SMART reactor power station based on multiple reactors with the above results. The layouts could be the original 21 reloading FAs core or three variant cores. The FAs could be withdrawn from an earlier build core and then be reused in the other core. The layout of a particular core is switchable in different refuelling cycles. A fuel self-sustaining and economic strategy

is expected for the whole development process, which means the produced half-depleted FAs in one cycle could satisfy the demand occurring from the next cycle, and the required fresh fuel should be optimised to as little as possible. Assuming the ultimate target is to build a power plant with $1100MWe$ capacity, which needs 10 SMART units then two construction paths are designed to achieve this target, and could satisfy the above requirement. Table 5.15 gives the number of fresh and reloading FAs in the above mentioned four core layouts.

Table 5.15: The number of fresh and reloading FAs in the different core layouts.

	Fresh FAs	Reloading FAs
Original two batch core	36	21
Variant(a)	57	
Variant(b)	44	13
Variant(c)	28	29

The first possible path is to couple the variant (a) and the original two batch refuelling core with 21 reloading FAs. The first core could adopt the variant layout (a), providing 57 half depleted FAs after one refuelling cycle. If the second SMART unit is ready to work in this period, these 57 FAs could be used in the reloading fuel area for both cores. The second refuelling only requires 72 fresh FAs to support the second operation period with two reactor units. The extension and fuel re-usage would continue with other units to achieve the planned total capacity.

The below table 5.16 demonstrates this hypothetical path. A total of 10 SMART units are installed in 6 refuelling cycles. After cycle 2, this is assuming that every period could receive two more reactor units into the plant. In this way, a refuelling cycle could supply enough half-depleted FAs for the next cycle. The only special point is in cycle 3, 4 original two batch refuelling scheme cores require 84 reloading FAs. The remaining 15 FAs

from cycle 1 can be in addition to the cycle 2's 72 depleted FAs and provide towards cycle 3 together.

Table 5.16: Two hypothetical paths to staggered build of a 1100 MWe, 10 SMART units nuclear power plant.

Path A	Reactor number	Fresh FAs	Reused FAs
Cycle 1	1(1× variant a)	57	0
Cycle 2	2(2× Original core)	72	42
Cycle 3	4(4× Original core)	144	84(72 + 15)
Cycle 4	6(6× Original core)	216	126
Cycle 5	8(8× Original core)	288	168
Cycle 6	10(10× Original core)	360	210
Path B			
Cycle 1	1(1× variant b)	44	13
Cycle 2	2(b+c)	72	42
Cycle 3	4($3 \times b$ +c)	160	68
Cycle 4	6($2 \times b + 4 \times c$)	200	142
Cycle 5	8($2 \times b + 6 \times c$)	256	200
Cycle 6	10($2 \times b + 8 \times c$)	312	258

Path A's advantages are adopting the originally designed FAs layout after the first core cycle, which does not require extra effort to redesign the fuel management procedures and reactivity control movements. However, variant (a) in the first cycle has significant excess reactivity that may affect operational safety. The extending process demands a relatively large number of fresh FAs, making it difficult to maximise the efficiency of fuel utilisation and raises the requirements for the fuel supplier. Therefore, the designed Path B that combines

and switches between variant (b) and c(c) aims to achieve the target installed capacity whilst having a better uranium economy.

The first core in Path B applies the variant (b) core layout, the produced 44 half-depleted FAs supply to the second cycle that has the variant layout (b) and (c). One reactor core would be rearranged from (b) to (c) in the third refuelling cycle for containing more reloading FAs. After cycle 4, the newly installed couple of cores would adopt the variant (c) layout. Therefore, the demand for fresh FAs is reduced in the later cycles. Cycle 6 with core layouts with two variant (b) and 8 variant (c) requires 258 reloading FAs but has 2 FAs in shortage from the last cycle. The remaining FAs from the earlier cycles could make up for this missing amount.

Whether it be via path A or path B, this just provides a potential idea for staggered build of a giga-watt scale SMART nuclear power plant. With the BeO neutron reflector's addition, the FAs layout in the cores could be flexible and variable but do not significantly affect the core power output and operation time. In the actual construction, the process does not necessarily have to be limited to Path A or B. Even though the plant owner aims to double the reactor numbers in one cycle, one still can find a suitable method to achieve the goal by changing the core layout selection whilst also ensuring the reactor's safe operation.

5.7 Chapter summary

This chapter presents and discusses the major findings of this study project. In the beginning, the verified and tested OpenMC 4×3 burn-up zones SMART reactor core model has been modified to be the originally designed two batch refuelling scheme FA layout core. After the neutron transport analysis and the follow-up depletion calculation, the results show that uranium-235 utilisation at the originally designed core edge area is unsatisfactory. If

an attempt is made to increase the number of full-power operation days by about 200 days, the central area reloading FAs would become overly depleted. The reason for these circumstances is the uneven neutron flux distribution in the reactor core. The neutron flux spatial distribution and energy spectrum also have been studied in this chapter.

Adding a neutron reflector between the core fission zone and steel barrier would be ideal for optimising the SMART power performance. A total of 7 kinds of materials have been selected as potential reflector materials. Except for the usual light atomic mass materials, they also include heavy metal materials, steel and tungsten carbide. The analysis and selection were carried out from nuclear cross-section data and the actual simulation aspects. Beryllium based materials BeO and Be metal have been seen to provide the most significant improvement to the fission rate of the core edge area. The BeO material was chosen for further studies due to its better thermal properties.

As a bonus from BeO reflector saving, three different variant core layouts, which have differing requirements on fresh and reloading FAs amounts are also available to supply similar power performance to the original layout. Based on the calculated neutronic parameters of these core layouts, two hypothetical paths are designed to staggered build a 1100 MWe, 10 SMART units nuclear power plant. Both of them have the characteristics of reloading fuel being self-sustaining and also a low fresh fuel requirement in every refuelling period.

Chapter Six

Conclusion

With the growing energy demand worldwide, SMR technologies are receiving more and more attention and interest. Many aspects of SMRs' technological characteristics, and feasibility of their applications, should be further assessed. In this thesis, the world's first licensed integral small PWR SMART is selected as a reference reactor to perform a series of neutronic investigations. The SMART technology is originally developed by South Korea Institute KAERI. Our partial industrial collaborator, Birmingham local power company GF nuclear is working with KAERI and trying to bring SMART into the UK energy market. Moreover, the experts from GF nuclear have suggested the power output of SMART should ideally have a $20\% - 30\%$ improvement in order to satisfy the demand from the market. Therefore, this thesis mainly focuses on the power performance and optimisation of SMART.

The studies in this thesis were carried out by Monte Carlo method codes, including the industry level code MONK and open-source scientific community developed code OpenMC. The numerical models of the SMART core have been built in both codes respectively. The models have been validated and verified, especially for the OpenMC model, using two versions of the ENDF data library and one of JEFF.

Thus a total of three different nuclear data libraries were used to perform the sensitivity study. And a 4×3 burn-up zone division model also has been built for acquiring accurate depletion calculation results. The eigenvalue k_{eff} calculation results have been compared with the widely used benchmark code MCNP, which shows good agreement.

Employing the OpenMC SMART core model, The first study focuses on the originally designed two batch refuelling scheme core layout. From the results it turns out that the original design can have a longer refuelling cycle and higher power output because part of the FAs at the edge area has not been effectively utilised. A neutron reflector placed surrounding the fission zone should scatter the leakage neutrons back and flatten the neutron flux distribution.

In order to determine the ideal neutron reflector material to optimise the power output four of the usual light atomic mass materials, including heavy water, graphite, beryllium metal and beryllium oxide, and two heavy metal materials, steel and tungsten carbide, are selected and analysed in this study. The effective isotopes' related neutron incident cross-sections have been cited and compared from their ENDF nuclear data libraries. And then, the above materials have been individually brought into the reflector region of the OpenMC SMART model. The neutron flux distribution, energy spectrum and induced fission rate spatial distributions have been tallied from the simulation process. By cross-comparing and analysing these results the BeO material is chosen as the most suitable reflector material and was then applied in the following studies.

The simulation results of a BeO reflected core truly have shown significant improvement. The updated k_{eff} value at the EOC is $1.0245 \pm 3.42 \times 10^{-4}$, thus still remaining higher than one. That means the core still remains in a potentially critical state. The refuelling period also could be extended, and the depletion rates for the edge zones has increased by 6.36% and 0.45%. Conversely, the depletion depths have a 3.90% and 7.70% decrease in the

central core zones. Thus, the power distribution peaks are broadened throughout the whole core range.

Considering the addition from the BeO material reflector, three variant FA layouts were designed and studied. The variant cores only change the position and number of high enrichment FAs, they do not affect the materials selection and geometry structure. The three variant layout cores all can provide a longer refuelling cycle than the original design. Their power distribution fluctuates due to the highly enriched fuels' location, but the peak size is still acceptable.

This SMART reactor study does not only focus on a single reactor unit. Based on the simulation results of the three variant layout cores, two hypothetical paths were proposed to combine a staggered build of the original and three variant layout cores until this forms a $1100MWe$ and 10 SMART units power plant. These two paths provide an idea of how to more economically build a giga-watt scale plant with SMART reactor technology.

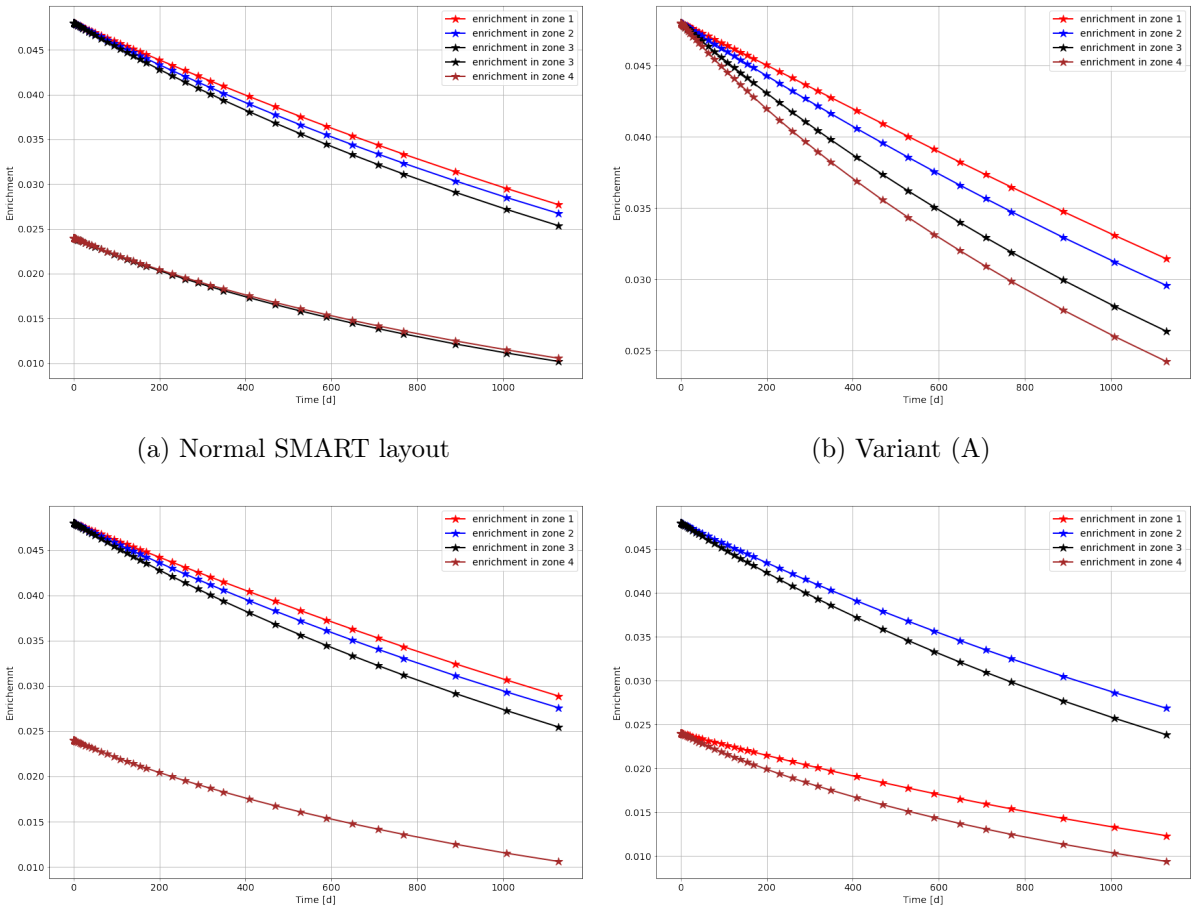
In summary, based on the full reactor core model MC simulation results, this thesis provides a greater potential incentive to build SMART. This work proposed higher power output optimisations that would make SMART more competitive in the UK nuclear power market, and even worldwide. Linked with this, they could possibly even help to create a contribution to the global decarbonisation targets. Moreover, some of the ideas and proposed schemes presented in this thesis are not limited only to SMART and could potentially affect the development of other integral PWRs, and advanced SMRs. Such as with the variant core layouts, staggered building plant plan, and optimised FAs shuffling between cores. With growing interest in such systems in the UK (and wider world) these findings may be useful at this rather pertinent time for reactors of this type and flavour. These ideas and innovations therefore may hopefully assist future ongoing research in these areas and the further evolution of small nuclear power systems.

Appendix One

Other reflector results

This appendix is aimed at providing some meaningful simulation results that have not been presented in the main body of the thesis. These results concern the combination of the aforementioned neutron reflector materials and three variant core layouts. The major findings and conclusion in the above chapters are based on the beryllium oxide reflector optimisation, which could bring the biggest reactivity increase to the originally designed SMART and variant layout cores.

In the investigation process, other reflector materials' effect has also been calculated and plotted. The following pages $173 - 181$ are the results from burn-up calculations. The rest of the pages are the normalised heating maps of the variant cores with different material reflectors.



(a) Normal SMART layout

(b) Variant (A)

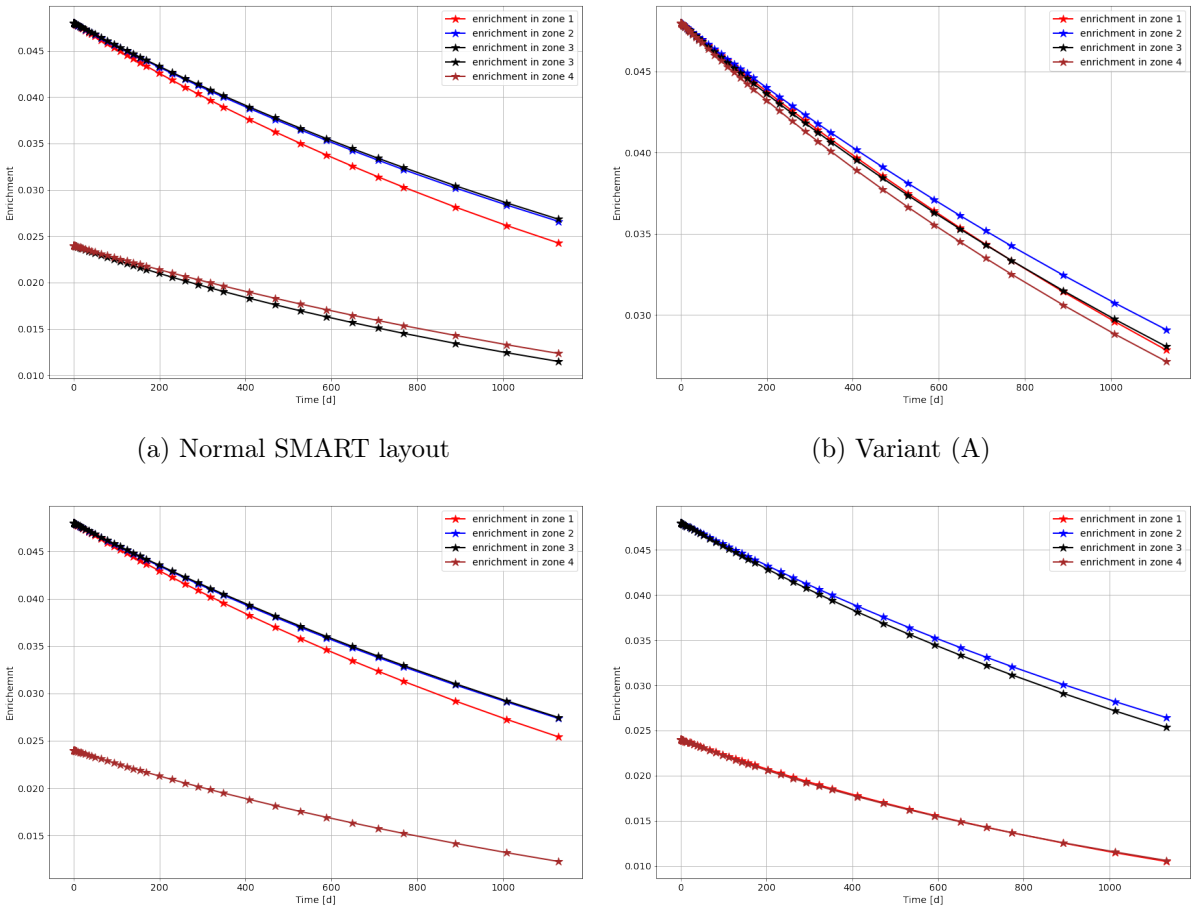
(c) Variant (B)

(d) Variant (C)

Figure A.1: The ^{235}U enrichment variations in light water-reflected core layouts.

Table A.1: The number of burned ^{235}U in light water-reflected core layouts.

Burned ^{235}U (10^{26})	Normal core	Variant(a)	Variant(b)	Variant(c)
Zone 1	2.65969496	2.16949793	2.5059419	1.53275371
Zone 2	2.78773733	2.41484897	2.67561455	2.77179064
Zone 3	1.646177719	2.12717908	2.21553159	2.37593437
Zone 4	1.43162521	2.53070971	1.42630804	1.558154274
Total	8.525235219	9.24223569	8.82339608	8.238632994



(a) Normal SMART layout

(b) Variant (A)

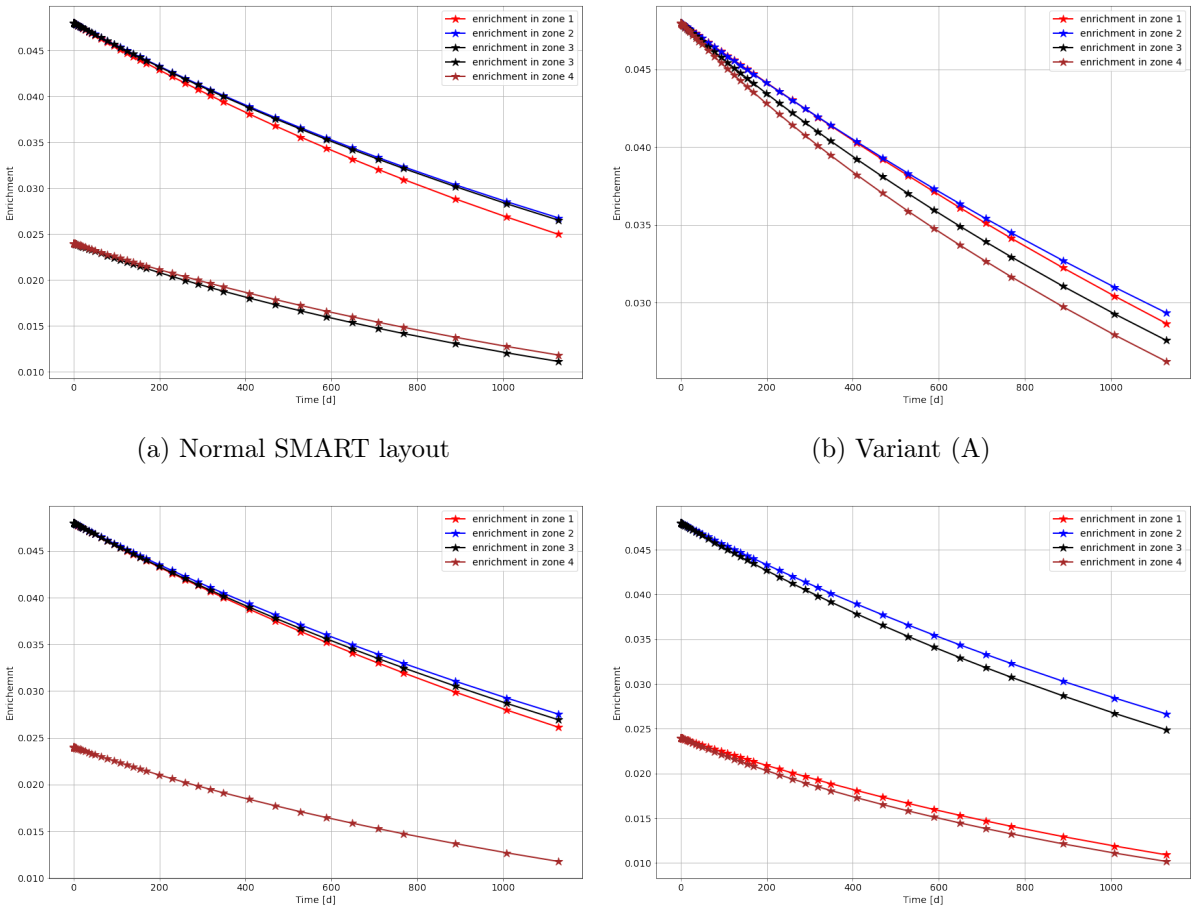
(c) Variant (B)

(d) Variant (C)

Figure A.2: The ^{235}U enrichment variations in beryllium-reflected core layouts.

Table A.2: The number of burned ^{235}U in beryllium-reflected core layouts.

Burned ^{235}U (10^{26})	Normal core	Variant(a)	Variant(b)	Variant(c)
Zone 1	3.11035392	2.64452056	2.96034351	1.77127674
Zone 2	2.80486055	2.47984169	2.70512583	2.8274199
Zone 3	1.513050431	1.96208772	2.01875097	2.22694656
Zone 4	1.23972882	2.22337429	1.25048215	1.42794665
Total	8.667993721	9.30982426	8.93470246	8.25358985



(a) Normal SMART layout

(b) Variant (A)

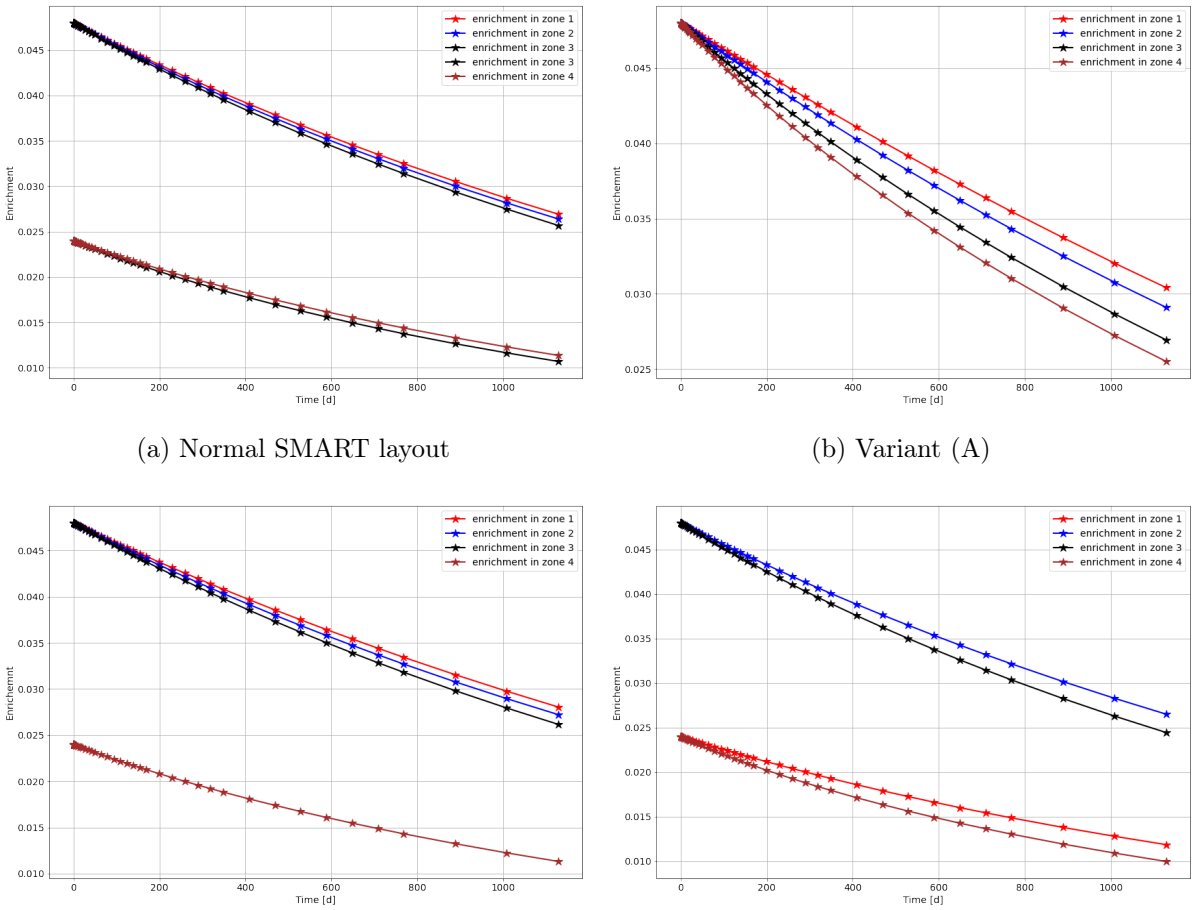
(c) Variant (B)

(d) Variant (C)

Figure A.3: The ^{235}U enrichment variations in heavy water-reflected core layouts.

Table A.3: The number of burned ^{235}U in heavy water-reflected core layouts.

Burned ^{235}U (10^{26})	Normal core	Variant(a)	Variant(b)	Variant(c)
Zone 1	3.01801958	2.5363332	2.86552261	1.71409355
Zone 2	2.78341972	2.44678737	2.68190422	2.79710926
Zone 3	1.547341246	2.00940078	2.07078329	2.27236388
Zone 4	1.29634112	2.32158466	1.30173027	1.47154526
Total	8.645121666	9.31410601	8.91994039	8.25511195



(a) Normal SMART layout

(b) Variant (A)

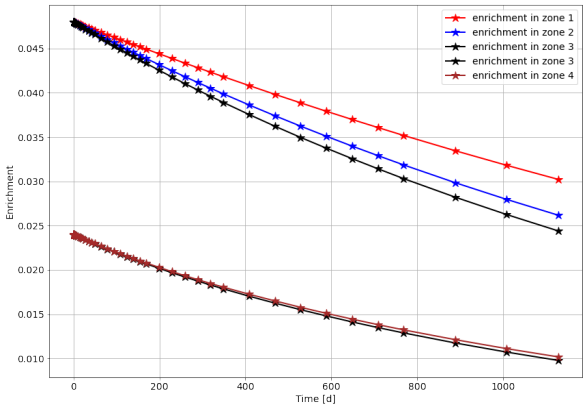
(c) Variant (B)

(d) Variant (C)

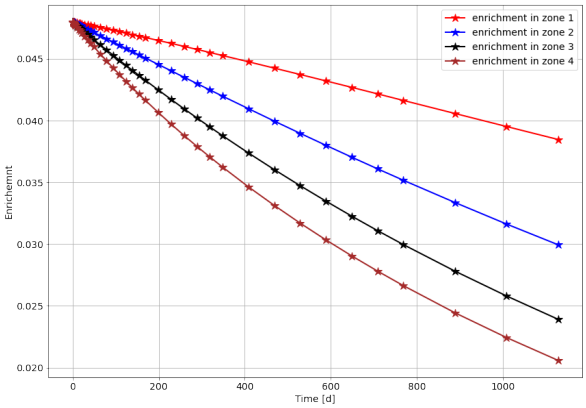
Figure A.4: The ^{235}U enrichment variations in graphite-reflected core layouts.

Table A.4: The number of burned ^{235}U in graphite-reflected core layouts.

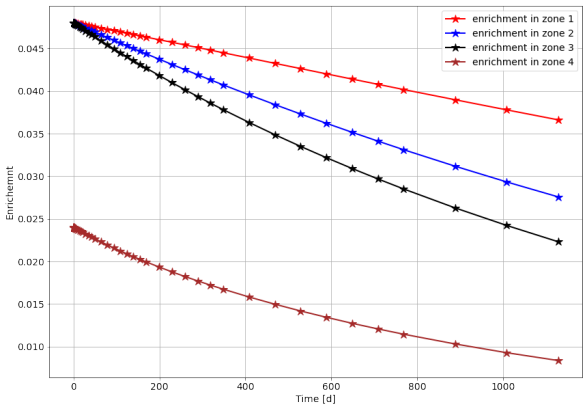
Burned ^{235}U (10^{26})	Normal core	Variant(a)	Variant(b)	Variant(c)
Zone 1	2.76238616	2.3055905	2.61455941	1.59182473
Zone 2	2.83143766	2.47744647	2.72267865	2.81715078
Zone 3	1.602786611	2.07058146	2.1457545	2.31552259
Zone 4	1.34537929	2.39516337	1.3497923	1.49423495
Total	8.541989721	9.2487818	8.83278486	8.21873305



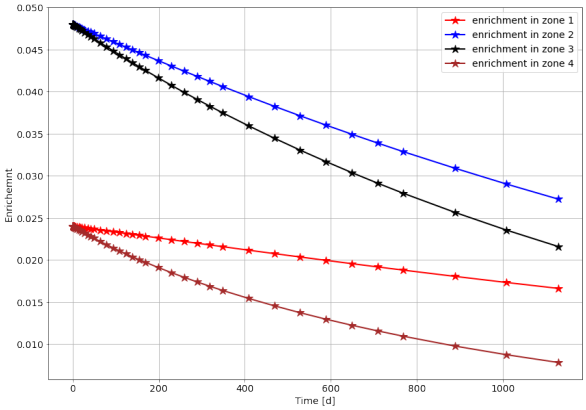
(a) Normal SMART layout



(b) Variant (A)



(c) Variant (B)

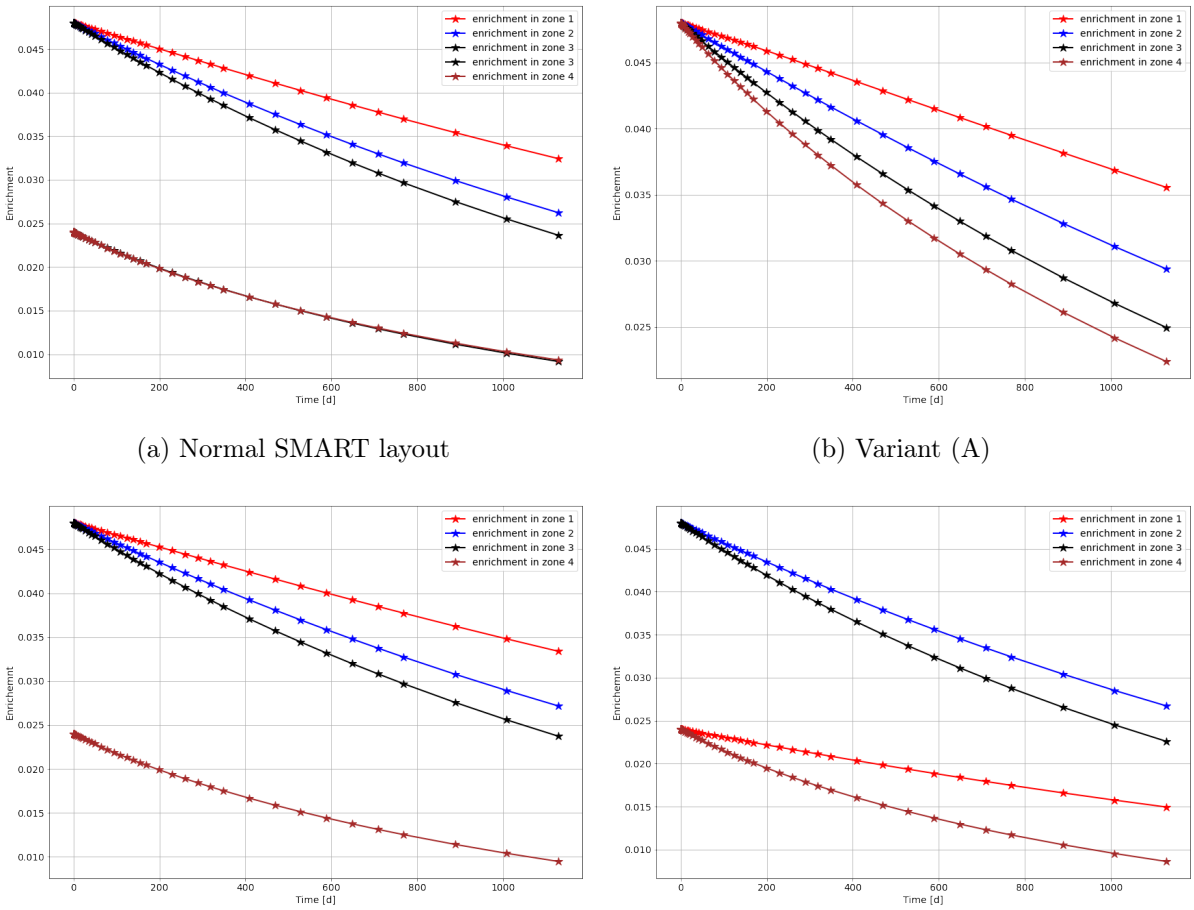


(d) Variant (C)

Figure A.5: The ^{235}U enrichment variations in steel-reflected core layouts.

Table A.5: The number of burned ^{235}U in steel-reflected core layouts.

Burned ^{235}U (10^{26})	Normal core	Variant(a)	Variant(b)	Variant(c)
Zone 1	2.33083588	1.24901673	1.49253951	0.9673993
Zone 2	2.86083761	2.36666788	2.67744275	2.72285535
Zone 3	1.705105146	2.36845147	2.52556028	2.59598413
Zone 4	1.47172757	2.92034122	1.664190888	1.723369633
Total	8.368506206	8.9044773	8.359733428	8.009608413



(a) Normal SMART layout

(b) Variant (A)

(c) Variant (B)

(d) Variant (C)

Figure A.6: The ^{235}U enrichment variations in tungsten carbide-reflected core layouts.

Table A.6: The number of burned ^{235}U in tungsten carbide-reflected core layouts.

Burned ^{235}U (10^{26})	Normal core	Variant(a)	Variant(b)	Variant(c)
Zone 1	2.04106831	1.63040593	1.91520042	1.1861708
Zone 2	2.85334498	2.4393358	2.73039572	2.79014802
Zone 3	1.770313047	2.26495165	2.38600243	2.49800812
Zone 4	1.562221047	2.72722712	1.54635926	1.638056992
Total	8.226947384	9.0619205	8.57795783	8.112383932

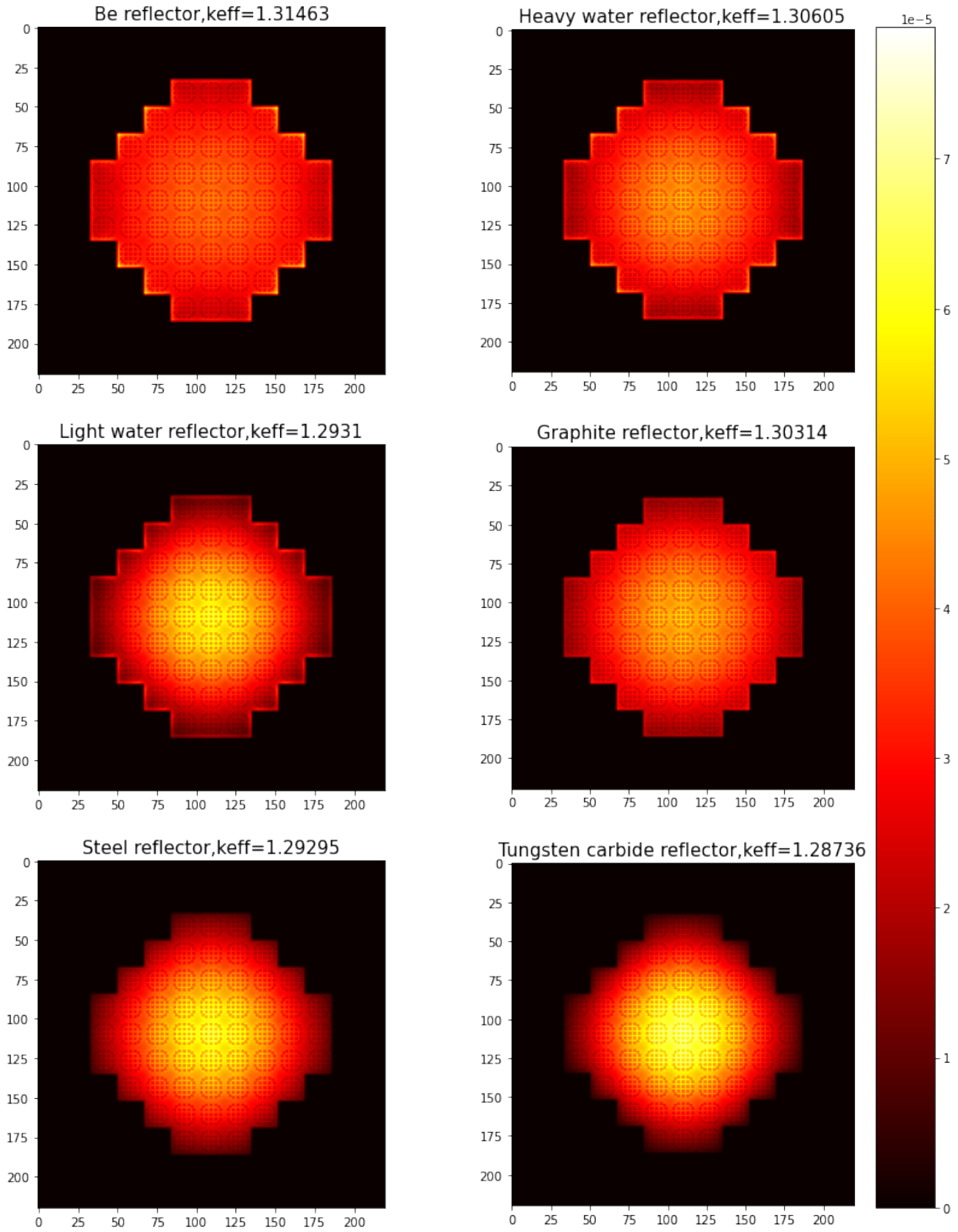


Figure A.7: Heating maps of variant(a) core layout with different material reflectors

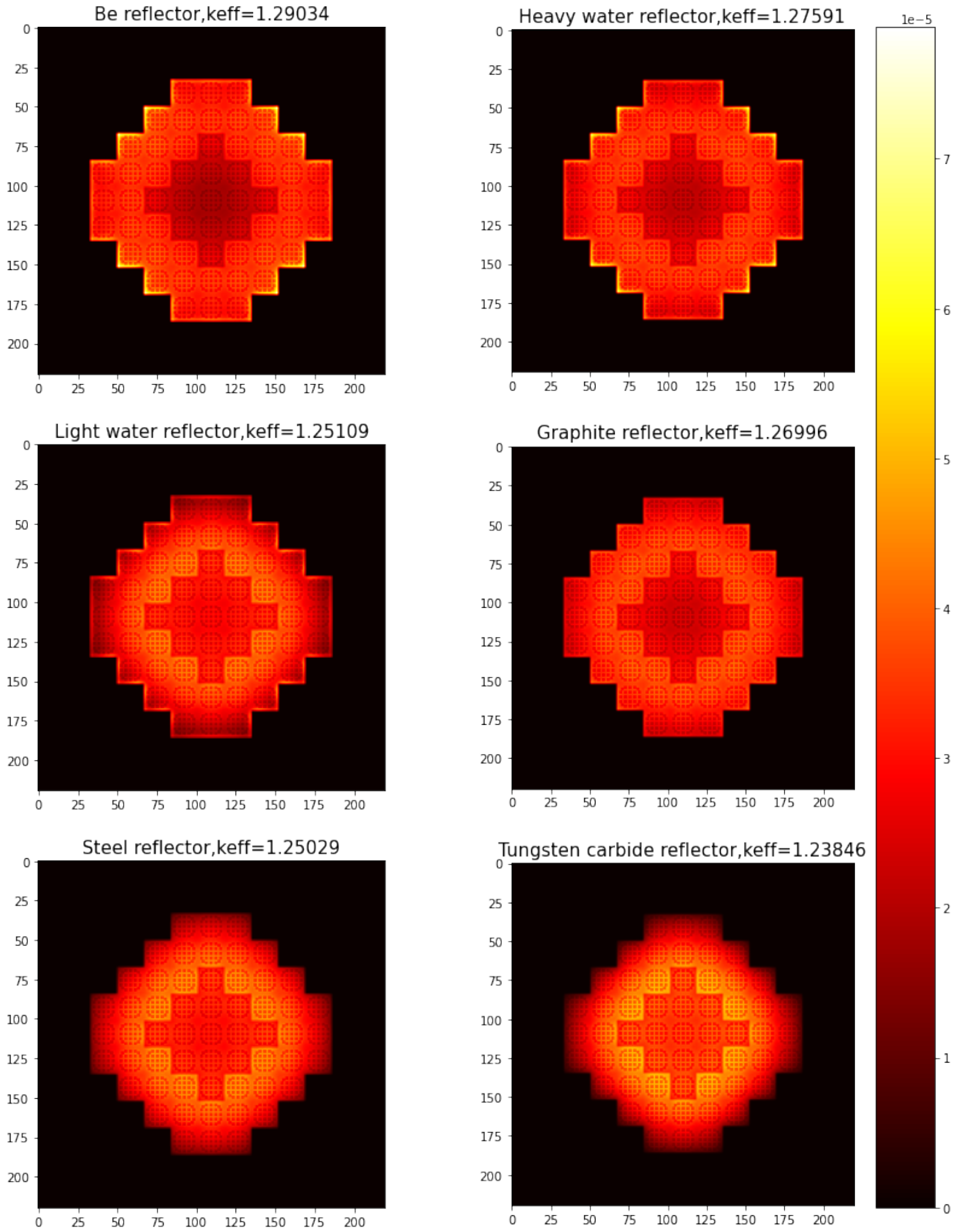


Figure A.8: Heating maps of variant(b) core layout with different material reflectors

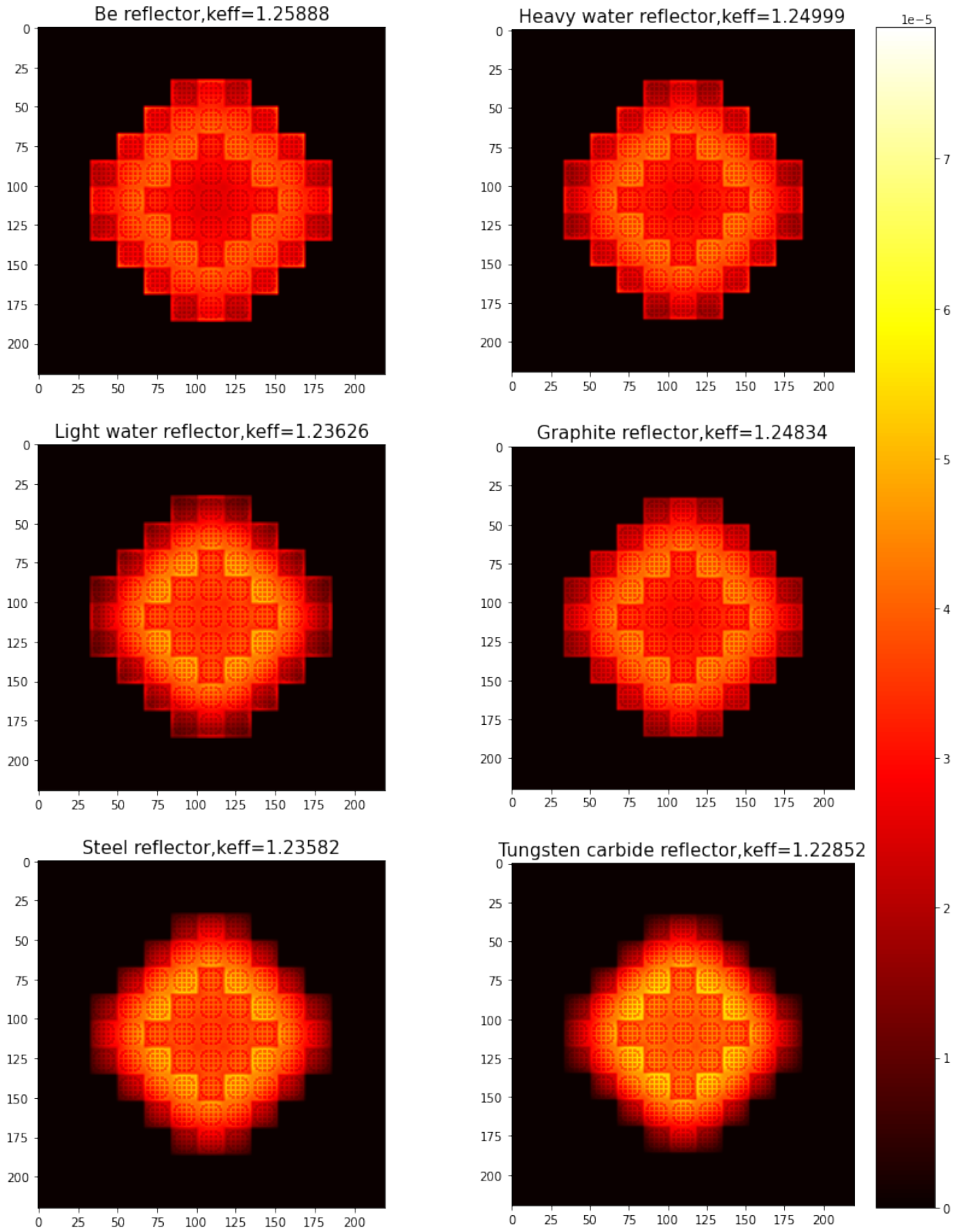


Figure A.9: Heating maps of variant(c) core layout with different material reflectors

Appendix Two

OpenMC model code

This second appendix provides a real SMART OpenMC model code that has been used in the thesis study. The below pages contain an independent PDF file exported by the original code editor Jupyterlab. Therefore, its page number does not follow the entire thesis.

This code can produce three executable XML files for geometry, materials and settings, which are necessary files for an OpenMC simulation. The cross-section.XML file links to the ENDF71 nuclear library storage in the BlueBEAR research data storage space by command from the OS package.

This model has three types, a total of 57 fuel assemblies and a beryllium oxide neutron reflector placed between the core edge and steel barrier. Each kind of fuel assembly has a different number of gadolinium oxide rods. The positions for control rods are occupied by water at the moment. However, the rod geometry cell has already been defined, the material could be replaced by the real control rod material in a few reasonably easy steps. The temperature of materials is set to the reactor operating conditions. The tally and burn-up settings are not included in this particular code version. The code output only has the k_{eff} eigenvalue calculation results. Due to it being a demonstration code, the number of neutron histories is relatively small and only has 15 thousand. In a real simulation on HPC, the neutron histories would be increased to around 1.5 million.

SMART-BeO-reflector-model

Yiming Zhong

June 30, 2021

[ ]:
```
import matplotlib.pyplot as plt
import numpy as np
import pandas as pd
import os
import math

import openmc
```

[ ]:
```
os.environ['OPENMC_CROSS_SECTIONS']='/rds/projects/n/normanpi01/Yiming_Zhong/
↪nucleardata/endfb71_hdf5/cross_sections.xml'
```

[ ]:
```
# high enrichment fuel
fuel=openmc.Material(name='high enrichment fuel')
fuel.set_density('g/cm3',10.97)
fuel.add_element('U', 1. , enrichment=4.8)
fuel.add_element('O', 2.)
fuel.temperature=1200.0

# fuel mixed with Gadolinlum
fuelGd=openmc.Material(name='2.4% enrichment fuel mix with gadolinium')
fuelGd.set_density('g/cm3',10.97)
fuelGd.add_element('U', 0.95 , enrichment=2.8)
fuelGd.add_element('Gd',0.05)
fuelGd.add_element('O', 2.)
fuelGd.temperature=1200.0

#Zircaloy
zircaloy=openmc.Material(name='Zircaloy')
zircaloy.set_density('g/cm3',6.56)
zircaloy.add_element('Zr',0.978)
zircaloy.add_element('Sn',0.012)
zircaloy.add_element('Nb',0.01)
zircaloy.temperature=1200

#Water
water=openmc.Material(name='water')
water.set_density('g/cm3',0.7)
```

```
water.add_nuclide('H1', 2.00)
water.add_nuclide('O16',1.00)
water.temperature=600

#Steel
steel=openmc.Material(name='steel')
steel.set_density('g/cm3',7.92)
steel.add_element('Fe',0.9655)
steel.add_element('Ni',0.007)
steel.add_element('Si',0.004)
steel.add_nuclide('Mo98',0.006)
steel.add_nuclide('Mn55',0.015)
steel.add_element('C',0.0025)
steel.temperature=600

# Reflector material beryllium oxide
BO=openmc.Material(name='Beryllium oxide')
BO.set_density('g/cm3',3.02)
BO.add_element('Be',1.00)
BO.add_element('O',1.00)
BO.temperature=600.0
BO.depletable = True

materials_file=openmc.Materials([fuel,fuelGd, zircaloy,water,steel,BO])


materials_file.export_to_xml()
```

[ ]:
```
#fuel pin
#create cylinder for the fuel and clad
fuel_outer=openmc.ZCylinder(r=0.4465)
clad_outer=openmc.ZCylinder(r=0.475)
#create the surfaces for the cells
left=openmc.XPlane(x0=-0.6)
right=openmc.XPlane(x0=0.6)
up=openmc.YPlane(y0=0.6)
down=openmc.YPlane(y0=-0.6)
```

[ ]:
```
fuel_region= -fuel_outer
absorber_region=-clad_outer
clad_region= +fuel_outer & -clad_outer
water_region= +left & -right & +down & -up & +clad_outer
fuelpin_region=+left & -right & +down & -up
```

[ ]:
```
#fuel cell
fuel_cell=openmc.Cell(name='enrichment fuel')
fuel_cell.fill=fuel
```

```
fuel_cell.region=fuel_region
#cladding cell
clad_cell=openmc.Cell(name='cladding')
clad_cell.fill=zircaloy
clad_cell.region=clad_region
#Moderator cell
moderator_cell=openmc.Cell(name='moderator')
moderator_cell.fill=water
moderator_cell.region= water_region

fuelpin_universe=openmc.Universe(name='fuel pin universe')
fuelpin_universe.add_cells([fuel_cell,clad_cell,moderator_cell])

fuelpin_cell=openmc.Cell(name='fuel pin')
fuelpin_cell.region=fuelpin_region
fuelpin_cell.fill=fuelpin_universe


#fuel_Gd cell
fuelGd_cell=openmc.Cell(name='fuel mixed Gd')
fuelGd_cell.fill=fuelGd
fuelGd_cell.region=fuel_region
#cladding cell
clad_cell=openmc.Cell(name='cladding')
clad_cell.fill=zircaloy
clad_cell.region=clad_region
#Moderator cell
moderator_cell=openmc.Cell(name='moderator')
moderator_cell.fill=water
moderator_cell.region=water_region

fuelGdpin_universe=openmc.Universe(name='fuel_Gd universe')
fuelGdpin_universe.add_cells([fuelGd_cell,clad_cell,moderator_cell])

fuelGdpin_cell=openmc.Cell(name='fuelGd pin')
fuelGdpin_cell.region=fuelpin_region
fuelGdpin_cell.fill=fuelGdpin_universe


#Neutron absorber cell(control rods)
rod_cell=openmc.Cell(name='burnable poison')
rod_cell.fill=water
rod_cell.region=absorber_region
#Moderator cell
moderator_cell=openmc.Cell(name='moderator')
moderator_cell.fill=water
moderator_cell.region=water_region
```

```
poison_universe=openmc.Universe(name='burnable poison')
poison_universe.add_cells([rod_cell,moderator_cell])

poison_cell=openmc.Cell(name='poison pin')
poison_cell.region=fuelpin_region
poison_cell.fill=poison_universe



# Instrumentation cell
ins_cell=openmc.Cell(name='instrumentation')
ins_cell.fill=water
ins_cell.region=absorber_region
# Moderator cell
moderator_cell=openmc.Cell(name='moderator')
moderator_cell.fill=water
moderator_cell.region=water_region

Ins_universe=openmc.Universe(name='Instrumentation')
Ins_universe.add_cells([ins_cell,moderator_cell])

ins_cell=openmc.Cell(name='Instrumentation')
ins_cell.region=fuelpin_region
ins_cell.fill=Ins_universe
```

[ ]:
```
# Define surface to surround the assembly geometry
x_left=openmc.XPlane (x0=-10.2, boundary_type='transmission')
x_right=openmc.XPlane(x0=+10.2, boundary_type='transmission')
y_up=openmc.YPlane   (y0=+10.2, boundary_type='transmission')
y_down=openmc.YPlane (y0=-10.2, boundary_type='transmission')

assembly_region=+x_left & -x_right & +y_down & -y_up



f=fuelpin_universe
g=fuelGdpin_universe
b=poison_universe
i=Ins_universe
```

[ ]:
```
#Instantiate the A type fuel assembly lattice
a1_lattices=openmc.RectLattice(name='8Gd_rods_FA')
a1_lattices.lower_left=[-10.2,-10.2]
a1_lattices.pitch=[1.20,1.20]

a1_lattices.universes=   [[f,f,f,f,f,f,f,f,f,f,f,f,f,f,f,f,f],
    [f,f,f,f,f,f,f,f,f,f,f,f,f,f,f,f,f],
```

```
    [f,f,g,f,f,b,f,f,b,f,f,b,f,f,g,f,f],
    [f,f,f,b,f,f,f,f,f,f,f,f,f,b,f,f,f],
    [f,f,f,f,f,f,f,f,g,f,f,f,f,f,f,f,f],
    [f,f,b,f,f,b,f,f,b,f,f,b,f,f,b,f,f],
    [f,f,f,f,f,f,f,f,f,f,f,f,f,f,f,f,f],
    [f,f,f,f,f,f,f,f,f,f,f,f,f,f,f,f,f],
    [f,f,b,f,g,b,f,f,i,f,f,b,g,f,b,f,f],
    [f,f,f,f,f,f,f,f,f,f,f,f,f,f,f,f,f],
    [f,f,f,f,f,f,f,f,f,f,f,f,f,f,f,f,f],
    [f,f,b,f,f,b,f,f,b,f,f,b,f,f,b,f,f],
    [f,f,f,f,f,f,f,f,g,f,f,f,f,f,f,f,f],
    [f,f,f,b,f,f,f,f,f,f,f,f,f,b,f,f,f],
    [f,f,g,f,f,b,f,f,b,f,f,b,f,f,g,f,f],
    [f,f,f,f,f,f,f,f,f,f,f,f,f,f,f,f,f],
    [f,f,f,f,f,f,f,f,f,f,f,f,f,f,f,f,f]]

FA8_cell=openmc.Cell(name='FA8')
FA8_cell.fill=a1_lattices
FA8_cell.region=assembly_region
FA8_universe=openmc.Universe(name='FA8')
FA8_universe.add_cell(FA8_cell)


#Instantiate the B type fuel assembly lattice
a2_lattices=openmc.RectLattice(name='20Gd_rods_FA')
a2_lattices.lower_left=[-10.2,-10.2]
a2_lattices.pitch=[1.20,1.20]

a2_lattices.universes=   [[f,f,f,f,f,f,f,f,f,f,f,f,f,f,f,f,f],
    [f,f,f,f,g,f,f,f,f,f,f,f,g,f,f,f,f],
    [f,f,f,f,f,b,f,f,b,f,f,b,f,f,f,f,f],
    [f,f,f,b,f,f,g,f,f,f,g,f,f,b,f,f,f],
    [f,g,f,f,f,f,f,f,f,f,f,f,f,f,f,g,f],
    [f,f,b,f,f,b,f,f,b,f,f,b,f,f,b,f,f],
    [f,f,f,g,f,f,g,f,f,f,g,f,f,g,f,f,f],
    [f,f,f,f,f,f,f,f,f,f,f,f,f,f,f,f,f],
    [f,f,b,f,f,b,f,f,i,f,f,b,f,f,b,f,f],
    [f,f,f,f,f,f,f,f,f,f,f,f,f,f,f,f,f],
    [f,f,f,g,f,f,g,f,f,f,g,f,f,g,f,f,f],
    [f,f,b,f,f,b,f,f,b,f,f,b,f,f,b,f,f],
    [f,g,f,f,f,f,f,f,f,f,f,f,f,f,f,g,f],
    [f,f,f,b,f,f,g,f,f,f,g,f,f,b,f,f,f],
    [f,f,f,f,f,b,f,f,b,f,f,b,f,f,f,f,f],
    [f,f,f,f,g,f,f,f,f,f,f,f,g,f,f,f,f],
    [f,f,f,f,f,f,f,f,f,f,f,f,f,f,f,f,f]]
```

```
FA20_cell=openmc.Cell(name='a2')
FA20_cell.fill=a2_lattices
FA20_cell.region=assembly_region
FA20_universe=openmc.Universe(name='a2')
FA20_universe.add_cell(FA20_cell)

#Instantiate the C type fuel assembly lattice
a3_lattices=openmc.RectLattice(name='24Gd_rods_FA')
a3_lattices.lower_left=[-10.2,-10.2]
a3_lattices.pitch=[1.20,1.20]

a3_lattices.universes=   [[f,f,f,f,f,f,f,f,f,f,f,f,f,f,f,f,f],
    [f,f,f,g,f,f,f,f,f,f,f,f,f,g,f,f,f],
    [f,f,f,f,f,b,f,f,b,f,f,b,f,f,f,f,f],
    [f,g,f,b,f,f,f,g,f,g,f,f,f,b,f,g,f],
    [f,f,f,f,g,f,f,f,f,f,f,f,g,f,f,f,f],
    [f,f,b,f,f,b,f,f,b,f,f,b,f,f,b,f,f],
    [f,f,f,f,f,f,g,f,f,f,g,f,f,f,f,f,f],
    [f,f,f,g,f,f,f,f,f,f,f,f,f,g,f,f,f],
    [f,f,b,f,f,b,f,f,i,f,f,b,f,f,b,f,f],
    [f,f,f,g,f,f,f,f,f,f,f,f,f,g,f,f,f],
    [f,f,f,f,f,f,g,f,f,f,g,f,f,f,f,f,f],
    [f,f,b,f,f,b,f,f,b,f,f,b,f,f,b,f,f],
    [f,f,f,f,g,f,f,f,f,f,f,f,g,f,f,f,f],
    [f,g,f,b,f,f,f,g,f,g,f,f,f,b,f,g,f],
    [f,f,f,f,f,b,f,f,b,f,f,b,f,f,f,f,f],
    [f,f,f,g,f,f,f,f,f,f,f,f,f,g,f,f,f],
    [f,f,f,f,f,f,f,f,f,f,f,f,f,f,f,f,f]]


FA24_cell=openmc.Cell(name='a3')
FA24_cell.fill=a3_lattices
FA24_cell.region= assembly_region
FA24_universe=openmc.Universe(name='a3')
FA24_universe.add_cell(FA24_cell)
```

[ ]:
```
# Create boundary planes to surround the core gepmetry
xp1=openmc.XPlane(x0=+30.6,boundary_type='transmission')
xp2=openmc.XPlane(x0=+51.0,boundary_type='transmission')
xp3=openmc.XPlane(x0=+71.4,boundary_type='transmission')
xp4=openmc.XPlane(x0=+91.8,boundary_type='transmission')

xn1=openmc.XPlane(x0=-30.6,boundary_type='transmission')
xn2=openmc.XPlane(x0=-51.0,boundary_type='transmission')
xn3=openmc.XPlane(x0=-71.4,boundary_type='transmission')
xn4=openmc.XPlane(x0=-91.8,boundary_type='transmission')
```

```
yp1=openmc.YPlane(y0=+30.6,boundary_type='transmission')
yp2=openmc.YPlane(y0=+51.0,boundary_type='transmission')
yp3=openmc.YPlane(y0=+71.4,boundary_type='transmission')
yp4=openmc.YPlane(y0=+91.8,boundary_type='transmission')

yn1=openmc.YPlane(y0=-30.6,boundary_type='transmission')
yn2=openmc.YPlane(y0=-51.0,boundary_type='transmission')
yn3=openmc.YPlane(y0=-71.4,boundary_type='transmission')
yn4=openmc.YPlane(y0=-91.8,boundary_type='transmission')

zp1=openmc.ZPlane(z0=+100.0,boundary_type='transmission')
zn1=openmc.ZPlane(z0=-100.0,boundary_type='transmission')
```

[ ]:
```
c4_region=-xp4 & +xn4 & -yp1 & +yn1 & -zp1 & +zn1
c1down_region=-xp1 & +xn1 & +yn4 & -yn3 & -zp1 & +zn1
c1up_region=-xp1 & +xn1 & +yp3 & -yp4 & -zp1 & +zn1
c2down_region=-xp2 & +xn2 & +yn3 & -yn2 & -zp1 & +zn1
c2up_region=-xp2 & +xn2 & +yp2 & -yp3 & -zp1 & +zn1
c3down_region=-xp3 & +xn3 & +yn2 & -yn1 & -zp1 & +zn1
c3up_region=-xp3 & +xn3 & +yp1 & -yp2 & -zp1 & +zn1
```

[ ]:
```
a=FA8_universe
b=FA20_universe
c=FA24_universe

# Instantiate the C4 core lattice
c4_lattices=openmc.RectLattice(name='c4')
c4_lattices.lower_left=[-91.8,-30.6]
c4_lattices.pitch=[20.40,20.40]
c4_lattices.dimensions=[9,3]
c4_lattices.universes=    [[a,b,a,c,a,c,a,b,a],
     [a,a,a,a,c,a,a,a,a],
     [a,b,a,c,a,c,a,b,a]]

c4_cell=openmc.Cell(name='c4')
c4_cell.fill=c4_lattices
c4_cell.region=c4_region
c4_universe=openmc.Universe(name='c4')
c4_universe.add_cell(c4_cell)



# Instantiate the C1 core lattice
c1down_lattices=openmc.RectLattice(name='c1down')
c1down_lattices.lower_left=[-30.6,-91.8]
c1down_lattices.pitch=[20.40,20.40]
c1down_lattices.dimensions=[3,1]
```

```
c1down_lattices.universes=    [[a,a,a]]

c1down_cell=openmc.Cell(name='c1down')
c1down_cell.fill=c1down_lattices
c1down_cell.region=c1down_region
c1down_universe=openmc.Universe(name='c1down')
c1down_universe.add_cell(c1down_cell)



# Instantiate the C1 core lattice
c1up_lattices=openmc.RectLattice(name='c1up')
c1up_lattices.lower_left=[-30.6,+71.4]
c1up_lattices.pitch=[20.40,20.40]
c1up_lattices.dimensions=[3,1]
c1up_lattices.universes=    [[a,a,a]]

c1up_cell=openmc.Cell(name='c1up')
c1up_cell.fill=c1up_lattices
c1up_cell.region=c1up_region
c1up_universe=openmc.Universe(name='c1up')
c1up_universe.add_cell(c1up_cell)



# Instantiate the C2 core lattice
c2down_lattices=openmc.RectLattice(name='c2down')
c2down_lattices.lower_left=[-51.0,-71.4]
c2down_lattices.pitch=[20.40,20.40]
c2down_lattices.dimensions=[5,1]
c2down_lattices.universes=    [[a,b,a,b,a]]

c2down_cell=openmc.Cell(name='c2down')
c2down_cell.fill=c2down_lattices
c2down_cell.region=c2down_region
c2down_universe=openmc.Universe(name='c2down')
c2down_universe.add_cell(c2down_cell)



# Instantiate the C2 core lattice
c2up_lattices=openmc.RectLattice(name='c2up')
c2up_lattices.lower_left=[-51.0,+51.0]
c2up_lattices.pitch=[20.40,20.40]
c2up_lattices.dimensions=[5,1]
c2up_lattices.universes=    [[a,b,a,b,a]]
```

```
c2up_cell=openmc.Cell(name='c2up')
c2up_cell.fill=c2up_lattices
c2up_cell.region=c2up_region
c2up_universe=openmc.Universe(name='c2up')
c2up_universe.add_cell(c2up_cell)



# Instantiate the C3 core lattice
c3down_lattices=openmc.RectLattice(name='c3down')
c3down_lattices.lower_left=[-71.4,-51.0]
c3down_lattices.pitch=[20.40,20.40]
c3down_lattices.dimensions=[7,1]
c3down_lattices.universes=    [[a,b,a,a,a,b,a]]

c3down_cell=openmc.Cell(name='c3down')
c3down_cell.fill=c3down_lattices
c3down_cell.region=c3down_region
c3down_universe=openmc.Universe(name='up')
c3down_universe.add_cell(c3down_cell)


# In[24]:


# Instantiate the C3 core lattice
c3up_lattices=openmc.RectLattice(name='c3up')
c3up_lattices.lower_left=[-71.4,+30.6]
c3up_lattices.pitch=[20.40,20.40]
c3up_lattices.dimensions=[7,1]
c3up_lattices.universes=    [[a,b,a,a,a,b,a]]

c3up_cell=openmc.Cell(name='c3up')
c3up_cell.fill=c3up_lattices
c3up_cell.region=c3up_region
c3up_universe=openmc.Universe(name='c3up')
c3up_universe.add_cell(c3up_cell)
```

[ ]:
```
core_region=(c4_region)|(c1down_region)|(c1up_region)|(c2down_region)|(c2up_region)|(c3down_reg

# Instantiate the core lattice
core_universe=openmc.Universe(name='core')
core_universe.add_cells((c3up_cell,c3down_cell,c2up_cell,c2down_cell,c1up_cell
                         ,c1down_cell,c4_cell))

core_cell=openmc.Cell(name='core')
core_cell.fill=core_universe
```

```
core_cell.region=core_region


# In[26]:


# coolant and barrier universe
# define the surface to surround the geometry
c1=openmc.ZCylinder(r=110.0,boundary_type='transmission')
c2=openmc.ZCylinder(r=120.0,boundary_type='vacuum')
z3=openmc.ZPlane(z0= 120.0, boundary_type='transmission')
z4=openmc.ZPlane(z0=-120.0, boundary_type='transmission')
z5=openmc.ZPlane(z0= 130.0, boundary_type='vacuum')
z6=openmc.ZPlane(z0=-130.0, boundary_type='vacuum')


# In[27]:


coolant_region=(-c1 & -z3 & +z4)& (~core_region)
barrier_region=(-c2&+c1) & -z3 & +z4
barrierup_region=-c2 & -z5 & +z3
barrierdown_region=-c2 & +z6 & -z4


# In[28]:


# Instantiate the coolant cell
coolant_cell=openmc.Cell(name='coolant')
coolant_cell.fill=water
coolant_cell.region=coolant_region

barrier_cell=openmc.Cell(name='barrier')
barrier_cell.fill=steel
barrier_cell.region=barrier_region

barrierup_cell=openmc.Cell(name='barrier_top')
barrierup_cell.fill=steel
barrierup_cell.region=barrierup_region

barrierdown_cell=openmc.Cell(name='barrier_down')
barrierdown_cell.fill=steel
barrierdown_cell.region=barrierdown_region


root=openmc.Universe(name='root')
```

```
root.
 ↪add_cells((core_cell,coolant_cell,barrier_cell,barrierup_cell,barrierdown_cell))

openmc_geometry=openmc.Geometry(root)
openmc_geometry.export_to_xml()
```

[ ]:
```
settings = openmc.Settings()
settings.batches =250
settings.inactive = 100
settings.particles = 15000

settings.energy_mode='continuous-energy'


settings.run_mode = 'eigenvalue'


# In[38]:


settings.export_to_xml()


# In[39]:


openmc.run()
```

References

[1] Jasmina Vujić et al. "Small modular reactors: Simpler, safer, cheaper?" In: *Energy* 45.1 (2012), pp. 288–295.

[2] WNA. *Emerging Nuclear Energy Countries*. Updated March 2020. URL: https://www.world-nuclear.org/information-library/country-profiles/others/emerging-nuclear-energy-countries.aspx.

[3] IEA. *Tracking Power*. Tech. rep. Paris, 2019. URL: https://www.iea.org/reports/tracking-power-2019.

[4] May Fawaz-Huber. *Going Long Term: US Nuclear Power Plants Could Extend Operating Life to 80 Years*. 2018. URL: https://www.iaea.org/newscenter/news/going-long-term-us-nuclear-power-plants-could-extend-operating-life-to-80-years.

[5] Gordon. Edwards. "Cost disadvantages of expanding the nulcear power industry". In: *Canadian Business Review* 9.1 (1982), pp. 19–30. ISSN: 0317-4026. URL: http://inis.iaea.org/search/search.aspx?orig%7B%5C_%7Dq=RN:16015254.

[6] Daniel T Ingersoll. "Deliberately small reactors and the second nuclear era". In: *Progress in Nuclear Energy* 51.4-5 (2009), pp. 589–603.

[7] IAEA. *Deployment Indicators for Small Modular Reactors*. TECDOC Series 1854. Vienna: INTERNATIONAL ATOMIC ENERGY AGENCY, 2018. ISBN: 978-92-0-

105718-1. URL: https://www.iaea.org/publications/13404/deployment-indicators-for-small-modular-reactors.

[8] Hassan Nawaz Butt et al. "Assessment of passive safety system of a Small Modular Reactor (SMR)". In: *Annals of Nuclear Energy* 98 (2016), pp. 191–199.

[9] IAEA. *Passive Safety Systems in Water Cooled Reactors: An Overview and Demonstration with Basic Principle Simulators*. Training Course Series 69. Vienna: INTERNATIONAL ATOMIC ENERGY AGENCY, 2019. URL: https://www.iaea.org/publications/13530/passive-safety-systems-in-water-cooled-reactors-an-overview-and-demonstration-with-basic-principle-simulators.

[10] José Reyes Jr and Daniel Ingersoll. "NuScale Power Plant Resilience". In: *Transactions* 118.1 (2018), pp. 608–611.

[11] Nuscale. *NRC INTERACTION*. URL: https://www.nuscalepower.com/technology/licensing.

[12] Geoffrey Black and Steven Peterson. "Economic Impact Report: Construction and Operation of a Small Modular Reactor Electric Power Generation Facility at the Idaho National Laboratory Site, Butte County, Idaho". In: (2019).

[13] Rolls Royce. "UK SMR: Technical Summary". In: (2017), p. 7. URL: http://www.rolls-royce.com/%7B~%7D/media/Files/R/Rolls-Royce/documents/customers/nuclear/smr-technical-summary.pdf.

[14] George Waddington. "SMR Feasibility Study December-2014". In: December (2014).

[15] Keung Koo Kim et al. "SMART: The First Licensed Advanced Integral Reactor". In: *Journal of Energy and Power Engineering* 8.1 (2015), pp. 94–102. ISSN: 19348975. DOI: 10.17265/1934-8975/2014.01.011.

[16] Rolls-Royce. "Small Modular Reactors - once in a lifetime opportunity for the UK". In: (2017). URL: https://www.rolls-royce.com/%7B~%7D/media/Files/R/Rolls-Royce/documents/customers/nuclear/smr-brochure-july-2017.pdf.

[17] Si-Hwan Kim et al. "Design Verification Program of SMART". In: 2003.

[18] IAEA. *System-Integrated Modular Advanced Reactor (SMART)*. Tech. rep. 2011. URL: https://aris.iaea.org/PDF/SMART.pdf.

[19] Kang Young Choi et al. "Integral effect non-loca test results for the integral type reactor SMART-P using the VISTA facility". In: 2007.

[20] S Choi. "Small modular reactors (SMRs): the case of the Republic of Korea". In: *Handbook of Small Modular Nuclear Reactors*. Elsevier, 2015, pp. 379–407.

[21] World Nuclear News. *Korea, Saudi Arabia to cooperate on SMART deployment*. 2019. URL: https://www.world-nuclear-news.org/Articles/Korea,-Saudi-Arabia-to-cooperate-on-SMART-deployme.

[22] Nuclear Engineering International. *South Korea and Saudi Arabia strengthen cooperation on SMART reactor*. 2020. URL: https://www.neimagazine.com/news/newssouth-korea-and-saudi-arabia-strengthen-cooperation-on-smart-reactor-7591629.

[23] Young Jong Chung et al. "Applicability of TASS/SMR using drift flux model for SMART LOCA analysis". In: *Nuclear Engineering and Design* 262.September 2013 (2013), pp. 228–234. ISSN: 00295493. DOI: 10.1016/j.nucengdes.2013.04.020. URL: http://dx.doi.org/10.1016/j.nucengdes.2013.04.020.

[24] Hee-Kyung Kim et al. "Thermal-hydraulic analysis of SMART steam generator tube rupture using TASS/SMR-S code". In: *Annals of Nuclear Energy* 55 (2013), pp. 331–340.

[25] *Assessment and Management of Ageing of Major Nuclear Power Plant Components Important to Safety: Steam Generators*. TECDOC Series 1668. Vienna: INTERNATIONAL ATOMIC ENERGY AGENCY, 2011. ISBN: 978-92-0-121410-2. URL: https://www.iaea.org/publications/8728/assessment-and-management-of-ageing-of-major-nuclear-power-plant-components-important-to-safety-steam-generators.

[26] Muhammad Ilyas and Fatih Aydogan. "Steam generator performance improvements for integral small modular reactors". In: *Nuclear Engineering and Technology* 49.8 (2017), pp. 1669–1679.

[27] SJ Green and G Hetsroni. "PWR steam generators". In: *International journal of multiphase flow* 21 (1995), pp. 1–97.

[28] Qiang Lian et al. "Code improvement, separate-effect validation, and benchmark calculation for thermal-hydraulic analysis of helical coil once-through steam generator". In: *Annals of Nuclear Energy* 141 (2020), p. 107333.

[29] YJ Chung et al. "Development and assessment of system analysis code, TASS/SMR for integral reactor, SMART". In: *Nuclear engineering and design* 244 (2012), pp. 52–60.

[30] Yeon-Sik Kim et al. "Application of direct passive residual heat removal system to the SMART reactor". In: *Annals of Nuclear Energy* 89 (2016), pp. 56–62.

[31] Hadid Subki. "Advances in Small Modular Reactor Technology Developments". In: (2020).

[32] Zupan Hu. "Developments of analyses on grid-to-rod fretting problems in pressurized water reactors". In: *Progress in Nuclear Energy* 106 (2018), pp. 293–299.

[33] Mostafa Sadighi, Saeid Setayeshi, and Ali Akbar Salehi. "PWR fuel management optimization using neural networks". In: *Annals of Nuclear Energy* 29.1 (2002), pp. 41–

51. ISSN: 0306-4549. DOI: https://doi.org/10.1016/S0306-4549(01)00024-X. URL: http://www.sciencedirect.com/science/article/pii/S030645490100024X.

[34] Han Gon Kim, Soon Heung Chang, and Byung Ho Lee. "Pressurized Water Reactor Core Parameter Prediction Using an Artificial Neural Network". In: *Nuclear Science and Engineering* 113.1 (1993), pp. 70–76. DOI: 10.13182/NSE93-A23994. eprint: https://doi.org/10.13182/NSE93-A23994. URL: https://doi.org/10.13182/NSE93-A23994.

[35] E K Fujita, M J Driscoll, and D D Lanning. "Design and fuel management of PWR cores to optimize the once-through fuel cycle". In: (Aug. 1978). DOI: 10.2172/6670045. URL: https://www.osti.gov/biblio/6670045.

[36] D. Song. "18 - Small modular reactors (SMRs): the case of China". In: *Handbook of Small Modular Nuclear Reactors*. Ed. by Mario D. Carelli and Daniel T. Ingersoll. Woodhead Publishing Series in Energy. Woodhead Publishing, 2015, pp. 455–468. ISBN: 978-0-85709-851-1. DOI: https://doi.org/10.1533/9780857098535.4.455. URL: https://www.sciencedirect.com/science/article/pii/B9780857098511500182.

[37] Jian Deng et al. "Analysis of post-LOCA long-term core safety characteristics for the Small Modular Reactor ACP100". In: *Annals of Nuclear Energy* 142 (2020), p. 107349. ISSN: 0306-4549. DOI: https://doi.org/10.1016/j.anucene.2020.107349. URL: http://www.sciencedirect.com/science/article/pii/S0306454920300475.

[38] Dahuan Zhu et al. "Evaluation of in-vessel corium retention margin for small modular reactor ACP100". In: *Annals of Nuclear Energy* 94 (2016), pp. 684–690. ISSN: 0306-4549. DOI: https://doi.org/10.1016/j.anucene.2016.04.015. URL: http://www.sciencedirect.com/science/article/pii/S0306454916301761.

[39] Jian Deng et al. "Research on level 1 PSA and risk-informed design for ACP100". In: *Annals of Nuclear Energy* 144 (2020), p. 107542. ISSN: 0306-4549. DOI: https:

//doi.org/10.1016/j.anucene.2020.107542. URL: http://www.sciencedirect.com/science/article/pii/S0306454920302401.

[40] Paul Breeze. "Chapter 7 - Advanced Reactor Design and Small Modular Reactors". In: ed. by Paul B T - Nuclear Power Breeze. Academic Press, 2017, pp. 63–73. ISBN: 978-0-08-101043-3. DOI: https://doi.org/10.1016/B978-0-08-101043-3.00007-9. URL: http://www.sciencedirect.com/science/article/pii/B9780081010433000079.

[41] Tim Abram and Sue Ion. "Generation-IV nuclear power: A review of the state of the science". In: *Energy Policy* 36.12 (2008). Foresight Sustainable Energy Management and the Built Environment Project, pp. 4323–4330. ISSN: 0301-4215. DOI: https://doi.org/10.1016/j.enpol.2008.09.059. URL: http://www.sciencedirect.com/science/article/pii/S0301421508004448.

[42] Sümer Şahin and Hacı Mehmet Şahin. "Generation-IV reactors and nuclear hydrogen production". In: *International Journal of Hydrogen Energy* (2021). ISSN: 0360-3199. DOI: https://doi.org/10.1016/j.ijhydene.2020.12.182. URL: http://www.sciencedirect.com/science/article/pii/S0360319920348175.

[43] Marat Margulis and Eugene Shwageraus. "Advanced Gas-cooled reactors technology for enabling molten-salt reactors design-Estimation of coolant impact on neutronic performance". In: *Progress in Nuclear Energy* 125 (2020), p. 103382.

[44] IAEA. "High Temperature Gas Cooled Reactor Fuels and Materials". In: *Iaea Tecdoc* (2010), pp. 1–182.

[45] Xiang-wen Zhou et al. "Carbon materials in a high temperature gas-cooled reactor pebble-bed module". In: *New Carbon Materials* 33.2 (2018), pp. 97–108. ISSN: 1872-5805. DOI: https://doi.org/10.1016/S1872-5805(18)60328-2. URL: http://www.sciencedirect.com/science/article/pii/S1872580518603282.

[46] Hiroyuki Sato et al. "GTHTR300—A nuclear power plant design with 50% generating efficiency". In: *Nuclear Engineering and Design* 275 (2014), pp. 190–196. ISSN: 0029-5493. DOI: https://doi.org/10.1016/j.nucengdes.2014.05.004. URL: http://www.sciencedirect.com/science/article/pii/S002954931400274X.

[47] Zuoyi Zhang et al. "The Shandong Shidao Bay 200 MWe High-Temperature Gas-Cooled Reactor Pebble-Bed Module (HTR-PM) Demonstration Power Plant: An Engineering and Technological Innovation". In: *Engineering* 2.1 (2016), pp. 112–118. ISSN: 20958099. DOI: 10.1016/J.ENG.2016.01.020.

[48] Eeshu Raaj Saasthaa Arumuga Kumar et al. "Neutronic performance of a thorium based mixed oxide fuel in a burner sodium-cooled fast reactor". In: *Energy* 212 (2020), p. 118744. ISSN: 0360-5442. DOI: https://doi.org/10.1016/j.energy.2020.118744. URL: http://www.sciencedirect.com/science/article/pii/S036054422031851X.

[49] Hailei Wang and Sean M. Kissick. "Modeling and simulation of a supercritical CO2-liquid sodium compact heat exchanger for sodium-cooled fast reactors". In: *Applied Thermal Engineering* 180 (2020), p. 115859. ISSN: 1359-4311. DOI: https://doi.org/10.1016/j.applthermaleng.2020.115859. URL: http://www.sciencedirect.com/science/article/pii/S135943112033341X.

[50] Mengqi Bai, Benjamin A. Lindley, and Tim Abram. "Fuel options for nuclear ship reactors featuring reactivity swing below one dollar". In: *Nuclear Engineering and Design* 360 (2020), p. 110494. ISSN: 0029-5493. DOI: https://doi.org/10.1016/j.nucengdes.2019.110494. URL: http://www.sciencedirect.com/science/article/pii/S0029549319305254.

[51] S. Bortot et al. "Core design investigation for a SUPERSTAR small modular lead-cooled fast reactor demonstrator". In: *Nuclear Engineering and Design* 241.8 (2011), pp. 3021–3031. ISSN: 0029-5493. DOI: https://doi.org/10.1016/j.nucengdes.2011.04.012. URL: http://www.sciencedirect.com/science/article/pii/S0029549311003153.

[52] M. Cross et al. "IAEA Nuclear Energy Series Publications: experimental facilities in support of liquid metal cooled fast neutron systems". In: NG-T.3.4 (2016), pp. 1–68. URL: http://www.iaea.org/Publications/index.html.

[53] Shripad T. Revankar. "Chapter Four - Nuclear Hydrogen Production". In: *Storage and Hybridization of Nuclear Energy*. Ed. by Hitesh Bindra and Shripad Revankar. Academic Press, 2019, pp. 49–117. ISBN: 978-0-12-813975-2. DOI: https://doi.org/10.1016/B978-0-12-813975-2.00004-1. URL: http://www.sciencedirect.com/science/article/pii/B9780128139752000041.

[54] Jérôme Serp et al. "The molten salt reactor (MSR) in generation IV: Overview and perspectives". In: *Progress in Nuclear Energy* 77 (2014), pp. 308–319. ISSN: 01491970. DOI: 10.1016/j.pnucene.2014.02.014.

[55] Y. Cui et al. "Development of a steady state analysis code for molten salt reactor based on nodal expansion method". In: *Annals of Nuclear Energy* 151 (2021), p. 107950. ISSN: 0306-4549. DOI: https://doi.org/10.1016/j.anucene.2020.107950. URL: http://www.sciencedirect.com/science/article/pii/S0306454920306460.

[56] Jinsen Xie et al. "Neutronic design and dynamic analysis of a 450 MWth graphite molten salt reactor core". In: *Annals of Nuclear Energy* 152 (2021), p. 107984. ISSN: 0306-4549. DOI: https://doi.org/10.1016/j.anucene.2020.107984. URL: http://www.sciencedirect.com/science/article/pii/S0306454920306800.

[57] "Moltex bags £6 million of crowd-funding for molten salt reactor." eng. In: *Utility Week* (Sept. 2019), pp. 19–19. ISSN: 13565532.

[58] Marc Verwerft and Brian Boer. "5.05 - Thorium Oxide Nuclear Fuels". In: *Comprehensive Nuclear Materials (Second Edition)*. Ed. by Rudy J.M. Konings and Roger E. Stoller. Second Edition. Oxford: Elsevier, 2020, pp. 139–168. ISBN: 978-0-08-102866-7. DOI: https://doi.org/10.1016/B978-0-12-803581-8.11770-9. URL: http://www.sciencedirect.com/science/article/pii/B9780128035818117709.

[59] Uguru Edwin Humphrey and Mayeen Uddin Khandaker. "Viability of thorium-based nuclear fuel cycle for the next generation nuclear reactor: Issues and prospects". In: *Renewable and Sustainable Energy Reviews* 97 (2018), pp. 259–275. ISSN: 1364-0321. DOI: https://doi.org/10.1016/j.rser.2018.08.019. URL: http://www.sciencedirect.com/science/article/pii/S1364032118305951.

[60] *Role of Thorium to Supplement Fuel Cycles of Future Nuclear Energy Systems*. Nuclear Energy Series NF-T-2.4. Vienna: INTERNATIONAL ATOMIC ENERGY AGENCY, 2012. ISBN: 978-92-0-125910-3. URL: https://www.iaea.org/publications/8703/role-of-thorium-to-supplement-fuel-cycles-of-future-nuclear-energy-systems.

[61] S.F. Ashley et al. "Life-cycle impacts from novel thorium–uranium-fuelled nuclear energy systems". In: *Energy Conversion and Management* 101 (2015), pp. 136–150. ISSN: 0196-8904. DOI: https://doi.org/10.1016/j.enconman.2015.04.041. URL: http://www.sciencedirect.com/science/article/pii/S0196890415003957.

[62] *Thorium Fuel Cycle - Potential Benefits and Challenges*. TECDOC Series 1450. Vienna: INTERNATIONAL ATOMIC ENERGY AGENCY, 2005. ISBN: 92-0-103405-9. URL: https://www.iaea.org/publications/7192/thorium-fuel-cycle-potential-benefits-and-challenges.

[63] Benjamin A. Lindley et al. "Steady-state and transient core feasibility analysis for a thorium-fuelled reduced-moderation PWR performing full transuranic recycle". In: *Annals of Nuclear Energy* 72 (2014), pp. 320–337. ISSN: 0306-4549. DOI: https://doi.org/10.1016/j.anucene.2014.05.027. URL: http://www.sciencedirect.com/science/article/pii/S0306454914002576.

[64] Yoshiaki Oka. *Nuclear reactor design*. Springer, 2014.

[65] K. Anantharaman, V. Shivakumar, and D. Saha. "Utilisation of thorium in reactors". In: *Journal of Nuclear Materials* 383.1 (2008). Advances in Nuclear Materials: Processing, Performance and Phenomena, pp. 119–121. ISSN: 0022-3115. DOI: https:

//doi.org/10.1016/j.jnucmat.2008.08.042. URL: http://www.sciencedirect.com/science/article/pii/S0022311508004856.

[66] MF Troyanov et al. "Some research and development of thorium fuel cycle in Russia". In: *Thorium fuel utilization: Options and trends* (2002), p. 77.

[67] G.L. Lunin et al. "Status and further development of nuclear power plants with WWER in Russia". In: *Nuclear Engineering and Design* 173.1 (1997), pp. 43–57. ISSN: 0029-5493. DOI: https://doi.org/10.1016/S0029-5493(97)00147-7. URL: http://www.sciencedirect.com/science/article/pii/S0029549397001477.

[68] Reza Akbari-Jeyhouni et al. "The utilization of thorium in Small Modular Reactors – Part I: Neutronic assessment". In: *Annals of Nuclear Energy* 120 (2018), pp. 422–430. ISSN: 0306-4549. DOI: https://doi.org/10.1016/j.anucene.2018.06.013. URL: http://www.sciencedirect.com/science/article/pii/S0306454918303153.

[69] P. Netter. "16 - Reprocessing of spent oxide fuel from nuclear power reactors". In: *Nuclear Fuel Cycle Science and Engineering*. Ed. by Ian Crossland. Woodhead Publishing Series in Energy. Woodhead Publishing, 2012, pp. 459–500. ISBN: 978-0-85709-073-7. DOI: https://doi.org/10.1533/9780857096388.4.459. URL: http://www.sciencedirect.com/science/article/pii/B9780857090737500167.

[70] Ritsuo Yoshioka et al. "9 - Environment, waste, and resources". In: *Molten Salt Reactors and Thorium Energy*. Ed. by Thomas J. Dolan. Woodhead Publishing, 2017, pp. 231–259. ISBN: 978-0-08-101126-3. DOI: https://doi.org/10.1016/B978-0-08-101126-3.00009-9. URL: http://www.sciencedirect.com/science/article/pii/B9780081011263000099.

[71] Eileen Supko. "13 - Nuclear fuel fabrication". In: *Uranium for Nuclear Power*. Ed. by Ian Hore-Lacy. Woodhead Publishing, 2016, pp. 353–382. ISBN: 978-0-08-100307-7. DOI: https://doi.org/10.1016/B978-0-08-100307-7.00013-2. URL: http://www.sciencedirect.com/science/article/pii/B9780081003077000132.

[72] *Status and Advances in MOX Fuel Technology*. Technical Reports Series 415. Vienna: INTERNATIONAL ATOMIC ENERGY AGENCY, 2003. ISBN: 92-0-103103-3. URL: https://www.iaea.org/publications/6562/status-and-advances-in-mox-fuel-technology.

[73] *MOX Fuel Cycle Technologies for Medium and Long Term Deployment*. C&S Papers Series (Print) 3. Vienna: INTERNATIONAL ATOMIC ENERGY AGENCY, 2000. URL: https://www.iaea.org/publications/5929/mox-fuel-cycle-technologies-for-medium-and-long-term-deployment.

[74] Fanny Courtin et al. "Neutronic predictors for PWR fuelled with multi-recycled plutonium and applications with the fuel cycle simulation tool CLASS". In: *Progress in Nuclear Energy* 100 (2017), pp. 33–47. ISSN: 0149-1970. DOI: https://doi.org/10.1016/j.pnucene.2017.04.018. URL: http://www.sciencedirect.com/science/article/pii/S0149197017300938.

[75] B. Mouginot et al. *Core library for advanced scenario simulation, C.L.A.S.S.: principle application*. International Conference "The Role of Reactor Physics toward a Sustainable Future" (PHYSOR 2014). Poster. Sept. 2014. URL: http://hal.in2p3.fr/in2p3-01119778.

[76] O Méplan et al. "MURE: MCNP Utility for Reactor Evolution, Description of the Methods, First Applications and Results". In: *ENC 2005 Proceedings, Versailles, France* June 2016 (2005).

[77] Christopher J Werner et al. "MCNP Users Manual-Code Version 6.2". In: *Los Alamos National Laboratory, LA-UR-17-29981* (2017).

[78] Christopher John Werner et al. *MCNP version 6.2 release notes*. Tech. rep. Los Alamos National Lab.(LANL), Los Alamos, NM (United States), 2018.

[79] Alain Hébert. "DRAGON5: Designing computational schemes dedicated to fission nuclear reactors for space". In: *Proceedings of Nuclear and Emerging Technologies for Space* (2013), pp. 25–28.

[80] Martin Guillet et al. "Coupled CLASS and DONJON5 3D full-core calculations and comparison with the neural network approach for fuel cycles involving MOX fueled PWRs". In: *Annals of Nuclear Energy* 152 (2021), p. 107971. ISSN: 0306-4549. DOI: https://doi.org/10.1016/j.anucene.2020.107971. URL: http://www.sciencedirect.com/science/article/pii/S0306454920306678.

[81] Alain Hébert. "DRAGON5 and DONJON5, the contribution of École Polytechnique de Montréal to the SALOME platform". In: *Annals of Nuclear Energy* 87 (2016), pp. 12–20.

[82] Silvia Phungky, Alexander Agung, and Sihana. "Analysis of natural convection capability in NuScale primary cooling systems with mixture of uranium and plutonium (mixed oxide) fuel using RELAP5-3D". In: *AIP Conference Proceedings*. Vol. 2223. 1. AIP Publishing LLC. 2020, p. 030002.

[83] World Nuclear News. *Study confirms NuScale reactor's MOX capability*. 2016. URL: https://www.world-nuclear-news.org/Articles/Study-confirms-NuScale-reactor-s-MOX-capability.

[84] Syed Bahauddin Alam et al. "Small modular reactor core design for civil marine propulsion using micro-heterogeneous duplex fuel. Part I: Assembly-level analysis". In: *Nuclear Engineering and Design* 346 (2019), pp. 157–175. ISSN: 0029-5493. DOI: https://doi.org/10.1016/j.nucengdes.2019.03.005. URL: http://www.sciencedirect.com/science/article/pii/S0029549319300391.

[85] Syed Bahauddin Alam et al. "Small modular reactor core design for civil marine propulsion using micro-heterogeneous duplex fuel. Part II: whole-core analysis". In: *Nuclear Engineering and Design* 346 (2019), pp. 176–191. ISSN: 0029-5493. DOI: https:

//doi.org/10.1016/j.nucengdes.2019.03.004. URL: http://www.sciencedirect.com/science/article/pii/S002954931930038X.

[86] Neil C. Hyatt. "Plutonium management policy in the United Kingdom: The need for a dual track strategy". In: *Energy Policy* 101 (2017), pp. 303–309. ISSN: 0301-4215. DOI: https://doi.org/10.1016/j.enpol.2016.08.033. URL: http://www.sciencedirect.com/science/article/pii/S030142151630458X.

[87] Nuclear Decommissioning Authority. "Progress on approaches to the management of separated plutonium". In: *Position Paper, January* (2014).

[88] Weston M Stacey. *Nuclear reactor physics*. Vol. 2. Wiley Online Library, 2007.

[89] John R Lamarsh, Anthony John Baratta, et al. *Introduction to nuclear engineering*. Vol. 3. Prentice hall Upper Saddle River, NJ, 2001.

[90] Roy F Kim Jr. *Neutron reflector*. US Patent 4,731,220. Mar. 1988.

[91] T Lötsch, V Khalimonchuk, and A Kuchin. "Proposal of a benchmark for core burnup calculations for a WWER-1000 reactor core". In: (2009).

[92] Pratik Joshi. *Which High-Performance Materials Are Used in Nuclear Reactors?* URL: https://matmatch.com/blog/materials-in-nuclear-reactors/.

[93] S. Yamanaka and K. Kurosaki. "2.11 - Neutron Reflector Materials (Be, Hydrides)". In: *Comprehensive Nuclear Materials*. Ed. by Rudy J.M. Konings. Oxford: Elsevier, 2012, pp. 307–321. ISBN: 978-0-08-056033-5. DOI: https://doi.org/10.1016/B978-0-08-056033-5.00021-5. URL: http://www.sciencedirect.com/science/article/pii/B9780080560335000215.

[94] S. Dawahra, K. Khattab, and G. Saba. "Study the effects of different reflector types on the neutronic parameters of the 10MW MTR reactor using the MCNP4C code". In: *Annals of Nuclear Energy* 85 (2015), pp. 1115–1118. ISSN: 0306-4549. DOI: https:

//doi.org/10.1016/j.anucene.2015.07.029. URL: http://www.sciencedirect.com/science/article/pii/S0306454915003928.

[95] *Research Reactor Core Conversion from the Use of Highly Enriched Uranium Fuels: Guidebook*. TECDOC Series 233. Vienna: INTERNATIONAL ATOMIC ENERGY AGENCY, 1980. URL: https://www.iaea.org/publications/484/research-reactor-core-conversion-from-the-use-of-highly-enriched-uranium-fuels-guidebook.

[96] S. Dawahra, K. Khattab, and G. Saba. "Calculation of fuel burnup and radionuclide inventory in the 10MW MTR type research reactor using the GETERA code". In: *Annals of Nuclear Energy* 78 (2015), pp. 89–92. ISSN: 0306-4549. DOI: https://doi.org/10.1016/j.anucene.2015.01.009. URL: http://www.sciencedirect.com/science/article/pii/S0306454915000109.

[97] Farrokh Khoshahval and Farhad Salari. "Sensitivity analyses of the use of different reflector materials on the neutronics parameters of Tehran research reactor". In: *Progress in Nuclear Energy* 93 (Nov. 2016), pp. 351–361. ISSN: 0149-1970. DOI: 10.1016/J.PNUCENE.2016.09.009. URL: https://www.sciencedirect.com/science/article/pii/S0149197016302104%7B%5C#%7D!.

[98] J R Deen, W L Woodruff, and C I Costescu. "WIMS-D4M user manual". In: (July 1995). DOI: 10.2172/197846. URL: https://www.osti.gov/biblio/197846.

[99] TB Fowler and DR Vondy. *Nuclear reactor core analysis code: CITATION*. Tech. rep. Oak Ridge National Lab., Tenn., 1969.

[100] J.M. Beeston. "Beryllium metal as a neutron moderator and reflector material". In: *Nuclear Engineering and Design* 14.3 (1971), pp. 445–474. ISSN: 0029-5493. DOI: https://doi.org/10.1016/0029-5493(70)90161-5. URL: http://www.sciencedirect.com/science/article/pii/0029549370901615.

[101] Dan Ilas. "Impact of HFIR LEU Conversion on Beryllium Reflector Degradation Factors". In: (Oct. 2013). DOI: 10.2172/1096323.

[102] Francesc Puig and Haile Dennis. "Neutron fluence effects on SLOWPOKE-2 beryllium reflector composition and reactivity". In: *Nuclear Engineering and Design* 305 (Aug. 2016), pp. 451–460. ISSN: 0029-5493. DOI: 10.1016/J.NUCENGDES.2016.05.033. URL: https://www.sciencedirect.com/science/article/pii/S0029549316301662%7B%5C#%7Db0025.

[103] S Atkinson et al. "Small modular high temperature reactor optimisation–Part 1: A comparison between beryllium oxide and nuclear graphite in a small scale high temperature reactor". In: *Progress in Nuclear Energy* 111 (2019), pp. 223–232.

[104] A. Sargeni, K. W. Burn, and G. B. Bruna. "The impact of heavy reflectors on power distribution perturbations in large PWR reactor cores". In: *Annals of Nuclear Energy* 94 (2016), pp. 566–575. ISSN: 18732100. DOI: 10.1016/j.anucene.2016.03.015. URL: http://dx.doi.org/10.1016/j.anucene.2016.03.015.

[105] Julien Taforeau, Marc Muller, and Vivian Salino. "Modeling of heavy reflectors using DONJON-5". In: *Annals of Nuclear Energy* 127 (May 2019), pp. 319–325. ISSN: 0306-4549. DOI: 10.1016/J.ANUCENE.2018.12.017. URL: https://www.sciencedirect.com/science/article/pii/S0306454918306728%7B%5C#%7D!.

[106] JJ Lautard and F Moreau. "A fast 3D parallel solver based on the mixed dual finite element approximation". In: *Proceedings of the American Nuclear Society Topical Meeting on Mathematical Methods and Supercomputing in Nuclear Applications, Karlsruhe, Allemagne*. 1993.

[107] JJ Lautard, S Loubière, and C Fedon-Magnaud. *CRONOS: a modular computational system for neutronic core calculations*. Tech. rep. 1992.

[108] Paul Reuss. *Neutron physics*. EDP sciences, 2012.

[109] John R Lamarsh. *Introduction to nuclear reactor theory / John R. Lamarsh.* eng. Reading, Mass., 1966.

[110] G. I. Bell and S. Glasstone. "Nuclear Reactor Theory". In: (Oct. 1970). URL: https://www.osti.gov/biblio/4074688.

[111] Madeline Anne Feltus. "Fission Reaction Physics". In: *Encyclopedia of Physical Science and Technology (Third Edition)*. Ed. by Robert A. Meyers. Third Edition. New York: Academic Press, 2003, pp. 893–906. ISBN: 978-0-12-227410-7. DOI: https://doi.org/10.1016/B0-12-227410-5/00245-3. URL: https://www.sciencedirect.com/science/article/pii/B0122274105002453.

[112] Raymond L. Murray and Keith E. Holbert. "Chapter 16 - Neutron Chain Reactions". In: *Nuclear Energy (Eighth Edition)*. Ed. by Raymond L. Murray and Keith E. Holbert. Eighth Edition. Butterworth-Heinemann, 2020, pp. 291–305. ISBN: 978-0-12-812881-7. DOI: https://doi.org/10.1016/B978-0-12-812881-7.00016-2. URL: https://www.sciencedirect.com/science/article/pii/B9780128128817000162.

[113] M.D. Siegel and C.R. Bryan. "11.6 - Radioactivity, Geochemistry, and Health". In: *Treatise on Geochemistry (Second Edition)*. Ed. by Heinrich D. Holland and Karl K. Turekian. Second Edition. Oxford: Elsevier, 2014, pp. 191–256. ISBN: 978-0-08-098300-4. DOI: https://doi.org/10.1016/B978-0-08-095975-7.00906-2. URL: https://www.sciencedirect.com/science/article/pii/B9780080959757009062.

[114] A. Worrall. "4 - Core and fuel technologies in integral pressurized-water reactors (iPWRs)". In: *Handbook of Small Modular Nuclear Reactors*. Ed. by Mario D. Carelli and Daniel T. Ingersoll. Woodhead Publishing Series in Energy. Woodhead Publishing, 2015, pp. 79–102. ISBN: 978-0-85709-851-1. DOI: https://doi.org/10.1533/9780857098535.2.79. URL: https://www.sciencedirect.com/science/article/pii/B9780857098511500042.

[115] D. Staicu. "2.17 - Thermal Properties of Irradiated UO2 and MOX". In: *Comprehensive Nuclear Materials*. Ed. by Rudy J.M. Konings. Oxford: Elsevier, 2012, pp. 439–464. ISBN: 978-0-08-056033-5. DOI: https://doi.org/10.1016/B978-0-08-056033-5.00038-0. URL: https://www.sciencedirect.com/science/article/pii/B9780080560335000380.

[116] Anil K Prinja and Edward W Larsen. "General principles of neutron transport". In: *Handbook of nuclear engineering*. 2010.

[117] Jure Beričič and Luka Snoj. "On the calculation of angular neutron flux in MCNP". In: *Annals of Nuclear Energy* 100 (2017), pp. 128–149. ISSN: 0306-4549. DOI: https://doi.org/10.1016/j.anucene.2016.10.014. URL: https://www.sciencedirect.com/science/article/pii/S0306454916309367.

[118] Edward W Larsen. "An overview of neutron transport problems and simulation techniques". In: *Computational Methods in Transport* (2006), pp. 513–534.

[119] Liangzhi Cao. "1 - Neutron transport equation". In: *Deterministic Numerical Methods for Unstructured-Mesh Neutron Transport Calculation*. Ed. by Liangzhi Cao and Hongchun Wu. Woodhead Publishing Series in Energy. Woodhead Publishing, 2021, pp. 1–34. ISBN: 978-0-12-818221-5. DOI: https://doi.org/10.1016/B978-0-12-818221-5.00003-9. URL: https://www.sciencedirect.com/science/article/pii/B9780128182215000039.

[120] British Electricity International. "CHAPTER 3 - Nuclear power station operation". In: *Nuclear Power Generation (Third Edition)*. Ed. by British Electricity International. Third Edition. British Electricity International. Oxford: Pergamon, 1992, pp. 341–483. ISBN: 978-0-08-040519-3. DOI: https://doi.org/10.1016/B978-0-08-040519-3.50010-X. URL: http://www.sciencedirect.com/science/article/pii/B978008040519350010X.

[121] Sümer Şahin and Yican Wu. "3.14 Fission Energy Production". In: *Comprehensive Energy Systems*. Ed. by Ibrahim Dincer. Oxford: Elsevier, 2018, pp. 590–637. ISBN:

978-0-12-814925-6. DOI: https://doi.org/10.1016/B978-0-12-809597-3.00331-X. URL: https://www.sciencedirect.com/science/article/pii/B978012809597300331X.

[122] E E Lewis and W F Miller. "Computational methods of neutron transport". In: (Jan. 1984). URL: https://www.osti.gov/biblio/5538794.

[123] Rainer Koch and Ralf Becker. "Evaluation of quadrature schemes for the discrete ordinates method". In: *Journal of Quantitative Spectroscopy and Radiative Transfer* 84.4 (2004). Eurotherm Seminar 73 - Computational Thermal Radiation in Participating Media, pp. 423–435. ISSN: 0022-4073. DOI: https://doi.org/10.1016/S0022-4073(03)00260-7. URL: https://www.sciencedirect.com/science/article/pii/S0022407303002607.

[124] WA Fiveland. "Discrete-ordinates solutions of the radiative transport equation for rectangular enclosures". In: (1984).

[125] Claus Müller. *Spherical harmonics*. Vol. 17. Springer, 2006.

[126] Dingkang Zhang and Farzad Rahnema. "An efficient hybrid stochastic/deterministic coarse mesh neutron transport method". In: *Annals of Nuclear Energy* 41 (2012), pp. 1–11. ISSN: 0306-4549. DOI: https://doi.org/10.1016/j.anucene.2011.09.024. URL: https://www.sciencedirect.com/science/article/pii/S0306454911003914.

[127] David Price and Kurt Skold. *Neutron scattering*. Academic Press, 1987.

[128] Reuven Y Rubinstein and Dirk P Kroese. *Simulation and the Monte Carlo method*. Vol. 10. John Wiley & Sons, 2016.

[129] Luc Devroye. "Sample-based non-uniform random variate generation". In: *Proceedings of the 18th conference on Winter simulation*. 1986, pp. 260–265.

[130] Jaakko Leppänen et al. *Development of a new Monte Carlo reactor physics code*. VTT Technical Research Centre of Finland, 2007.

[131] William L. Dunn and J. Kenneth Shultis. "4 - Sampling, Scoring, and Precision". In: *Exploring Monte Carlo Methods*. Ed. by William L. Dunn and J. Kenneth Shultis. Amsterdam: Elsevier, 2012, pp. 69–96. ISBN: 978-0-444-51575-9. DOI: https://doi.org/10.1016/B978-0-444-51575-9.00004-X. URL: https://www.sciencedirect.com/science/article/pii/B978044451575900004X.

[132] Sheldon Ross. "- Simulation". In: *Introduction to Probability Models (Eleventh Edition)*. Ed. by Sheldon Ross. Eleventh Edition. Boston: Academic Press, 2014, pp. 645–706. ISBN: 978-0-12-407948-9. DOI: https://doi.org/10.1016/B978-0-12-407948-9.00011-6. URL: https://www.sciencedirect.com/science/article/pii/B9780124079489000116.

[133] Jeffery Lewins. "CHAPTER 4 - Linear Reactor Process Dynamics with Feedback". In: *Nuclear Reactor Kinetics and Control*. Ed. by Jeffery Lewins. Pergamon, 1978, pp. 76–127. ISBN: 978-0-08-021682-9. DOI: https://doi.org/10.1016/B978-0-08-021682-9.50011-7. URL: https://www.sciencedirect.com/science/article/pii/B9780080216829500117.

[134] Ivan Lux. *Monte Carlo particle transport methods*. CRC press, 2018.

[135] DF Hollenbach, LM Petrie, NF Landers, et al. "KENO-VI: a general quadratic version of the KENO program". In: *ORNL/TM-2005/39, Version* 6 (1995).

[136] Yousef Alzaben, Victor H Sánchez-Espinoza, and Robert Stieglitz. "On the Use of Serpent for SMR Modeling and Cross Section Generation". In: (2016).

[137] Paul K. Romano et al. "Depletion capabilities in the OpenMC Monte Carlo particle transport code". In: *Annals of Nuclear Energy* 152 (2021), p. 107989. ISSN: 0306-4549. DOI: https://doi.org/10.1016/j.anucene.2020.107989. URL: https://www.sciencedirect.com/science/article/pii/S030645492030685X.

[138] Paul K. Romano et al. "OpenMC: A state-of-the-art Monte Carlo code for research and development". In: *Annals of Nuclear Energy* 82 (2015). Joint International Con-

ference on Supercomputing in Nuclear Applications and Monte Carlo 2013, SNA + MC 2013. Pluri- and Trans-disciplinarity, Towards New Modeling and Numerical Simulation Paradigms, pp. 90–97. ISSN: 0306-4549. DOI: https://doi.org/10.1016/j.anucene.2014.07.048. URL: https://www.sciencedirect.com/science/article/pii/S030645491400379X.

[139] Paul K. Romano and Benoit Forget. "The OpenMC Monte Carlo particle transport code". In: *Annals of Nuclear Energy* 51 (2013), pp. 274–281. ISSN: 03064549. DOI: 10.1016/j.anucene.2012.06.040.

[140] Jaakko Leppänen et al. "The Serpent Monte Carlo code: Status, development and applications in 2013". In: *Annals of Nuclear Energy* 82 (2015). Joint International Conference on Supercomputing in Nuclear Applications and Monte Carlo 2013, SNA + MC 2013. Pluri- and Trans-disciplinarity, Towards New Modeling and Numerical Simulation Paradigms, pp. 142–150. ISSN: 0306-4549. DOI: https://doi.org/10.1016/j.anucene.2014.08.024. URL: https://www.sciencedirect.com/science/article/pii/S0306454914004095.

[141] L. Dagum and R. Menon. "OpenMP: an industry standard API for shared-memory programming". In: *IEEE Computational Science and Engineering* 5.1 (1998), pp. 46–55. DOI: 10.1109/99.660313.

[142] D. A. Brown et al. "ENDF/B-VIII.0: The 8th Major Release of the Nuclear Reaction Data Library with CIELO-project Cross Sections, New Standards and Thermal Scattering Data". In: *Nuclear Data Sheets* 148 (2018), pp. 1–142. ISSN: 00903752. DOI: 10.1016/j.nds.2018.02.001.

[143] Arjan JM Plompen et al. "The joint evaluated fission and fusion nuclear data library, JEFF-3.3". In: *The European Physical Journal A* 56.7 (2020), pp. 1–108.

[144] Aarno Isotalo. "Comparison of Neutronics-Depletion Coupling Schemes for Burnup Calculations–Continued Study". In: *Nuclear Science and Engineering* 180.3 (2015),

pp. 286–300. DOI: 10.13182/NSE14-92. eprint: https://doi.org/10.13182/NSE14-92. URL: https://doi.org/10.13182/NSE14-92.

[145] Giorgio Locatelli, Chris Bingham, and Mauro Mancini. "Small modular reactors: A comprehensive overview of their economics and strategic aspects". In: *Progress in Nuclear Energy* 73 (2014), pp. 75–85.

[146] Department of Energy and Climate Change (DECC). "Small Modular Reactors Competition Phase One". In: *HM Government Webpages* March (2016). URL: http://rebrand.ly/il1mow.

[147] Ian Scott. "21 - Stable salt fast reactor". In: *Molten Salt Reactors and Thorium Energy*. Ed. by Thomas J. Dolan. Woodhead Publishing, 2017, pp. 571–580. ISBN: 978-0-08-101126-3. DOI: https://doi.org/10.1016/B978-0-08-101126-3.00021-X. URL: http://www.sciencedirect.com/science/article/pii/B978008101126300021X.

[148] PN Smith, JN Lillington, and CA Middlemas. "Radiation Transport Modelling and the ANSWERS Code Suite". In: *Nuclear Future* 2.2 (2011), pp. 44–49.

[149] International Atomic Energy Agency. "Advances in Small Modular Reactor Technology Developments". In: (2014), p. 150.